Etude expérimentale de la modification des charges aérodynamiques sur pale d'éolienne par du contrôle d'écoulement actif

Sophie Baleriola

Centre Val de Loire UNIVERSITÉ Spirit of the Loire Valley

UNIVERSITÉ D'ORLÉANS

UNIVERSITE D'ORLEANS

ÉCOLE DOCTORALE ÉNERGIE, MATÉRIAUX, SCIENCES DE LA TERRE ET DE L'UNIVERS

Laboratoire PRISME

Thèse présentée par :

Sophie BALERIOLA

Soutenue le : **7 décembre 2018**

pour obtenir le grade de : **Docteur de l'Université d'Orléans**

Discipline: **Énergétique et Mécanique des Fluides**

Étude expérimentale de la modification des charges aérodynamiques sur pale d'éolienne par du contrôle d'écoulement actif

Experimental investigation of aerodynamic loads modification on wind turbine blades with active flow control

THÈSE dirigée par:

Annie LEROY	Maître de Conférences, HDR, Université d'Orléans, PRISME, Directrice de thèse
Philippe DEVINANT	Professeur, Université d'Orléans, PRISME, Directeur de thèse

RAPPORTEURS:

Gerard VAN BUSSEL	Professeur, Delft University of Technology
Christian MASSON	Professeur, École de Technologie Supérieure de Montréal

---

JURY :

Gerard VAN BUSSEL	Professeur, Delft University of Technology
Christian MASSON	Professeur, École de Technologie Supérieure de Montréal
Christophe SICOT	Maître de Conférences, ISAE-ENSMA, PPRIME
Laurent KEIRSBULCK	Professeur, Université de Valenciennes, LAMIH
Sandrine AUBRUN	Professeur, École Centrale de Nantes, LHEEA
Annie LEROY	Maître de Conférences, HDR, Université d'Orléans, PRISME
Philippe DEVINANT	Professeur, Université d'Orléans, PRISME

Acknowledgements

Je tiens tout d'abord à remercier les deux personnes qui ont dirigé et encadré ce travail pendant ces trois années de thèse: Annie Leroy et Philippe Devinant. Je vous remercie chaleureusement pour vos conseils, votre écoute et votre disponibilité tout au long de l'aventure. Merci pour la liberté que vous m'avez accordée dans l'organisation de mon projet et travail de thèse. Je suis très heureuse d'avoir travaillé avec vous. Merci également de m'avoir donné la possibilité de présenter mon travail lors de congrès ainsi que d'effectuer de l'enseignement pendant ces trois ans.

Je remercie également Sandrine Aubrun, coordinatrice du projet SMARTEOLE (chef!) et animatrice de l'axe ESA avant son départ pour Nantes. Merci pour ta sympathie, tes conseils et ton aide, en particulier lors des essais expérimentaux. Travailler avec toi et continuer ton travail sur le banc éolien du laboratoire a été un réel plaisir.

Je remercie aussi Christian Masson et Gerard van Bussel pour avoir accepté de rapporter ce travail de thèse ainsi que pour leurs remarques et leurs critiques constructives avant et pendant la soutenance. Merci beaucoup également à Christophe Sicot, qui a été mon professeur à l'ENSMA, et à Laurent Keirsbulck pour leur participation à mon jury de thèse.

Merci énormément à Stéphane (patate!) Loyer (ou chèvre), gardien de la soufflerie, sans qui cette thèse n'aurait pu être. Merci d'avoir accompagné les meilleurs essais des meilleurs délires. Merci pour ta bonne humeur, ta patience (eh si!), ton énergie et ton talent! Merci également à Julien Lemaire (Juju) la personne la plus tenace et appliquée que je connais. Merci beaucoup de m'avoir écoutée, conseillée et soutenue tout au long de la thèse et merci pour toutes les blagues foireuses (ou pas) qu'on a pu concocter ensemble. On aura bien rigolé quand même (Stéphane moins). Je remercie aussi Nicolas (Dumuis), l'électron libre de la troupe. Merci pour tous ces cafés qu'on a pris ensemble, pour ta joie et ta bonne humeur. Bonne chance pour tous tes projets, tu mérites le meilleur! Merci aussi à Monsieur Pierric Joseph, Anne-Lise (Chouchou) et Eugénie pour leur amitié lors de leur période orléanaise. Vous êtes géniaux, ne changez pas!

Merci également à mon "chevalier de la tour rose", Kévin Chatelain (Kéké) qui m'a formé aux décharges plasma et à Raffaele Volpe (Raff) pour qui la PIV n'a aucun secret. Merci à vous deux pour ce que vous m'avez apporté, bien au delà du cadre de la thèse! Vous resterez toujours un petit peu mon petit frère et mon grand frère respectivement...

Merci beaucoup à mes collègues de bureau: Audrey Feuvrier, Francesco Stella, Marco Castagna, Stefano Macrì, Eliott Varon, et les petits nouveaux Roshan Shanmughan et Wassim Zeidan, bon courage à vous tous! Sans oublier les stagiaires qui sont passés par l'équipe tout au long de ces trois ans: Bastien, Lucas, Binh, Alexis et Tâm. Muchísimas gracias también a Ana Ibarra y a Eulalio Torres pour vuestro cariño y apoyo. Os deseo todo lo mejor para el futuro.

Je remercie aussi les membres de l'équipe ECM sans qui les cafés seraient un peu moins égayés: merci à Yahia Haidous, Pierre Bréquigny, Bruno Moreau, Benoît Bellicaud, Camille Hespel, Fabrice Foucher, Kristan Gillet et en particulier à Christine Rousselle: merci pour ta joie, ton

soutien et tes encouragements permanents! Je n'oublie pas les doctorants de l'équipe avec qui on a partagé maints repas au RU: Nicolas Seignour, Anthony Roque, Ob Nilaphai, Salim Sayssouk, Antoine Simon, Charles Lhuillier, Marco Di Lorenzo, Mounia Hammoudi et Jean Kuchly.

Je remercie aussi les personnes avec lesquelles j'ai pu travailler dans le cadre de l'enseignement à Polytech'Orléans: Nicolas Mazellier, Régine Webber et Guillaume Colin. Bon courage également à Pierre-Yves Passaggia dans son aventure au sein de l'école et de l'équipe ESA. Merci également à tous ceux qui nous aident au quotidien d'un point de vue administratif et technique: Sylvie Plessard, Benoît Clavier, Pierre Amelot et Muriel Obert.

Je souhaite également remercier les membres du projet SMARTEOLE avec lesquels j'ai pu échanger et travailler de près ou de loin: Dominique Nelson-Gruel, Caroline Braud, Vincent Jaunet, Emmanuel Guilmineau, Fabrice Guillemin, Nicolas Girard, Thomas Duc, Matthieu Boquet, Dimitri Peaucelle, Daniel Averbuch et Frédéric Blondel. Merci beaucoup également à Hervé Rabat et à Dunpin Hong du GREMI avec qui j'ai pu collaborer durant cette thèse.

Je remercie également ma famille et mes amis les plus proches pour m'avoir soutenu tout le long de ce périple. Et surtout, merci à toi, Gwen, compagnon d'aventures.

Contents

List of Figures

List of Tables

List of Symbols

c	Airfoil chord [m]
α	Angle of attack [°]
ρ	Air density [kg/m^3]
ν	Air kinetic viscosity [m^2/s]
Γ	Circulation [m^2/s]
U_∞	Incoming flow velocity [m/s]
P_∞	Static pressure upstream of the model [Pa]
Re	Reynolds number []
St	Strouhal number []
C_L	Global lift coefficient []
C_l	Local lift coefficient []
C_D	Global drag coefficient []
C_d	Local drag coefficient []
C_n	Local normal force coefficient []
C_t	Local tangential force coefficient []
C_p	Pressure coefficient []
C_μ	Momentum coefficient []
C_R	Roll coefficient []
V_{AC}	Applied voltage to the plasma actuator [V]
f_{AC}	Applied frequency to the plasma actuator [Hz]
U	Velocity in the streamwise direction [m/s]
V	Velocity in the direction normal to the airfoil chord [m/s]
T_u	Turbulence intensity in the streamwise direction [%]
k	Turbulent kinetic energy [m^2/s^2]
Ω	Rotational velocity of the turbine [rad s^{-1}]
β	Blade pitch angle [°]
R	Radius of the turbine [m]
W_r	Relative velocity at a blade radial position r [m/s]
λ	Tip-speed ratio of the turbine []
C_{power}	Power coefficient of the turbine []
C_{thrust}	Thrust coefficient of the turbine []
M_{fbm}	Flapwise Bending Moment at the blade root [N m]

List of Abbreviations

ABL	Atmospheric Boundary Layer
AFC	Active Flow Control
BL	Boundary Layer
CoE	Cost of Energy
CC	Circulation Control
DBD	Dielectric Barrier Discharge
EAWE	European Academy of Wind Energy
EHD	ElectroHydroDynamic
HAWT	Horizontal Axis Wind Turbine
HW	Hot-Wire
HWA	Hot-Wire Anemometry
LE	Leading-Edge
LiDAR	Light Detection And Ranging
PIV	Particle Image Velocimetry
POD	Proper Orthogonal Decomposition
PSD	Power Spectral Density
TE	Trailing-Edge
TKE	Turbulent Kinetic Energy
WJ	Wall Jet
WT	Wind Turbine

Introduction

Wind energy is a clean and renewable source of energy that remains one of the solutions to cut carbon emissions and curb global warming in the field of power generation. However, wind energy technology is wrongly considered as mature as there is still room for improvement, specially to increase the rotor lifetime.

The wind that arrives to a turbine is highly turbulent i.e. highly unsteady and inhomogeneous. This turbulence is evidenced by wind gusts that abruptly change the angle of attack and the velocity of the flow arriving to the rotor. When these gusts reach the rotor, blades endure important mechanical loads that damage the blade roots and reduce the rotor life duration. Load fluctuation reduction is indeed one of the current priorities of the wind energy research community.

Nowadays, wind turbines take the information about the incoming wind above their nacelle, with a wind vane for the wind direction and an anemometer for the wind velocity. Turbines can therefore be yawed to face the wind and adapt the blade pitch angle depending on the incoming wind. However, as the information is taken on the turbine itself, the turbine pitch reaction arrives when the gust is already at the rotor location or even past it. This response takes place often too late, is more curative than preventive and uses the pitch variation system in a meaningless way.

To address this issue, the idea is to look towards the future, towards the flow that will arrive to the turbine while keeping also an eye on the flow over the blades. Hence, this smart rotor, equipped with a series of sensors and actuators, would react in real time to the incoming wind to immediately compensate the overloads. Pitch regulation would be used to counteract large wind perturbations whereas other innovative flow control strategies would target smaller scales by acting on some well chosen blade spans.

Active flow control strategies aiming at reducing these fluctuations are not mature enough yet to be implemented in operating wind turbines but are actively studied at a laboratory scale. In the framework of the SMARTEOLE project, two not conventional flow control strategies, plasma actuators and fluidic jets, are implemented and tested in the controlled environment of a wind-tunnel to perform a circulation control by acting in the vicinity of the rounded trailing-edge of the blade in order to modify its lift force. Both devices are not intrusive, do not require mobile parts and are relatively simple to implement.

The present thesis objective is the optimisation of the wind energy production by alleviating blade load fluctuations with active flow control strategies. The approach taken for the intended flow control applications is purely experimental and takes place within the Aerodynamics Group of PRISME laboratory.

Chapter 1 introduces the context of the project. An overview of horizontal axis wind turbines is done as well as an analysis of blade load fluctuations. A bibliographical review about active flow control devices is also presented. Finally, the present thesis work is placed within the context of the SMARTEOLE project and the motivations of the work are described.

Both plasma and fluidic strategies are first tested in parallel in a two-dimensional configuration. In the scope of the present thesis, only the experimental work concerning the plasma

actuation is carried out and is presented in **chapter 2**. Each investigated actuator is positioned around the trailing-edge in a way that allows to increase or to decrease the lift force. The purpose of the chapter is to evaluate the effects of the actuation on the aerodynamic loads and to analyse the actuation impact on the wake flow. Furthermore, the topologies of the jets induced by the actuators around the model curvature in quiescent air conditions are assessed. The chapter closes with the comparison between plasma and fluidic strategies for this 2D-configuration. It will be explained that, for efficiency and reliability reasons, it is chosen to pursue the project towards the rotational configuration with the fluidic jets actuation.

Blades designed for being mounted in the wind turbine bench of the laboratory are first tested in a translational configuration as presented in **chapter 3**. These blades blow compressed air near the trailing-edge with a series of discrete jets. The purpose of this preliminary study is to evaluate the potential of the jet actuation without rotational effects but with a free blade tip set-up. The efficiency of the actuation is explored through load and pressure distribution measurements. An important sensor is added, however: strain gages are implemented at the blade root to measure its flapwise bending moment with a sensor integrated into the blade.

Chapter 4 is devoted to the fluidic flow control testings in a rotational configuration i.e. on the wind turbine bench of the laboratory. The bench is instrumented with several sensors that permit to measure the blade flapwise bending moment, the torque and drag of the turbine and the chordwise pressure distribution at two radial positions. The objective of the chapter is to understand the mechanisms of the actuation in a rotational configuration for different rotational velocities and pitch angles. Furthermore, the potentialities of the actuation for load modification are assessed.

A short **chapter 5** tries to step back and analyse the overall efficiency of the implemented actuations in terms of power but also regarding the aerodynamical loads. In order to quantify the eventual gains on life duration with the actuation, fatigue models are also considered.

The last chapter presents the conclusions of the thesis work and the main perspectives. It will be explained that the work in the field of active flow control applied to wind turbine blades has to be continued both through experimental and numerical approaches.

Chapter 1

General context of the project

Contents

1.1 Introduction

This chapter introduces the thesis manuscript and is devoted to place the overall project in its context. In the ongoing dynamic of greenhouse gases emission reduction, green energies such as solar, biomass, hydraulic or wind energy are becoming global and industrialised sources of power. In 2015, the EWEA[1]'s Central Scenario predicted 320 GW of wind power in Europe in 2030 (254 GW on-shore and 66 GW off-shore). This wind power capacity is actually more than twice as much as the installed power in 2014. In this framework, wind energy technologies are wrongly considered as mature because there is still room for optimisations, specially in the domain of rotor life duration increase and cost of energy (CoE) reduction.

First, this chapter presents an overview of horizontal axis wind turbines (HAWT) characteristics. A description of the different components of an industrial turbine is made. The working principle of a wind turbine is explained through the simplified model of the actuator disk theory. Also, the aerodynamics of an airfoil in a translational and a rotational configuration are

[1]European Wind Energy Association, now WindEurope

explained. A section is also devoted to the atmospheric boundary layer, its properties and its impact on operating wind turbines.

The second part of the chapter concerns the load fluctuations on wind turbine blades induced by wind turbulence. Are explained in this section the characteristics of load fluctuations, the gains that should be performed with active flow control strategies to overcome the wind perturbations and the methods of a wind modification reproduction at a wind-tunnel scale.

The third part goes through the currently investigated flow control strategies applied to wind turbine blades. The principles of circulation control and of separation control, the two main flow control approaches, are described. Then, a short state of the art introduces several flow control devices and their potential gains in terms of load alleviation.

Finally is explained the context of the present study within the French national project SMARTEOLE as well as the work carried out in the scope of the thesis work.

1.2 Overview on HAWT features

1.2.1 HAWTs architecture & components

Nowadays, most of the wind turbines devoted to electricity production are horizontal axis wind turbines in an upwind configuration, meaning that the rotor is located in the front of the power unit as turbines in figure 1.1. Generally, the **rotor** is composed of three **blades** rotating with the incoming wind, capturing its kinetic energy and converting it to mechanical energy. In the last decades, rotor diameters kept increasing to capture as much wind as possible and the current largest wind turbine (Vestas V164) has a rotor diameter of 164 m. Turbine rotor is attached to a **low-speed shaft**, itself connected to a **gear box** that increases the rotor speed (≈ 20 rpm) to the higher rotational velocities (1200 to 1800 rpm) required by the electricity generator. This **generator** converts the mechanical energy of the **high-speed shaft** into electrical energy which can be transferred to the power grid or stored. Gear box and shafts are enclosed in the **nacelle**, located at the top of the **tower** and containing several turbine components. Above the nacelle, wind turbines have two important sensors: an anemometer to measure the wind velocity and a wind vane that determines the wind direction. Both informations are acquired by the **turbine controller** that stops and starts the turbine and makes adjustments when the wind changes. These adjustments result in a modification of the blade pitch (rotation of the blades along their axis) or a change in the turbine yaw (turbine facing the wind). Wind turbines also have emergency brakes used mainly in case of extreme wind conditions or during parking.

Today, energy is one of the biggest challenges faced by our society and renewable technologies will become increasingly important. Even if wind energy is a quite mature technology, van Kuik et al. [2016] presented the long-term challenges in the wind energy field in behalf of the EAWE[2]. This report explores several topics related to the wind industry, assesses the technological and scientific barriers and defines the priorities for future works. Discussed topics are very diverse: materials and structures, aerodynamics and wind turbulence, turbine control, electromechanical conversion, reliability, design methods, off-shore challenges, the electrical power system as well as the societal and economical aspects.

1.2.2 Working principle - Betz theory

The ***actuator disk*** theory is a simplified model of a wind turbine working principle where the rotor is represented by a disk traversed by the air flow. This model allows to understand and evaluate the global efficiency of a turbine but does not take into account the geometrical properties of the rotor and its blades (number of blades, blade twist, change of the blade airfoil along the span...).

[2]European Academy of Wind Energy

Figure 1.1: Picture of an off-shore wind farm (from Zentilia)

Figure 1.2 describes the *actuator disk* model: A represents the stream tube section, U the flow velocity and P its pressure. Subscript $\langle\cdot\rangle_0$ refers to the position upstream of the turbine, subscript $\langle\cdot\rangle_1$ to downstream of the turbine, and subscript $\langle\cdot\rangle_r$ refers to the rotor location. At the turbine, U_r is smaller than U_0 and the rotor experiences a pressure drop from P_{r0} to P_{r1}.

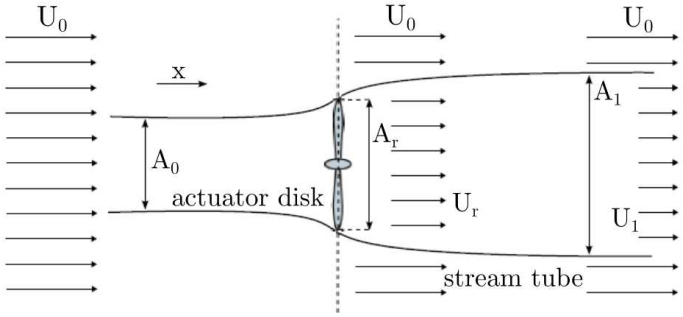

Figure 1.2: Scheme illustrating the *actuator disk* principle (adapted from Dialoupis [2014])

Power extracted by the turbine $\mathcal{P}$ can be written as:

$$\mathcal{P} = (P_{r1} - P_{r0}) A_r U_r \tag{1.1}$$

Assuming air density a constant, mass flow conservation over the stream tube gives:

$$A_0 U_0 = A_r U_r = A_1 U_1 \tag{1.2}$$

As the flow is slowed down in the vicinity of the turbine and along its wake, tube sections are ordered as $A_0 < A_r < A_1$. Velocity at the rotor location is given by the formula $U_r = (1 - a)U_0$ where a is the axial induction factor (Burton et al. [2001]). Momentum conservation between the incoming flow and the turbine wake results in equation 1.5, where ρ is the air density, mV the flow momentum et $\dot{m}$ the mass flow rate.

$$\frac{\mathrm{d}(mV)}{\mathrm{d}t} = \Delta(\dot{m}V) \tag{1.3}$$

$$= (U_0 - U_1)\rho A_r U_r \tag{1.4}$$

$$= (P_{r0} - P_{r1}) A_r \tag{1.5}$$

Bernoulli theorem between A_0 and A_r, on one hand, and between A_r and A_1 on the other, gives:

$$P_0 - P_{r0} = \frac{1}{2}\rho(U_r^2 - U_0^2) \qquad (1.6) \qquad P_1 - P_{r1} = \frac{1}{2}\rho(U_r^2 - U_1^2) \qquad (1.7)$$

Pressure drop through the rotor can be written as:

$$P_{r0} - P_{r1} = \frac{1}{2}\rho(U_0^2 - U_1^2) \qquad (1.8)$$

By combining with equation 1.5, it yields:

$$U_1 = (1 - 2a)U_0 \qquad (1.9)$$

This equation shows that half of the velocity drop takes place at the turbine location. Force applied to the actuator disk can be written as $\mathcal{F} = (P_{r0} - P_{r1})A_r = 2\rho A_r U_0^2 a(1-a)$. Extracted power $\mathcal{P}$ and power coefficient C_{power} can also be rewritten as:

$$\mathcal{P} = \mathcal{F}U_r = 2\rho A_r U_0^3 a(1-a)^2 \qquad (1.10) \qquad C_{power} = \frac{\mathcal{P}}{\frac{1}{2}\rho U_0^3 A_r} = 4a(1-a)^2 \qquad (1.11)$$

where $\frac{1}{2}\rho U_0^3 A_r$ represents the wind power in the rotor absence. C_{power} is maximal when $\frac{\mathrm{d}C_{power}}{\mathrm{d}a} = 4(1-a)(1-3a) = 0$, which gives a value of $a = \frac{1}{3}$. Then, power coefficient C_{power} is equal to:

$$C_{power_{max}} = \frac{16}{27} = 0.593 \qquad (1.12)$$

This power coefficient limit is known as the **Betz limit**. Figure 1.3 shows the evolution of C_{power} as a function of the axial induction factor a. This limit does not come from the turbine conception but from the fact that the stream tube traversing the turbine expands immediately upstream of the rotor implying that the tube section where the velocity is equal to U_0 is smaller than the section of the actuator disk A_r (area swept by the blades). Existing operational wind turbines attain a power coefficient up to 65% of the Betz limit and extract approximately 40% of the total wind power. Innovative concepts such as ducted wind turbines enhance power output with respect to bare wind turbines by increasing the mass flow passing through the turbine as can be read in van Bussel [2007].

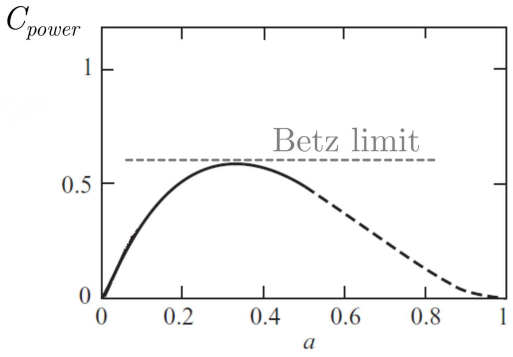

Figure 1.3: Power coefficient C_{power} evolution as a function of the axial induction factor a (from Burton et al. [2001])

1.2.3 Airfoil aerodynamics

In reality, wind turbine blades are composed of several airfoils in the radial direction. These airfoils are of different shape and size along the blade span. This section introduces basic notions of airfoil aerodynamics in translational and rotational configurations.

Translational configuration

When an airfoil is immersed in a fluid in motion, an aerodynamic force acts on the body that can be decomposed in two forces: the **lift** force and the **drag** force. Usually, loads are normalised by the dynamic pressure multiplied per the airfoil surface, giving lift and drag coefficients (C_L and C_D respectively) such as:

$$C_L = \frac{\text{Lift}}{\frac{1}{2}\rho U_\infty^2 S} \tag{1.13}$$

$$C_D = \frac{\text{Drag}}{\frac{1}{2}\rho U_\infty^2 S} \tag{1.14}$$

where ρ is the air density, U_∞ the incoming flow velocity and S the airfoil reference surface. Figure 1.4 shows force coefficients for an airfoil with an **angle of attack** α, defined between the wind direction and the airfoil chord. Normal and tangential force coefficients (C_N and C_T respectively) are in the coordinate system of the airfoil i.e. C_T follows the airfoil chord and C_N is in the chord-normal direction. Lift and drag coefficients are in the wind-related coordinate system as C_D is in the flow direction and C_L is normal to the incoming wind.

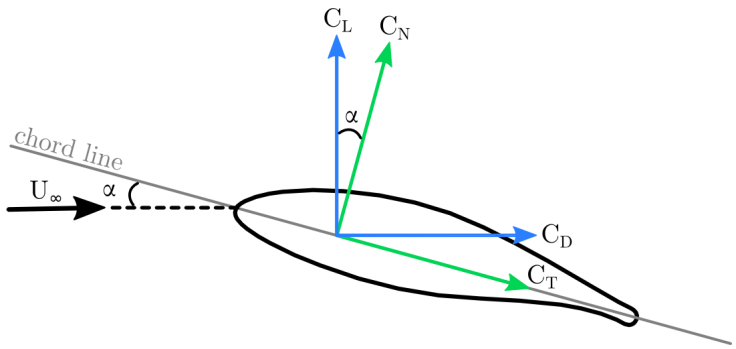

Figure 1.4: Scheme of load coefficients for an airfoil immersed in a 2D-flow

Pitching moment is also of interest and is defined as the moment of the aerodynamic force applied at the aerodynamic center of the airfoil, located at 25% of chord position. Pitch coefficient C_{pitch} is defined as follows, where c is the airfoil chord:

$$C_{pitch} = \frac{\text{Pitch}}{\frac{1}{2}\rho U_\infty^2 S c} \tag{1.15}$$

As reported in Devinant et al. [2002], the properties of an airfoil show three distinct phases for different ranges of angles of attack as shown in figure 1.5:

- **Phase 1:** corresponds to the linear part of the lift curve, where the boundary layer is developed along the pressure and suction sides of the airfoil and remains attached to the model. Drag coefficient in this region is very low and is mainly caused by friction

- **Phase 2:** separation point moves from the trailing-edge (TE) of the airfoil to the leading-edge (LE) inducing an increase in drag. This phenomenon is called *stall*. Two main stall mechanisms are possible: the separation point switches from TE to LE suddenly at a fixed angle of attack, generally due to the burst of a laminar reattachment bubble near the LE (*leading-edge stall*); or, the separation point moves progressively from TE to LE (*trailing-edge stall*). In the case of leading-edge stall, the lift coefficient drops suddenly, whereas for trailing-edge stall its decrease is gradual

- **Phase 3:** the entire airfoil is stalled. Loads are mainly due to the differential pressure between both sides of the airfoil and tend to go towards zero lift and maximal drag at $\alpha = 90°$

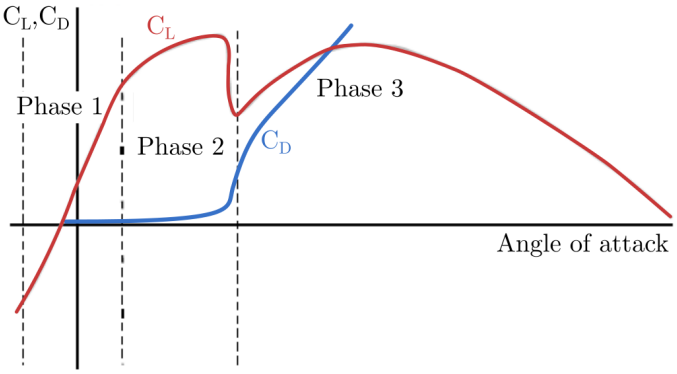

Figure 1.5: Schematic behaviour of lift and drag coefficients (C_L and C_D) evolution with the angle of attack α (adapted from Devinant et al. [2002])

Rotational configuration

Blade airfoil aerodynamics is strongly influenced by the rotation of the rotor. Figure 1.6 shows a two-dimensional blade section at a radial position r subjected to an incoming flow U_∞ and to the turbine rotation at a rotational velocity Ω. The figure assumes that the turbine is not yawed. Incoming velocity is equal to $U_\infty(1-a)$ and rotational velocity to $\Omega r(1+a')$, where a and a' are the axial and radial induction factors respectively. These induction factors take into account the velocity decrease upstream of the rotor induced by the presence of the turbine and its wake. Pitch angle β corresponds to the angle between the chord line and the plane of rotation and is the sum of the blade twist β_{twist} and of the blade pitch angle. Angle α is the angle of attack defined between the blade chord line and the relative velocity $W_r(r)$ direction. Finally, angle ϕ is defined as $\alpha+\beta$. Normal and tangential coefficients (C_N and C_T respectively) are in the airfoil-related coordinate system, whereas lift and drag coefficients (C_L and C_D respectively) are related to the relative velocity coordinate system.

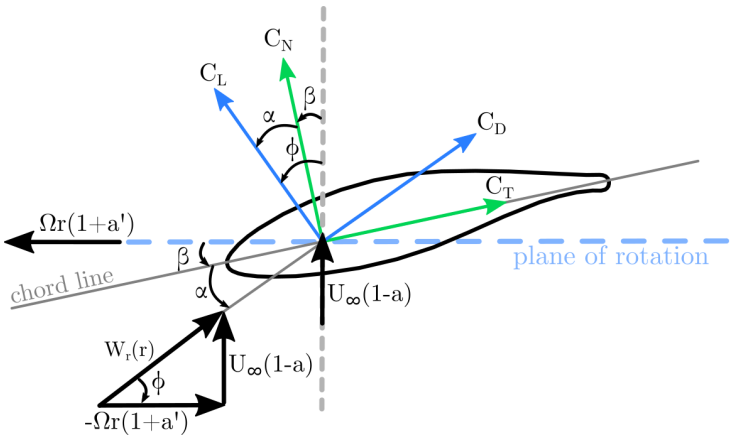

Figure 1.6: Scheme of load coefficients for a rotating blade section

Because of the radial forces and flow separation brought by rotation, the flow field around a rotating blade is highly three-dimensional with extended regions of spanwise flow. 3D-stall spreads from blade root to blade tip with radial centrifugal forces. Rotation delays stall to higher angles of attack as demonstrated by Schreck and Robinson [2002] and Schreck and Robinson [2007] from NREL phase VI wind tunnel testings at NASA Ames. As pointed out in Wood [2005], this phenomenon is due to the reduction of the adverse pressure gradient imposed by the external flow but also by Coriolis and centrifugal forces due to rotation. Radial surface pressure

gradients are linked to the intensity of normal forces and to the chordwise pressure distribution increase. Rotation also induces amplified loads, pronounced unsteadiness, large scale vortical structures and leading-edge vorticity production. With respect to a 2D configuration, rotational loads show higher lift forces for the lower spans (from the hub to $\frac{r}{R} \approx 0.4$) and lower lift and drag forces at the blade tip due to the tip vortex presence. This was shown by Tangler [2004] also on NREL Unsteady Aerodynamics Experiment and their results were also validated by Le Pape and Lecanu [2004] with elsA Navier-Stokes code from ONERA.

Operating HAWT blade characteristics

Scalings related to an industrial-scale wind-turbine are explained below to assess the order of magnitude of real rotors characteristics.

Parameters of the NREL off-shore 5 MW reference wind turbine are shown in table 1.1. It is a three-bladed upwind turbine with variable speed and variable collective pitch (see Jonkman et al. [2009]). This turbine has a rotor diameter of 126 m and its blades are composed of 7 different airfoil shapes from blade root to blade tip, the thicker airfoils being at the lower radial positions. Blades are twisted and maximal chord is equal to 4.6 m. The rated wind speed for this turbine is of 11.4 m/s.

Parameter	Value
Rotor radius R	63 m
Airfoils	Cylinder for blade root, 5 DU airfoils[3] from 18%R to 72%R and NACA64-618 to blade tip
Blade airfoil chord c	Max. 4.6 m at 26%R - Min. 1.4 min at blade tip
Blade airfoil thickness	From 40%c to 18%c at blade tip
Twist β_{twist}	From 13° at blade root to 0.1° at blade tip
Wind speed U_∞	11.4 m/s (rated)
Reynolds number Re	3×10^6 - 5×10^6

Table 1.1: Order of magnitude of blade geometrical properties and turbine charcateristics for a NREL 5 MW turbine (data obtained from Jonkman et al. [2009] and Kooijman et al. [2003])

1.2.4 Atmospheric Boundary Layer - temporal and spatial scales

Wind turbines operate in the **atmospheric boundary layer** (ABL) i.e. the lowest portion of the atmosphere, going from the ground (or ocean) to roughly 1 km above. Wind energy production is therefore subjected to atmospheric conditions and specially to the **inhomogeneity** and the **unsteadiness** of wind. The comprehension of the atmospheric boundary layer stability is of great importance to predict the performances of wind turbines and the annual energy production of a given site. Numerical models and computations are often used to reproduce the ABL and quantify the wind velocity arriving at the turbine as can be read in Sumner and Masson [2006] and Sathe et al. [2012]. Also, LiDAR[4] measurements allow to measure the on-site wind resources as carried out by Torres et al. [2018] to capture wake-to-wake interactions and in Mann et al. [2018] for wind analysis in complex terrain. Most of the turbines operate in a wind velocity range from 4 m/s to 25 m/s and cannot work for higher wind velocities as shown in figure 1.7. Beyond the rated output speed of 14 m/s, the output power of the turbine is constant and equal to its rated power.

[3] DU99-W-405LM, DU99-W-350LM, DU97-W-300LM, DU91-W2-250LM and DU93-W-210LM
[4] Light Detection And Ranging

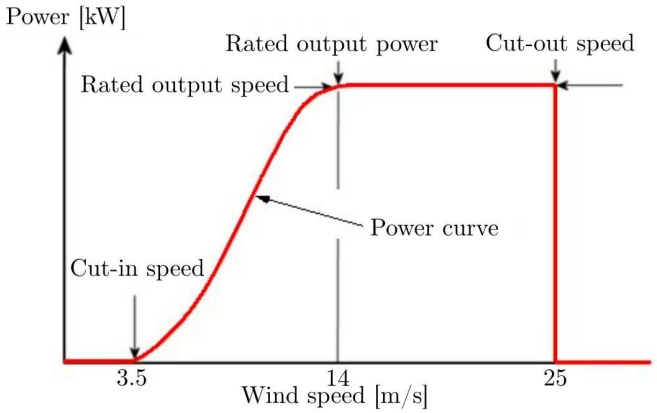

Figure 1.7: Power output as a function of the wind speed for a typical wind turbine (from http://wind-power-program.com/turbine_characteristics.htm)

The electrical production of a wind farm is strongly dependent on the strength and the quality of its wind, which varies in time with various **time scales** (see figure 1.8):

- Small time scales (from seconds to minutes) due to turbulence and inducing load fluctuations on blades. Wind turbulence is characterised by stochastic changes in wind velocity, pressure and direction
- Diurnal and nocturnal variations (time scale of a day)
- Synoptic variations depending on climate conditions (time scale of a few days)
- Annual or longer variations (remain partly unknown and depend strongly on the farm site)

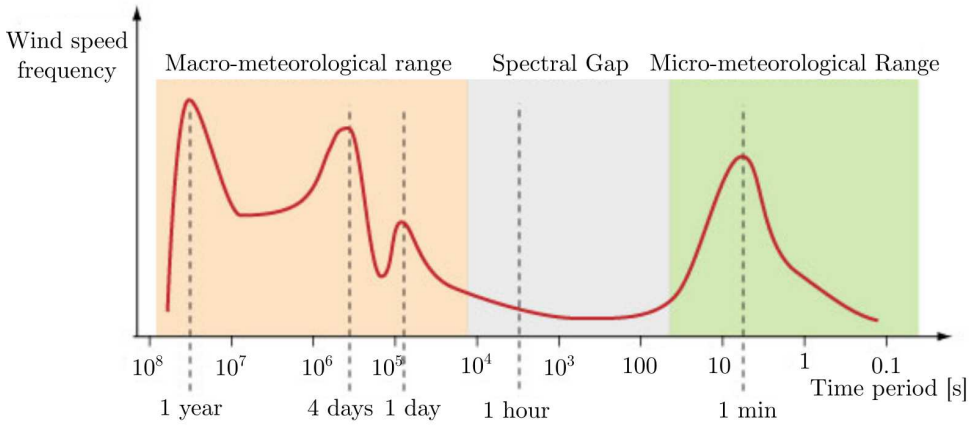

Figure 1.8: Temporal spectra of wind (from http://greenrhinoenergy.com/renewable/wind/wind_characteristics.php)

Furthermore, the atmospheric boundary layer is strongly influenced by the surface roughness, the air temperature and atmospheric Coriolis forces. Such as a *regular* boundary layer, the ABL is divided in several layers and the time-averaged velocity profile increases progressively from the ground to the ABL top. This implies that the higher the turbine mast, the higher the wind speeds experienced by the rotor. Wind turbines operate in the lowest part of this ABL meaning that vertical and horizontal wind shears may be significant. Wind spatial variations can be classified in three main **spatial scales**:

– Small scales (from 1 m to 100 m, corresponding roughly to the blade chord and the rotor diameter respectively) due to wind turbulence. On average, wind turbulence is characterised by temporal scales of about 1 to 10 min and their intensity is of about 16% for a wind speed of 15 m/s

– Local scales due to surface roughness (field topography, nearby obstacles, type of soil and vegetation...)

– Global scales induced by meteorological conditions, the proximity to sea, to mountains, to a flat area...

Small temporal and spatial scales i.e. wind gusts and their stochastic behaviour are one of the main causes of load fluctuations on blades. Apart from wind unsteadiness, turbines are also impacted by the wakes of other turbines which are areas of high turbulence and low wind velocity, leading to power production deficits for downstream turbines. Also, as wind turbine blades are permanently in rotation and due to wind shear and turbulence, blades are subjected to dynamic stall. This phenomena is specially important for vertical axis wind turbines that have a strongly unsteady aerodynamic behaviour that was characterised via PIV measurements in Ferreira et al. [2009].

Table 1.2 (from van Kuik et al. [2016]) summarises the order of magnitude of length, velocity and time scales corresponding to different turbine scales from the **micro** ones (blade boundary layer) to the **macro** scales (cluster of wind farms). Involved scales are very broad and should be taken into account as a whole to properly assess the turbine environment.

	Length scale [m]	Velocity scale [m/s]	Time scale [s]
Airfoil boundary layer	0.001	100	0.000 01
Airfoil	1	100	0.01
Rotor	100	10	10
Cluster of rotors	1000	10	100 ($\approx$ 2 min)
Wind farm	10 000	10	1000 ($\approx$ 15 min)
Cluster of wind farms	100 000	10	10 000 ($\approx$ 3 h)

Table 1.2: Aerodynamical scales related to a wind turbine and its environment (from van Kuik et al. [2016])

For the present study, the characteristic scales of a conventional turbine are analysed to obtain the order of magnitude of its related spatial and temporal scales. Table 1.3 shows spatial and temporal scales of a NREL 5 MW turbine. The reference radial position is equal to $\frac{2}{3}R$ for a wind speed of 14 m/s and a rotational velocity of 14 rpm. Time constant related to the chord τ_c is equal to 0.04 s. The settling time of an eventual actuation impulse τ_{set} is of about $10\tau_c$ equal to 0.4 s. Rotational time scale is approximately of 4 s which corresponds to grossly $100\tau_c$. Time scale related to wind turbulence is equal to 3 s i.e. approximately $75\tau_c$. This same table and these reference scales will be used all along the manuscript for scaling comparisons between this reference turbine and our wind-tunnel models. Also, the awareness of these scales permits to determine the actuation strategies and their requirements in terms of dynamic specifications.

Standard deviation of the incoming flow velocity σ_u is equal to 2.6 m/s for a regular wind. Variations in the angle of attack α due to turbulence can be estimated as follows:

$$\arctan\left(\frac{-2\sigma_u + U_\infty}{\Omega r}\right) < \alpha + \beta < \arctan\left(\frac{2\sigma_u + U_\infty}{\Omega r}\right) \tag{1.16}$$

Which gives:

Variable	Unit	NREL 5MW
Rotor radius R	m	63
Chord at $\frac{2}{3}R$	m	2.4
Ω	rpm	14
Rated wind velocity U_∞	m/s	14
Turbulent scale λ_u (Kaimal et al. [1972])	m	42
$r = \frac{2}{3}R$	m	42
Ωr	m/s	61
Relative velocity W_r	m/s	63
$\tau_c = \frac{c}{W_r}$	s	0.04
$\tau_{set} \approx 10\tau_c$	s	0.4
$\tau_{rot} = \frac{2\pi}{\Omega}$	s	$4.2 \approx 100\tau_c$
$\tau_{turb} = \frac{\lambda_u}{U_\infty}$	s	$3 \approx 75\tau_c$

Table 1.3: Spatial and temporal scales related to the NREL 5 MW wind turbine

$$9.1^\circ < \alpha + \beta < 19.2^\circ \tag{1.17}$$

For a fixed pitch angle β, it results in a variation of the angle of attack α seen by the blade equal to $\Delta\alpha = \pm 5^\circ$ due to wind turbulence.

1.3 Load fluctuations on blades

1.3.1 Load fluctuation sources

As mentioned above, wind turbines operate in the hostile environment of the atmospheric boundary layer that induces important **load fluctuations** on blades. As rotor diameters and tower heights keep increasing, blade deflections are becoming more and more important and problematic. These load fluctuations cause **fatigue** damage that decreases the rotor lifetime and may even cause structural failure of the blades. Even if fluctuations are strongly reduced with variable pitch mechanisms in large wind turbines, the rotors (blades and hub) remain the second source of failure in operating turbines as reported in the IET[5] Renewable Power Generation report on turbine reliability (Spinato et al. [2009]). At the turbine scale, load fluctuations are caused by:

- Horizontal and vertical wind shears due to the presence of the ABL (periodic)
- Tower shadow (periodic)
- Wind turbulence (stochastic)
- Yaw misalignment (periodic)
- Gravity (periodic)
- Influence of other turbine wakes

In Rezaeiha et al. [2017] the authors quantify the importance of atmospheric and operational parameters in turbine loads. They use BEM (Blade Element Method) aeroelastic code HAWC2 of DTU[6] Wind Energy for a 10 MW wind turbine. They determine that in the case of flapwise

[5]Institution of Engineering and Technology
[6]Technical University of Denmark

fatigue, 65% of load fluctuations are caused by turbulence, 20% by gravity and rotor imbalances, 10% by wind shear and 5% by yaw misalignment (see figure 1.9). Load fluctuations proved to be very local on blades as they are caused by turbulent eddies ranging from 1 m to 100 m, meaning that active flow control strategies distributed along the blade span may be very effective to control these loads.

An alleviation of load fluctuations would lead to an increase in the rotor lifetime (blades and gear box mainly), an augmentation of the turbine reliability and a reduction of the operating costs and maintenance. Also, for a given turbine design, load reduction gives the possibility to implement *lighter* or *longer* blades. This last approach is called *grow-the-rotor* (Berg et al. [2009]) and determines how much large a rotor can be by alleviating load fluctuations without exceeding the fatigue loading of the original rotor. In the scope of the SMARTEOLE project and through LiDAR site measurements, Guillemin et al. [2016] performed wind field reconstructions to anticipate the pitch regulation response. Blade fatigue was reduced by 63% and by 75% when the actuation dynamics was taken into account.

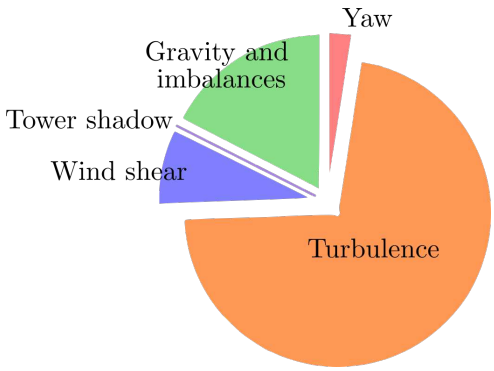

Figure 1.9: Contributions of unsteady loads to flapwise bending moment (from Rezaeiha et al. [2017])

Turbines are subjected to two kinds of loads: **design loads** fluctuating around nominal loads and mainly inducing structural fatigue; and **extreme loads** corresponding to emergency stops or specially strong gusts, involving forces well over nominal loads and demanding blade oversizing at the conception stage. Most of the currently available turbines use collective or individual **pitch control** to alleviate the periodical nominal loads such as tower shadow, wind shear or turbine yaw misalignment. However, pitch control has several disadvantages. It is limited by the blade mass and its inertia and does not allow to react to the smaller turbulent scales and to sudden wind gusts as the actuation is quite slow ($\approx 2\,^\circ\,\mathrm{s}^{-1}$). Also, as the information of velocity for pitch regulation is taken at the turbine hub, the system reaction takes place too late leading to a more curative than preventive action. As pitch control is currently the most mature control strategy, mechanical pitch systems may be overburdened because they are permanently used. Furthermore, a change in pitch modifies the overall orientation of the blade whereas it may be more suitable to act only on a certain blade span and chord location, specially on the areas contributing to most of the torque production.

A large panel of **active flow control strategies** emerged in the last decades in order to respond to this load fluctuation alleviation challenge. Current orientations target design loads that cannot be alleviated with the pitch monitoring.

1.3.2 *How much* efficient an actuator should be?

To overcome problematic load fluctuations, several active flow control (AFC) strategies have been and are still investigated. **But, what are the time and spatial scales to target with these AFC strategies? How much gain an AFC system should give *ideally* to alleviate these load fluctuations?**

To answer this question, I will focus on the loads sensed by an industrial wind turbine, the NREL offshore 5 MW wind turbine (Jonkman et al. [2009]). Figure 1.10 shows the incoming wind velocity at the turbine hub, angle of attack, lift coefficient, root flapwise bending moment and pitch angle as a function of time for a wind speed of 14 m/s. The lift coefficient and the angle of attack are plotted for a radial position of 75%R. This data is obtained with HAWC2[7] BEM aeroelastic code of DTU Wind Energy. Larger wind fluctuations shown in figure 1.10a

[7] http://www.hawc2.dk

($\approx \pm 8\,\mathrm{m/s}$) with time scales in the order of magnitude of 100 s lead to fluctuations of $\Delta\alpha \approx \pm 9°$[8], $\Delta C_L \approx \pm 1$ and $\Delta M_{fbm} \approx \pm 10\,000\,\mathrm{kN\,m}$. These fluctuations are rather well alleviated with the pitch controller of the turbine. However, wind fluctuations with lower time scales visible in zoomed figure 1.10b ($\approx 1\,\mathrm{s}$ to $10\,\mathrm{s}$ and $\approx \pm 4\,\mathrm{m/s}$) induce variations of $\Delta\alpha \approx \pm 2.5°$, $\Delta C_L \approx \pm 0.25$ and $\Delta M_{fbm} \approx \pm 2500\,\mathrm{kN\,m}$ which are not reduced by the pitch controller, too slow to react to these fast solicitations. It should be pointed out here that the **objective of AFC strategies is not to substitute the pitch regulation**, but to be **complementary** with it by targeting these small spatial and temporal scales that pitch regulation cannot alleviate. Hence, AFC devices should address the weaknesses of pitch control and therefore have short time responses, have an action distributed along the blade span and be mechanically simple.

Concept of SMART rotors

An ideal **"SMART rotor"** would take the information about the incoming wind **upstream** of the turbine thanks to LiDAR devices, for example, but would also take the current state of the flow **along the blade span** with distributed pressure sensors or strain gages, for example. The turbine controller would be then capable of managing both pitch and/or AFC systems in **real time** to react to the incoming wind fluctuations in the best possible way and alleviate as much as possible the load fluctuations on blades.

1.3.3 How to model a wind perturbation at a wind-tunnel scale?

Research at a laboratory scale is of high relevance because it permits to test SMART rotor concepts at its early conception stages. Indeed, wind-tunnels are often used to test airfoils and embedded control strategies in a **controlled environment**: constant velocity and temperature, low and calibrated turbulence. Also, as models are small, they can be instrumented with several sensors that cannot be used in operating turbines. Furthermore, a large panel of non-intrusive optical methods can be implemented in the confined area of the wind-tunnel test-section to learn more about the flow around the blade and along its wake. However, to analyse the impact of a wind perturbation on a given airfoil, it is necessary to model the disturbances considering scale and Reynolds effects. At a laboratory scale, a wind perturbation can be reproduced via several methods. In a 2D-configuration, the disturbance can be made in the following ways:

- A modification of the wind-tunnel velocity requires a monitoring of the wind-tunnel fan speed which is not possible in every wind-tunnel. A wind direction and velocity variation requires an active grid system. Kröger et al. [2018] described an active grid composed of square flaps that block and deflect the wind depending on their angle with the incoming flow. This kind of device is quite rare though
- An angle of attack α variation that simulates a wind direction variation. This technique implies that the airfoil rotation can be monitored as presented in Jaunet and Braud [2018]
- To analyse the dynamics of an aerodynamic control system it is possible to apply an actuation step (step to a given flow rate for fluidic devices, a certain voltage for plasma actuators, a certain deflection angle for flaps...) and to measure how the system reacts. This method, however, does not allow to perform a closed-loop control as it is not a real and external wind perturbation

In a rotational configuration, a gust can be created in a wind-tunnel test-section with several techniques:

[8] This value is in agreement with the estimation made in equations 1.16 and 1.17 in which the average $\Delta\alpha$ due to wind turbulence was of $\pm 5°$

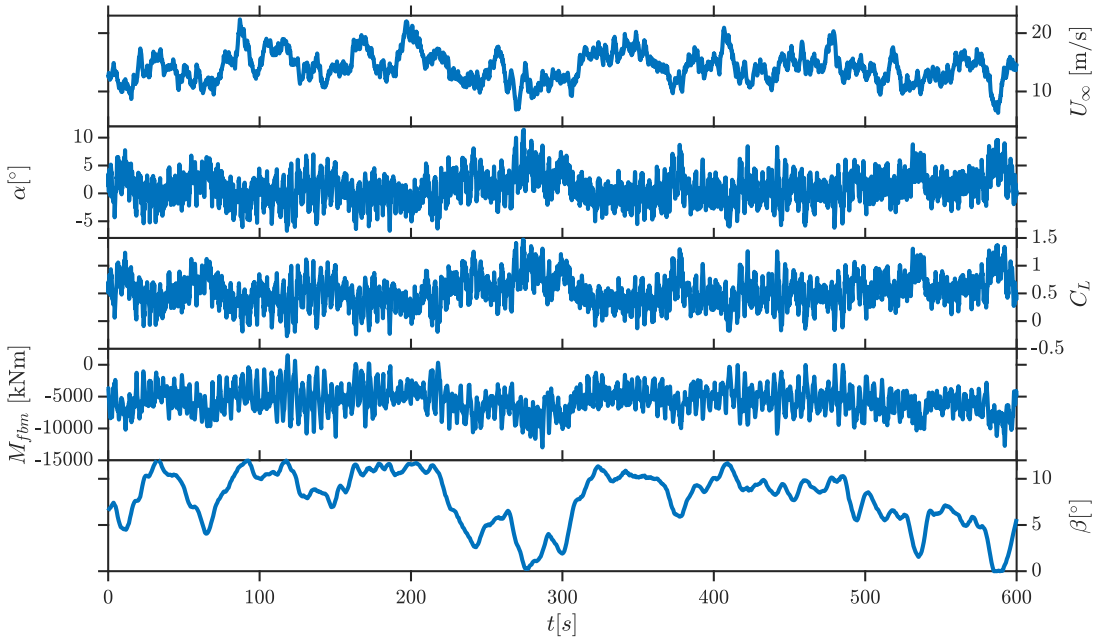

(a) Large time range

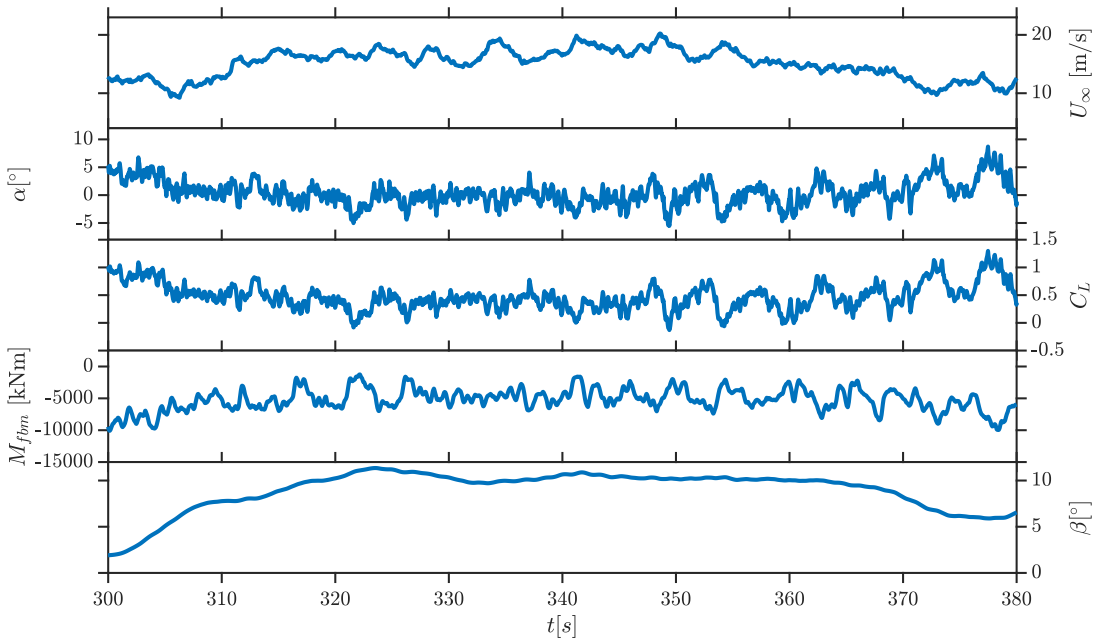

(b) Zoomed time range

Figure 1.10: Aerodynamic and turbine variables as a function of time for a NREL 5 MW wind turbine subjected to a 14 m/s wind (obtained with HAWC2[7] aeroelastic code and courtesy of Pr. Morten H. Hansen (DTU, currently in SDU))

– To increase progressively the velocity in the wind-tunnel test-section

– To yaw the turbine creating a periodical perturbation

– To implement a turbulence grid upstream of the turbine with two different porosities generating an asymmetrical flow

– To employ an active grid as mentioned above for a 2D-airfoil

Wind-tunnel testings are important to test and assess innovative control strategies. To demonstrate a load fluctuation reduction, most of the time, a wind perturbation has to be reproduced in the test-section. Several strategies of different degree of complexity are potentially available.

1.4 Flow control applied to wind turbine blades

This section presents a short review of previous studies concerning flow control strategies in the perspective of a wind turbine application. Principles of flow control will be explained as well as a bibliographical review on the matter. Usually, the objective of actuation is to improve the performance of the turbines (increase of the lift to drag ratio or the power output, for example) or reduce the load fluctuations for a given working point of the turbine. This review concerns the most relevant active flow control devices, such as flaps, microtabs, plasma actuators and fluidic devices.

1.4.1 Principle of flow manipulation

Flow control strategies

Generally, flow control devices can be separated in two groups: **passive** and **active** strategies. **Passive devices** are currently installed in operating wind turbines as, for example, vortex generators on blade roots (see Baldacchino et al. [2018]), slots or rods[9] along the blade span or the use of flexible and twisted blades. The frontier between passive flow control and shape optimisation is often blurry. Passive devices are by definition not removable and aim at optimising the rotor performance without any addition of external energy. Passive control cannot be real-time and is therefore not adapted to the real operating conditions of wind turbines. Also, these devices may add a non-negligible drag detrimental to the rotor performance.

In the case of **active** flow control, an external addition of energy is necessary and the objective is to add a minimal amount of energy to obtain a maximal gain. However, in the perspective of load fluctuation reduction and blade life duration increase, the last assumption might not be always strictly applied. Most of the time, the action takes place at the origin of the phenomena (flow separation point, for example) to minimise the added energy. Active control can be **open-loop** i.e. activated and deactivated according to a predefined strategy but without feedback, or **closed-loop** meaning that the system reacts by itself and adapts in real time to the current flow conditions. To perform a closed-loop control, sensors are needed in order to know the present state of the flow but also a controller that analyses the sensor data and reacts to properly command the actuators to attain the desired set-point.

In wind energy, active flow control strategies are not mature enough to be implemented at an industrial scale but several investigations try to make progress in the field as we are going to see in the following.

Flow control action on blade aerodynamics

Most flow control devices try to increase and/or reduce the lift force, which is directly related to the blade bending moment and therefore to the loads experienced by the blades. Two very different strategies lead to a lift modification: **circulation control** and **separation control**. The impact of both approaches on the lift curve is drawn in figures 1.13a and 1.13b for circulation and separation control respectively.

[9] These devices generate vortices that are convected downstream enhancing the boundary layer mixing and energy. At certain angles of attack, they can maintain the boundary layer attached to the model and delay stall

The objective of **circulation control** is to increase or decrease the lift force at a given angle of attack. It consists in changing the circulation Γ around the airfoil which is directly related to the lift force (see figure 1.11):

$$\text{Lift} = \rho U \Gamma \tag{1.18}$$

$$\Gamma = \oint_C U ds \tag{1.19}$$

where U is the velocity and s the curvilinear abscissa of a closed contour around the airfoil.

Usually, the actuation takes place at the trailing-edge of the blade as done by trailing-edge flaps. This principle has been extensively studied in the field of aerodynamics and aviation as can be read in Joslin and Jones [2006] and Kweder et al. [2010]. Circulation control actuation translates the linear part of the lift curve where the flow is attached to the airfoil. To perform a circulation control without moving parts but with a momentum injection (jets, plasma actuators...), it is required to have a rounded trailing-edge to be able to change the Kutta condition and displace the rear stagnation point. This kind of actuation is inspired from the Coanda effect which stipulates that fluids have a tendency to follow the wall curvature when centrifugal forces and pressure gradient are balanced. The stagnation point displacement changes circulation and then the airfoil lift. A displacement towards the pressure side causes a lift increase whereas a displacement towards the suction side will decrease lift as shown in figure 1.12.

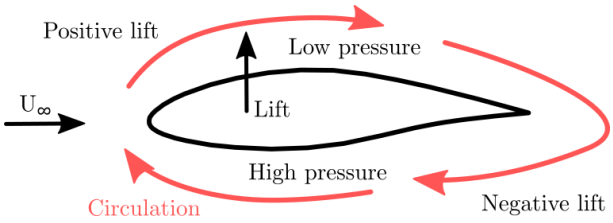

Figure 1.11: Circulation Γ definition

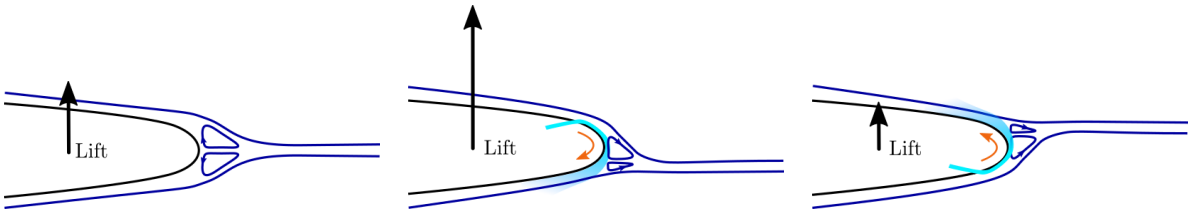

(a) Baseline (b) Control ON - suction side (c) Control ON - pressure side

Figure 1.12: Scheme of the principle of circulation control with a rounded trailing-edged airfoil

Curves on figure 1.13a show the impact of a gust on lift and the result of a circulation control actuation for two cases: a change in wind angle (left), and a change in wind speed (right). In the first case, the change in wind direction displaces the working point towards higher or lower angles of attack. Actuation translates the lift curve in order to reduce or increase the lift and be back to the initial lift force. On the other hand, a sudden increase in wind velocity changes the slope of the lift curve. In the same way, actuation translates this new baseline curve to attain the desired lift working point.

Separation control aims at delaying stall towards higher angles of attack and augment the maximal lift coefficient of the airfoil (see figure 1.13b). This is performed by delaying the boundary layer separation to greater angles of attack and displacing the separation point to greater chord positions at a given α. Hence, the actuation does not modify the linear part of the lift curve but acts in the area where the flow is separated or partially separated. Usually, the actuation takes place at the leading-edge of the blade or is distributed along its chord, preferably along the first half of it. In Gad-el Hak et al. [2003] the authors presented flow control fundamentals including separation control. Another publication is worth of consideration: Greenblatt and Wygnanski [2000] published an extended review about the control of flow separation with periodic excitations.

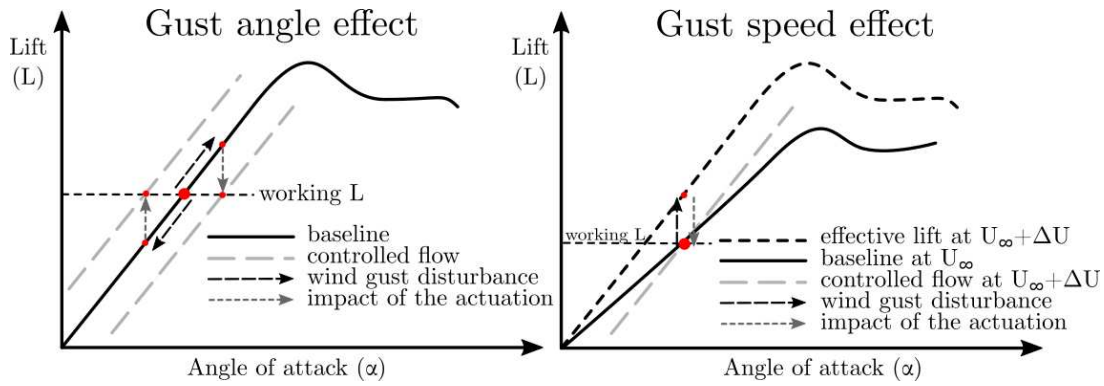

(a) Circulation control

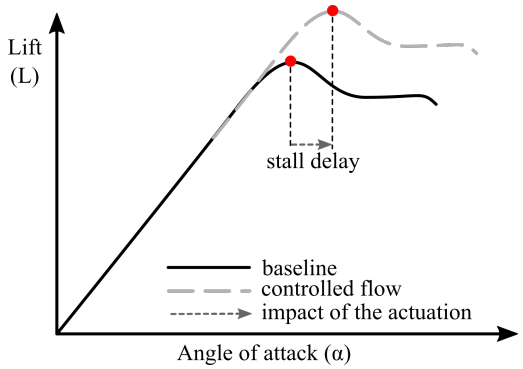

(b) Separation control

Figure 1.13: Schematic principles of circulation and separation control

1.4.2 Flow control state of the art

This section presents a short review of the previous studies dealing with flow manipulation for wind turbine applications. Only relevant results and publications are detailed. A more complete review of a large panel of flow control strategies can be read in Aubrun et al. [2017] and a careful review of actuation devices is also made in Johnson et al. [2008]. At this stage, it should be remembered that AFC strategies target small spatial and temporal scales inducing angle of attack variations equal to $\boldsymbol{\Delta\alpha = \pm 2.5°}$ and lift variations of $\boldsymbol{\Delta C_L = \pm 0.25}$.

Trailing-edge flaps & adaptive trailing-edge

Principle **Trailing-edge flaps** have been widely used for decades in the field of aviation. Rigid flaps consist in the split of the airfoil in two parts: a main front part that remains unchanged whereas the trailing-edge can rotate around a hinge (see figure 1.14a). **Adaptive trailing-edges** have an internal deflection system that bends the blade TE continuously, eliminating the angular deflection between the flap and the main part and reducing noise generation (see figure 1.14b). Both devices modify the airfoil camber increasing the lift coefficient (but also drag) and are considered to perform a circulation control. Flaps are not yet implemented in industrial wind turbines but their potential benefits are expected to be high in terms of load alleviation but also in the purpose of power regulation. They remain however complex to implement because of the number of mechanical and mobile parts added to the blade and the electrical and pneumatic components involved in this strategy.

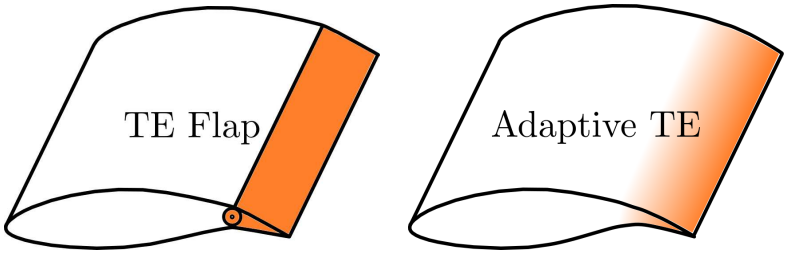

(a) Trailing-edge flap (b) Adaptive trailing-edge

Figure 1.14: Scheme of a trailing-edge flap and an adaptive trailing-edge

Previous studies First studies with flaps for a wind turbine application were carried out by Troldborg [2005] who performed RANS[10] simulations on a Risø-B1-18 airfoil with a 10%c hinged flap immersed in a 2D-flow ($Re = 1.6 \times 10^6$). The author concluded that the flap deflection should be small in order to reduce the induced drag penalty. A lift coefficient gain of $+0.50$ was performed and a loss of -0.70. Berg et al. [2009] use the NREL FAST/AeroDyn code on a 1.5 MW turbine with flaps on the last 20% of the blade chord. It was determined that the rotor size could be increased by 10% and therefore the energy capture might be increased by 10% to 15% leading to a decrease in the CoE[11] of about 7%. Also, flapwise bending moment was reduced of 30%. More recently, Pechlivanoglou et al. [2010] carried out experimental testings at a wind-tunnel scale with 20%c flexible flaps on a DU96W180 airfoil ($Re = 1.3 \times 10^6$) and performed a lift coefficient increase and decrease of ± 0.80. Adaptive trailing-edge geometries have also shown promising results as it can be read in Bak et al. [2007] who obtained a ΔC_L equal to $+0.10$. Bergami and Poulsen [2015] used DTU HAWC2 code on a 5 MW wind turbine with adaptive trailing-edges in the last 10%c and obtained a $\Delta C_L = \pm 0.40$ in a 2D-configuration.

Regarding experimental rotational configurations, Castaignet et al. [2014] implemented flaps over an operating wind turbine (Vestas V27) that were located at 13%c and 18%c depending on the radial position along the blade. Bending moment was reduced by 14% and the amplitude of 1p loads by 20% (1p loads correspond to the rotational frequency of the turbine). Bartholomay et al. [2018] implemented TE flaps (30%c) on a model wind-turbine and implemented a closed-loop control reacting to three different perturbations: a global gust (progressive increase of U_∞), a local gust (differential porosity of the test-section entry grid) and yaw misalignment of the turbine. The actuation reduced the cumulative PSD (energy value for fatigue damage) of about 10% for a global gust (0-1p loads), of 25% for a local gust (3p-4p loads) and 50% when the turbine was yawed. Recently, Barlas et al. [2018] performed a field test and implemented a morphing TE (20%c) on a test rig. Variations of about $\Delta C_L = +0.20$ and -0.25 could be obtained and standard deviation of the flapwise bending moment was reduced by 11%.

Microtabs & Gurney flaps

Principle Microtabs and Gurney flaps have a similar working principle. **Microtabs** consist in small tabs that emerge from the airfoil with a typical heigh of 1% of the chord and perpendicularly to the model surface as shown in figures 1.15a and 1.15b (tabs are not to scale). Usually they are located near the trailing-edge of the blade. A **Gurney flap** (see figure 1.15c) is a flat plate of the same dimensions (1%c) located at the TE and perpendicular to the airfoil chord. Both

[10] Reynolds Averaged Navier Stokes

[11] Cost of Energy: allows the comparison between different electricity production methods. It averages the total cost to build and operate an electricity production asset over its lifetime divided by the total energy output of the asset over its lifetime. This variable includes the initial capital, discount rate, the costs of continuous operation, fuel, and maintenance

devices can emerge from the pressure or suction sides of the blade. If the devices are correctly dimensioned, the lift coefficient is increased and drag can be reduced. Such as TE flaps, these devices perform a circulation control and are not implemented yet in operating wind turbines. Their implementation would be expensive and maintenance expenses would also increase.

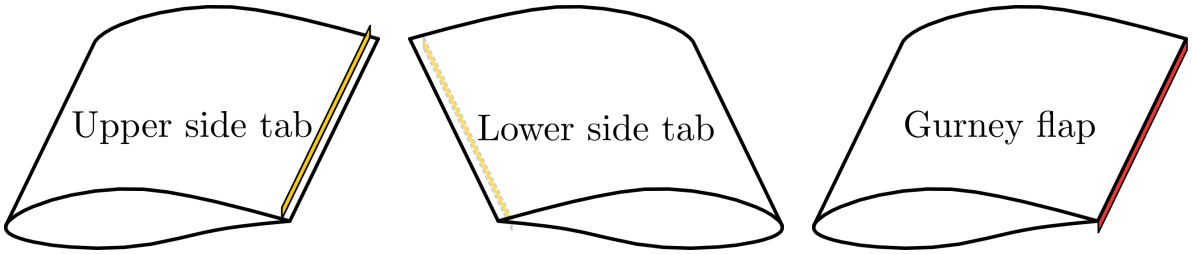

(a) Upper side tab (b) Lower side tab (c) Gurney flap

Figure 1.15: Scheme of microtabs and a Gurney flap (devices are not to scale)

Previous studies Microtabs were implemented by Baker and Standish [2007] in the vicinity of the TE of a S809 airfoil. The authors concluded that the optimal tab height was equal to the boundary layer thickness and a ΔC_L of -0.40 and $+0.30$ was performed. Cooperman et al. [2014] performed wind-tunnel experiments with microtabs on a S819 airfoil. Tabs were in the vicinity of the TE (80%c on the suction side and 90%c on the pressure side). A closed-loop was implemented and the airfoil was subjected to wind gusts. Finally, an overall ΔC_L of $+0.10$ was obtained. Holst et al. [2015] tested the implementation of a Gurney flap on a 40 kW wind turbine using NREL FAST/AeroDyn code and proved that the turbine output power could be increased with this device and that Gurney flaps could replace pitch control for this turbine.

Plasma actuators

Principle **Dielectric Barrier Discharge** (DBD) actuators are widely studied for flow control applications in the wind energy and aerospace fields. These actuators will be deeply analysed here as they are used in the present project. They consist in two electrodes placed asymmetrically on both sides of a dielectric material as can be seen in figure 1.16a. By the application of a high voltage between the two electrodes, the ambient air is ionised and the charged particles are set in motion. A momentum transfer occurs between these charged particles accelerating the quiescent air that moves along the dielectric surface, generating an ionic wind of a few meters per second.

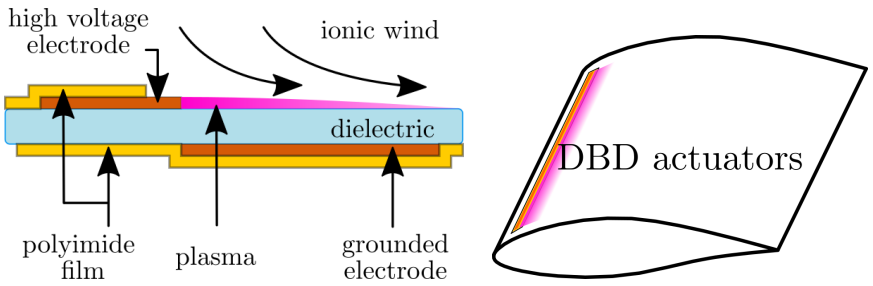

(a) Principle of a DBD actuator (b) DBD actuator

Figure 1.16: Principle and scheme of a DBD actuator

The grounded electrode (or passive electrode) is encapsulated with several layers of a dielectric material (polyimide film or Kapton®) to avoid plasma formation in the lower side of the

electrode. The high voltage electrode (or active electrode) is subjected to a sinusoidal voltage with a frequency of a few kHz and an amplitude ranging from 10 to 20 kV. A review on the influence of the geometrical parameters of an actuator such as the electrode length, the dielectric thickness or the distance between the electrodes can be read in Forte et al. [2007]. In Benard and Moreau [2014] one can find a complete review about the electrical and mechanical characteristics of surface DBD actuators applied to airflow control.

Regarding their application for flow control, DBD actuators can be placed at the leading-edge (see figure 1.16b) or along the chord to perform flow separation control; or in the vicinity of the trailing-edge in a perspective of circulation control. Plasma actuators have great advantages for flow control applications on wind turbine blades. The actuators are light and small because they are applied only at the blade surface. They can also be adapted to curved surfaces and can be implemented on an existing blade in a relatively simple way. Actuation has short time responses (under 1 ms) because the system is purely electrical and not mechanical and power consumption is weak ($\approx 1\,\mathrm{W\,cm^{-1}}$). However, plasma homogeneity along a large span may be difficult to obtain and the currently achievable ionic winds show low velocities (max. 8 m/s in Moreau [2007]). Also, high voltages are required which can be dangerous during maintenance periods and problematic in case of lightning strikes.

Previous studies Plasma actuators have been widely used for flow control applications in the field of wind turbines for both circulation and separation controls. In the case of circulation control on 2D airfoils, Zhang et al. [2010] performed a numerical RANS study on an elliptical airfoil with a DBD actuation at the trailing-edge. The authors obtained a lift coefficient gain of +0.80 at $Re = 700\,000$ with a particularly strong (and unrealistic) actuation. Another numerical study by Meijerink and Hoeijmakers [2011] on a NACA0018 airfoil proved a ΔC_L up to +0.30 at $Re = 720\,000$ with a distributed action from leading to trailing-edge. An excellent experimental study was published by Kotsonis et al. [2014] who implemented DBD actuators on the rounded TE of a NACA64-2-A015 symmetrical airfoil. The authors analyse the influence of the actuator position around the TE as a function of the angle of attack of the model and conclude that the higher the angle of attack, the more the actuator should be placed near the pressure side of the airfoil. A ΔC_L gain up to +0.10 was obtained at $Re = 140\,000$ for the angles of attack corresponding to the highest lift coefficients. The authors also highlighted the presence of a small recirculation zone in the wake of the semi-cylindrical trailing-edge. This area showed two counter-rotating vortices that were alternatively shed and that correspond to a Von Karman vortex shedding.

Nelson et al. [2008] combined separation and circulation control with the implementation of DBD vortex generators at the blade LE and DBD actuators at 78%c on a S827 airfoil. They conclude that circulation control increases the effective blade camber and obtained a $\Delta C_L = +0.08$. Experimentally, plasma actuators for purely separation control on 2D-airfoils perform lift coefficient variations up to +0.30 (Brownstein et al. [2014]) and between −0.06 and +0.12 (Cooney et al. [2016]). These last authors also carried out a field test and implemented DBD actuators on a VP-20 20 kW operating wind turbine and concluded that its power output could be increased, despite their not statistically converged results.

A few studies deal with plasma actuation on rotating airfoils and turbines. In partnership with Toshiba, Tanaka et al. [2013] implemented plasma actuators over the blades on an industrial 30 kW wind turbine, which represents actually one of the most developed projects of active flow control on large wind turbines. Turbine power coefficient could be increased by $\Delta C_{power} = +0.20$. At a wind-tunnel scale, two studies are worthy of consideration. Jukes [2015] performed separation control on a model wind-turbine with chordwise DBD vortex generators and LE dual DBD actuators. Power due to drag could be increased and decreased by +8% and −24% respectively. Also, even if it remains a little far from the present application, Greenblatt et al. [2012] implemented plasma actuators on the blade leading-edges of a vertical axis wind turbine.

The objective was to monitor the boundary layer separation and dynamic stall phenomenon. With this flow control strategy, the turbine power was increased up to about 38%.

Fluidic devices

Principle Fluidic devices are very diverse in their working principle but also in their positioning along the chord and their implementation. The two main devices studied by the scientific community are **synthetic jets** and **blowing jets or slots** represented in figure 1.17.

Synthetic jets are generated by the displacement of a membrane that moves back and forth inside a cavity. With the diaphragm movement, the cavity fluid is ejected and suctioned periodically through a series of small orifices or through a slot. Usually, this kind of actuators are made with piezoelectric or mechanical drivers. One of the advantages of this technique is that there is no mass addition but only momentum addition to the controlled flow. Furthermore, these actuators do not require any fluid supply and their power consumption is very low.

Fluidic blowing jets or slots are connected to a plenum chamber that supplies the jets (or slots) with compressed air. This chamber is maintained at a high pressure and the system requires an air compressor. In this case, when the actuation takes place, as the jets blow from the inside of the model to the outside, there is mass addition to the controlled flow.

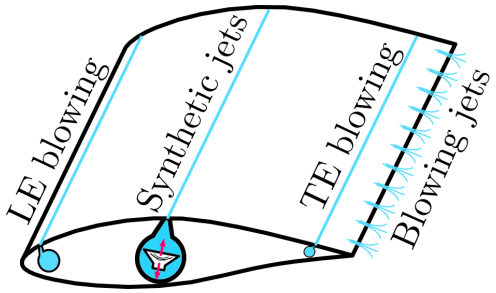

Figure 1.17: Fluidic devices

Both synthetic and fluidic jets are usually placed near the leading-edge of an airfoil or remain distributed along the chord in order to perform a separation control. The main advantages of these techniques is that the actuation can be strong with high jet velocities that make flow control easier. They also do not require mechanical moving components and the blade shape can be preserved. However, overall systems can be quite heavy and may be complex to implement on industrial wind turbine blades.

Previous studies Fluidic devices are mainly used to delay flow separation and the most common devices are synthetic jets. Some important experimental studies in 2D-configurations are explained in the following. Stalnov et al. [2010] implemented synthetic jets at 37%c of an IAIPr8-SE airfoil and for Reynolds numbers ranging from 200 000 to 800 000. The authors proved that the actuation could replace passive vortex generators and obtained a ΔC_L of +0.25. Shun and Ahmed [2012] obtained very similar results ($\Delta C_L = +0.20$) by using blowing jets as vortex generators at 12.5%c. Troshin and Seifert [2013] worked on a degradated airfoil in order to study the effects of bugs and depositions on blades. The authors implemented synthetic jets at 35%c, 50%c and 65%c and obtained a ΔC_L of +0.30. Niether et al. [2015] also implemented blowing slots on a DU97-W-300 airfoil to perform separation control acting on the first half of the chord and achieved a ΔC_L of +0.15. Müller-Vahl et al. [2015] performed constant leading-edge blowing (5%c) over a NACA0018 airfoil to target dynamic stall at Re between 1.3×10^5 and 3.8×10^5. The authors used low flow rates to destabilise the boundary layer and trigger separation in order to reduce the C_L and higher flow rates to increase it. The order of magnitude of the obtained C_L variations were of $\Delta C_L \approx \pm 0.50$. Mid-chord blowing was effective for TE stall control but not for pure LE separation. Finally, Braud and Guilmineau [2016] and Jaunet and Braud [2018] conducted a circulation control with fluidic jets at the trailing-edge of a 2D airfoil in open and closed-loop configurations. Lift coefficient gain was of about +0.40 at $Re = 200\,000$.

One study performs flow control in a rotational configuration with a fluidic strategy: Anik et al. [2014] controlled the tip vortex of a model wind turbine using tip injection and augmented the power coefficient of the turbine of about +0.15, which corresponds to a 75% augmentation with respect to the baseline case.

Bibliographical conclusion

A wide range of active flow control devices are available for lift control on wind turbine blades. Trailing-edge flaps can perform lift coefficient variations of about ± 0.40 to ± 0.80, which would target the largest load fluctuations that were mentioned above. Indeed, large wind fluctuations with high time and spatial scales induce ΔC_L equal to ± 1. Flaps will be an interesting device if the blade pitch regulation can be indeed replaced. They show very high gains and losses of C_L, have suitable time responses for closed-loop control applications but are however difficult to implement, heavy and expensive.

On the other side, simpler and less mature active control strategies are microtabs, plasma actuators and fluidic devices. Microtabs can perform ΔC_L of ± 0.30, plasma actuators of approximately ± 0.10 and fluidic devices, mainly used for separation control, show gains of about $+0.30$. These strategies should be complementary to pitch regulation and target small time and spatial scales which lead to variations of $\Delta\alpha = \pm 2.5°$ and $\Delta C_L = \pm 0.25$. As mentioned in Cattafesta and Sheplak [2011], fluidic jets have the advantage to induce high jet velocities but a feedback control is compromised when valves are involved in the pneumatic system. Synthetic jets do not need an external fluid source, can be implemented in very different surfaces and models and are suitable for closed-loop control. However, these actuators induce low jet (or slot) velocities. Regarding plasma actuation, DBD actuators are easy to implement, have a low mass, have no moving parts and a fast time responses. Though, they require high voltages and generate low induced velocities.

Next two tables summarise this bibliographical study: table 1.4 shows previous studies results on flow control with trailing-edge flaps and microtabs; table 1.5 for plasma actuation and fluidic devices.

Actuator type	Actuator location	Airfoil or WT model	*Re*	Gain	Type of study	Authors
Trailing-edge flaps - 2D cfg.	10%c	Risø-B1-18 (2D)	1.6×10^6	$\Delta C_L = -0.7$ to $+0.5$	Comp. (RANS)	Troldborg [2005]
	10%c	NREL 5 MW WT	-	$\Delta M_{fbm} = -24\%$	Comp. (FAST)	Berg et al. [2009]
	20%c	DU96W180 (2D)	1.3×10^6	$\Delta C_L = \pm 0.8$	Exp.	Pechlivanoglou et al. [2010]
	10%c	5 MW WT	-	$\Delta C_L = \pm 0.4$	Comp. (HAWC2)	Bergami and Poulsen [2015]
Trailing-edge flaps - Rot. cfg.	13-18%c	Vestas V27 (2D)	-	$\Delta M_{fbm} = -14\%$	Field test	Castaignet et al. [2014]
	30%c	BeRT turbine	-	$\Delta \text{PSD} = -25\%$	Exp.	Bartholomay et al. [2018]
	20%c	Test rig	-	$\Delta C_L = -0.25$ to $+0.2$	Field test	Barlas et al. [2018]
Microtabs	40%c, 60%c, 90%c and TE	NREL S809 (2D)	10^6	$\Delta C_L = -0.4$ to $+0.3$	Exp.	Baker and Standish [2007]
	80%c SS, 90%c PS	NREL S819 (2D)	10^6	$\Delta C_L = +0.1$	Exp.	Cooperman et al. [2014]
	TE Gurney flap	40 kW WT	-	GF replace β control	Comp. (FAST)	Holst et al. [2015]

Abbreviation	Meaning
WT	Wind Turbine
SS	Suction Side
PS	Pressure Side
Circ.	Circulation control
Sep.	Separation control
Num.	Numerical study
Exp.	Experimental study
FAST	NREL Aeroelastic code for HAWT (https://nwtc.nrel.gov/FAST)
HAWC2	DTU Aeroelastic code for HAWT (http://www.hawc2.dk/)
RANS	Reynolds Averaged Navier Stokes CFD method
Rot.	Rotational configuration

Table 1.4: Table summarising previous studies results on flow control with **trailing-edge flaps** and **microtabs** - abbreviations are defined

Actuator type	Actuator location	Airfoil or WT model	*Re*	Gain	Type of study	Authors
Plasma actuators - 2D cfg.	78%c	NREL S827	1.5×10^5	Circ. $\Delta C_L = +0.08$	Exp.	Nelson et al. [2008]
	Chordwise	NACA0018	7.2×10^5	Sep. $\Delta C_L = +0.3$	Num. (RANS)	Meijerink and Hoeijmakers [2011]
	TE	NACA64-2-A015	1.4×10^5	Circ. $\Delta C_L = +0.1$	Exp.	Kotsonis et al. [2014]
	50%c	GOE735	1.5×10^5	Sep. $\Delta C_L = +0.3$	Exp.	Brownstein et al. [2014]
	50%c to TE	VP-20 WT	2.0×10^5	Sep. $\Delta C_L = -0.06$ to $+0.12$	Exp.	Cooney et al. [2016]
Plasma actuators - Rot. cfg.	LE	VAWT (NACA0015)	1.7×10^5	Sep. $\Delta C_{power} = +38\%$	Exp.	Greenblatt et al. [2012]
	LE	30 kW WT	-	Sep. $\Delta C_{power} = +0.2$	Field test	Tanaka et al. [2013]
	LE to 40%c	NREL S822	4.0×10^5	Sep. $\Delta C_{power} = -24\%$ to $+8\%$	Exp.	Jukes [2015]
Fluidic - 2D cfg.	Synth. jets 37%c	Mod. IAIPr8-SE	2.0×10^5 to 8.0×10^5	Circ. $\Delta C_L = +0.25$	Exp.	Stalnov et al. [2010]
	Synth. jets 25%c	NACA4415	7.0×10^4 to 2.4×10^5	Sep. $\Delta C_L = +0.12$	Exp.	Maldonado et al. [2010]
	Fluidic VG 13%c	NACA63-421	6.4×10^5	Sep. $\Delta C_L = +0.2$	Exp.	Shun and Ahmed [2012]
	Chordwise	AH-93-W-300	5.0×10^5	Sep. $\Delta C_L = +0.3$	Exp.	Troshin and Seifert [2013]
	Blowing jets LE to 0.5%c	DU97-W-300	2.2×10^5	Sep. $\Delta C_L = +0.15$	Exp.	Niether et al. [2015]
	Blowing slot LE 5%c	NACA0018	1.3×10^5	Sep. $\Delta C_L = +0.5$	Exp.	Müller-Vahl et al. [2015]
	Chordwise blowing jets	$NACA65_4$-421-CC	2.0×10^5	Circ. $\Delta C_L = +0.4$	Exp.	Braud and Guilmineau [2016] and Jaunet and Braud [2018]
Fluidic - Rot. cfg.	Jet tip injection	NREL S826 blades	-	$C_{power} = +0.15$	Exp.	Anik et al. [2014]

Table 1.5: Table summarising previous studies results on flow control with **plasma actuators** and **fluidic** devices - abbreviations are specified in table 1.4

1.5 Context of the thesis work

1.5.1 SMARTEOLE project

The present thesis work is part of the French national project SMARTEOLE (ANR-14-CE05-0034) that aims at improving the efficiency of wind energy production. The project proposes innovative control solutions for load regulation at three different scales: the **blade** scale, the **rotor** scale and the **farm** scale. The consortium includes two industrial partners: Engie Green, a French electricity supplier; and Leosphere, a LiDAR manufacturer. Also, four laboratories are involved: LAAS (Laboratoire d'Analyse et d'Architecture des Systèmes), IFPEn (Institut Français du Pétrole Energie nouvelle), LHEEA (Laboratoire de recherche en Hydrodynamique, Énergétique et Environnement Atmosphérique) of ECN (Ecole Centrale de Nantes) and PRISME laboratory (Laboratoire Pluridisciplinaire de Recherche en Ingénierie des Systèmes, Mécanique, Energétique). The goal of the project is to explore the concept of a "SMART rotor" which would be monitored by LiDAR-assisted control strategies. This hypothetical rotor would be equipped with a LiDAR device along with distributed sensors in order to have an anticipated vision of the incoming flow but also know the present state of the flow over the blades. This turbine would react in real time to the stochastic wind variations and therefore immediately compensate the overloads and alleviate the load fluctuations on blades. This strategy would reduce the cost of energy by increasing the robustness of the turbines and the blade life duration. Two kinds of experiments are proposed in the project: **field tests** experiments on an Engie Green wind farm with control strategies developed by IFPEn; and **laboratory scale** wind-tunnel testings performed at PRISME laboratory with flow control devices developed by LHEEA and PRISME.

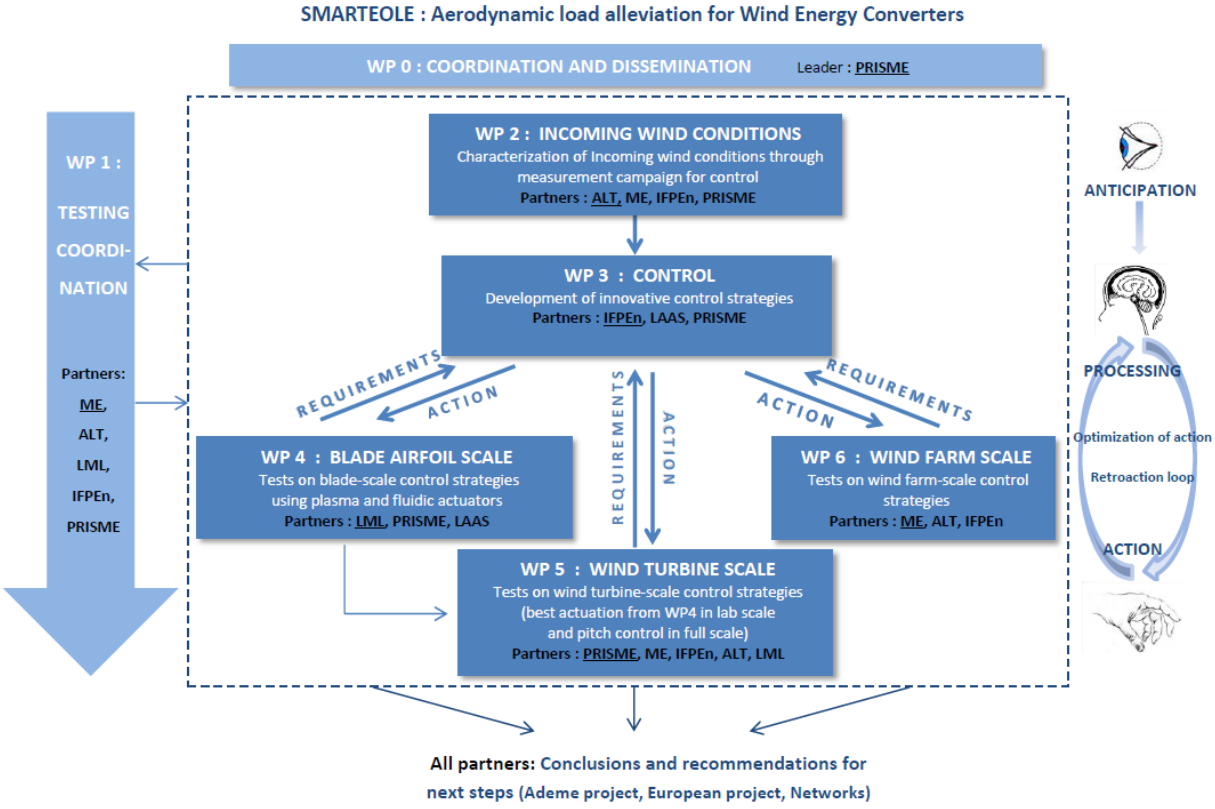

Figure 1.18: Diagram of the SMARTEOLE project work packages

Within the SMARTEOLE project...

This thesis work focuses on flow control actuation at the **blade** and **rotor** scales. Both testings are performed at a **laboratory scale** and at the PRISME wind-tunnel facility (WP4 and WP5 of SMARTEOLE project presented in figure 1.18).

For load alleviation at the blade scale, two actuation strategies are considered: a **plasma** actuation and a **fluidic** strategy with blowing jets. Both intended actuations are meant to perform a **circulation control** with an action at the trailing-edge of the airfoil. The final objective of the wind-tunnel experiments is the implementation of a closed-loop control for load fluctuation alleviation. For this reason, automaticians (LAAS, PRISME) and aerodynamicists (LHEEA, PRISME) work together in the implementation of these two flow control strategies at a laboratory scale. Prior to feedback control testings, control strategies are tested in an open-loop configuration. One of the main goals of this first step is to determine an actuator/sensor pair that would be suitable for the closed-loop control. Also, thanks to these tests, the evaluation of the time response of the systems but also the efficiency of the actuations can be assessed.

1.5.2 Existing experimental means

NACA65$_4$-421 airfoil

The objective of the performed circulation control is to modify the aerodynamic performance of the blade by changing the chordwise pressure distribution and therefore its lift. As mentioned above, this kind of actuation needs a rounded trailing-edge to be able to displace the rear stagnation point and monitor the lift force. For these experiments a **NACA65$_4$-421** is used with a rounded trailing-edge with a curvature radius of 2% of the chord. The resulting airfoil for circulation control is named **NACA65$_4$-421-CC**. Both airfoils are shown in figure 1.19. Dashed orange line represents the line between the leading-edge and the trailing-edge and is defined as the 0° angle of attack line. The original NACA airfoil has been used in small wind turbines because of its maximal thickness of 21%c located near 40%c. Wind turbines using this kind of airfoil are stall regulated meaning that the boundary layer separation on the blade is used to reduce the rotational velocity of the turbine and limit its output power.

This NACA65$_4$-421 airfoil has already been studied at PRISME laboratory for several years, in particular to understand the behaviour of its aerodynamical performances in turbulent flows. Devinant et al. [2002] concluded that the behaviour of the airfoil at stall depends strongly on the turbulence intensity of the incoming flow. In fact, when turbulence intensity is increased, the separation point motion along the chord happens for higher angles of attack and stall is delayed. This phenomenon was explained by the kinetic energy transfer from the external flow to the boundary layer which, for high turbulence flows, is energised and becomes more difficult to separate from the model. Following this work, Sicot [2005] worked on the influence of turbulent intensity in translational and rotational configurations. An unsteady approach for a 2D-flow at high angles of attack (over 20°) and high turbulence intensity showed that a single separation point cannot be defined but that it is more appropriate to define a displacement zone of this separation point. It was proved that turbulence intensity has no real influence on the position and the length of the separation zone for a 2D-configuration. In the case of the rotational configuration, turbulence intensity did not seem to have an important effect neither on the power and thrust coefficients of the turbine nor on the stall behaviour of the airfoil.

Wind-tunnel facility

All the testings are performed in the "Lucien Malavard" closed-circuit wind-tunnel of PRISME laboratory (University of Orléans) shown in figure 1.20. The wind-tunnel has two test-sections: the **main test-section** which dimensions are 2 m × 2 m × 5 m with a maximal flow velocity of

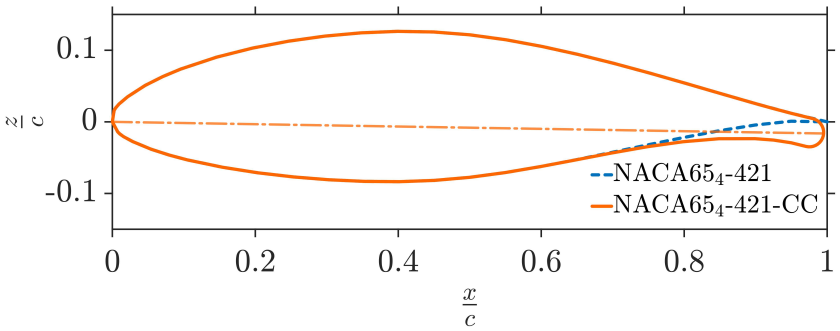

Figure 1.19: Original NACA65$_4$-421 airfoil and NACA65$_4$-421-CC modified airfoil for circulation control

50 m/s; and the **return test-section** that is 5 m × 5 m × 20 m with a maximal velocity of 25 m/s. The fan is located at the end of the main test-section and has a power of 265 kW.

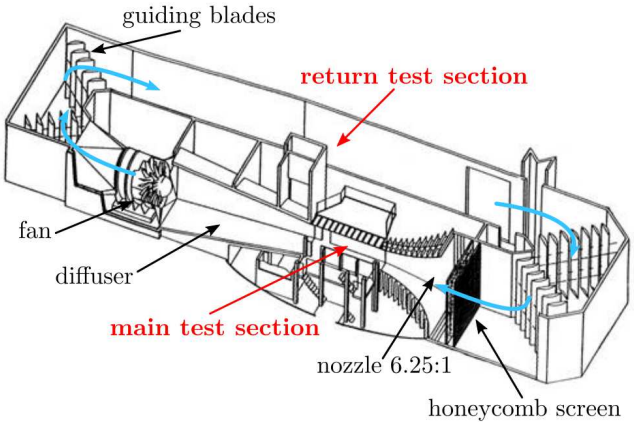

Figure 1.20: Scheme of the "Lucien Malavard" closed-circuit wind-tunnel of the University of Orléans

Wind turbine bench

A wind turbine bench, located in the return test-section, was under development at PRISME laboratory. The first results concerning this bench were published in Aubrun et al. [2015]. The bench was equipped with a torque and drag meter, and blades were designed to allow the measurement of the chordwise pressure distribution and the bending moment at the blade roots. However, the bench was not equipped to perform active flow control, either plasma of fluidic, in a rotational configuration.

1.6 Motivations and outline of the thesis work

The objective of the thesis work is to assess two flow control strategies, plasma and fluidic, in a load alleviation perspective. As explained above in the bibliographical review, the load mitigation objective for flow control application in a 2D-configuration is the lift coefficient variation ΔC_L. To the author's knowledge, only a few AFC studies are implemented on a wind turbine bench (rotational configuration), and do so is an important goal of the present project. For the rotational case, the target variable to control is the flapwise bending moment variation ΔM_{fbm}. All the work is carried out with an **experimental approach** and at a **wind-tunnel**

scale. Within the framework of the thesis, all the carried experiments are done in an open-loop configuration but aim at providing the basis for feedback control applications.

Considering previous flow control studies, two innovative active flow control strategies are developed in the scope of the SMARTEOLE project: plasma actuators and fluidic devices. Both concepts do not require mobile parts and do not affect the blade shape. Plasma actuators are interesting for their simplicity of implementation, their light weight and their fast time response. Fluidic jets have strong exhaust velocities and a chordwise distributed action was initially considered in the project. In this thesis work, only the action near the trailing-edge is examined, meant to perform a circulation control in the linear part of the lift curve. The validation of both plasma and fluidic flow control devices is carried out in parallel for both open and closed-loop configurations over a 2D-airfoil: plasma flow control tests are carried out by PRISME laboratory and fluidic devices are studied by LHEEA laboratory of ECN.

The first part of the thesis work was devoted to the implementation of the plasma actuation on a large **2D-airfoil** and is presented in chapter 2. Simultaneously, LHEEA laboratory performed similar testings with the fluidic actuation. After the comparison of the two approaches and the assessment of their respective advantages and limitations, one of the two devices, the fluidic jets, was chosen to pursue the project towards the rotational configuration and be implemented and tested in the rotor bench of the laboratory. This continuation is part of the present thesis and the second step of the work was to implement the fluidic approach on the wind turbine bench of the laboratory. Blades were manufactured and two different configurations were then tested. The first one, named **translational configuration**, took place in the main test-section and one blade was mounted vertically in a 2D-configuration but with a free blade tip as reported in chapter 3. This first analysis permitted to understand the physics and the mechanisms of the actuation. Finally, blades were mounted in the wind turbine bench and this fluidic flow control strategy was tested in a **rotational configuration** as described in chapter 4. A last chapter 5 presents some first calculations on the efficiency of the actuations presented along the manuscript.

Chapter 2

Plasma flow control on a wind turbine airfoil - 2D-configuration

Contents

2.1 Introduction

In the scope of the SMARTEOLE project, the load alleviation objective at the **blade scale** starts with the implementation in an open-loop configuration of two different control strategies: **fluidic jets**, carried out by LHEEA laboratory; and **plasma actuators** performed by PRISME laboratory (present study). Both approaches are carried out with the same airfoil and in the same wind-tunnel at the University of Orléans.

This chapter presents the results obtained for the circulation control performed with plasma actuators. The objective of the study is to implement DBD actuators at the trailing-edge of a 2D-airfoil and to quantify the gains of the actuation on the aerodynamic performances. The influence of the DBD actuator position around the trailing-edge is analysed. An augmentation as well as a reduction of the lift force in the linear part of the lift curve are expected.

Actuators are first characterised in quiescent air conditions which gives the induced jet topology around the trailing-edge and allows the calculation of the thrust force produced by the actuation. This kind of characterisation allows the understanding of the mechanisms of interaction between the induced jet and the outer flow for in-flow conditions. As DBD induced jets are similar to a fluidic wall jet, a theoretical comparison with plane and curved canonical wall jets is performed.

Then, the effect of the actuation on the aerodynamic loads and on the pressure distribution is analysed. Velocity field analysis allows to assess the impact of the actuation on the airfoil wake as well as hot wire measurements performed beyond the trailing-edge.

Finally, the comparison between plasma and fluidic actuations in a 2D-configuration is performed as well as a dynamic analysis of the time responses of the aerodynamical flow control system.

2.2 Experimental set-up

The present section introduces the different experimental set-ups employed for the testing of DBD actuators used for a circulation control on a wind turbine airfoil (2D-configuration). First are explained the model characteristics, the geometry of the actuators and the electrical set-up implemented for the actuation. Then, the third part deals with the experimental set-up used for the characterisation of the DBD actuators in quiescent air conditions. Finally, the wind-tunnel set-up used for in-flow testings and the carried measurements are illustrated.

2.2.1 Model & actuators

The model used for the circulation control application is a two-dimensional $NACA65_4$-421-CC airfoil with a chord c of 0.3 m and a span of 1.1 m. This model is designed to be implemented between the two flat plates of the wind-tunnel test-section as will be explained in paragraph 2.2.4 (p.38). The model is manufactured by two external companies and is composed of three different parts as shown in figure 2.1:

- The **main part**, from the leading edge to 70% of the chord. This part is made from POM (PolyOxyMethylene) and is done in four different blocks held together by two traversing rods
- The **trailing-edge**, composed itself by a **holder** and a **cap**. This two-part arrangement is adopted for the intended implementation of DBD actuators around the TE. This TE is machined from PMMA (PolyMethylMethAcrylate)

Several trailing-edges are available for the testings and each one has a different actuator implemented on it. Hence, one trailing-edge can be easily removed from the main part of the model and be replaced by another one that will lead to a different actuation. The implemented actuators are based on the well known technology of DBD actuation investigated for aerospace applications (Forte et al. [2007] and Benard and Moreau [2014]). All the studied actuators are multi-DBD actuators made of two single DBD actuators in a row that allow to have an extended discharge and a longer actuation area. To have high induced jet velocities and an increased actuator reliability it has been chosen to work with surface DBD involving a thick dielectric material. In order to perform a circulation control, actuators are implemented at the trailing-edge of the airfoil to displace the rear stagnation point and thus modify the Kutta condition.

Two series of three actuators each have been studied and are shown in figure 2.2 for the A-series and in figure 2.3 for the B-series[1]. As commonly done in the litterature, electrodes

[1]This electrode configuration was suggested by Berendt et al. [2011] within the framework of the European project PLASMAERO

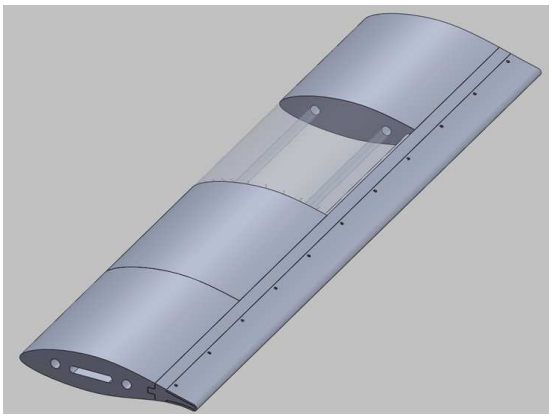

(a) 3D-view of the model

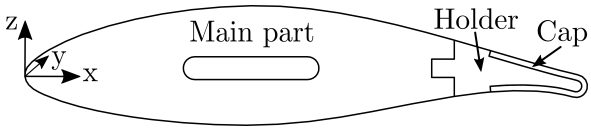

(b) 2D-view of the model

Figure 2.1: Different views of the 2D-airfoil used for the DBD flow control application

are made of copper (60 µm-thick[2]) and are separated by the 3 mm-thick PMMA dielectric of the model cap, a material frequently used as a dielectic as can be read in Moreau et al. [2008], Benard et al. [2009] and Debien et al. [2011]. Grounded electrodes are encapsulated by the dielectric of the model itself (holder part). To prevent plasma formation in the counter-flow direction, active electrodes are partly covered with a 60 µm thick[3] Kapton tape. Within each series, the electrode arrangement (distances between the electrodes) is identical for the three actuators, the only changing feature is their positioning around the trailing-edge.

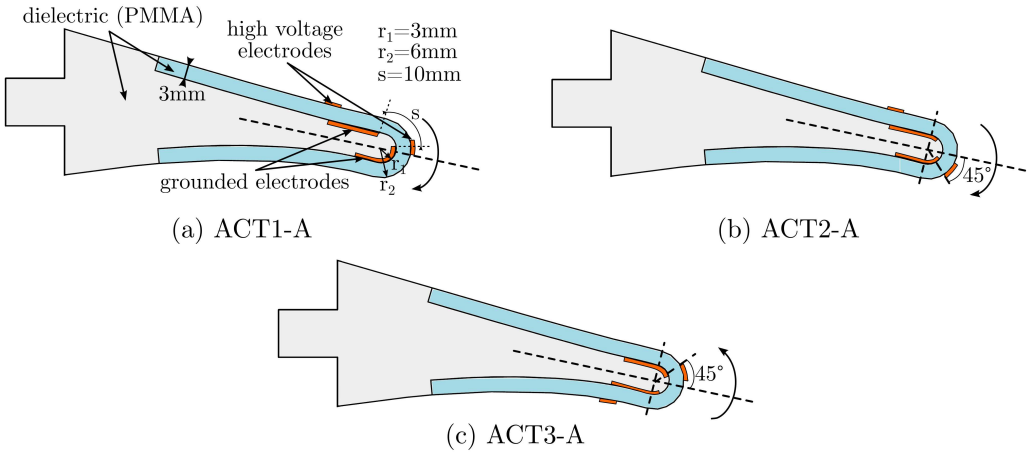

(a) ACT1-A

(b) ACT2-A

(c) ACT3-A

Figure 2.2: Drawing of electrode position around the trailing-edge of the airfoil for the A-series

Electrode arrangement of actuators ACT**1**-X (X representing either A or B series) is centred on the middle line of the trailing-edge, whereas for actuators ACT**2**-X the whole set of electrodes is shifted with an angle of 45° towards the pressure side. Actuators ACT**3**-X are also shifted with an angle of 45° but towards the suction side. **Consequently, actuators ACT1-X and ACT2-X blow from the suction side to the pressure side of the airfoil and are meant for increasing the lift force. On the other hand, actuators ACT3-X create an induced jet from the pressure side to the suction side decreasing the lift force.**

Figure 2.4 shows the geometry and the top-view of the electrodes for both series. In both cases, grounded electrodes are linear (strip electrodes) and 12 mm wide. High voltage electrodes are serrated (triangular pattern in series) to ensure plasma homogeneity along the blade span.

[2] 35 µm copper, 25 µm glue
[3] 25 µm Kapton, 35 µm glue

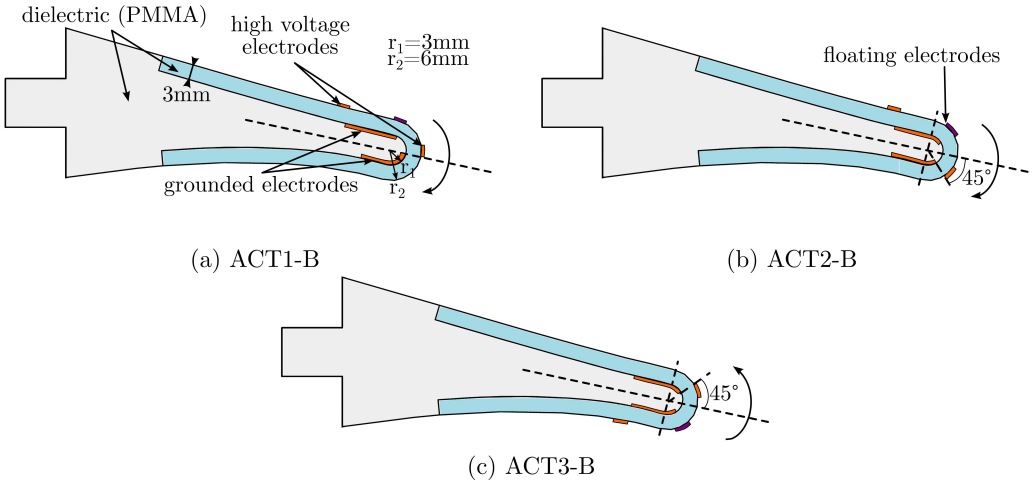

(a) ACT1-B

(b) ACT2-B

(c) ACT3-B

Figure 2.3: Drawing of the electrode position around the trailing-edge of the airfoil for the B-series

The floating electrode (FE) used in the B-series is composed by sequential small triangles that do not touch each other. This electrode is called *floating* because it is neither connected to the high voltage supply nor to the earth of the circuit but gets charged and allows to generate plasma over a long distance as reported in Berendt et al. [2011]. Both grounded and floating electrodes are partially covered by a polyimide film that prevents plasma formation on the edge of the electrode that is not in front of its corresponding grounded electrode. Spanwise length of the actuators is between 850 mm and 950 mm depending on each actuator and its respective trailing-edge. Even if the arrangement of the electrodes is slightly different and the size of the high voltage electrodes teeth differs, **actuators of both series remain very similar**.

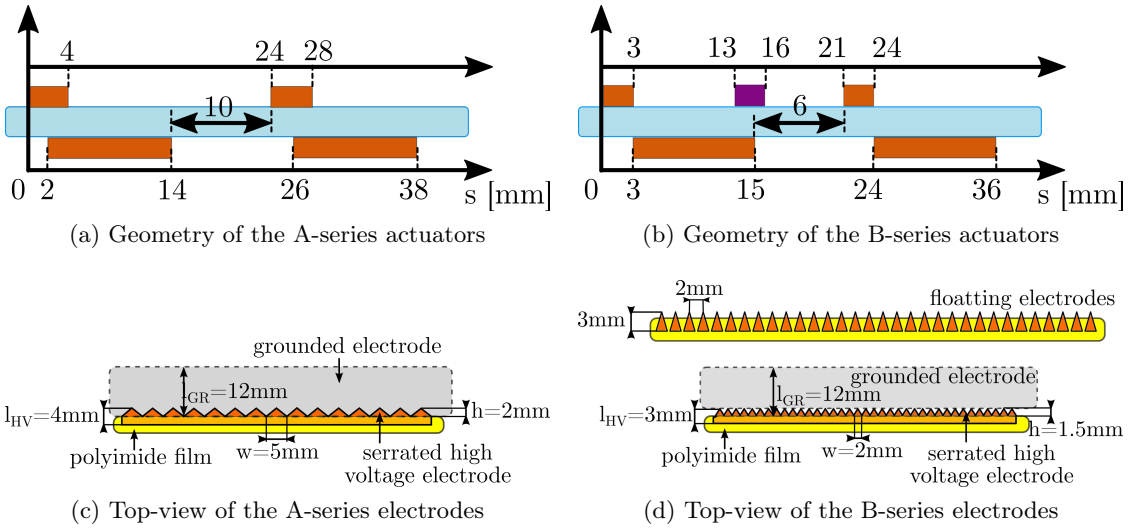

(a) Geometry of the A-series actuators

(b) Geometry of the B-series actuators

(c) Top-view of the A-series electrodes

(d) Top-view of the B-series electrodes

Figure 2.4: Geometry and top-view of the electrodes belonging to the A-series on the left, and B-series on the right

A picture of the 2D-airfoil is shown in figure 2.5. Are shown in the picture the front part of the model and its trailing-edge with the actuators implemented over it.

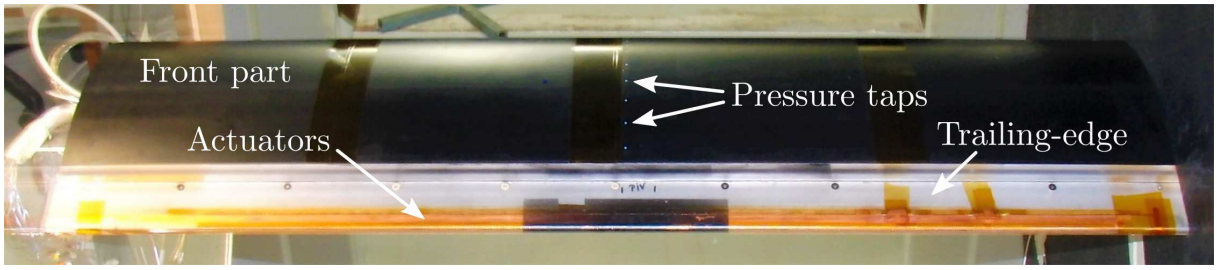

Figure 2.5: Picture of the 2D-airfoil

2.2.2 Electrical set-up & power characterisation

Description of the setup

A high voltage power supply is necessary to power the DBD actuators. The power supply used during the project is made by GREMI[4] laboratory and allows the amplification of a sinusoidal signal. This power supply is made by a Crown amplifier (XS1200 series, 22 Hz-22 kHz, 2.3 kW) and by a single-phase transformer Trabo (90 V-20 kV, 2 kW, 20 Hz-20 kHz). Its maximum voltage output is of about 20 kV and 2 kW. The used function generator is a TTi (TGA1241, 40 MHz, 10 V).

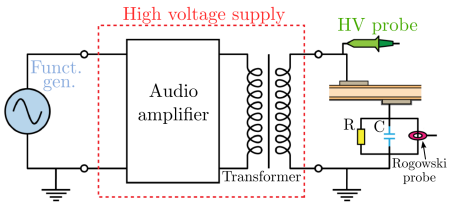

Figure 2.6: Scheme of the electrical set-up (from Joussot [2010])

The electrical installation is shown in figure 2.6. The applied high voltage is measured with a high voltage probe Tektronix (P6015A series, 75 MHz, 3 pF). Discharge current is measured with a Rogowski probe Bergoz (CT-C1.0-B series, 200 Hz-500 MHz). For the power consumption measurements, a silver mica capacitor (47 nF$\pm$ 1%) is used and wired in series with the actuator. For the visualisation of the electrical signals and their acquisition a numerical oscilloscope LeCroy (WaveSurfer 64Xs-A series, 600 MHz, 2.5 GS s^{-1}, 8 bits) is used. This whole set of components, probes and devices is necessary for power measurements but also for the visual control of the plasma proper behaviour during the actuation.

Electrical wiring is carefully done, especially the insulation of the parts and wires that carry the high voltage. To preserve the safety of the users and to get rid of electromagnetic disturbances induced by the high voltage, a Faraday cage is implemented around the base that contained the electrical equipment.

Power measurements

Power measurements are essential for the evaluation of the efficiency of the actuator in flow control applications. The electrical power consumption P_{elec} of a plasma actuator can be deduced from voltage and current measurements:

$$\mathcal{P}_{elec} = \frac{1}{T_{AC}} \int_{t=0}^{T_{AC}} v(t)i(t)dt = f_{AC} \int_{t=0}^{T_{AC}} v(t)i(t)dt \tag{2.1}$$

where $v(t)$ and $i(t)$ are respectively the actuator voltage and current as a function of time, T_{AC} is the period of the applied sinusoidal signal and f_{AC} its frequency. The amplitude of the applied sinusoidal signal $v(t)$ is defined as V_{AB}. Usually, a capacitor is placed between the grounded electrode and the earth of the circuit. Plotting the capacitor charge Q_{capa} as a function of the high voltage forms a Lissajous curve which inside area corresponds to the energy dissipated by the discharge per period. By multiplying its value by the frequency of the sinusoidal signal f_{AC} one can obtain the total electrical power consumed:

[4]Groupe de Recherches sur l'Energetique des Milieux Ionisés of the University of Orléans

$$\mathcal{P}_{elec} = f_{AC} \int_{cycle} v(t) dQ_{capa} \tag{2.2}$$

For thick dielectrics, the typical consumed power is of about $1\,\mathrm{W\,cm^{-1}}$. In the following are solely examined the influence of the applied voltage V_{AC} and the carrier frequency of the sinusoidal signal f_{AC} but other parameters may impact the consumed power such as the dielectric material and its thickness or the shape of the high voltage signal. Dong et al. [2008] fit their experimental data with a second order polynomial function as follows:

$$P_{elec} = K f_{AC} (V_{AC} - V_0)^2 \tag{2.3}$$

where V_0 and K are constants depending on the actuator geometry, the experimental conditions and the dielectric characteristics. Voltage V_0 corresponds roughly to the ignition voltage of the discharge.

Figures 2.7a and 2.7b present the electrical power consumption P_{elec} as a function of V_{AC} and f_{AC} respectively. The electrical power has been divided by the actuator length that may slightly vary from one actuator to another[5], the electrical power is therefore shown in $\mathrm{W\,m^{-1}}$. Concerning the consumed power as a function of the applied voltage, the data of the two series has been fitted with the empirical formula written in equation 2.3. The curves fit the experimental data for V_0 equal to 3 kV and K of approximately 3.2 to $3.5 \times 10^{-10}\,\mathrm{W\,Hz^{-1}\,V^{-2}}$. Both constants are in the order of magnitude of the ones obtained by Dong et al. [2008] with a PCB[6] epoxy panel 0.8 mm thick. On the other hand, the electrical power is known to be proportional to the carrier frequency of the applied signal (Dong et al. [2008]) and the experimental data has been fitted thanks to a linear regression.

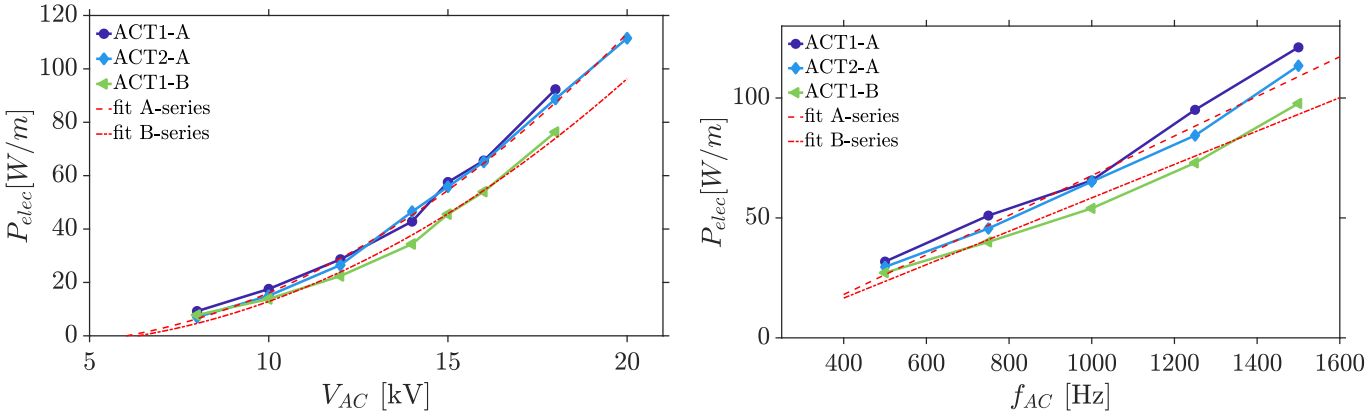

(a) Influence of the applied voltage V_{AC}

(b) Influence of the applied frequency f_{AC}

Figure 2.7: Electrical power consumption P_{elec} for different DBD actuators as a function of the applied voltage V_{AC} and carried frequency f_{AC}

Actuators belonging to the A-series have a power consumption slightly greater than the B-series, specially for the higher voltages. The dielectric material and thickness remain the same in both series and the environmental conditions are similar for every test. This difference in the power consumption may come from the difference in the actuator geometry and the different shape of the serrated active electrodes that might generate a slightly different discharge.

[5] As explained above, each multi-DBD actuator is made of 2 single-DBD actuators of approximately 900 mm long. Consumed power has been divided by the "actuator span" (i.e. ≈ 900 mm) and not the "effective electrode length" ($\approx 2 \times 900$ mm)

[6] Printed Circuit Board

Consumed power of actuator ACT1-A (circle symbols) and actuator ACT2-A (diamond symbols) is alike. A difference is visible at the higher frequencies tested ($f_{AC} = 1.25\,\text{kHz}$ and $f_{AC} = 1.5\,\text{kHz}$). However, all the control cases (characterisation and flow control in the wind-tunnel) are done at a sinusoidal frequency of 1 kHz, frequency for which both actuators have the same power consumption. Hence, power consumption of actuators belonging to the same series will be considered as equal.

The order of magnitude of the obtained P_{elec} is in good agreement with the parametric study made by Forte et al. [2006]: for a 3 mm-thick PMMA powered at 18 kV and a frequency of 1 kHz they obtained a power consumption of $0.6\,\text{W cm}^{-1}$. Furthermore, Kotsonis et al. [2014] used a PET (PolyEthyleneTerephthalate) dielectric 3 mm-thick and power consumption was estimated at $0.4\,\text{W cm}^{-1}$ for a high voltage V_{AC} equal to 17.5 kV and a frequency of 1 kHz. In the present study, the electrical consumption is of about $0.5\,\text{W cm}^{-1}$ considering the *effective electrode length* (two times the actuator span) at $V_{AC} = 18\,\text{kV}$ and $f_{AC} = 1\,\text{kHz}$. Hence, the order of magnitude of the obtained power P_{elec} is perfectly comparable with the previous studies.

Conclusion

The position of the electrodes around the TE seems to have no influence on the electrical power consumption. The actuators inside each series will therefore be considered as identical regarding the consumed power. Electrical power consumption of one set of actuators is of about $\mathbf{100\,W\,m^{-1}}$.

2.2.3 Characterisation of DBD induced jets

PIV set-up

DBD induced flows can be characterised thanks to a wide variety of diagnosis techniques. Kotsonis [2015] presented an overview of these techniques applied to DBD actuators concerning mechanical, electrical and thermal characterisations. Most common techniques are pressure measurements performed with a Pitot probe (PP), Particle Image Velocimetry (PIV), Laser Doppler Anemometry (LDA) or even Hot Wire Anemometry (HWA). PIV technique allows to have a two-dimensional velocity field and is widely used to characterise DBD induced flows as can be read in Corke et al. [2002], Chuan et al. [2009] or Kotsonis and Ghaemi [2011] among others.

In the present study, actuators are characterised in quiescent air conditions using a PIV system. Principle of PIV technique is explained in appendix A. The experimental set-up used is shown in figure 2.8. The trailing-edges holding the actuators are tested inside a wooden box ($1.1\,\text{m} \times 0.5\,\text{m} \times 0.5\,\text{m}$) with a seeding arrival and an aspiration system that removes the seeding particles if required. The laser is placed on the top of the box and the camera on one side. Both top and lateral panels are transparent. Apart from the actuators implemented around the trailing-edges, **an equivalent plane configuration for both series is also characterised in order to compare curved and plane induced jet developments.**

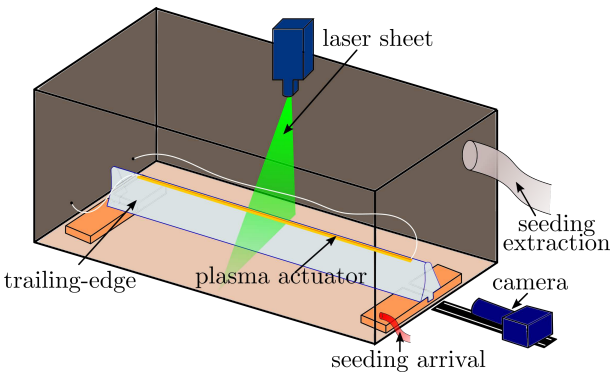

Figure 2.8: Scheme of the PIV set-up used to characterise the plasma actuators in quiescent air conditions

The laser used is a Nd:Yag Quantel Twins (Ultra series, $2 \times 200\,\text{mJ}$, 532 nm) coupled with a laser sheet generator lens. Images are recorded with a TSI PowerView 4M Plus camera with a sensor size of $2048\,\text{px} \times 2048\,\text{px}$ and equipped with a Nikon 200 mm focal length objective (Nikkor

series) set at a f-number of 5.6. 600 images pairs are recorded at a frequency of 4 Hz. Images are analysed with the Insight 4G of TSI. The final interrogation window is of 32 px × 32 px and an overlap factor of 50% is used. The dimensions of the field of view are of 60 mm × 60 mm and the vector fields are produced at a final resolution of 0.47 mm/vec (0.03 mm/px).

PIV analysis of the plane configuration is performed with different set-up parameters due to the different geometry. The dimensions of the field of view are 102 mm × 102 mm and the final interrogation window is of 16 px × 16 px with an overlap factor of 50%. Final resolution is 0.4 mm/vec (0.05 mm/px). In this case, time averaging is performed with 1000 image pairs. The time interval Δt between the two frames is equal to 58 µs, scaling to the maximal velocity of the DBD induced jet. For both curved and plane cases, seeding particles are micro-sized olive oil droplets sprayed by a PIVTEC seeding system and particle diameter is of about 1 µm. The flow induced by the plasma actuator is supposed two-dimensional and PIV measurements are carried out in the plane of symmetry of the TE or of the plane induced jet. In both plane and curved configurations, statistical convergence of the mean flow and its turbulent components is reached.

Statistical uncertainty of the mean velocity can be computed using the central limit theorem (Coleman and Steele [2009]). This method has been recently used by Van Hooff et al. [2012] and Kaffel et al. [2015] for the evaluation of the repeatability error of PIV measurements on a wall jet in a confined space and a wall jet subjected to an external lateral flow respectively. The statistical error $\widetilde{u_r}$ is defined as:

$$\widetilde{u_r} = \frac{1}{\sqrt{N_s}} z_{\frac{\alpha}{2}} \frac{U_{RMS}}{U} \tag{2.4}$$

where N_s is the number of samples, $z_{\frac{\alpha}{2}}$ is equal to 1.96 for a confidence interval of 95%, U_{RMS} is the local root mean square velocity and U the mean velocity at the same location. The uncertainty calculated in the worst configuration (maximum U_{RMS}) is of about 2% for the plane configuration and of about 3.5% for the curved ones.

2.2.4 Wind-tunnel testings

Wind-tunnel testings are performed in the "Lucien Malavard" subsonic closed-circuit wind-tunnel of PRISME laboratory. The model is mounted in the **main test-section** with a natural turbulence intensity smaller than 0.5%. The airfoil is fixed to two rotating disks that allow the variation of the airfoil angle of attack α. These disks are placed without contact within two panels spaced by 1.1 m that ensure the two-dimensionality of the flow (see figure 2.9).

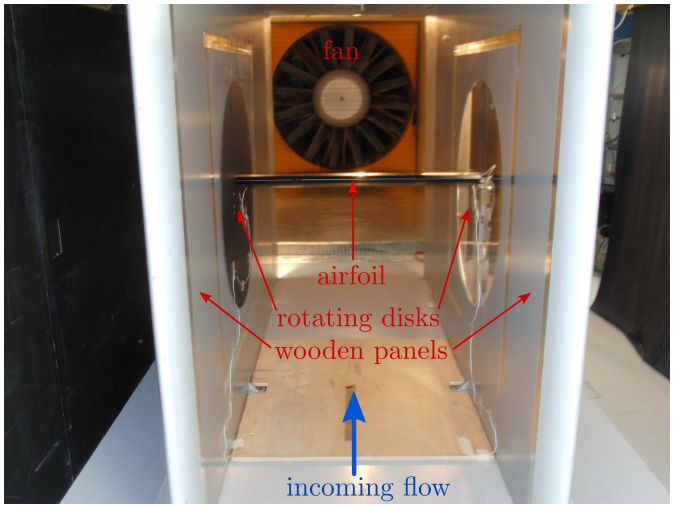

Figure 2.9: Picture of the test-section panels and the 2D-airfoil

Aerodynamic platform balance

A platform balance is located underneath the main test-section and measures the six components of the aerodynamic efforts acting on the model: drag, lift and side forces as well as roll, pitch and yaw moments. Both model and rotating disks are connected to the balance meaning that the drag force of the disks is included in the measures. Drag measurements without the airfoil in the test-section are carried out and the evaluation of the disk contribution to drag has been subtracted to the data. Balance uncertainty for the lift force is of about 6% for angles of attack corresponding to attached flows and about 3% for detached cases. Given the lift coefficient variations ΔC_L obtained, balance uncertainty is approximately equal to 25% of ΔC_L. Appendix B gets into more details on balance measurements and presents as well an analysis of the uncertainties.

Balance measurements give time-averaged lift and drag (F_L and F_D respectively) that lead to the calculation of lift and drag coefficients (C_L and C_D) defined as:

$$C_L = \frac{F_L}{\frac{1}{2}\rho U_\infty^2 cl} \qquad (2.5) \qquad\qquad C_D = \frac{F_D}{\frac{1}{2}\rho U_\infty^2 cl} \qquad (2.6)$$

where ρ is the air density, U_∞ the incoming flow velocity, c the airfoil chord and l its span. Balance measurements are taken at a frequency of 1 kHz and 20 000 samples are acquired (20 s).

Surface pressure distribution

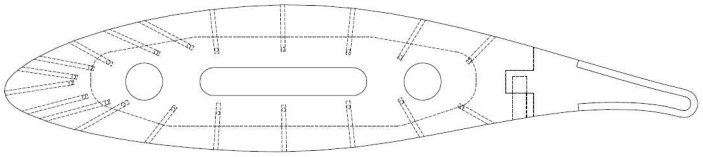

Figure 2.10: Position of the pressure taps (2D-airfoil)

Pressure distribution on the model is measured with 20 pressure taps distributed around the airfoil as shown in figure 2.10. Pressure taps are located in the middle plane of the airfoil. They are available only in the main part of the model i.e. from the leading-edge to 70% of the chord due to the impossibility to drill near the DBD actuators. Measures are taken with a 32-channel differential pressure scanner ESP-32HD (GE, ±1 PSI) embedded in a MicroDAQ system (SHELL). This scanner measures the differential pressure between the model surface pressure and the static pressure in the test-section upstream of the model. Accuracy of the pressure sensor is of ±0.25% of the full scale, i.e. approximately 17 Pa, which corresponds to about 30% of the measured pressure levels.

Pressure measurements lead to the calculation of a time-averaged pressure coefficient C_p defined as:

$$C_p = \frac{P - P_\infty}{\frac{1}{2}\rho U_\infty^2} \qquad (2.7)$$

where P is the pressure measured at the airfoil surface and P_∞ the static pressure in the wind-tunnel test-section upstream of the model measured with a Pitot probe. Measures are taken at a frequency of 500 Hz (maximal sensor frequency) and 10 000 samples are acquired (20 s). This measure was not synchronised with the load measurements of the platform balance.

PIV measurements

To analyse the flow topology around the trailing-edge and the flow behaviour under actuation, PIV measurements are carried out in the test-section (refer to appendix A for the technique principles). Thanks to a laser guiding arm, the light sheet is oriented in order to visualise

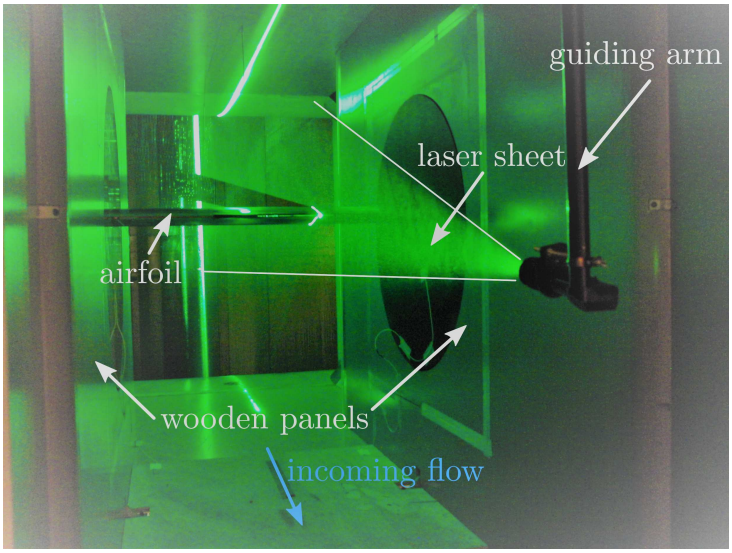

Figure 2.11: Picture of the PIV experimental set-up in the wind-tunnel test-section (2D-airfoil)

simultaneously the pressure and suction sides of the airfoil as shown in figure 2.11. The camera was placed outside of the test-section (on the left hand side in picture 2.11). The laser used is a Nd:Yag Evergreen (series 200, $2 \times 200\,\text{mJ}$, 532 nm) coupled with a laser sheet generator lens (10 mm focal length). Images are recorded with a LaVision LX11M camera with a sensor size of $4032\,\text{px} \times 2688\,\text{px}$ and equipped with a Nikon 200 mm focal length objective (Nikkor series) set at a f-number of 4 and a $\lambda = 532\,\text{nm}$ filter. 1000 images pairs are recorded at a frequency of about 2.5 Hz. Images are analysed with the DaVis software v.8.1.6 of LaVision.

The final interrogation window is of $32\,\text{px} \times 32\,\text{px}$ (or $16\,\text{px} \times 16\,\text{px}$) and an overlap factor of 50% is used. The dimensions of the field of view are of $195\,\text{mm} \times 130\,\text{mm}$ and the vector fields are produced at a final resolution of 0.77 mm/vec (or 0.39 mm/vec). The time interval Δt between the two frames is equal to 34 µs (or 20 µs), scaling to the incoming flow velocity $U_\infty = 10\,\text{m/s}$. Seeding particles are micro-sized olive oil droplets sprayed by a PIVTEC seeding system and particle diameter is of about 1 µm. The flow around the airfoil is supposed two-dimensional and PIV measurements are carried out in the plane of symmetry of the airfoil.

Hot wire anemometry

Hot wire anemometry is carried out in order to characterise the specific frequencies of the airfoil wake. A dual sensor probe (Dantec Dynamics 55P61) is used. The hot wire is fixed to one of the rotating disks so it could rotate with the airfoil. The hot wire probe is located 225 mm ($\frac{3}{4}$ of the airfoil chord) downstream of the trailing-edge, 20 mm above it in the vertical direction and 450 mm apart from the rotating disk. The number of taken samples is equal to 2^{20} ($\approx 10^6$) at 15 kHz.

2.3 Characterisation of DBD induced jets in quiescent air conditions

The characterisation of DBD induced flows in quiescent air conditions is primordial for the understanding of the jet development over the model surface and the possible mechanisms of interaction with the external flow in the perspective of the flow control application. However, this kind of characterisation has not been carried out, to the author's knowledge, for actuators positioned around a curved wall as done in the present case. This investigation, performed through PIV measurements, allows to obtain the induced jet topology but also the order of

magnitude of the jet velocity and thickness. Also, velocity fields can be post-treated to obtain the thrust force produced by the actuator and calculate a momentum coefficient C_μ, that quantifies the *strength* of the actuation for a given incoming flow, and remains a variable of comparison between flow control strategies. Also, this study allows to determine if an eventual Coanda effect might be highlighted in the case of our curved DBD induced jets. Furthermore, this kind of characterisation may be helpful for the implementation and validation of numerical models that would reproduce the DBD actuation. Indeed, unlike experimental testings, numerical simulations allow the collection of data for a large range of test cases and in a relatively reduced time and cost. Numerical investigations require, though, experimental results to be validated against.

2.3.1 Analysis in the airfoil-related coordinate system

Mean topology of DBD induced flows along a curved surface

The airfoil-related coordinate system (x, y, z) is defined as: x-axis in the direction of the airfoil chord, y-axis in the wingspan direction and z-axis in the vertical direction (see figure 2.12). Velocity average and fluctuating parts are defined according to the following Reynolds decomposition where t represents the time dependency: longitudinal velocity defined as $U(x,z,t) = \overline{U}(x,z) + u'(x,z,t)$ and vertical velocity as $V(x,z,t) = \overline{V}(x,z) + v'(x,z,t)$.

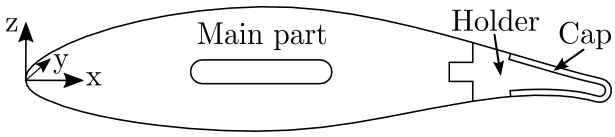

Figure 2.12: Airfoil-related coordinate system

Figure 2.13 shows time-averaged magnitude velocity fields for the three actuators of the A-series. Electrode position and geometry are superimposed in the figures. Normal velocity profiles are also plotted and are computed with a linear interpolation in the normal direction to the wall using a spatial step equal to the PIV resolution (0.47 mm/vec). Even though the three actuators have the same electrode lengths, the same dielectric thickness and are powered at the same voltage V_{AC} and frequency f_{AC} (and therefore consuming the same electrical power), their respective induced jets topologies are different.

The induced flow of actuator ACT1-A follows partially the TE curvature but does not remain perfectly attached to the model and detaches beyond the TE circumvention. On the contrary, the wall jet from actuator ACT2-A follows the wall curvature and perfectly adheres to the model wall beyond the 180° sharp turn. Actuator ACT3-A, blowing in the opposite direction of the two previous actuators, also remains attached to the wall and diffuses along the upper side of the airfoil. This different jet behaviour can be explained by the electrode arrangement of the three actuators. For ACT1-A, the actuator ends up too early to allow a complete TE circumvention. In the cases of ACT2-A and ACT3-A, which have the same electrode arrangement but blow in opposite directions, the region of ElectroHydroDynamic (EHD) interaction reaches the end of the TE curvature and the wall jet is forced to completely follow the sharp turn curvature of the trailing-edge.

Momentum coefficient C_μ calculation

The computing of the velocity profiles normal to the wall allows to obtain flow quantities important for the comparison between flow control devices. For the calculation of these integral values, a characteristic length of actuation is needed and is defined as L_p corresponding to the actuator span set to $L_p = 0.9\,\text{m}$. Enloe et al. [2006] estimated the air density ρ fluctuations in the vicinity of the actuator smaller than 2% of the background density. Hence, ρ will be considered as a constant and set to $1.2\,\text{kg}\,\text{m}^{-3}$. Flow variables and characteristic quantities are defined as follows, where z^* is the normal direction to the airfoil wall:

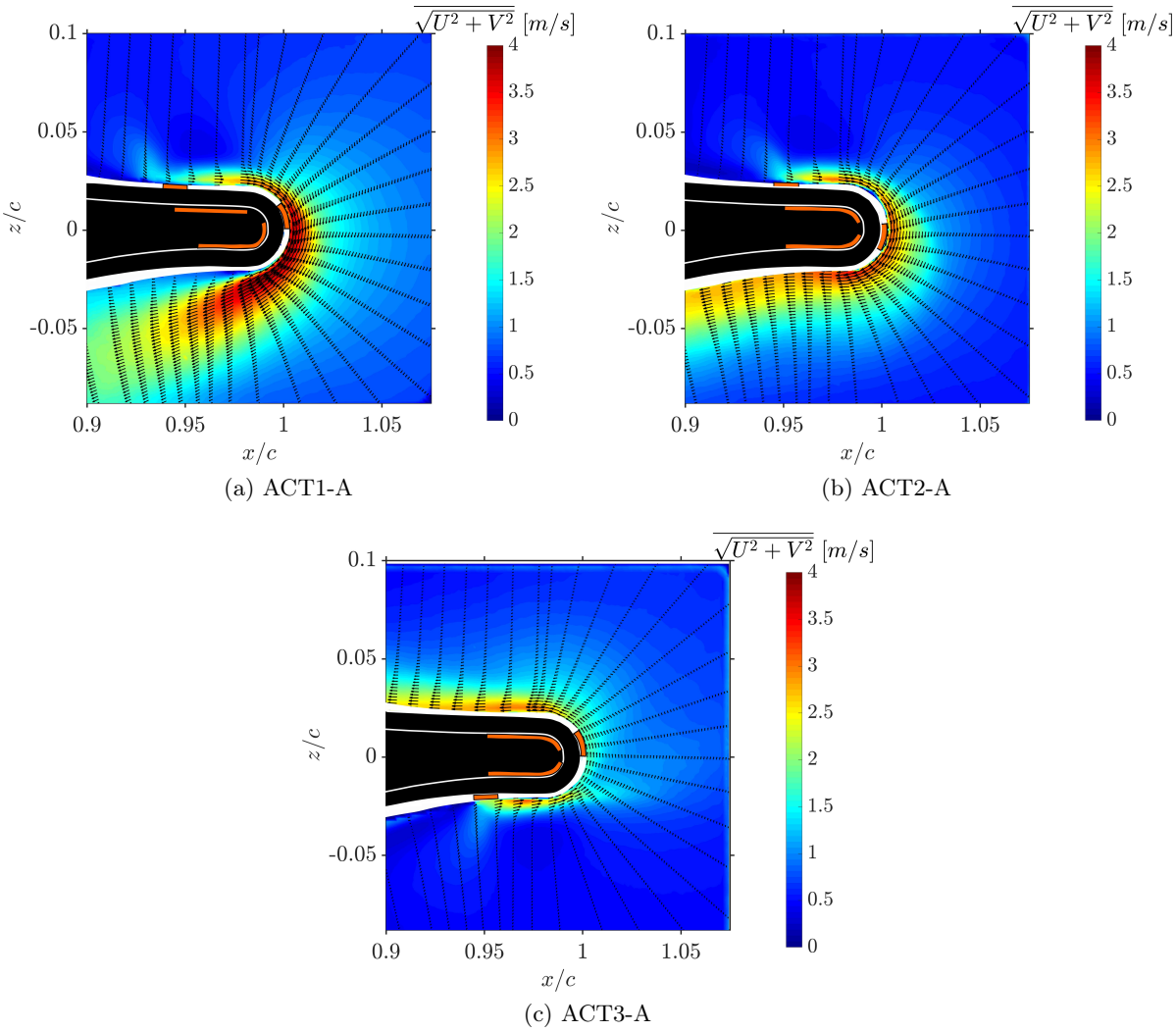

(a) ACT1-A

(b) ACT2-A

(c) ACT3-A

Figure 2.13: Time-averaged velocity fields for the three actuators of the A-series in quiescent air conditions ($V_{AC} = 18\,\text{kV}$ and $f_{AC} = 1\,\text{kHz}$)

– Mass flow Q_m:

$$Q_m = \rho L_p \int_0^\infty U(z^*)dz^* \tag{2.8}$$

– Momentum coefficient C_μ:

$$C_\mu = \frac{\rho L_p \int_0^\infty U^2(z^*)dz^*}{q_\infty S_{ref}} \tag{2.9}$$

where S_{ref} is defined as the reference surface of the airfoil i.e. the product of the chord c and the wingspan of the model l: $S_{ref} = cl = 0.33\,\text{m}^2$. The dynamic pressure q_∞ is defined as $q_\infty = \frac{1}{2}\rho U_\infty^2$, where U_∞ is the wind-tunnel flow velocity. When low momentum is introduced in the boundary layer near the LE, the actuation can destabilise the BL and trigger separation. Usually, this phenomenon occurs when the injected jet velocity is lower than the local velocity of the flow. For very low C_μ this parameter might not be appropriate and Kelly [1956] suggested another definition C'_μ to be used when the injected velocity U_{inj} is in the order of magnitude of the external flow velocity U_{ext}:

$$C'_\mu = C_\mu \left(1 - \frac{U_{ext}}{U_{inj}}\right) \tag{2.10}$$

However, as C_μ is commonly used in the literature it will be used in this work for consistency with previous studies. This classical definition neglects, however, the external velocity at the actuation location and the state of the flow i.e. the location of the separation point that changes with the angle of attack.

– Mechanical power P_{mec}:

$$P_{mec} = \rho L_p \int_0^\infty U^3(z^*)dz^* \tag{2.11}$$

– Actuator efficiency η_{act}:

$$\eta_{act} = \frac{P_{mec}}{P_{elec}} \tag{2.12}$$

Table 2.1 summarises the computed mass flow Q_m, mechanical power P_{mec}, momentum coefficient C_μ and efficiency η_{act} for actuators ACT1-A and ACT2-A[7] as well as their plane equivalent. As there is one value of each variable per velocity profile, the values showed in the table correspond to the maximal value obtained in the jet streamwise direction. Mechanical power induced by the actuator is of about 0.1 to 0.2 W and mass flow ranges from 30 to 45 $\mathrm{g\,s^{-1}}$.

Momentum coefficient

As the curved jets show different thicknesses and jet topologies, the momentum coefficient that will be used in the following sections for the flow control application corresponds to the **plane configuration**. This C_μ is equal to 0.7×10^{-3}, 1.4×10^{-3} and 2.2×10^{-3} for applied voltages equal to 15 kV, 18 kV and 20 kV respectively. This simplification is also carried out by Kotsonis et al. [2014] who assumed the momentum coefficient in plane and curved configurations as equal.

	ACT1-A		ACT2-A		Plane A		
V_{AC}	15 kV	18 kV	15 kV	18 kV	15 kV	18 kV	20 kV
P_{elec} [W]	50.7	79.8	50.7	79.8	50.7	79.8	100
P_{mec} [W]	0.147	0.236	0.0805	0.113	0.026	0.065	0.14
η_{act} [%]	0.184	0.295	0.207	0.275	0.052	0.081	0.14
Q_m [$\mathrm{g\,s^{-1}}$]	38.7	46.7	30.0	34.6	12.4	16.3	19.1
C_μ [$\times 10^{-3}$]	3.2	4.5	2.1	2.7	0.7	1.4	2.2

Momentum coefficient is calculated for an incoming flow velocity of U_∞ = 10 m/s corresponding to the velocity of all the tested cases performed in the wind-tunnel

Table 2.1: Table summarising the integral flow quantities of the actuators studied

Velocity fields obtained by PIV may be used to calculate the thrust per unit span produced by a plasma actuator. This method requires the definition of a control volume that allows the calculation of the momentum flux across the boundaries of the domain as done by Hoskinson et al. [2008]. The body force expression derives from momentum balance equation:

[7] ACT3-A is analog to ACT2-A and is not shown

$$\frac{\partial\left(\rho\vec{U}\right)}{\partial t}+\vec{\nabla}\cdot\left(\rho\vec{U}\otimes\vec{U}\right)=-\vec{\nabla}P+\vec{\nabla}\cdot\overline{\overline{\tau}}+\rho\vec{F} \tag{2.13}$$

where $\vec{U}=(U,V)$ is the eulerian velocity vector of the flow, P is the pressure, $\overline{\overline{\tau}}$ is the shear stress tensor and $\vec{F}=(F_x,F_z)$ is the unknown plasma force.

Kriegseis et al. [2013b] compare different integral methods to estimate the total body force. They show that 30% of the induced momentum is consumed by wall friction. Due to the low PIV resolution near the model wall (first vector at about 1 mm from the wall) the shear stress term could not be computed and only the momentum flux across the control volume boundaries will be considered. Hence, the calculated thrust $\vec{F}$ includes surface forces (pressure forces and shear forces) between the wall and the fluid. Furthermore, as pressure fields are not available with the present experimental set-up, it will be considered that the control volume is far enough from the plasma region and that the static pressure at the boundaries can be considered as uniform and equal. With the previous assumptions and assuming a steady, incompressible and 2D-flow, equation 2.13 is reduced to:

$$\frac{\vec{F}}{L_p}=\oint_{VC}\rho\vec{U}(\vec{U}\cdot\vec{n})dS \tag{2.14}$$

where $\vec{n}$ is the surface unit normal vector pointing towards the exterior of the surface of the control volume. Figure 2.14 shows an example of a control volume contour for actuator ACT2-A. The projection of equation 2.14 in x and z directions gives:

$$\frac{F_x}{L_p}=-\rho\int_{12}U^2dz+\rho\int_{23}UVdx+\rho\int_{34}U^2dz-\rho\int_{45}UVdx-\rho\int_{56}U^2dz \tag{2.15}$$

$$\frac{F_z}{L_p}=-\rho\int_{12}UVdz+\rho\int_{23}V^2dx+\rho\int_{34}UVdz-\rho\int_{45}V^2dx-\rho\int_{56}UVdz \tag{2.16}$$

The total ElectroHydroDynamic force produced by the plasma actuator F_{EHD} i.e. the total thrust is then obtained by:

$$F_{EHD}=\sqrt{F_x^2+F_z^2} \tag{2.17}$$

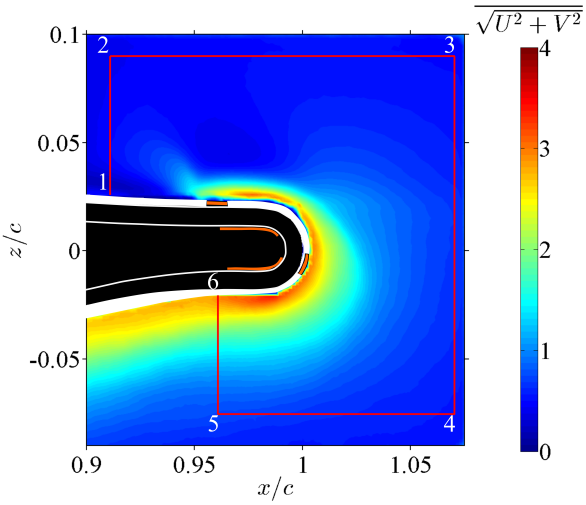

Figure 2.14: Time-averaged velocity field for actuator ACT2-A in quiescent air conditions - $V_{AC}=18\,\text{kV}$ and $f_{AC}=1\,\text{kHz}$ - red line shows the control volume contour

Table 2.2 summarises the computed EHD forces F_{EHD} for actuators ACT1-A and ACT2-A. The momentum coefficient can be computed again with the thrust force and according to

definition $C_\mu = \frac{F_{EHD}}{q_\infty S_{ref}}$. The thrust values obtained are in the order of magnitude of the ones obtained by Kotsonis and Ghaemi [2012] who obtained $30\,\mathrm{mN\,m^{-1}}$ for a single DBD in a plane configuration. In the present study, actuators are composed of two single DBD in a row and thrust forces are grossly two times higher. Momentum coefficients computed with the two methods (velocity profiles and thrust force) show very similar values.

	ACT1-A		ACT2-A	
V_{AC}	15 kV	18 kV	15 kV	18 kV
F_{EHD} [mN m^{-1}]	72.9	102	49.5	65.3
F_x [mN m^{-1}]	72.3	101.6	48.4	64.1
F_z [mN m^{-1}]	9.3	8.6	−10.5	−12.0
C_μ [$\times 10^{-3}$]	3.3	4.6	2.2	3.0

Table 2.2: Table summarising the EHD force F_{EHD} and its components

2.3.2 Analysis in the jet-related coordinate system

DBD induced jets can be compared to fluidic wall jets (WJ) as their share a similar topology. Indeed, in the case of a DBD induced jet, the electrically charged particles located close to the wall are accelerated from the active electrodes and along the grounded ones, following the electrical field. This particle motion entrains the ambient air creating an induced jet parallel to the wall. However, there is no nozzle or jet exit and the flow accelerates continuously until roughly the end of the last grounded electrode beyond which it starts diffusing. Velocity magnitude induced by a single DBD actuator is weak (max. $\approx 8\,\mathrm{m/s}$ in Moreau [2007]) compared to fluidic actuators. In the case of a DBD induced jet, there is no mass addition by the actuator but only mass entrainment and momentum transfer.

In order to assess the similarities and the discrepancies between both flows, the DBD induced jets of the present study are compared to canonical fluidic wall jets flowing along plane and curved surfaces.

Plane and curved wall jet variables

To analyse a classical wall jet development over a two-dimensional plane surface some quantities are usually defined as shown in figure 2.15. A new coordinate system related to the WJ and different from the airfoil-related coordinate system is defined: x is in the longitudinal direction of the jet and the ordinate z is in the normal direction. The origin of the x-coordinate is the exit of the nozzle and the z-coordinate origin is the surface of the wall. Each velocity profile along the x-coordinate has its local maximum velocity named $U_{max}(x)$ located at a distance $z_{max}(x)$ from the wall. The variable $z_{\frac{1}{2}}(x)$ is defined as the distance from the wall to the location at which the mean velocity decreases to one half of its local maximum value in the outer flow. The jet maximum velocity U_j is the jet velocity slightly downstream of the exit of the nozzle, at the x_0 abscissa defined as $U_{max}(x_0) = U_j$. The Reynolds number of the jet is defined as $Re_j = \frac{U_j b}{\nu}$ where b is the nozzle width and ν is the kinematic viscosity of the flow. In the case of a plane WJ induced by a DBD actuator (DBD-WJ), as there is no physical nozzle (see figure 2.16), the origin of the x coordinate ($x = 0$) is set at the beginning of the first active electrode and the abscissa of the virtual origin x_0, corresponding to the maximum jet velocity, is also defined as $U_{max}(x_0) = U_j$. The virtual slot width b is defined as the jet thickness at the virtual origin $b = z_{\frac{1}{2}}(x_0)$. Assuming that the surface discharge has a negligible effect on the gas properties as mentioned in Moreau [2007], the kinematic viscosity ν of the induced jet is supposed equal to the kinematic viscosity of air. Then, the jet Reynolds number Re_j can be defined in analogy

with the fluidic WJ definition mentioned above. A local Reynolds number $Re_x = \frac{U_{max}(x) z_{\frac{1}{2}}(x)}{\nu}$ is also defined.

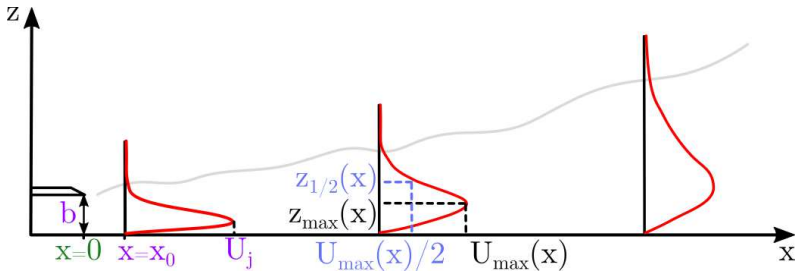

Figure 2.15: Scheme of a fluidic WJ over a plane surface and its specific variables

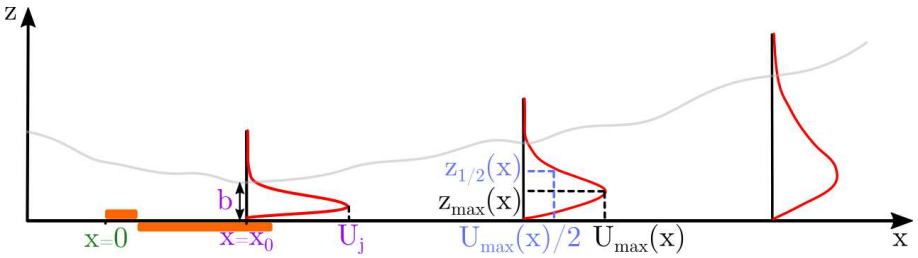

Figure 2.16: Scheme of a DBD-WJ over a plane surface and its specific variables

A second coordinate system is defined to follow a wall jet evolution over a curved surface. Neuendorf and Wygnanski [1999] studied a WJ flowing around a circular cylinder and defined an angle θ^* (figure 2.17a) between the nozzle and the azimuthal position of the velocity profile. In the present case (figure 2.17b), as the trailing-edge is not axisymmetrical, a curvilinear abscissa x^* is defined along the curvature with a related vertical coordinate z^* normal to the model wall. The origin of the x^* coordinate ($x^* = 0$) is set at the beginning of the actuator (first active electrode). Local variables $z^*_{max}(x^*)$, $U_{max}(x^*)$ and $z_{\frac{1}{2}}(x^*)$ are defined in the same way as the plane DBD-WJ described above. Global variables as the maximum jet velocity U_j, the virtual origin x^*_0, the virtual slot width b^*, the jet Reynolds number Re_j and the local Reynolds number Re_{x^*} are also defined as mentioned above. Angle β is defined as the angle between the trailing-edge extremity and the virtual origin x^*_0.

Jet main characteristics

Table 2.3 shows the DBD-WJ characteristics for actuators ACT1-A and ACT2-A[8]. Virtual origin x^*_0 is located at an angle β with respect to the TE extremity of 60° and 70° for ACT1-A and ACT2-A respectively. The position of the virtual origin around the curvature is directly related to the positioning of the electrodes around the TE and therefore to the WJ topology: the greater the β angle, the more the DBD-WJ attaches to the model curvature. While the jet velocity magnitude U_j is equivalent between plane and curved DBD-WJs, the jet thickness b (or b^*) remains smaller for the plane cases leading to lower Reynolds numbers. Jet velocities and thicknesses found in the literature for plane DBD-WJ match the values obtained for the plane DBD case as can be read in Balcon et al. [2009], Durscher and Roy [2012] or Benard and Moreau [2014] among others. Hence, for similar dielectric thicknesses (2 mm to 3 mm), U_j ranges from 3 to 5 m/s and b^* from 2 to 5 mm at the beginning of jet diffusion.

The jet Reynolds number Re_j for the curved DBD-WJs of the present study varies from 1100 to 1900 meaning that all the DBD induced jets are close to the turbulent regime according to the

[8] Again, as ACT3-A and ACT2-A have a similar topology, only ACT2-A is shown

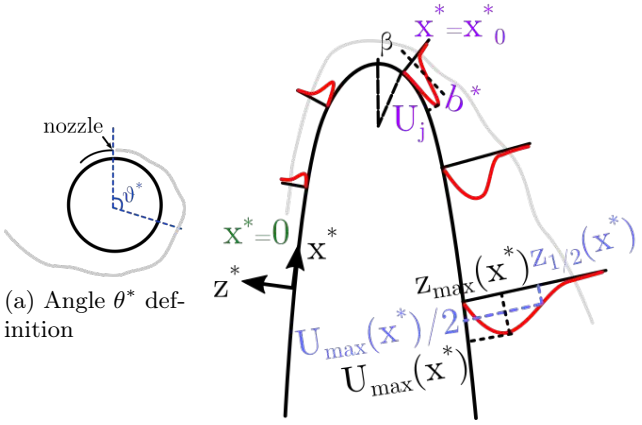

(a) Angle θ^* definition

(b) Scheme of a DBD-WJ over a curved surface

Figure 2.17: (a) θ^* angle definition over a cylinder, (b) Scheme of a DBD-WJ flowing over a rounded trailing-edge and its specific variables

	V_{AC} [kV]	b or b^* [mm]	U_j [m s^{-1}]	β [°]	Re_j
ACT1-A	15	7.2	3.4	50	1600
	18	7.7	3.8	60	1900
ACT2-A	15	5.7	3.0	70	1100
	18	6.2	3.3	70	1300
Plane DBD	15	2.5	2.8	-	450
	18	2.9	2.9	-	600

Table 2.3: DBD-WJ characteristics

critical Reynolds number suggested by Murphy et al. [2013] that is $Re_{jc} \approx 100$ for DBD induced jets. An experimental stability investigation of a laminar 2D plane fluidic WJ was carried out by Bajura and Szewczyk [1970] and the authors concluded that the critical value of Re_{jc} lies between 500 and 2000, which is the order of magnitude of the Re_j obtained in the present investigation.

Electrode position has a direct impact on the DBD-WJ topology specially whether the induced jet is going to follow the model curvature or not. However, the reason why DBD-WJs stay attached to the wall seems to be more an electrical effect than a phenomenon due to the dynamics of the fluid. Fekete [1963] studied the Coanda effect of a WJ over a cylinder and found, for jet Reynolds numbers Re_j between 1500 and 2000, that separation occurred at an azimuthal angle from the nozzle θ^*_{sep} from 60° to 75°, very far from a complete circumvention (180°). Vít and Maršík [2004] studied a heated Coanda laminar WJ and for Re_j of 740 and 950 obtained an angle θ^*_{sep} of 40° and 90° respectively for a ratio $\frac{b}{R} = 0.25$, b being the jet thickness and R the radius of curvature of the cylinder. Their results showed that over this ratio (present case: $\frac{b}{R} \approx 1$) separation occurs at even smaller θ^* angles. Hence, Coanda effect does not seem to be applicable for curved DBD-WJs of the present study in the view of the Reynolds numbers and jet thicknesses involved but also due to the small radius of curvature of the trailing-edge.

Self-similarity of the mean velocity profiles and of the turbulent components

Plane and curved induced jets are here characterised here in terms of self-similarity of the velocity profiles. Both plane and curved DBD-WJs are powered at $V_{AC} = 18\,\text{kV}$ but have distinct Reynolds numbers: 600 for the plane DBD and 1300 for the curved DBD of ACT2-A ($C_\mu = 0.003$). This last curved case behaves the closest to the plane WJ of all the curved actuators studied, specially in the **diffusion zone**. Velocity profiles normal to the wall are computed in the jet-related coordinates (x^*, z^*). First, the equation of the perpendicular lines to the surface and the angle with the horizontal direction are found. Then, the coordinates of the velocity profiles are computed in the curvilinear framework. Finally, the velocity values are linearly interpolated along the profile coordinates. Analysed velocity profiles located in the diffusion zone of each actuator are shown in figure 2.18a and 2.18b for the plane and curved DBD-WJs respectively. Markers and line colors shown in the figures correspond to the ones used in the following at each given abscissa: the lighter the gray-scale color and the farther the profile is in the jet streamwise direction.

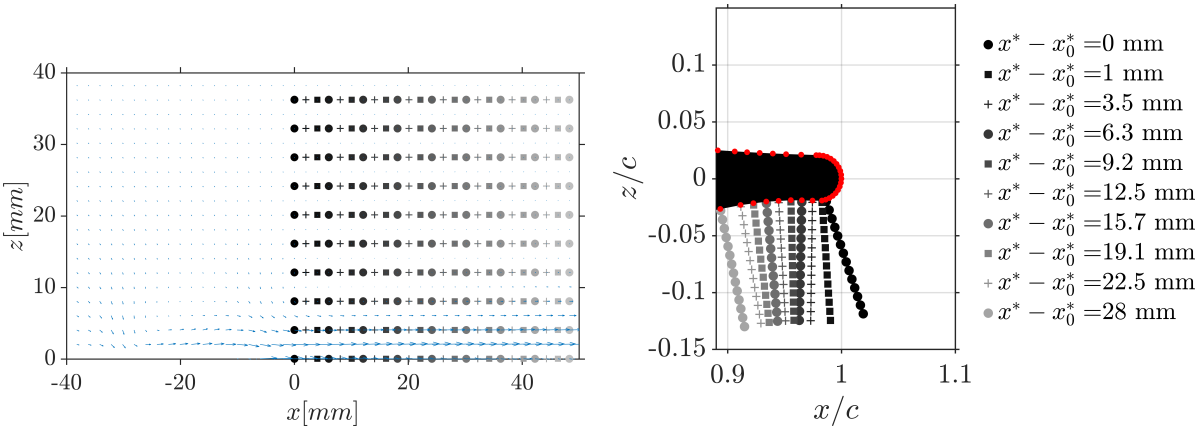

(a) Plane DBD

(b) Curved DBD

Figure 2.18: Location of the analysed velocity profiles and their respective markers

Velocity profiles are shown in figure 2.19. The difference between both DBD-WJs is clear as the plane induced jet is much thinner than its curved equivalent. The spread of both DBD-WJs is also highlighted as the greater the x (or x^*) abscissa, the lower the maximum velocity and the higher the jet thickness. In the case of the curved DBD case, the three first profiles in the streamwise direction (darker greys) are just beyond the virtual origin x_0^*. The velocity maximum value is near its maximal value and the profiles show a high velocity gradient in the vicinity of the wall.

The commonly used normalisation for velocity profiles involves the jet velocity U_j and its thickness b^*. These profiles are plotted in figure 2.20. Plots also compare the obtained velocity profiles with the laminar and turbulent cases obtained by Glauert [1956] and Schneider and Goldstein [1994] respectively. For the plane DBD-WJ (figure 2.20a), this scaling collapses reasonably well the experimental data except in the area in the very vicinity of the wall and the outer flow where the data scatter becomes larger. The ordinate of the maximum velocity is located at $\frac{z^*_{max}}{z^*_{\frac{1}{2}}} = 0.35$ right between the laminar and the turbulent profiles (0.6 for a laminar WJ, 0.15 to 0.2 for a turbulent WJ). Boucinha et al. [2008], Murphy et al. [2013] and Maden et al. [2013] studied the evolution of plane DBD induced jets and also found velocity profiles between laminar and turbulent ones. The velocity gradient in the inner part seems closer to the laminar WJ, but the outer part tends to follow the turbulent velocity distribution. The ordinate of the maximum velocity peak confirms that plane DBD-WJs are in a transitional regime.

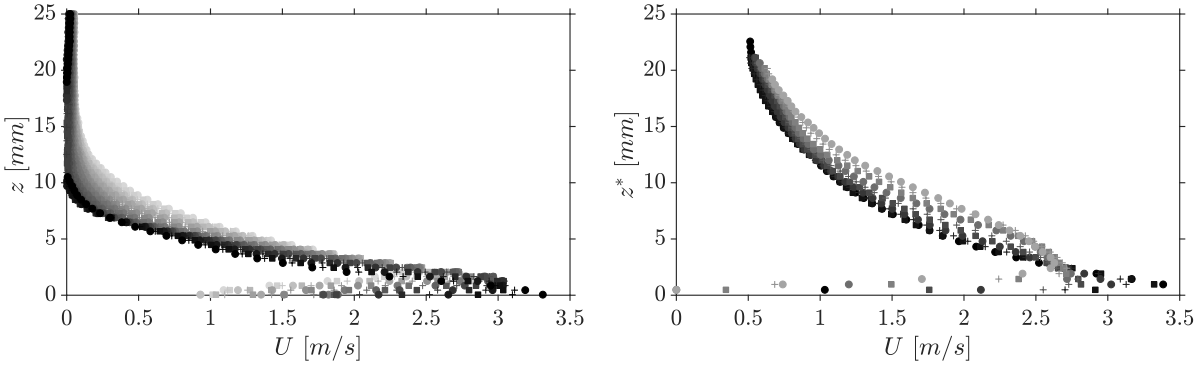

(a) Plane DBD (diffusion zone)

(b) Curved DBD (ACT2-A - diffusion zone)

Figure 2.19: Dimensional velocity profiles at different x^* positions

In the case of the curved DBD configuration (figure 2.20b), the profiles of the higher abscissas x^* (lighter greys) fit well the turbulent profile but the first velocity profiles beyond the virtual origin (darker greys) do not really fit laminar nor turbulent profiles. However, the ordinate of $\frac{z^*_{max}}{z^*_{\frac{1}{2}}}$ is equal to 0.15 in agreement with the turbulent case. This scaling does not perfectly collapse the mean velocity distribution in one single curve but a quasi-similarity is however reached. Curved DBD-WJ matches almost perfectly the turbulent velocity profile for the higher abscissas x^*.

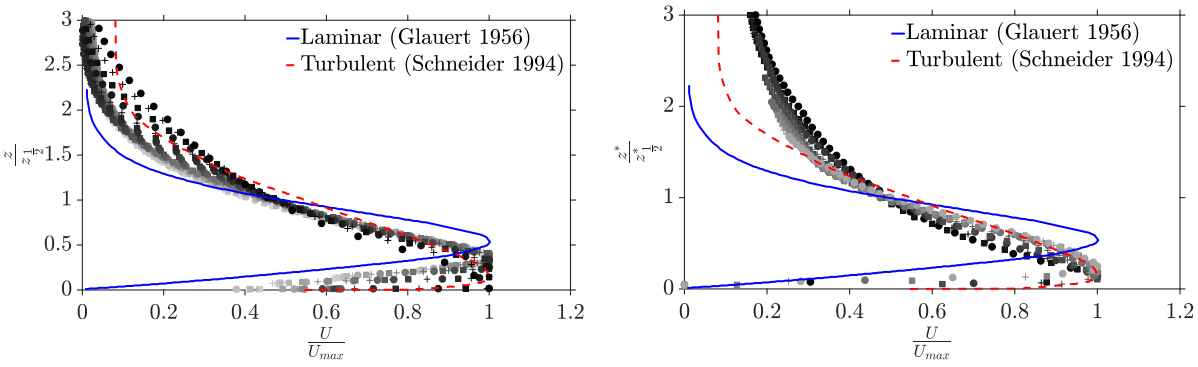

(a) Plane DBD (diffusion zone)

(b) Curved DBD (ACT2-A - diffusion zone)

Figure 2.20: Normalised velocity profiles at different x^* positions (scaling based on U_{max} and $z_{\frac{1}{2}}$)

Jet evolution with dimensional variables

Four variables, $z^*_{\frac{1}{2}}$, z^*_{max}, U_{max} and Re^*_x are used in this paragraph to describe the DBD induced WJs evolution along the x-direction. Actuators are powered at a voltage $V_{AC} = 15\,\text{kV}$ and a frequency $f_{AC} = 1\,\text{kHz}$ ($C_\mu = 0.002$). Figure 2.21a shows the evolution of z^*_{max} with x^* and figure 2.21b plots the evolution of $z^*_{\frac{1}{2}}$ with x^*. All the following variables are plotted with respect to the virtual origin x^*_0, the abscissa where the local jet velocity is maximal, meaning that $x^* - x^*_0 > 0$ corresponds to the jet diffusion zone. In the case of the plane DBD-WJ, a polynomial fitting is performed in the diffusion zone to address the low PIV resolution in the vertical direction. The three zones that distinguish a DBD induced jet can be identified.

Aspiration is characterised by a decrease of z^*_{max} and $z^*_{\frac{1}{2}}$. The **acceleration** zone corresponds to an almost constant z^*_{max} located very close to the wall and a progressive increase of $z^*_{\frac{1}{2}}$ revealing the induced WJ spread. Finally, beyond the virtual origin the jet does not accelerate anymore, gets thicker, and diffuses along the model wall (**diffusion zone**). This generates a z^*_{max} progressive increase and consequently a $z^*_{\frac{1}{2}}$ augmentation.

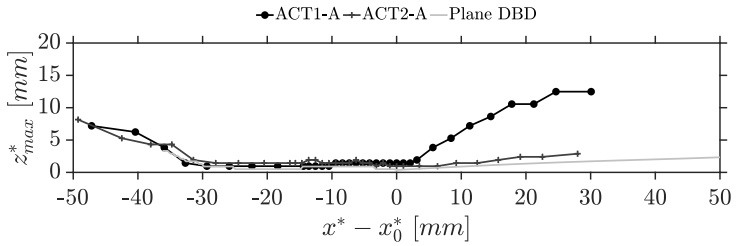

(a) Maximum velocity ordinate z^*_{max} evolution

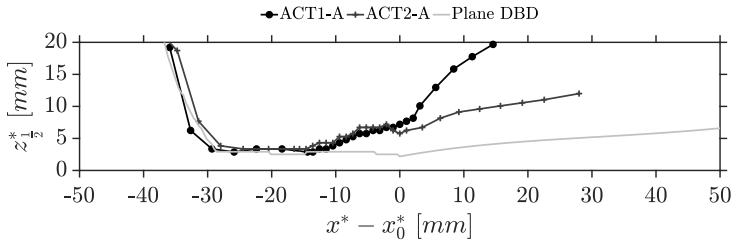

(b) Ordinate $z^*_{\frac{1}{2}}$ evolution

Figure 2.21: Maximum velocity ordinate z^*_{max} and ordinate $z^*_{\frac{1}{2}}$ evolution in the flow direction x^*

Due to the detached topology of the induced jet of ACT1-A, z^*_{max} moves away from the wall beyond the virtual origin. However, both plane DBD-WJ and curved DBD of ACT2-A show a similar evolution of z^*_{max}, especially in the diffusion zone. For these two attached jets, the actuator geometry, plane or curved, does not interfere in the ordinate of the maximal velocity that is close to 2.5 mm at the end of the diffusion zone actually visible in the PIV window. Regarding the evolution of $z^*_{\frac{1}{2}}$ ordinate, curved DBD-WJs prove to have a higher spread than the plane one reaching 10 mm to 20 mm when their plane equivalent reaches 7 mm at the end of their respective diffusion zones. Induced jet of ACT1-A reveals a spread two times higher than the one of ACT2-A that is itself two times greater than the one corresponding to the plane configuration. This evolution is in reasonable agreement with the results obtained by Bradshaw and Gee [1960] who found that the spread of a fluidic WJ over a cylinder is 1.5 higher than over a flat plate.

Local maximum velocity $U_{max}(x^*)$ in the streamwise direction x^* is plotted in figure 2.22a. By definition, the velocity decay appears for all the actuators beyond the virtual origin x^*_0. Maximum velocity is of the same order of magnitude for the three actuators plotted but the velocity decay is considerably slower for the plane DBD-WJ. For this jet, the multi-DBD actuation is clearly visible as the velocity increase is performed in two steps reaching 2.6 m/s. The velocity maximum corresponding to the second DBD actuator reaches the same value as the first DBD actuator. A two-stepped velocity increase is also visible for the curved flows whose velocity gap between the two single-DBD is of about 1 m/s.

Local Reynolds number Re_{x^*} evolution with x^* is shown in figure 2.22b. In the case of the plane DBD-WJ, the Reynolds number increase is significant over the first actuator ($x^* - x^*_0 \in [-30, 0]$) where there is a sudden velocity increase but also at the beginning of the diffusion zone where there is a high rate of spread. Beyond the virtual origin, the Re_{x^*} increase continues. This happens because spread is more important than the velocity decay in the diffusion zone and the

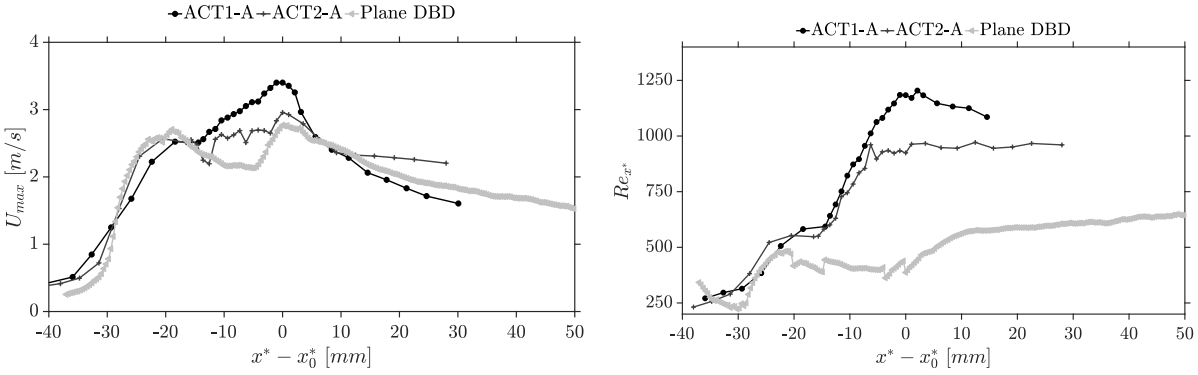

(a) Maximum velocity U_{max} evolution

(b) Local Reynolds number Re_{x^*} evolution

Figure 2.22: Maximum velocity U_{max} and local Reynolds number Re_{x^*} evolution in the flow direction x^*

Reynolds number tends to augment up to 600. On the contrary, curved DBD-WJ of ACT1-A shows a slight decrease after the virtual origin because its velocity decrease is more important than the rate of spread increase as mentioned in Glauert [1956]. Curved DBD-WJ of ACT2-A shows a Reynolds number plateau in the diffusion zone. For both curved jets, the Reynolds number increase is done in two distinct steps that give evidence again of the multi-DBD actuator implementation. Because of the higher thickness of curved DBD-WJs, their overall Re_{x^*} level is greater than for the plane DBD induced jet.

Jet evolutions with normalised variables

As mentioned above, a wall jet development over a surface can be characterised by the evolution of two parameters: the maximum **velocity decay** and the **rate of spread**. These parameters can be normalised by two length and velocity scales b^* and U_j respectively. As pointed out by Förthmann [1936], the decay of the maximum jet velocity is expected to vary as $x^{-\frac{1}{2}}$. In order to accentuate the decay, the ratio $\left(\frac{U_j}{U_{max}}\right)^2$ is commonly plotted versus $\frac{x^* - x_0^*}{b^*}$ and is shown in figure 2.23a for the diffusion zone only i.e. $x^* - x_0^* > 0$. Figure 2.23b shows the rate of spread in the streamwise direction i.e. $\frac{z^*_{\frac{1}{2}}}{b^*}$ as a function of $\frac{x^* - x_0^*}{b^*}$. Lines in the plots show the linear interpolation of the experimental points.

Beyond the virtual origin x_0^*, the evolution of $\left(\frac{U_j}{U_{max}}\right)^2$ is linear for both curved and plane DBD-WJs confirming the theoretical $x^{-\frac{1}{2}}$ evolution of the velocity decay. In the same way, the rate of spread of DBD induced jets behaves as a classical fluidic WJ and evolves linearly in the diffusion zone. DBD curved WJs show a maximum velocity decay much more important than the plane DBD and a higher rate of spread as well. The effect of the jet Reynolds number is significant in the present study. The higher the Re_j, the higher the slopes of the curves. Indeed, slopes of actuator ACT1-A are almost 10 times higher than the ones concerning the plane WJ. It is, indeed, a Reynolds number effect arising from the jet thickness b^*, itself directly related to the electrode position around the TE. This Re_j evolution is not in agreement with the results obtained by Wygnanski et al. [1992] that found an opposite behaviour for a classical fluidic plane WJ. However, DBD induced jets remain of different nature than purely fluidic ones and comparisons should be taken carefully.

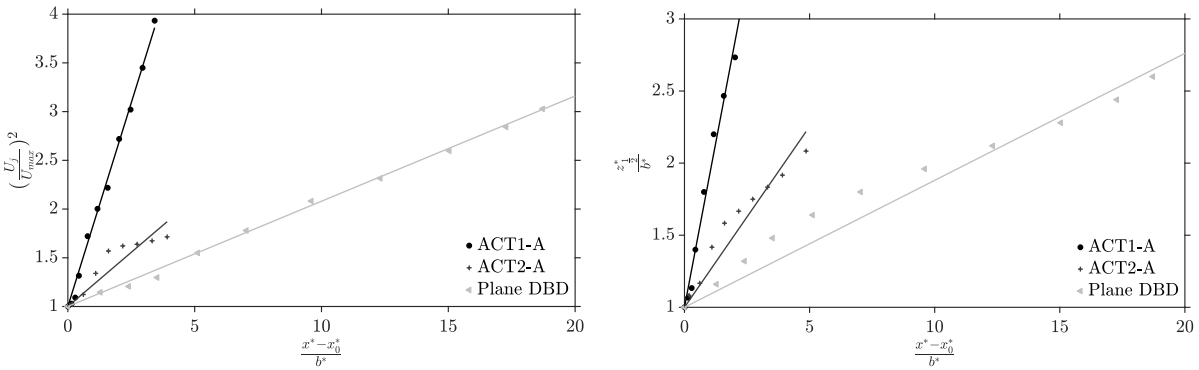

(a) Maximum velocity decay

(b) Rate of spread

Figure 2.23: Maximum velocity decay and rate of spread in the flow direction (scaling based on b^* and U_j)

2.3.3 Main features of DBD induced jets over curved surfaces

- Electrode positioning around the curvature has a direct impact on the jet topology specially whether the induced jet is going to follow the model curvature or not. The configuration where the zone of EHD interaction reaches the end of the curvature allows a complete adhesion of the induced wall jet to the wall
- Plane DBD-WJs show jet Reynolds numbers between 450 and 600; curved DBD-WJs from 1100 to 1900 meaning that DBD induced jets are close to transition
- Mean velocity profiles confirm that DBD induced wall jets are in a transitional regime as the ordinate of the maximum velocity is in between the fluidic laminar and turbulent cases for the plane case. Velocity profiles match the turbulent profile for the curved actuator. Scaling based on the jet half-width and on the jet maximum velocity does not perfectly collapse the mean velocity profiles in one single curve but a quasi-similarity is however reached
- With this same scaling, DBD induced jets evolve, in the streamwise direction, such as plane and curved fluidic wall jets do: linearly in terms of rate of spread and as $x^{-\frac{1}{2}}$ for the velocity decay. Velocity decay and spread of curved DBD-WJs is considerably higher than the ones concerning the plane configuration
- The reason why the wall jet stays attached to the wall seems to be more an electrical effect than a phenomenon due to the dynamics of the fluid (Coanda effect)
- PIV velocity fields allow the calculation of a thrust force and therefore of a momentum coefficient. This C_μ is estimated to be between 3.2×10^{-3} and 6.0×10^{-3} for an incoming flow of 10 m/s

2.4 Flow control results

This section is devoted to the flow control testings performed with the plasma actuators presented above. These actuators, implemented around the trailing-edge of the airfoil, are meant for the increase or the decrease of the 2D-airfoil lift force. Because their lift modification is greater, and in the sake of brevity, this section is focused on the actuators belonging to the **B-series**: ACT1-B and ACT2-B flow from the upper side to the lower side of the airfoil, and ACT3-B blows in the opposite direction.

2.4.1 Baseline analysis: validity of the set-up

This paragraph presents the validity of the set-up implemented in the wind-tunnel test-section. First, the circulation control-oriented airfoil is compared to the unmodified one, with a sharp trailing-edge. The intrusiveness of the plasma actuators is also analysed as well as the relevance of the boundary layer transition forcing.

Comparison with the unmodified NACA airfoil

The first issue to assess is the influence of the Reynolds number on the baseline flow and the comparison of the modified NACA airfoil (NACA65_4-421-CC) used in this project with the original one having a sharp TE (NACA65_4-421). Figure 2.24 shows lift and drag coefficients for both airfoils at different chord Reynolds numbers Re defined as $Re = \frac{cU_\infty}{\nu}$, where ν is the kinematic viscosity of air. Sharp trailing-edge data was obtained by Sicot [2005] during the investigation about the influence of turbulence on a wind-tunnel scale wind turbine at PRISME laboratory. Regarding the modified NACA airfoil data, tests were performed with a single part model (without a removable trailing-edge) and are presented in Aubrun et al. [2015].

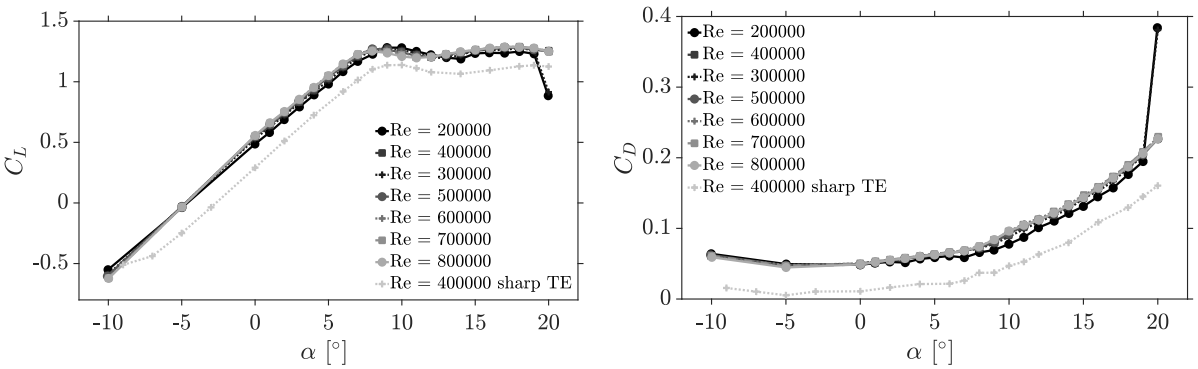

(a) Lift coefficient C_L

(b) Drag coefficient C_D

Figure 2.24: Lift and drag coefficients (C_L and C_D respectively) of NACA65_4-421 and NACA65_4-421-CC at different Reynolds numbers

Lift coefficient curve shows a linear evolution for a range of angles of attack between $-10°$ and $9°$. For this range of α, the flow in the suction side of the airfoil remains attached to the model. A lift plateau at $C_L = 1.3$ is noticeable from $8°$ (beginning of stall) to $20°$ indicating the displacement of the separation point along the chord of the airfoil from the trailing-edge to the leading-edge. For a Reynolds number of 200 000 the complete stall phenomenon is visible at $20°$ by a sudden decrease of C_L and an increase of C_D: for high α values the flow is completely detached from the airfoil with a separation point at the leading-edge. Hence, drag coefficient shows a low value below 0.05 from $\alpha = -10°$ to $\alpha = 5°$. When separation appears and moves towards the leading-edge, the drag coefficient augments up to 0.25 (0.4 for leading-edge separation at $Re = 200\,000$). Reynolds number does not seem to have a great effect on the lift and drag coefficients curves.

Lift and drag coefficients of the unmodified NACA65_4-421 airfoil are lower than the ones of the modified airfoil. The NACA65_4-421-CC airfoil has an additional curvature on the pressure side from 80% of the chord to the trailing-edge adding a camber to the airfoil that increases the lift force in a similar way as a trailing-edge flap would do. However, the rounded trailing-edge creates a small recirculation area on the TE wake that generates an additional important drag force.

Intrusiveness of plasma actuators

The second point that should be assessed concerns the plasma actuator intrusiveness. Copper electrodes have a total thickness of 60 µm and are partly covered by a Kapton® film 60 µm-thick resulting in an overall thickness of the actuators up to 120 µm. Tests were carried out to evaluate the influence of this additional thickness induced by the actuators presence over the airfoil. Figure 2.25 shows lift and drag coefficients at two Reynolds numbers with and without an actuator implemented over the model.

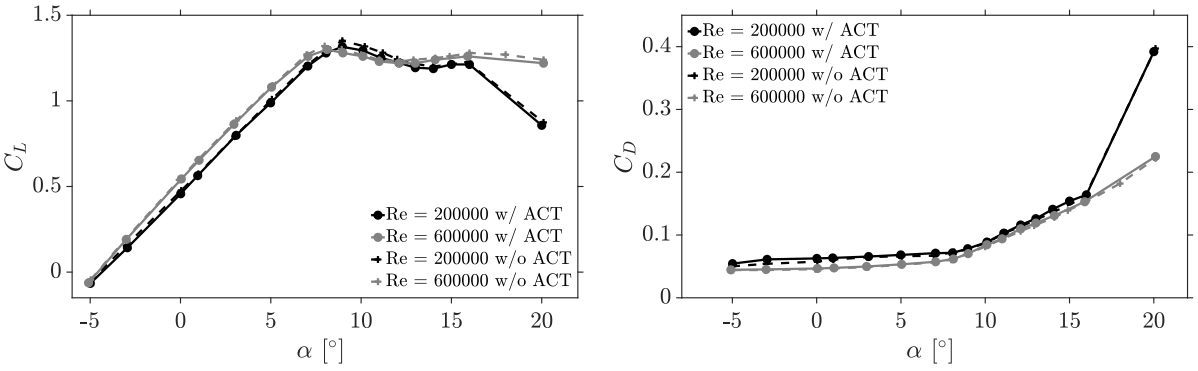

(a) Lift coefficient C_L

(b) Drag coefficient C_D

Figure 2.25: Lift and drag coefficients (C_L and C_D respectively) for the NACA65$_4$-421-CC model with and without a plasma actuator implemented over the model

Both lift and drag coefficients are almost identical whether the actuator is present over the airfoil or not and so for the two Reynolds numbers presented. We can therefore conclude that, apart from the measurement uncertainty of the platform balance, the intrusiveness of plasma actuators can be considered as negligible.

Forced laminar to turbulent transition

Because of the reduced dimensions of the models, wind-tunnel testings have to assess scaling issues such as the nature of the boundary layer (BL). Laminar to turbulent transition forcing may be required for wind-tunnel testings in order to be able to extrapolate the results to higher Reynolds numbers. The location of the transition over an airfoil depends, among others, on: the Reynolds number, the model roughness, the pressure gradient over the suction side of the airfoil and the turbulence level of the external flow.

An artificial roughness can be placed over the model in order to fix the BL transition position. Since the higher the Reynolds number the sooner the transition occurs over the airfoil and the thinner the boundary layer is, two pairs of trip strips were used: one pair for a Reynolds number $Re = 200\,000$ and another scaling to $Re = 600\,000$. They were placed based on the recommendations of Arnal [1984]: the height of the roughness should be equal to the displacement thickness and the Reynolds number based on the momentum thickness Re_θ should be higher than 200. Calculations were made with XFLR5 software for the two above mentioned Reynolds numbers and an angle of attack of 5°. For $Re = 200\,000$, the trip strips are 200 µm thick, located at 2% of the chord on the suction side and 13% on the pressure side; for $Re = 600\,000$ they are 100 µm thick and located at 1% of the chord on the suction side and 5% on the pressure side.

Figure 2.26 shows lift and drag coefficients for two Reynolds numbers with and without the transition forcing. For a Reynolds number of 200 000, lift and drag coefficients do not seem to be altered by the trip strips presence. However, at $Re = 600\,000$ the transition fixation alters the BL separation that seems to appear at lower angles of attack. As a turbulent boundary layer

has a greater shear than a laminar one, a drag increase was expected in the forced transition cases that was highlighted only for the angles of attack between 5° and 10°. Considering the uncertainty of the platform balance, it can be assumed that the drag coefficient penalty is in the order of magnitude of the platform balance uncertainty for the angles of attack corresponding to the linear part of the lift curve.

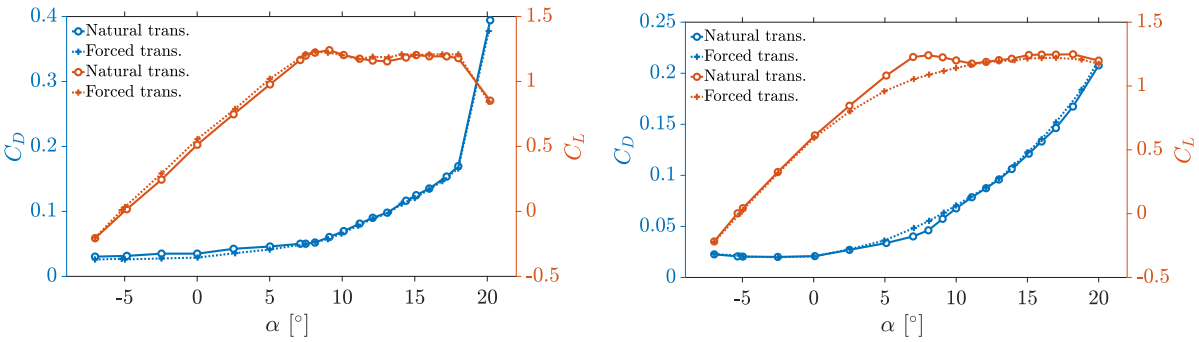

(a) $Re = 200\,000$ (b) $Re = 600\,000$

Figure 2.26: Lift and drag coefficients at two Reynolds numbers with and without a forced transition

Chosen transition

All the flow control test cases are carried out at $Re = 200\,000$ ($U_\infty = 10\,\text{m/s}$) where both curves collapse for the two transitional cases (natural and forced transition). Also, the circulation control carried out in this project focuses on the linear part of the lift curve and the actuation on the separation zone is not examined. It was decided to work without a transition forcing, in **natural transition** conditions. XFLR5 software estimates the location of the natural transition at $Re = 200\,000$ at 34 to 67%c[a] on the suction side and 68 to 79%c on the pressure side which ensures that the boundary layer is turbulent in the vicinity of the trailing-edge, where the actuation takes place.

[a] Depending on the angle of attack α i.e. the adverse pressure gradient

2.4.2 Effect of the actuation on the aerodynamic loads

Load modification under actuation

Figure 2.27 shows **lift and drag coefficients** (C_L and C_D respectively) as a function of the angle of attack α for two actuators: ACT1-B that increases the lift force and ACT3-B that aims at decreasing it. These results are obtained with the platform balance located under the wind-tunnel test-section. All the controlled cases are carried out in the linear part of the lift curve between the angles of attack $-7°$ and 9° and the electrical parameters of the actuation are $V_{AC} = 18\,\text{kV}$ and $f_{AC} = 1\,\text{kHz}$ corresponding to a momentum coefficient of 1.4×10^{-3}. One can observe in figure 2.27a that the actuation translates the baseline curve towards higher lift forces (ACT1-B) or lower ones (ACT3-B) giving evidence of a circulation control. With regard to the drag coefficient plotted in figure 2.27b, both controlled cases are superimposed to the baseline one suggesting that the drag increase due to the actuation is in the order of magnitude of the uncertainty of the drag measurement. Hence, drag penalty induced by the actuation can be considered as negligible.

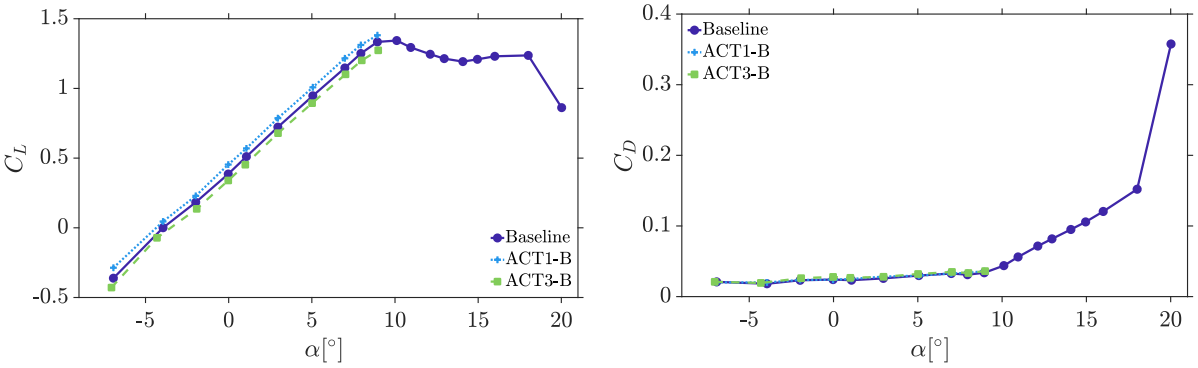

(a) Lift coefficient C_L

(b) Drag coefficient C_D

Figure 2.27: Lift and drag coefficients (C_L and C_D) for actuators ACT1-B and ACT3-B as a function of the angle of attack α - $Re = 200\,000$ and $C_\mu = 1.4 \times 10^{-3}$

A variable that allows the comparison of the three actuators performances is ΔC_L defined as the **lift coefficient variation** (positive for an increase, negative for a decrease) with respect to the baseline case. The ΔC_L evolution as a function of the angle of attack and for the B-series is plotted in figure 2.28 for three applied voltages $V_{AC} = 15\,\text{kV}$, $18\,\text{kV}$ and $20\,\text{kV}$ that correspond to momentum coefficients equal to $C_\mu = 0.7 \times 10^{-3}$, 1.4×10^{-3} and 2.2×10^{-3} respectively. This plot of ΔC_L reflects the **sensitivity** of the actuation to α and C_μ.

Lift increase of actuators ACT1-B and ACT2-B is very similar for the three tested voltages and a maximum lift coefficient increase of $+0.08$ is obtained. However, the greater lift decrease that could be performed was of about -0.11 with ACT3-B. Kotsonis et al. [2014] implemented DBD actuators around a trailing-edge of a symmetrical airfoil at 5 distinct positions around the curvature. They obtained a maximal ΔC_L equal to $+0.15$ at $Re = 140\,000$ that is in the order of magnitude of the present gains. However, their ΔC_L was not constant as a function of the angle of attack: ΔC_L was constant and equal to $+0.08$ in the linear part of the lift curve and augmented up to $+0.10$ to $+0.15$ near stall. The authors showed that the effect of the actuation in terms of lift coefficient gain was reduced with the increase of the Reynolds number. To a given applied voltage corresponds an actuator thrust (or F_{EHD}) and therefore a C_μ, that is reduced with the Re augmentation. They showed, however, a similar $\frac{\Delta C_L}{C_\mu}$ ratio for different Re meaning that the effect of the DBD actuation is governed by Reynolds numbers effects and not momentum coefficient effects. The numerical study made by Zhang et al. [2010] suggested gains in ΔC_L equal to $+0.8$ with DBD actuation over an elliptical airfoil. This spectacular gain is due to a particularly strong and unrealistic momentum coefficient used.

The higher the momentum coefficient, the higher the effect of the actuation on the lift coefficient is. These dependency of the actuation on the electrical parameters will be detailed in the next section. Despite some fluctuations, at a fixed voltage, the ΔC_L as a function of α is not far to be constant. Decreasing the lift force with ACT3-B permits to obtain a wider range of lift coefficients, between -0.05 and -0.11. Also, the actuation has a stronger effect when decreasing the lift force than when increasing it.

The performed circulation control in the vicinity of the trailing-edge modifies the whole pressure distribution around the model. Pressure coefficient C_p distribution along the chord is shown in figure 2.29 for actuators ACT1-B and ACT3-B at $\alpha = 5^\circ$ and three momentum coefficients C_μ. The controlled flow with ACT1-B (figure 2.29a) shows a reduction of the pressure coefficient in the suction side of the airfoil and an increase in the pressure side leading to a higher area inside the C_p curve and therefore a higher lift coefficient compared to the baseline. On the contrary, in the case of the actuator ACT3-B, meant for lift decrease, the area inside the

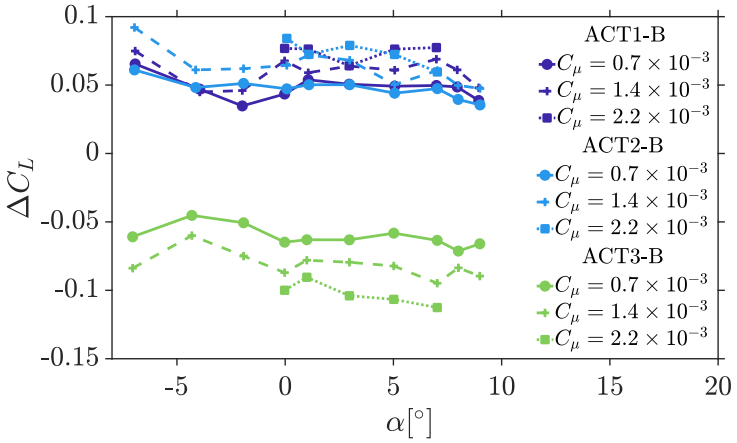

Figure 2.28: Lift coefficient variation ΔC_L as a function of the angle of attack α for different C_μ - B-series and $Re = 200\,000$

pressure coefficient curve is reduced leading to a lower C_L, which confirms the platform balance measurements.

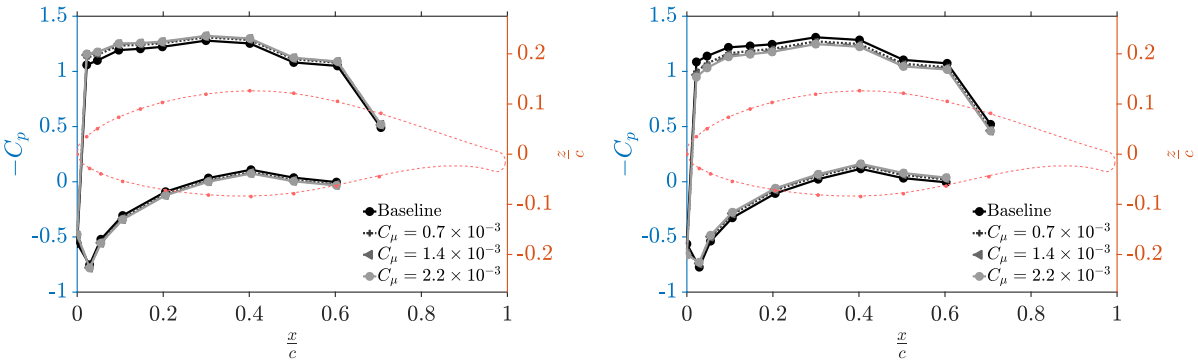

(a) ACT1-B (b) ACT3-B

Figure 2.29: Pressure coefficient C_p distribution for actuators ACT1-B and ACT3-B for different C_μ - $\alpha = 5^\circ$ and $Re = 200\,000$

Pressure coefficient variation ΔC_p can be defined as the difference between the controlled pressure distribution and the baseline one. Figure 2.30 shows the ΔC_p over the airfoil for $\alpha = 5^\circ$ and three C_μ. Except from the pressure taps at the leading-edge, the pressure coefficient variation is homogeneous on the pressure side and on the suction side of the airfoil and varies with the momentum coefficient: the higher the C_μ, the higher the pressure variation. The results confirm that even though the action takes place very locally at the trailing-edge of the airfoil, the whole pressure distribution around the model is modified. The pressure taps close to the leading-edge seem particularly receptive to the actuation as the ΔC_p reaches its maximum values in this area (first 2 taps on suction and pressure sides). In the perspective of a closed-loop control, these pressure taps could be good candidates to be the output parameters of the system and linked to the lift regulation.

Effect of the electrical parameters

Most of the control cases carried out have three input voltages V_{AC} (15 kV, 18 kV and 20 kV) coupled with a single frequency f_{AC} equal to 1 kHz. A wider analysis at two fixed angles of attack (0° and 5°) and an incoming flow velocity of 10 m/s has been carried out in order to analyse the

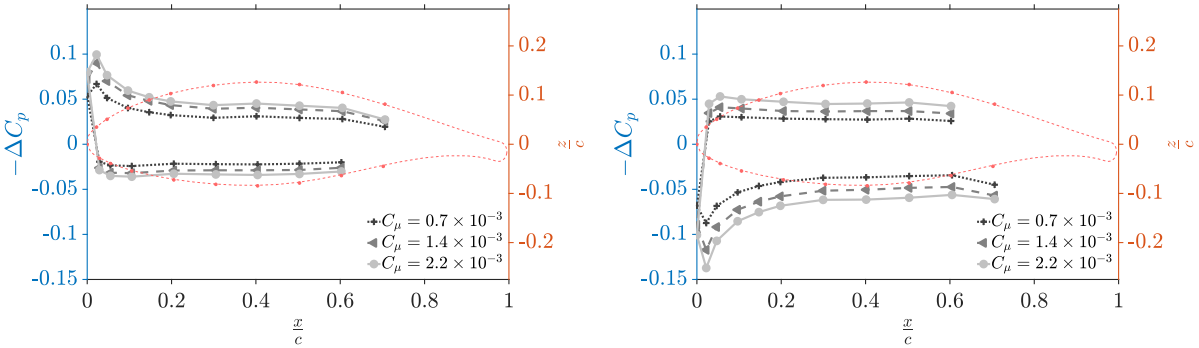

(a) ACT1-B (b) ACT3-B

Figure 2.30: Pressure coefficient variation ΔC_p for actuators ACT1-B and ACT3-B for different C_μ - $\alpha = 5°$ and $Re = 200\,000$

influence of the electrical parameters V_{AC} and f_{AC} on the lift force. In this section the variables that quantify the actuation are therefore V_{AC} and f_{AC} and not C_μ. Indeed, in the present study the momentum coefficients have been obtained via the analysis of PIV velocity fields that are not available for all the voltages and frequencies involved in the following. Kotsonis et al. [2014] showed that C_μ evolves exponentially with V_{AC} and grows linearly with f_{AC}.

Figure 2.31 shows the lift variation ΔC_L as a function of the applied voltage V_{AC} and frequency f_{AC} for $\alpha = 0°$ and $5°$ (B-series). Testings varying the input voltage are carried out at a fixed frequency f_{AC} equal to 1 kHz and the ones with a changing frequency are done at a fixed voltage V_{AC} equal to 16 kV. The higher the applied voltage or the signal frequency, the higher the lift modification ΔC_L. Indeed, a voltage augmentation leads to an increase of the ionic wind velocity in the very vicinity of the wall. The overall velocity of the induced jet around the trailing-edge of the airfoil is therefore increased and the flow modification is therefore more important, leading to higher lift modifications. But, why does this increase in V_{AC} or f_{AC} induce a higher plasma jet velocity? As shown in paragraph 2.2.2 (p.35), when increasing V_{AC} and/or f_{AC} the power consumption augments with the square of the voltage and linearly with the frequency. The maximum velocity of the ionic wind and also the ElectroHydroDynamic force F_{EHD} are directly related to this electrical power. The EHD force is proportional to the electrical field $\overrightarrow{E}$, but also to the charged particles density, mass, velocity and mobility (Boeuf et al. [2007]). The only parameter that can be modified is the electrical field that depends on the geometry of the actuators, the dielectric material and the input high voltage signals. Thus, increasing the electrical field by increasing V_{AC} or f_{AC} will increase the ElectroHydroDynamic force and thrust, the ionic wind velocity and therefore increase the effectiveness of the actuation.

For most of the experimental test points, actuator ACT2-B is slightly more efficient than actuator ACT1-B suggesting that a shifted configuration, where the whole actuator is slightly tilted to the pressure side, is better for the circulation control application. As we have seen in section 2.3 (p.40), the positioning of the electrodes around the trailing-edge of ACT2-B tends to help the induced plasma jet to circumvent the trailing-edge curvature. Indeed, we can expect this configuration to displace the rear stagnation point in a greater extend than ACT1-B and to enhance the performances of the actuation. This result is in agreement with the results obtained by Kotsonis et al. [2014]. Indeed, this actuator ACT2-B blows closer than ACT1-B to the outer part of the recirculation and vortical zone that will be detailed later with the analysis of the PIV velocity fields. This TE action is similar to the mechanical actuation performed with Gurney flaps or microtabs. According to Kotsonis et al. [2014], the lift coefficient variation can be caused by either a manipulation of the Kutta condition and/or an addition of circulation Γ. If the ΔC_L was solely due to an addition of Γ, the gain would equal for the three positions studied. However,

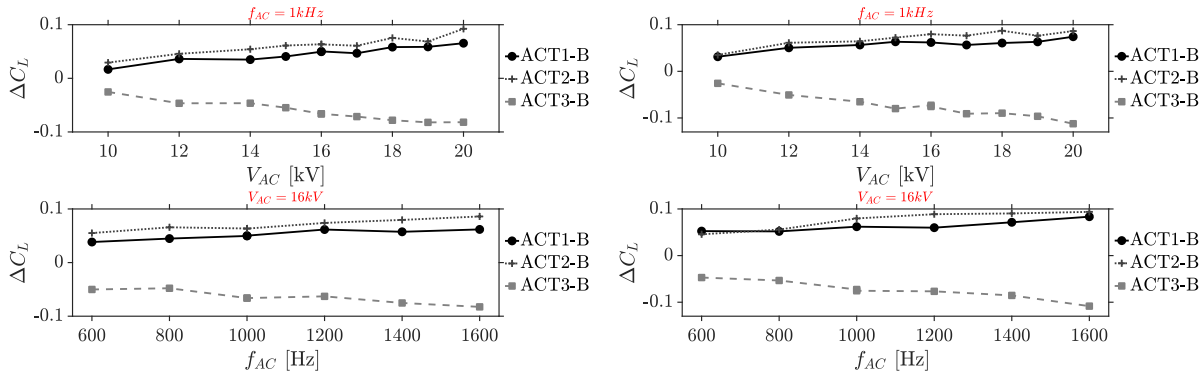

(a) $\alpha = 0°$ (b) $\alpha = 5°$

Figure 2.31: Lift coefficient variation ΔC_L as a function of the applied voltage V_{AC} and frequency f_{AC} for $\alpha = 0°$ and $\alpha = 5°$ - B-series and $Re = 200\,000$

as the position of the electrodes has an influence on the ΔC_L, the authors concluded that the lift augmentation is mostly due to a displacement of the stagnation point (Kutta condition).

In the same way, pressure coefficient ΔC_p variation can be evaluated as a function of the applied voltage and frequency V_{AC} and f_{AC} as plotted in figure 2.32 for $\alpha = 5°$. As expected, the higher the voltage (or the frequency), the higher the effect on the pressure distribution. The maximum ΔC_p obtained at the leading-edge is of about -0.1 ($+0.15$ for ACT3-B, not shown here). This variation corresponds to a pressure variation of 6 Pa to 9 Pa. It should be noted that the increase in the pressure coefficient is not linear i.e. an increase of 1 kV in the input voltage does not always increment the C_p of an equal amount. For the higher voltages an increment in V_{AC} does not seem to change the pressure distribution suggesting that the effect of the actuation stagnates beyond a certain voltage. The same can be said about the variation of the input frequency, an increase of 200 Hz does not always have the same impact in terms of ΔC_p and the actuation effect on the C_p stagnates after 1.2 kHz.

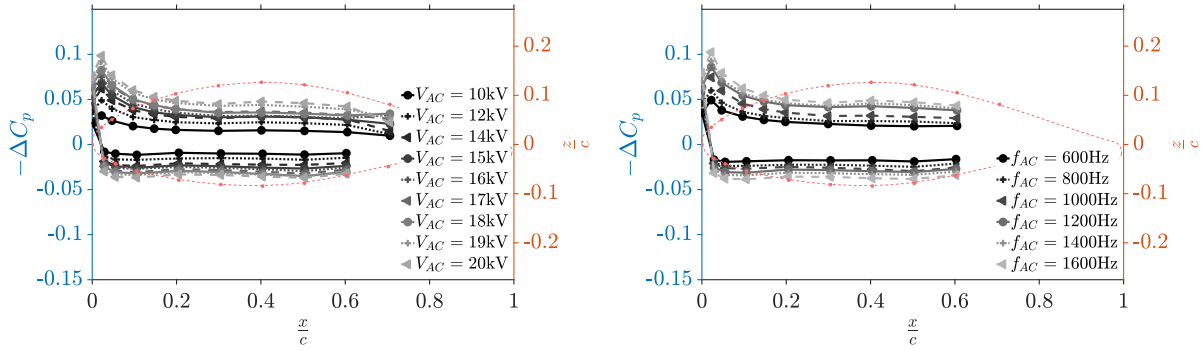

(a) Voltage influence (b) Frequency influence

Figure 2.32: Pressure coefficient variation ΔC_p as a function of the applied voltage V_{AC} and frequency f_{AC} - ACT2-B, $\alpha = 5°$ and $Re = 200\,000$

2.4.3 Flow field analysis: impact of the actuation

PIV measurements are carried out in order to characterise the effect of the actuation on the wake of the airfoil. This technique allows to obtain the topology of the mean flow field around the

model as well as an insight of the wake flow velocity fluctuations. This section focuses on the analysis of the PIV fields for actuator ACT2-B meant for lift increase. Velocity profiles on the wake of the airfoil will also be compared for the three actuators. Velocity average and fluctuating parts are defined according to the following Reynolds decomposition where t represents the time dependency: longitudinal velocity defined as $U(x,z,t) = \overline{U}(x,z) + u'(x,z,t)$ and vertical velocity as $V(x,z,t) = \overline{V}(x,z) + v'(x,z,t)$.

Mean velocity fields

Actuator ACT2-B blows from the suction side to the pressure side of the airfoil and is therefore meant for a lift increase. Figure 2.33 shows the mean velocity field and streamlines for this actuator, with and without actuation. The voltage input is of 20 kV at 1 kHz which corresponds to $C_\mu = 2.2 \times 10^{-3}$ and the angle of attack is set to $\alpha = 5°$.

The rounded trailing-edge induces, in a time-averaged perspective, a recirculation area in the wake of the airfoil made up of two counter-rotating vortices at the base of the airfoil and symmetrical to the chord line. This low velocity area extends from the trailing-edge to $\frac{x}{c} = 1.05$ which is in the order of magnitude of the TE diameter i.e. the characteristic length of a bluff body recirculation. In an unsteady point of view, these coherent structures are actually a Von Karman vortex shedding as will be explained in section 2.4.4 (p.62). The actuation does not alter significantly the mean topology of the wake. Both vortical structures are preserved with the actuation suggesting that the actuation is not strong enough to modify consequently the wake topology. But, as the actuation takes place in the very vicinity of the wall, its effects may not be captured considering the PIV field resolution near the wall. Kotsonis et al. [2014] showed strong effects of the actuation on the wake, with an important displacement of saddle and stagnation points. Their results are, however, performed at lower Reynolds numbers which can explain our less sensitivity of the wake to the actuation.

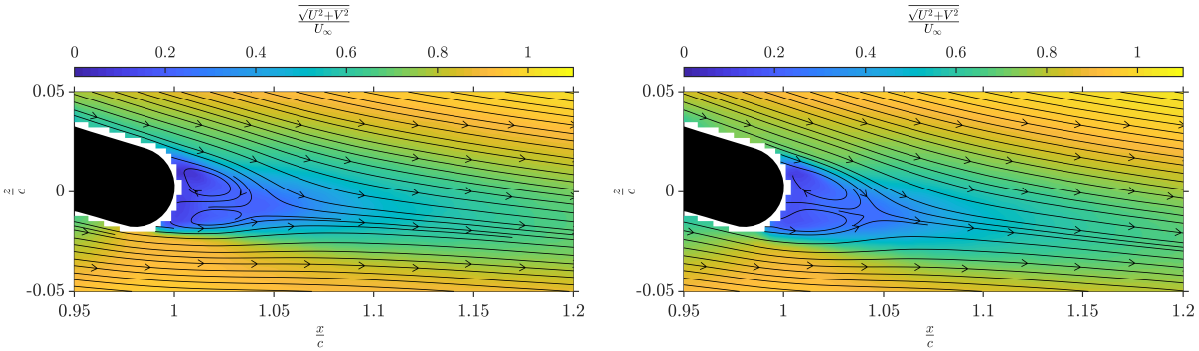

(a) Baseline

(b) $C_\mu = 2.2 \times 10^{-3}$

Figure 2.33: Mean velocity fields with and without actuation - ACT2-B, $\alpha = 5°$ and $Re = 200\,000$

The difference between the baseline and the controlled cases can be highlighted by plotting the differential velocity $\overline{\sqrt{U^2+V^2}}_{on-off}$ defined as the subtraction of the mean velocity field with and without actuation:

$$\overline{\sqrt{U^2+V^2}}_{on-off} = \overline{\sqrt{U^2+V^2}}_{on} - \overline{\sqrt{U^2+V^2}}_{off} \tag{2.18}$$

This time-averaged field distribution is presented in figure 2.34 for ACT2-B and the parameters stated above. Light coloured areas correspond to the zones where the flow is *faster* when the actuation is turned on, and the dark coloured ones indicate of a *lower* velocity with the actuation powered. In the area where the actuation takes place in the suction side, the flow velocity is increased up to about 2 m/s over an elongated area extended up to $\frac{x}{c} = 1.1$. The second

actuator is located in the trailing-edge curvature and acts slightly in a counter-flow direction. This actuator pushes back the flow coming from the pressure side and consequently induces a slight wake deflection towards the pressure side. Because of this flow difficulty, the flow is slower in the lower part of the wake when the actuator is turned on.

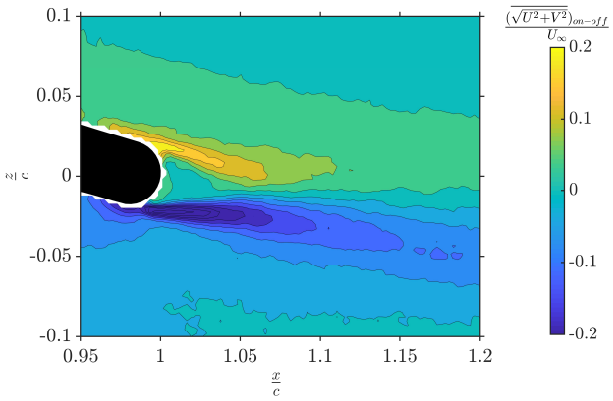

Figure 2.34: Differential velocity field - ACT2-B, $\alpha = 5°$, $Re = 200\,000$ and $C_\mu = 2.2 \times 10^{-3}$

Turbulence intensity

Turbulent kinetic energy (TKE), defined as $k = \frac{\overline{u'^2}+\overline{v'^2}}{2U_\infty^2}$, quantifies the strength of the velocity fluctuations of the flow. Figure 2.35 shows time-averaged kinetic energy k fields with and without actuation for ACT2-B and $\alpha = 5°$. With the actuation, velocity fluctuations and mixing are increased specially in the upper area of the wake, in the shear layer between the recirculation area and the outer flow. This phenomenon highlights the manipulation of the vortical structures with the flow control actuation.

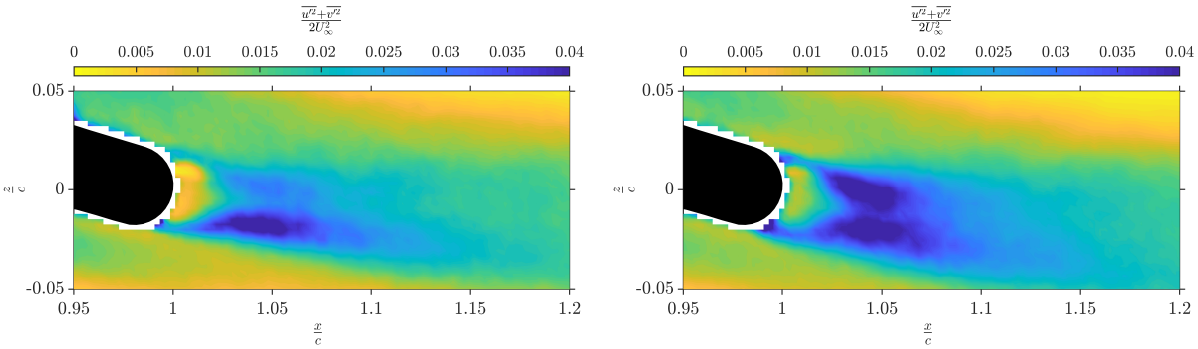

(a) Baseline

(b) $C_\mu = 2.2 \times 10^{-3}$

Figure 2.35: Kinetic turbulent energy k fields with and without actuation - ACT2-B, $\alpha = 5°$ and $Re = 200\,000$

On another hand, Reynolds shear stress $Re_{xz} = \frac{\overline{u'v'}}{U_\infty^2}$ allows to characterise the areas of turbulence production. Figure 2.36 shows Re_{xz} fields for ACT2-B with and without actuation at $\alpha = 5°$. By comparing the two fields, it can be concluded that the actuation enhances turbulence on both sides of the wake i.e. on the shear layers developing in the continuation of the suction and the pressure sides of the airfoil. The areas of turbulence production are visible further downstream on the wake in the controlled case than for the baseline one, meaning that actuation strongly modifies the wake in terms of turbulence production.

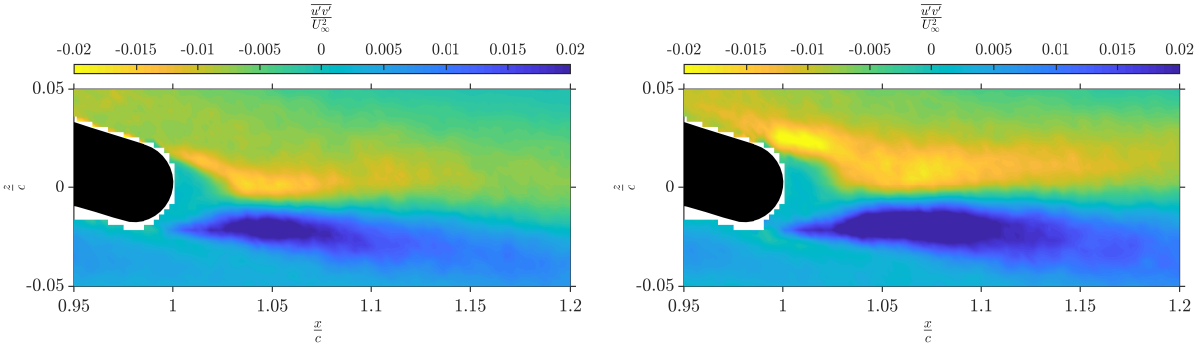

(a) Baseline

(b) $C_\mu = 2.2 \times 10^{-3}$

Figure 2.36: Mean Reynolds shear stress Re_{xz} with and without actuation - ACT2-B, $\alpha = 5°$ and $Re = 200\,000$

Wake evolution: comparison between actuators

An analysis of the wake evolution downstream of the trailing-edge allows to compare the behaviour of the three actuators. This wake development can be described with the ratio of the minimal longitudinal velocity $\overline{U_{min}}$ at each longitudinal profile beyond the TE and the free stream velocity. This curve is shown in figure 2.37 for the B-series. Negative values of $\frac{\overline{U_{min}}}{U_\infty}$ indicate that the minimal velocity is negative i.e. that the given profile is located in the recirculation area beyond the TE. For ACT1-B and ACT2-B both baseline and controlled curves superimpose except from the first points in the very vicinity of the trailing-edge. This suggests that, in terms of mean velocity, the actuation modifies the very near wake but not its downstream main topology. However, in the case of ACT3-B, the minimal velocity evolution along the wake is changed, the controlled case showing lower values than the baseline one.

This different behaviour is confirmed by the analysis of the velocity profiles in the wake of the airfoil plotted in figure 2.38 at $\frac{x}{c} = 1.05$ for the same actuators and electrical parameters mentioned above. For the three cases, the actuation displaces the wake in the direction of the blowing: to the pressure side for ACT1-B and ACT2-B, and to the suction side for ACT3-B. But, for ACT1-B and ACT2-B, the value of the velocity deficit remains unchanged, whereas for ACT3-B it is significantly reduced.

2.4.4 Analysis of the wake instabilities

Wake instabilities, such as the above mentioned Von Karman vortex shedding, induce flow fluctuations that may provoke an additional trailing-edge noise and detrimental structural vibrations. It is therefore important to characterise these instabilities in terms of spatial and temporal scales and to determine to what extend they are affected by the actuation.

Hot wire measurements

Hot Wire Anemometry (HWA) performed in the wake of the airfoil allows to obtain the effect of the actuation on the wake instabilities in the frequency domain. Figure 2.39 shows the Power Spectral Density (PSD) in the wake of the airfoil for ACT1-B at $\alpha = 5°$. The positioning of the probe and the parameters of the acquisition are explained in paragraph 2.2.4 (p.40). For both baseline and controlled cases, the PSD spectrum is very similar except from a power peak visible for the controlled configuration at 142 Hz. A Strouhal number based on the trailing-edge thickness can be defined as $St = \frac{fe}{U_\infty}$ where f is the frequency of the instability and e the TE thickness equal to 12 mm. The Strouhal number corresponding to $f = 142$ Hz is equal to 0.17,

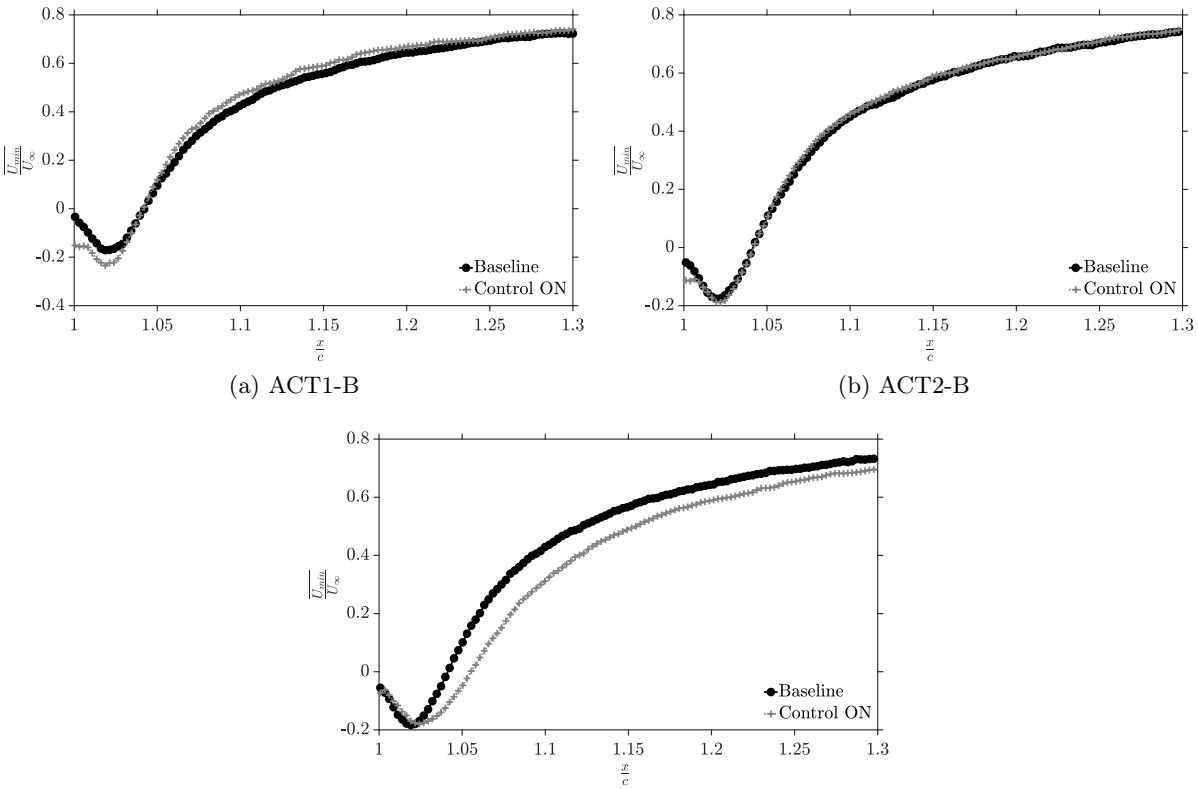

(a) ACT1-B

(b) ACT2-B

(c) ACT3-B

Figure 2.37: Wake longitudinal velocity deficit $\frac{\overline{U_{min}}}{U_\infty}$ with and without actuation - B-series, $\alpha = 5°$, $Re = 200\,000$ and $C_\mu = 2.2 \times 10^{-3}$

which is in the order of magnitude of a Von Karman vortex shedding. The shedding is originated by the roundness of the trailing-edge that has the shape of half a cylinder inducing a bluff-body wake as evidenced in the above velocity fields analysis. The fact that this peak is specially visible for the controlled case shows that the actuation triggers this instability.

Proper Orthogonal Decomposition

Vortical structures can also be highlighted with a Proper Orthogonal Decomposition (POD) of PIV velocity fields. Indeed, instantaneous velocity fields contain the signature of present coherent structures (vortex shedding, flapping...) but also of non coherent data coming from the stochastic nature of the flow and its turbulence. POD is a mathematical method that allows to extract the signature of these coherent structures. It also allows to analyse and sort them depending on their energy (contribution to the mean field and to the turbulent kinetic energy production).

As the performed PIV is not time-resolved, snapshot POD (Sirovich [1987]) is carried out based on the instantaneous velocity fields in the wake of the airfoil from $\frac{x}{c} = 1.01$ to $\frac{x}{c} = 1.52$ and avoiding the area around the model. Each instantaneous velocity field $U(x,z,t)$ and $V(x,z,t)$ can be expressed as:

$$U(x,z,t) = \overline{U}(x,z) + u'(x,z,t) = \overline{U}(x,z) + \sum_{n=1}^{N} a_{u'}^{(n)}(t)\Phi_{u'}^{(n)}(x,z) \tag{2.19}$$

$$V(x,z,t) = \overline{V}(x,z) + v'(x,z,t) = \overline{V}(x,z) + \sum_{n=1}^{N} a_{v'}^{(n)}(t)\Phi_{v'}^{(n)}(x,z) \tag{2.20}$$

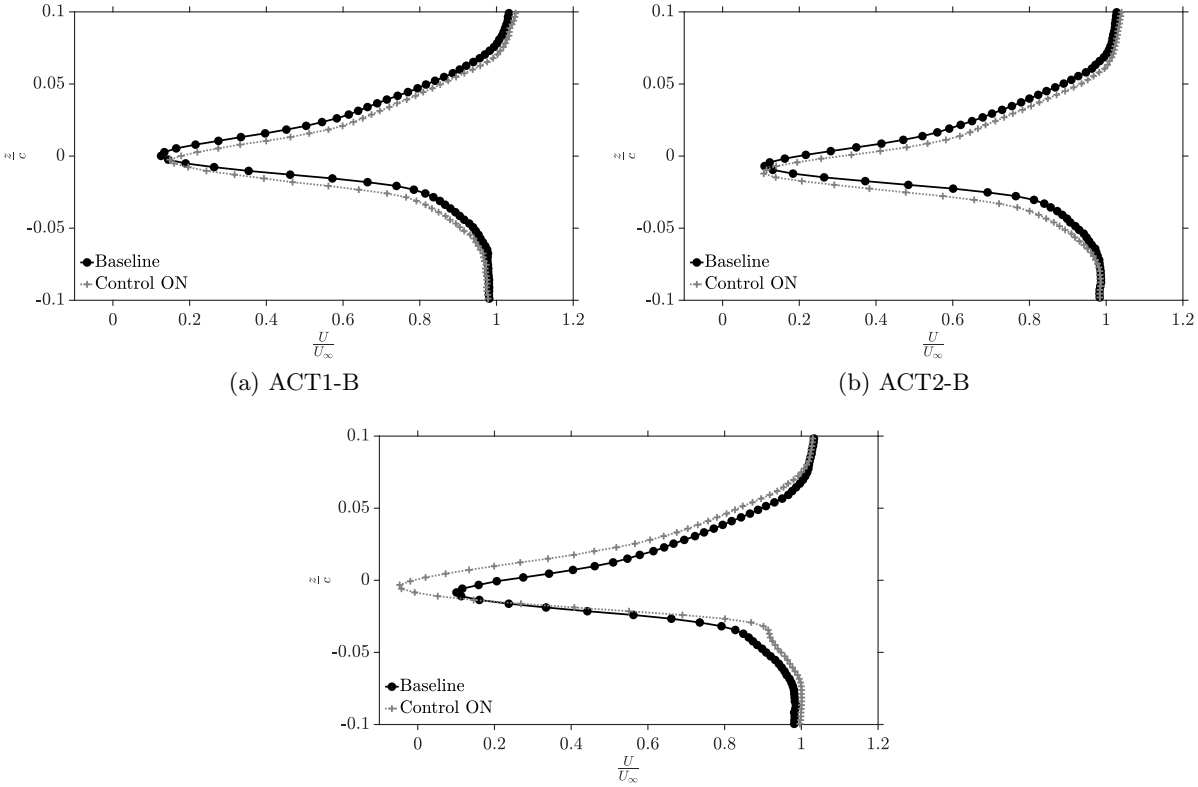

(a) ACT1-B

(b) ACT2-B

(c) ACT3-B

Figure 2.38: Wake velocity profiles at $\frac{x}{c} = 1.05$ with and without actuation - B-series, $\alpha = 5°$, $Re = 200\,000$ and $C_\mu = 2.2 \times 10^{-3}$

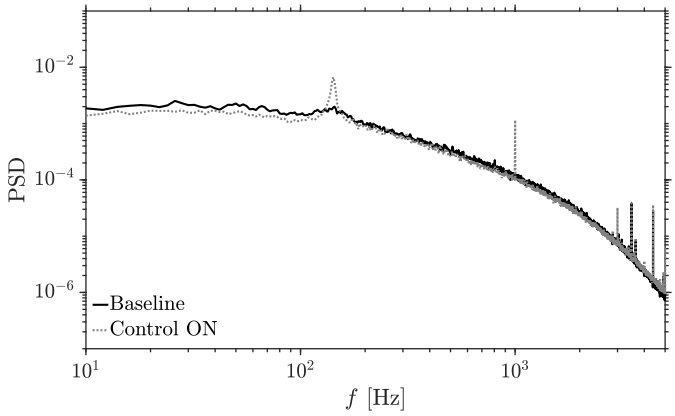

Figure 2.39: Power spectrum obtained with HWA in the wake of the airfoil for ACT1-B - $\alpha = 5°$, $Re = 200\,000$ and $C_\mu = 1.7 \times 10^{-3}$

where $\Phi_{u'}^{(n)}$ and $\Phi_{v'}^{(n)}$ are the n$^{\text{th}}$ proper mode functions, $a_{u'}^{(n)}$ and $a_{v'}^{(n)}$ are the n$^{\text{th}}$ POD mode coefficients of the related instantaneous velocity field and N is the total number of modes equal to 1000, the number of PIV samples used for the decomposition.

POD modes merge the temporal information of the flow creating a spatial field statistically present in time on the wake. First modes correspond to the most energetic coherent structures of the flow dominated by largest vortical structures. Next modes correspond to smaller coherent structures and, beyond a certain mode, they only highlight the non coherent structures due to the turbulence of the flow. More detailed principles of POD can be read in Cordier and Bergmann

[2008].

Figure 2.40 shows the first POD mode associated to the longitudinal and vertical components of the velocity with and without actuation for ACT1-B and $\alpha = 5°$. Two counter rotating vortices are visible showing the Von Karman vortex shedding convecting downstream of the flow. These structures are visible on the baseline case and on the controlled flow. However, actuation changes the coherence of these vortical structures as the shedding is displaced upstream, closer to the trailing-edge of the airfoil. However, the spatial lengthscale of the instability remains approximately identical in both configurations suggesting that the temporal scale of the shedding might not be altered, confirming the power spectra results obtained with HWA.

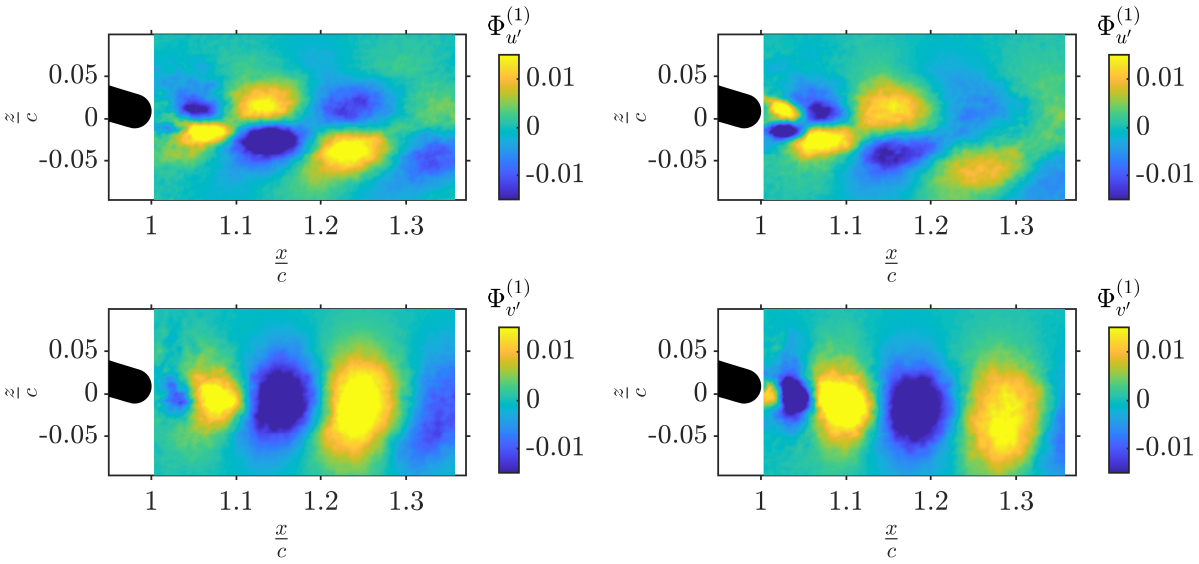

(a) Baseline

(b) $C_\mu = 2.2 \times 10^{-3}$

Figure 2.40: First POD mode associated to the longitudinal and vertical components of the velocity ($\Phi^{(n)}_{u'}$ and $\Phi^{(n)}_{v'}$) with and without actuation - ACT1-B, $\alpha = 5°$ and $Re = 200\,000$

Energy ratio for the 30 first POD modes with and without actuation is shown in figure 2.41 for ACT1-B and $\alpha = 5°$. It is clearly apparent that actuation enhances the energy of the two first modes that is equal to 5% for the baseline case and reaches 10 to 11% for the controlled case. This POD analysis confirms that the Von Karman instability is stronger with the actuation. This might be due to the low Reynolds number $Re = 200\,000$ of the present test cases that does not allow a *full* trigger and setting of the instability for the baseline case.

2.4.5 Comparison with fluidic jets actuation

In the scope of the SMARTEOLE project, plasma and fluidic flow control approaches over a 2D-airfoil are carried out in parallel. Plasma actuation, performed by PRISME laboratory, has been explained all along this chapter. Fluidic strategy is carried out by LHEEA laboratory (ECN, France). After the evaluation of the performances, advantages and disadvantages of both strategies, one of them has to be chosen to be implemented in the wind turbine bench of PRISME laboratory. The objective of this section is to compare both flow control approaches, their respective lift coefficient gains, effectiveness and flow control mechanisms. The results marked as "DBD" correspond to the plasma actuation (ACT2-B and ACT3-B) that has been presented in the previous sections. Curves labelled as "FJ" (fluidic jets) are for the fluidic jet actuation, whose data is courtesy of V. Jaunet and C. Braud and is partially published in Braud and Guilmineau [2016] and Jaunet and Braud [2018].

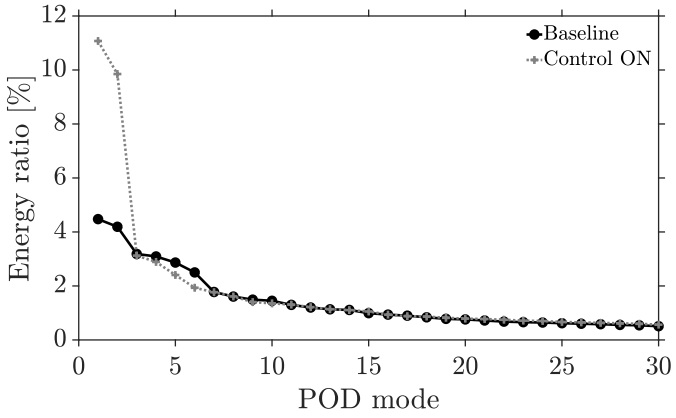

Figure 2.41: Energy ratio of first POD modes with and without actuation - ACT1-B, $\alpha = 5°$, $Re = 200\,000$ and $C_\mu = 2.2 \times 10^{-3}$

As for the DBD application, the airfoil used for the fluidic control is a NACA-65_4-421-CC airfoil and the dimensions of the model are identical, with a chord c of 0.3 m and a span of 1.1 m. Tests with fluidic jets are also performed in the "Lucien Malavard" wind-tunnel of the University of Orléans, and the overall set-up in the test-section is analog to the one presented in section 2.2 (p.32). The model is equipped with a series of distributed jets along the wing span: the model is a stack of non-blind thin profiles (1 mm) and thick blind profiles (10 mm) as can be seen in figure 2.42. The thin profiles are opened, via thin air channels, to the model surface, whereas, the blind sections have no connection with the surface. When all the sections are stacked, a plenum chamber is created in the spanwise direction of the airfoil. This chamber, when pressurised, feeds the discrete squared fluidic microjets in compressed air. The same mechanism but in the opposite direction is used to measure the pressure distribution along the chord. Hence, measured pressure is an **integration of the pressure along the model span** and provides results close to what can be obtained in a 2D pressure field.

Actuation discrepancies...

It is important to remark that the two actuation strategies are fundamentally different as the DBD actuation is supposed purely **two-dimensional**, whereas the fluidic jet strategy is made of several **discrete** jets distributed along the airfoil span.

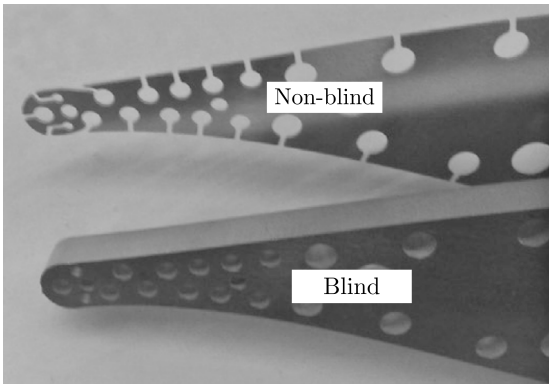

(a) Blind and non-blind sections

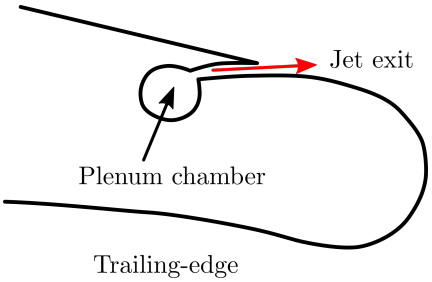

(b) Jet used for the actuation

Figure 2.42: Picture of blind and non-blind sections concatenated to form the model (left), and diagram of the jet used for the actuation (right) (from Jaunet and Braud [2018])

Lift coefficient variation

Both strategies can be compared first by their respective lift coefficient variation ΔC_L. The **lift coefficient variation** as a function of the angle of attack α is shown in figure 2.43 for the two control approaches and their respective momentum coefficients C_μ. The fluidic actuation performs much higher lift coefficient gains than the DBD strategy. DBD actuation ΔC_L is almost constant for a large range of angles of attack with gains and losses of about ± 0.1, giving evidence of a circulation control. A momentum coefficient increase does not have a major effect on the C_L increase of decrease. However, in the case of the FJ actuation, the lift coefficient increase is not constant with the variation of the angle of attack α: it increases with α and is especially important for the angles above 10°, where the flow starts to separate along the suction side. Fluidic actuation achieves circulation control in the linear part of the lift curve but also separation control at high angles of attack. Maximal lift coefficient increase is equal to 0.45. For this FJ actuation, the influence of the momentum coefficient is clearly visible on the ΔC_L curves as the higher the C_μ, the higher the C_L gains.

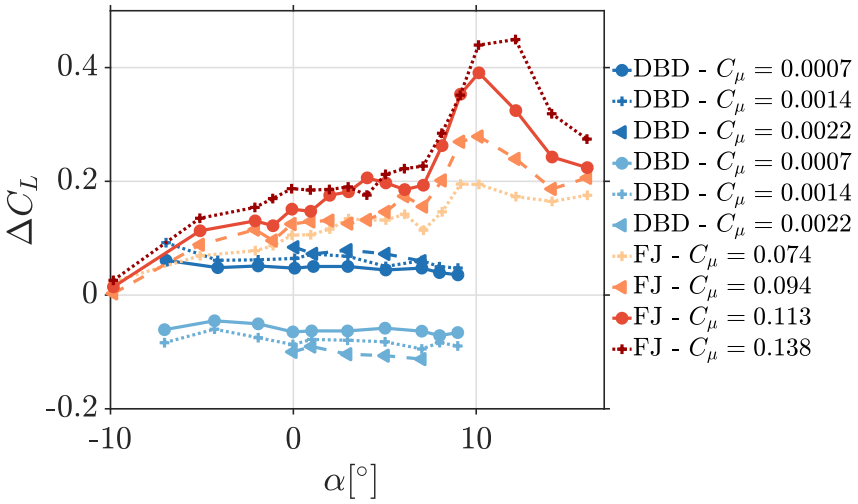

Figure 2.43: Lift coefficient variation ΔC_L as a function of the angle of attack α for DBD (ACT2-B and ACT3-B) and FJ actuations - $Re = 200\,000$

The lift coefficient gain can be normalised by the momentum coefficient to give a **lift augmentation efficiency** $\frac{\Delta C_L}{C_\mu}$ (or **lift augmentation ratio**) that is shown in figure 2.44 for both actuation strategies. Even if the lift coefficient gains induced by plasma actuation are modest compared to the fluidic actuation, the efficiency is huge due to the very low C_μ coefficients involved. Lift augmentation efficiency is of about 70 to 90 for DBD actuators, in the same order of magnitude of the results obtained by Zhang et al. [2010] and Kotsonis et al. [2014]. Fluidic jets show low $\frac{\Delta C_L}{C_\mu}$ from 1 to 4 which remain 10 to 20 times lower than the ones concerning the DBD actuation.

Also, it is important to remark that, with two different electrode arrangements, the lift coefficient could be **increased and decreased** with a DBD actuation. However, using fluidic jets the lift coefficient could only be increased but never decreased, even when blowing from the pressure side of the airfoil. In fact, the blowing location tested in the lower side of the airfoil was probably too far from the trailing-edge and the jet diffused too much to perform the desired lift decrease.

Pressure coefficient

Pressure distribution around the airfoil also reflects the flow modification with the actuation. Figures 2.45, 2.46 and 2.47 show the pressure coefficient variation ΔC_p around the airfoil for the

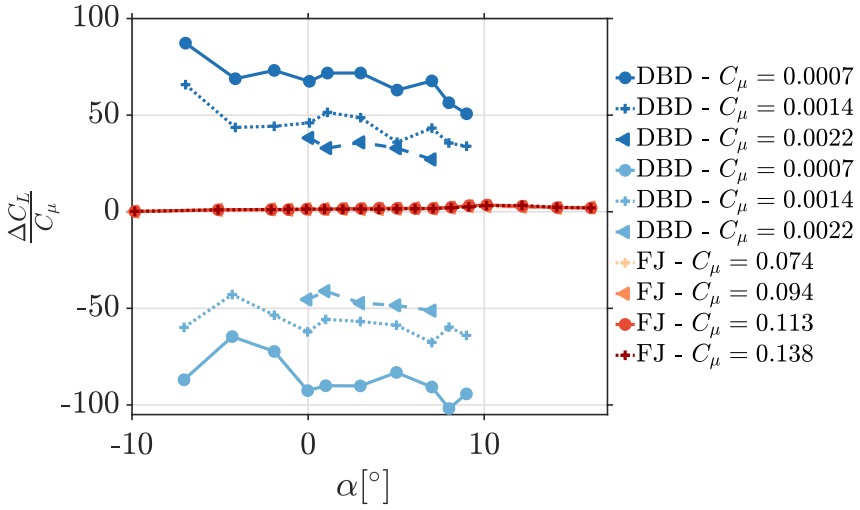

Figure 2.44: Lift augmentation efficiency $\frac{\Delta C_L}{C_\mu}$ as a function of the angle of attack α for DBD (ACT2-B and ACT3-B) and FJ actuations - $Re = 200\,000$

two actuation strategies and various angles of attack. As mentioned above for the lift coefficient gain, pressure coefficient gains do not change dramatically with the angle of attack α for the DBD actuation. For this case, ΔC_p remains constant along the chord with a slightly greater increase near the leading-edge of the airfoil. On the other hand, for the fluidic actuation, the momentum coefficient has a great impact on the ΔC_p that shows important ΔC_p at the leading-edge of the airfoil as well as near the trailing-edge as was also shown in Wetzel et al. [2013].

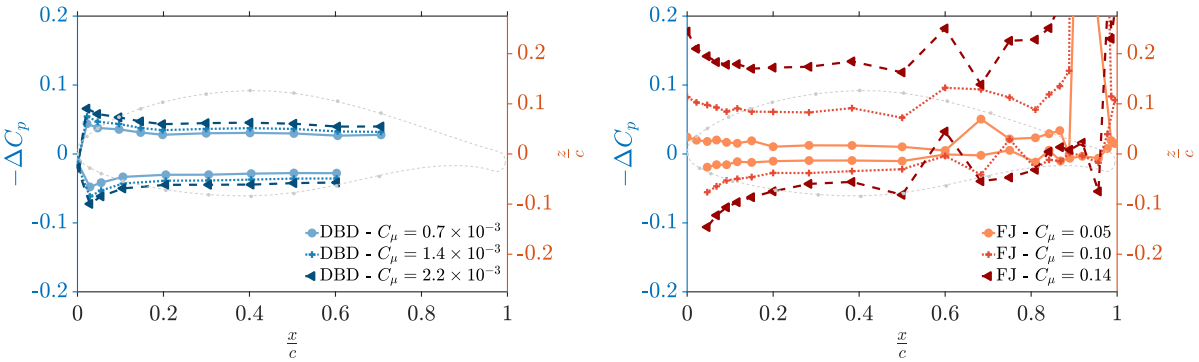

(a) DBD (ACT2-B) - $\alpha = 0°$

(b) FJ - $\alpha = 0°$

Figure 2.45: Pressure coefficient variation ΔC_p distribution for the two control strategies and different C_μ - $Re = 200\,000$

Such as the DBD actuation, the blowing modifies the whole pressure distribution along the chord but generates an important suction peak close and above the blowing location ($\frac{x}{c} = 0.96$) that is not visible in the figures for clarity. This suction peak, characteristic of circulation control devices, is not visible for the DBD actuation as there is not pressure taps near the trailing-edge of the airfoil. It is assumed that the suction peak exists but does not have the considerable magnitude of the FJ induced peak. In the case of FJ actuation, with the angle of attack augmentation, ΔC_p increases up to values between -0.3 and -0.4 for the higher C_μ at $\alpha = 8°$ whereas ΔC_p equals -0.1 for DBD actuation.

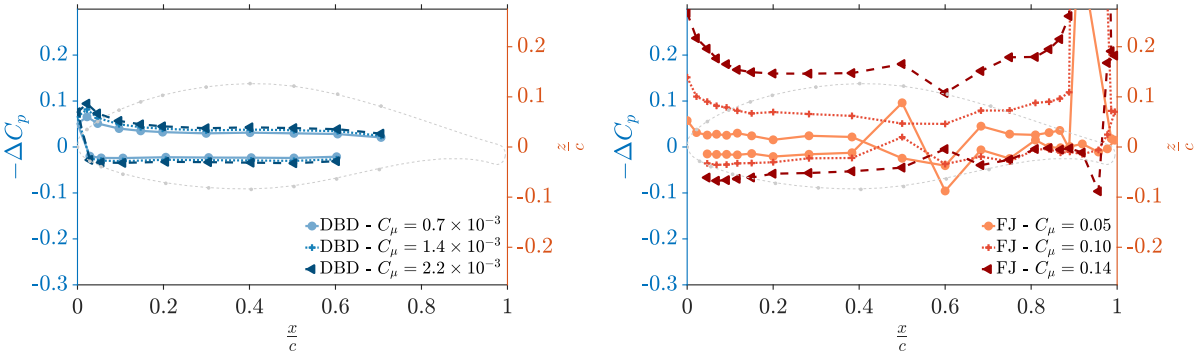

(a) DBD (ACT2-B) - $\alpha = 5°$ (b) FJ - $\alpha = 4°$

Figure 2.46: Pressure coefficient variation ΔC_p distribution for the two control strategies and different C_μ - $Re = 200\,000$

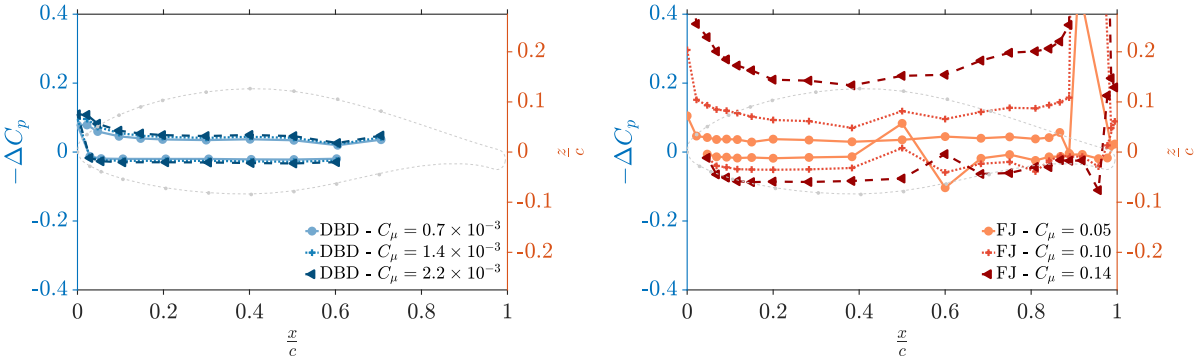

(a) DBD (ACT2-B) - $\alpha = 7°$ (b) FJ - $\alpha = 8°$

Figure 2.47: Pressure coefficient variation ΔC_p distribution for the two control strategies and different C_μ - $Re = 200\,000$

Coanda effect

It has been shown in section 2.3 (p.40) that the Coanda effect does not seem applicable to the present DBD actuation. Indeed, the fact that DBD induced jets adhere to the model wall is caused by the electrical field between active and grounded electrodes and not by the dynamics of the fluid.

In the case of fluidic jets, Jaunet and Braud [2018] show that locally i.e. at a jet section, the blowing reduces the recirculation bubble. Actuation increases both downwards and upwards vertical velocities coming from the upper and lower sides of the airfoil respectively. In the spanwise direction, the authors conclude that the incoming flow circumvents the jets by deviating on both sides of each jet. Hence, fluidic actuation is three dimensional with an important recirculation motion in the spanwise direction. However, the jet does not adhere to the model wall, does not follow the trailing-edge curvature and separates early from the wall. This is probably due to the significant jet thickness with respect to the TE curvature (such as DBD induced jets) and to the jet finite span (discrete actuation).

Conclusive remarks

DBD and FJ actuations are implemented at the trailing-edge of a 2D airfoil to perform a circulation control. Results show that both strategies remain very different though.

DBD actuation is a purely two-dimensional action that shows low momentum coefficients and a moderate lift coefficient variation of about $\Delta C_L = \pm 0.1$. Fluidic jets is a discrete actuation distributed along the airfoil span, with high momentum coefficients and strong lift coefficient gains (ΔC_L up to $+0.4$). In this last case, lift coefficient could not be reduced when blowing from the lower side of the airfoil.

This very different nature of actuation induces different mechanisms of actuation. DBD actuation shows a very low modification of the wake as well as a small modification of the pressure over the airfoil. Fluidic strategy, however, strongly affects the airfoil wake and a pressure peak is visible close to the blowing location highlighting a strong pressure reduction near the TE.

For both approaches but for different reasons, Coanda effect is not applicable. In the case of fluidic jets, actuation is strongly three dimensional and jets are too thick to induce the adhesion to the wall curvature. For DBD actuators, jets do follow the curvature but merely thanks to the electrical nature of the actuation.

2.4.6 Dynamic analysis

In the perspective of a closed-loop control, the dynamic response of the system has been analysed. First are presented the time and spatial scales of the system compared to the ones of an operating wind turbine. The results presented in the following show the flow response to an actuation impulse that is divided into a *positive step*, from the baseline state to a controlled state; and a *negative step*, from a controlled state to the baseline state again. One of the advantages of plasma actuation is that the setting of the actuation is almost instantaneous ($\sim$ ms) as the actuation is purely electrical. Applied C_μ (or voltage) steps are therefore *real* actuation steps.

Samplings lasted 50 s, MicroDAQ pressure transducer worked at 500 Hz and the platform balance at 10 kHz. Step responses are obtained by averaging 10 different uncorrelated tests.

Time, spatial and velocity scales

Table 2.4 shows temporal and spatial scales related to the NREL 5 MW wind turbine and to the present 2D-airfoil. The airfoil has a constant chord equal to 0.3 m and is immersed in a 10 m/s flow. Chord time τ_c is therefore equal to 0.03 s. The aerodynamic time response of the flow to the actuation (grossly $\approx 10\tau_c$) is equal to 0.3 s. For the NREL 5 MW turbine, the time scale of the aerodynamic perturbations is of about $100\tau_c$ which leads, for the present 2D-case, to perturbations with time scales of 3 s necessary for the implementation of a closed-loop.

Pressure coefficient response

Figure 2.48 shows the pressure response to a positive and negative actuation step for a pressure tap located at $\frac{x}{c} = 0.2$ and $\frac{z}{c} = 0.1$ (vicinity of the LE in the suction side), for an angle of attack of 0° and a voltage V_{AC} equal to 18 kV corresponding to a $C_\mu = 1.4 \times 10^{-3}$. Step responses are approximated with a first order system response as shown in equation 2.21.

$$C_p(t) - C_p(t=0) = u(t)K(1 - e^{-\frac{t}{\tau}}) \tag{2.21}$$

where $u(t)$ is the input command equal to 1 when the actuation is powered and 0 otherwise, K is the steady state gain and τ the time constant of the system i.e. the time of the system to reach 63% of its final asymptotic value. C_p is the pressure coefficient for a given pressure tap and $C_p(t=0)$ is its initial value before the step. Both negative and positive steps show a similar gain highlighting that the flow comes back easily to its original state without hysteresis effects. This behaviour is due to the state of the flow that is attached to the airfoil at this angle of attack of 0°. Time constants τ for the two step responses have the same order of magnitude but the negative step induces a faster response: $\tau = 0.37$ s for the positive step and $\tau = 0.26$ s for the negative step. These values correspond respectively to 12 and 8 chord convective times

Variable	Unit	NREL 5MW	2D-airfoil
Rotor radius R	m	57	-
Chord at $\frac{2}{3}R$	m	2.4	0.3
Ω	rpm	14	-
Rated wind velocity U_∞	m/s	14	10
Turbulent scale λ_u (Kaimal et al. [1972])	m	42	-
$r = \frac{2}{3}R$	m	38	-
Ωr	m/s	56	-
Relative velocity W_r	m/s	58	10
$\tau_c = \frac{c}{W_r}$	s	0.04	0.03
$\tau_{set} \approx 10\tau_c$	s	0.4	0.3
$\tau_{rot} = \frac{2\pi}{\Omega}$	s	$4.2 \approx 100\tau_c$	3
$\tau_{turb} = \frac{\lambda_u}{U_\infty}$	s	$3 \approx 75\tau_c$	2.25

Table 2.4: Spatial and temporal scales related to the NREL 5 MW wind turbine and to the present 2D-airfoil

$\frac{c}{U_\infty}$. Superimposed first order transfer function estimations seem to fit correctly the pressure coefficient responses.

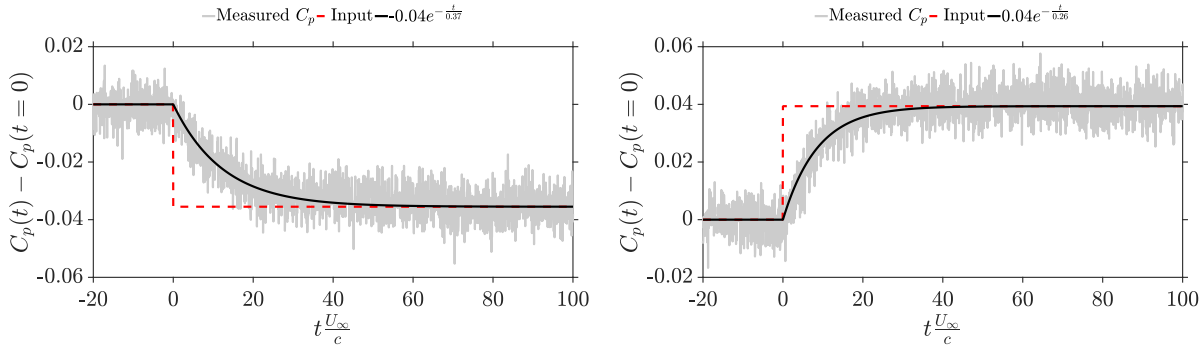

(a) Positive step

(b) Negative step

Figure 2.48: Pressure coefficient response to a positive step (left) and a negative step (right) for a pressure tap at $\frac{x}{c} = 0.2$ and $\frac{z}{c} = 0.1$ - ACT2-B, $\alpha = 0°$, $Re = 200\,000$ and $C_\mu = \pm 1.4 \times 10^{-3}$

Figure 2.49 shows the distribution of the system time constants τ along the chord of the airfoil (all the pressure taps) and for different control inputs. Variable τ is normalised by the length and velocity scales of the tests, c and U_∞ respectively. In the view of these plots, there is not a clear trend or evolution that detaches. Shortest time responses seem however to be near the leading-edge of the airfoil. This is opposed to the results obtained by Jaunet and Braud [2018] that found that the time constant increases with the distance from the actuation, located at $\frac{x}{c} = 0.96$. Also, time constants are particularly high compared to those obtained in Jaunet and Braud [2018]: the authors obtained time constants from 1 to 4 convective times $\frac{c}{U_\infty}$ for an attached flow. Comparisons with their study have to be, however, taken carefully as their fluidic actuation induces a pressure deficit at the actuation location that is absent (or strongly reduced) in the present case. Also, they averaged their data with 10 more samples than the present cases. Our data reports, though, that the actuation *strength* i.e. its C_μ (or voltage) does not seem to change the time response of the system.

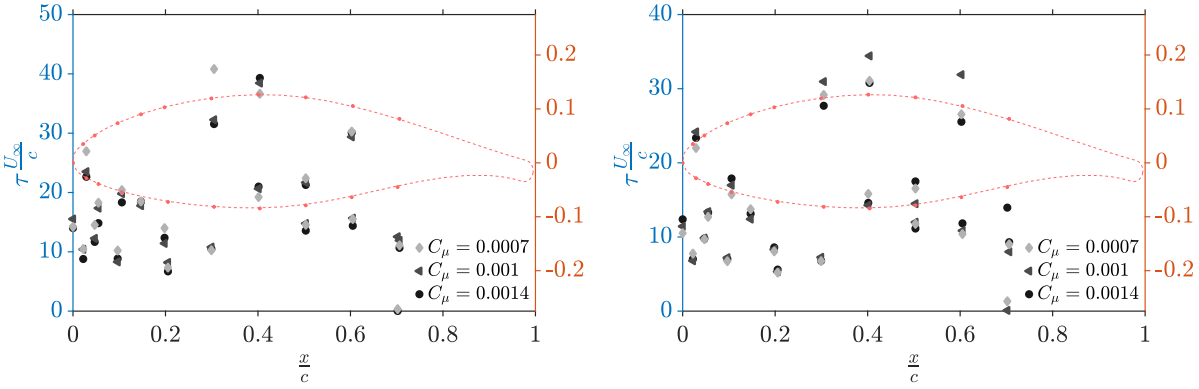

(a) Positive step (b) Negative step

Figure 2.49: Normalised time constant $\tau\frac{U_\infty}{c}$ of the system along the chord of the airfoil for different control inputs C_μ (positive step (left), negative step (right)) - ACT2-B, $\alpha = 0°$ and $Re = 200\,000$

Lift coefficient response

The time response of the lift coefficient C_L measured with the platform balance is shown in figure 2.50 for a positive and negative step at $\alpha = 0°$[9]. Step heigh is equal to $\pm C_\mu = 1.4 \times 10^{-3}$ (or $\pm 18\,\text{kV}$). The time responses of the platform balance are shorter than the ones obtained with pressure measurements. C_L time response of the positive step ($\tau = 0.06\,\text{s}$) corresponds to 2 convective times $\frac{c}{U_\infty}$ and for a negative step, the response is faster, as for the pressure response: $\tau = 0.02\,\text{s}$ leading to 0.7 convective times. These values are clearly in the order of magnitude of the ones obtained by Jaunet and Braud [2018] for an attached flow and the same airfoil but a fluidic actuation.

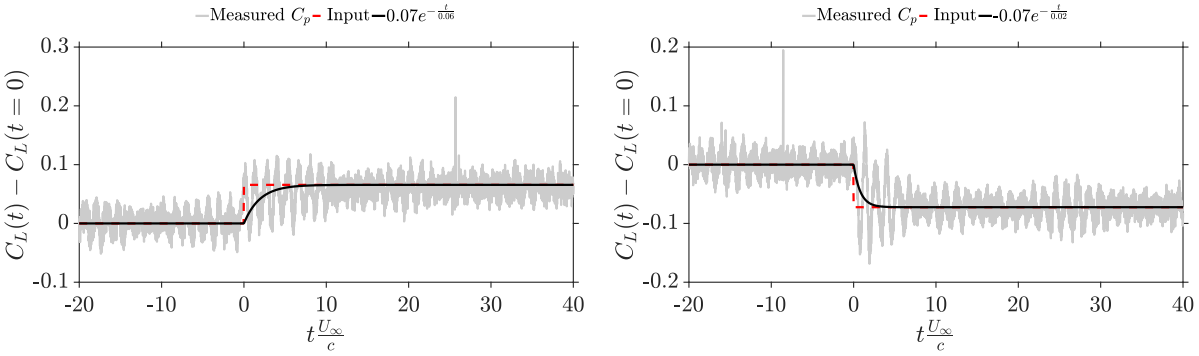

(a) Positive step (b) Negative step

Figure 2.50: Lift coefficient C_L response to a positive step (left) and a negative step (right) for different control inputs - ACT2-B, $\alpha = 0°$, $Re = 200\,000$ and $\pm C_\mu = 1.4 \times 10^{-3}$

A local normal force coefficient C_n can be obtained via the integration of the pressure coefficient C_p along the chord of the airfoil. A fictive pressure tap is added at the trailing-edge ($\frac{x}{c} = 1$ and $\frac{z}{c} = 0$) and with a C_p value equal to the average of C_p of the two extremal pressure taps at $\frac{x}{c} \approx 0.7$ on both pressure and suction sides. C_n is calculated as:

[9]The platform balance signal is very noisy at the 50 Hz frequency of the electrical grid. A filtering of the signal suppresses the dynamics of the system as both characteristic time scales are very close

$$C_n = \sum_{i=1}^{N_{taps}+1} \frac{C_{p,i+1} + C_{p,i}}{2} \left(\frac{x_{tap,i+1} - x_{tap,i}}{c} \right) \tag{2.22}$$

where N_{taps} is the number of pressure taps and x_{tap} the distance along the chord line from the leading-edge to ith pressure tap. As the airfoil is at $\alpha = 0°$, local lift coefficient C_l is equal to C_n[10]. Figure 2.51 shows the local lift coefficient response to a positive and a negative step for $\alpha = 0°$ and several control inputs. The lift coefficient gain is normalised by the steady state gain $C_{l,max}$ in the case of a positive step and $C_{l,min}$ for a negative step. In the sake of clarity, only one point out of 35 is plotted. All the curves for different C_μ collapse in a single curve that can be estimated with a first order transfer function:

$$\frac{C_l(t) - C_l(t=0)}{C_{l,max/min}} = u(t)(1 - e^{-\frac{t}{\tau_l}}) \tag{2.23}$$

where τ_l is defined as the time constant of the C_l response. This response curve is superimposed in the figure as well as the response obtained by Jaunet and Braud [2018] for a fluidic actuation and at the same angle of attack $\alpha = 0°$. Jones [1940] determined the lift response to an incoming gust using the potential flow theory and his result is also plotted in the figures.

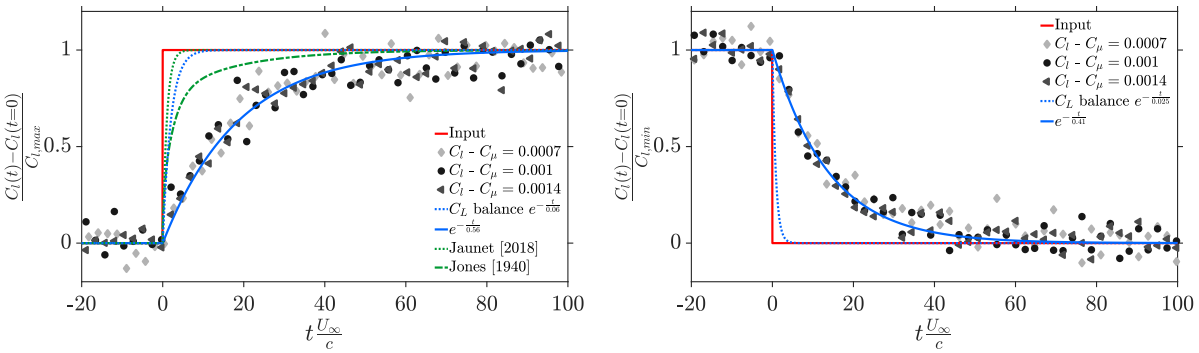

(a) Positive step

(b) Negative step

Figure 2.51: Lift coefficient response to a positive step (left) and a negative step (right) for different control inputs - ACT2-B, $\alpha = 0°$ and $Re = 200\,000$

As mentioned above, pressure response and consequently C_l response are very slow with time scales of approximately 18 convective times $\frac{c}{U_\infty}$, suggesting that the aerodynamic response of the flow is not captured by the pressure sensor. As the time response of the pressure scanner (≈ 2 kHz) is well over the characteristic time scales of the system, it can be said that the pressure settling on the vinyl tubes connecting the pressure taps to the scanner (i.e. time response of the actuation settling) damps the system dynamics. Indeed, because the electromagnetic interferences induced by the plasma actuation, the scanner couldn't be too close to the airfoil. Pressure dynamic response can be computed with Pr. J. Ruud van Ommen (TU Delft) code and using Bergh and Tijdeman [1965] methodology. Maximal time delay in the pressure tubes is estimated to be of about 0.01 s which corresponds to 0.33 convective times. This time is however small and does not seem to explain the pressure response delay. The obtained response of the C_L measured with the platform balance shows a very similar behaviour than the one obtained by Jaunet and Braud [2018] for a positive step. The discrepancies between the result of Jones [1940] are diverse as suggested by Jaunet and Braud [2018]. The theoretical model uses an inviscid flow that does not capture flow separation near the TE. Also, the effect of a gust is modelled by

[10] *Lower case subscript* indices (C_l, C_n) are used for local pressure integrated values and *capital letter subscripts* (C_L) indicate global measures with the platform balance

an airfoil camber addition while in the present case an actuation i.e. a momentum addition is supplied at the TE.

The order of magnitude of the Strouhal number corresponding to the time response of the system is $St \approx 1$ which is well over the reduced frequencies characteristic of an operating wind turbine. Indeed, for $c = 1\,\text{m}$ and $U = 60\,\text{m/s}$, the most energetic perturbations in the atmospheric boundary layer are between $St = 0.005$ and 0.01 for a turbine operating with a $8\,\text{m/s}$ wind and at an altitude of 80 m (Kaimal et al. [1972] and Jaunet and Braud [2018]). This shows that the system is fast enough to address perturbations scaling the atmospheric boundary layer ones.

The effect of a gust at a wind-tunnel scale is often studied in two possible ways: a velocity variation and an angle of attack variation. A velocity variation (or Reynolds number increase) through active grids (Kröger et al. [2018]) that simulate an incoming gust is not possible in the present wind-tunnel. Gusts also induce an angle of attack effect on the blades as does the natural shear of the atmospheric boundary layer. The chosen strategy for the closed-loop control is the rotation of the airfoil to simulate a change in the angle of attack. It was chosen to perform the closed-loop with one pressure tap near the leading-edge. Despite its perfectible time response, the pressure scanner remains more reliable and exploitable than the platform balance signals given the involved time-scales of the angle of attack perturbation. This closed-loop control is, however, out of the scope of the present thesis work and was carried out by a post-doc student within the framework of the SMARTEOLE project.

2.5 Conclusion

General conclusion

This second chapter dealt with the DBD actuation over an airfoil in a 2D-configuration with the objective of performing a circulation control that would increase and decrease the lift coefficient of the airfoil.

First, PIV characterisation of DBD actuators in quiescent air conditions allows the calculation of an actuator thrust force and the estimation of a momentum coefficient C_μ, which is between 3.2×10^{-3} and 6.0×10^{-3} for curved induced jets. It is shown that the electrode position around the trailing-edge curvature has a direct impact on the jet topology specially whether the induced jet is going to follow the model curvature or not. To obtain a complete jet adhesion to the trailing-edge wall, the region of EHD interaction should reach the end of the curvature. Given the induced jet Reynolds numbers, ranging from 450 to 1900, DBD induced jets appear to be in a transitional regime which is confirmed by the normalised velocity profiles: the maximum velocity ordinate is in between laminar and turbulent wall jet cases for the plane configuration and analog to turbulent for curved induced jets. A normalisation of the jet development in the x-direction shows that DBD induced jets evolve linearly in terms of rate of spread and as $x^{-\frac{1}{2}}$ for the velocity decay, such as plane fluidic wall jets do. However, velocity decay and spread of curved DBD induced jets are considerably higher than the respective variables in a plane configuration.

Regarding flow control testings, actuation translates the baseline lift coefficient curve towards higher lift or lower lift forces highlighting the achievement of a circulation control. Maximum lift coefficient increase is of $+0.08$ and the maximum C_L decrease that could be performed was of about -0.11. The higher the momentum coefficient (or applied voltage), the higher the effect of the actuation on the lift coefficient. Also, the performed circulation control in the vicinity of the trailing-edge modifies the whole pressure distribution around the model, with equal action on pressure and suction sides. However, maximal C_p gains and losses are obtained at the leading-edge of the airfoil, an area very receptive to the actuation.

Velocity fields show that the rounded trailing-edge induces a recirculation area in the wake of the airfoil made up of two symmetrical counter-rotating vortices at the airfoil base. These coherent structures are actually the signature of a Von Karman vortex shedding. Actuation does

not alter significantly the topology of the wake but velocity fluctuations are increased and turbulence is enhanced on both sides of the wake i.e. on the shear layer developing in the continuation of the suction and the pressure sides of the airfoil. Velocity profiles beyond the TE show that the actuation displaces the wake in the direction of the blowing. Hot wire measurements in the wake of the airfoil show that the actuation triggers the Von Karman instability, a result that is confirmed with POD analysis in the downstream flow.

Strategy selection for the following

Within the SMARTEOLE project, plasma and fluidic control strategies were carried out in parallel in a 2D-configuration. Only one approach has to be chosen for the flow control implementation in the wind turbine bench of the laboratory. By comparing both actuations it can be concluded that the fluidic jets allow to obtain high lift coefficients gains, over the $\Delta C_L \approx 0.25$ that is required for flow control application on wind turbine blades stated in chapter 1. This actuation performs important gains in the linear part of the lift curve and even higher performances at higher angles of attack, when separation rises along the suction side of the airfoil. DBD actuators have short time responses as they are merely electrical devices but, even if their lift augmentation efficiency $\frac{\Delta C_L}{C_\mu}$ is very important, the overall lift coefficient variation remains of about ± 0.1. Furthermore, the implementation of plasma actuators in the turbine bench of the laboratory would require the use of a high voltage slip ring around the turbine shaft. The use of DBD technology brings up arcing probability reducing the reliability and robustness of the actuators. Also, in the perspective of an eventual implementation of these AFC techniques in full scale models, DBD actuators show serious scaling problems as the induced jet velocities cannot be easily increased. Indeed, in a rotational configuration the relative velocities seen by the blades are near 50 m/s, an order of magnitude more suitable to a fluidic actuation. For these efficiency and reliability reasons, **it has been chosen to continue the project with the fluidic jet strategy** and to implement it in the wind turbine bench of PRISME laboratory. As a preliminary step before the rotational testings, blades equipped with fluidic control are tested in a translational configuration, where the blade does not rotate but the blade tip is free. This configuration is detailed in the next chapter.

Chapter 3

Fluidic flow control on a wind turbine blade - translational configuration

Contents

3.1 Introduction

After the preliminary testing campaigns carried out in parallel in a 2D-configuration with plasma actuators and fluidic jets (Braud and Guilmineau [2016] and Jaunet and Braud [2018]), it has been chosen to pursue the work towards the rotational configuration with the fluidic actuation. This decision is based on the high momentum coefficient of the jets and their higher potential regarding the lift coefficient increase. Also, fluidic jets remain a purely pneumatic system easier to implement on the turbine bench than DBD actuation, a strategy that involves high voltages. Therefore, the implementation of a fluidic control in a rotational configuration seemed more reliable, reproducible and worthwhile.

Blades designed to be mounted later on the wind turbine bench are manufactured. This chapter presents a first study that aims to evaluate the potential of this jet actuation with these new blades: flow control effects are characterised in a translational configuration, meaning that the blade is flush mounted on one extremity (blade root) and that the blade tip is free. In this configuration, there is not rotational effects involved.

The first section of the chapter presents the experimental set-ups implemented for the testings: the used blades are described as well as the experimental means. Then the jet characterisation

in quiescent air conditions is investigated, an analysis that allows to obtain the jet exit velocity but also the jet topology. Finally, the last part concerns the flow control results performed in the wind-tunnel main test-section. In addition to the classical measurements such as loads, surface pressure and PIV, strain gages are implemented at the blade roots to measure the flapwise bending moment of the blade. Indeed, bending moment is a characteristic variable that gives evidence of the load fluctuations endured by the blades of operating wind turbines where lift or pressure distribution data are not available. Hence, in the perspective of a closed-loop control for load fluctuation reduction, the bending moment information would be a suitable measurement to perform the regulation.

3.2 Experimental set-up

This section deals with the experimental set-up implemented for the translational configuration. First are described the wind turbine blades tested in this configuration but designed to be mounted later on the rotor bench of the laboratory as will be described in chapter 4. The pneumatic system that provides compressed air on the blades for the flow control actuation is also explained. The experimental set-up implemented for the jet characterisation in quiescent air conditions is presented and, finally, the experimental means used for the wind-tunnel testings of the blade in the translational configuration are explained.

3.2.1 Blades

Each blade is made of several parts as shown in figure 3.1: the blade root fixation made of stainless steel and the streamlined part of the blade, made of aluminium (root section and blade tip) and POM for the main sections of the blade coloured in the figure. Two steel rods go through the blade to hold the parts together and to ensure the blade mechanical strength and resistance. Blades are not twisted nor tapered. They are designed to be mounted in the wind turbine bench of the laboratory which rotor radius R is equal to 0.7 m and the blade chord c is of 100 mm. With respect to the previous 2D-configuration the blade chord is divided by three. Wind velocity will be of 20 m/s which will lead to lower Reynolds numbers than the 2D case (130 000 here, 200 000 for the 2D case). It will be seen below the problematic effects driven by this low Reynolds number and the challenging Reynolds analogies.

In order to be able to study the effect of a lift force increase and decrease, two blowing configurations are investigated. Hence, two sets of two blades each were manufactured: one set blowing from the pressure side and another acting from the suction side. Within each set only one blade is equipped with pressure taps.

Lift control is performed with these two blade sets equipped of continuously blowing jets located in the vicinity of the trailing-edge ($\frac{x}{c} = 0.96$). A crossing plenum chamber with a diameter of $\phi_p = 6$ mm supplies the holes in compressed air. The diameter of the blowing holes is equal to $\phi_h = 0.6$ mm and each row is composed by 72 holes spaced by 4.86 mm. Figure 3.2 shows the jet position and direction for the two blowing configurations on the upper-side and lower-side of the blade. Blowing jets are only present on the second half of the blade, between $r \approx 0.5R$ and $r \approx R$ (red and green sections in figure 3.1), the area producing most of the turbine torque.

Important remark

In the following, all the results of jet characterisation and flow control application will be presented for the **upper-side blowing** only. At the end of the chapter, a short section will be devoted to the drawbacks of the testings and some results about the lower-side blowing will be included.

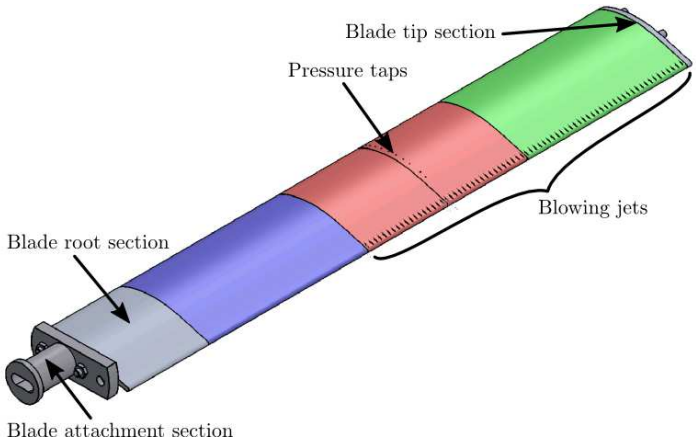

Figure 3.1: CAO representation of a blade

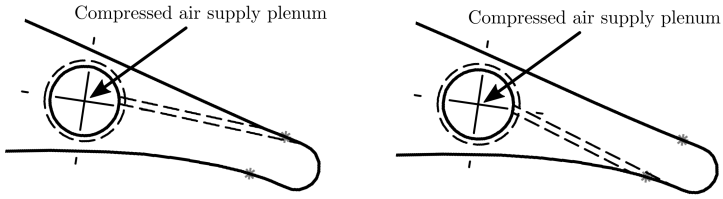

(a) Upper-side blowing (b) Lower-side blowing

Figure 3.2: Schemes of jets position and direction for the two blowing configurations

3.2.2 Pneumatic system & jet characterisation

The pneumatic system used for the flow control application in this non-rotating configuration is described in figure 3.3. The compressed air network of the laboratory is used to supply the model with pressurised air. The pneumatic system has, however, several intermediary elements before the compressed air reaches the blade plenum chamber:

- A pressure regulator (Joucomatic 34207162 - $P_{max} = 17.5\,\text{bar}$) that regulates the inlet pressure of the flowmeter (from 4 bar to 7 bar) and filters the supplied air
- A flowmeter regulator (Brooks 5853E - $Q_{max} = 500\,\text{l}_\text{n}/\text{min}$ - $\pm 0.1\%$) that allows to set and fix the flow rate Q_{fm} in the pneumatic system[1]
- A temperature probe (4 wire platinum RTD[2] probe (PT100) - $\pm 0.3\,°\text{C}$) that provides the flow temperature at the flowmeter exit

The plenum chamber is cylindrical and has a diameter equal to 6 mm which is equal to the internal diameter of the tubes used in the air circuit in order to avoid sharp contractions in the circuit and the resulting pressure losses. Furthermore, the plenum chamber feeds the jets in compressed air and works as a small buffer tank or chamber where the flow is nearly stopped.

For the jet characterisation in quiescent air conditions and to measure the jet exit velocity, a total pressure probe made of a series of nested thin aluminium tubes is used. Its outer diameter at the tip is of 0.5 mm and the inner diameter of 0.25 mm. Two pressure sensors are used to measure the jet stagnation pressure: either a GE LPM 9331 (0 to 2 bar - $\pm 0.1\%$) for the higher

[1] The flowmeter regulator is calibrated in $\text{l}_\text{n}/\text{min}$ which corresponds to a flow at 0 °C and at a pressure of 1 atm. To convert this values to l/min a multiplication by $\frac{T_j}{273.15}\frac{101325}{P_{atm}}$ is performed

[2] Resistance Temperature Detector

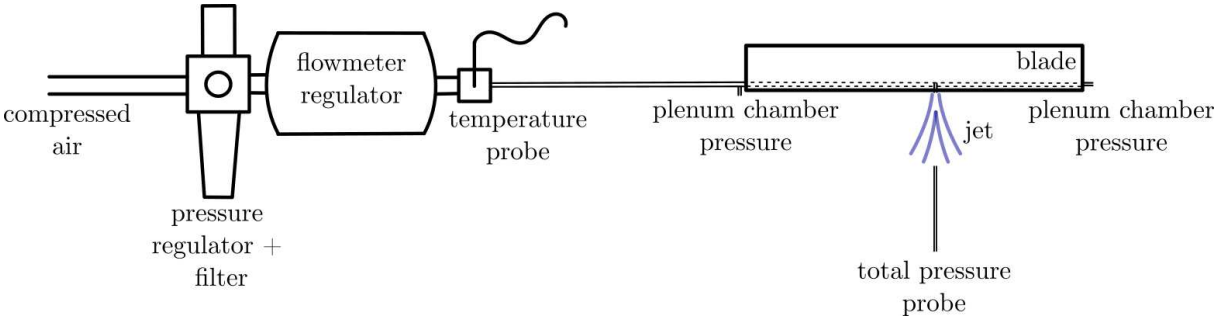

Figure 3.3: Scheme of the pneumatic system that supplies the model in compressed air (not to scale)

pressures or a Sedeme FAS64/50A (0 to 5000 Pa - ±0.2%) for pressure in the low velocity areas. All the measurements are the average of 512 samples taken at 100 Hz after a waiting time of 5 to 7 s that ensures the pressure stabilisation and the traverse system steadiness. A third pressure sensor (Sensortechnics, 144SB005D-PCB, 0-5 bar) is used for the measurement of the stagnation pressure in the plenum chamber. This pressure is measured at the blade root (entry of blade plenum chamber) and at the blade tip (inside the pressure chamber, at blade tip).

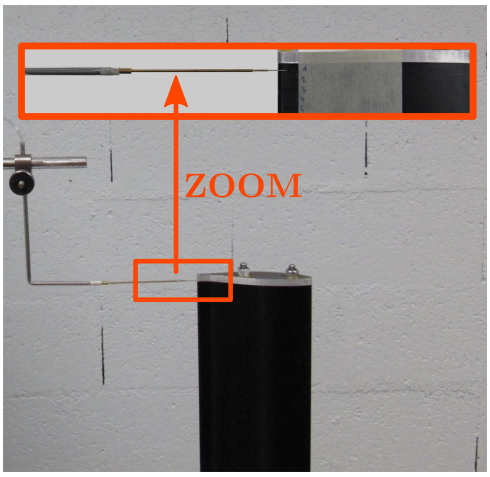

Figure 3.4: Pictures of the total pressure probe used for the jet characterisation in quiescent air conditions

3.2.3 Wind-tunnel instrumentation

Set-up of the model in the test-section

Tests are performed in the **main test-section** of the "Lucien Malavard" wind-tunnel of PRISME laboratory. The blade is mounted vertically in the center of the test-section at the extremity of a mast as shown in figure 3.5a. The blade tip is free leading to a **translational configuration**: the blade does not rotate but the flow over the blade is three dimensional because of the free blade tip. The mast is shielded with a streamlined fairing of height equal to 740 mm up to the blade root. The pneumatic system used is identical to the one described previously and drawn in figure 3.3.

In this configuration, wind-tunnel tests are performed with an incoming flow velocity U_∞ of 20 m/s corresponding to a chord Reynolds number $Re = \frac{U_\infty c}{\nu}$ of 130 000, ν being the kinematic viscosity of the flow. At this Re and with the natural turbulence of the wind-tunnel equal to 0.5%, low-Reynolds effects appear as the boundary layer developing along the suction side of

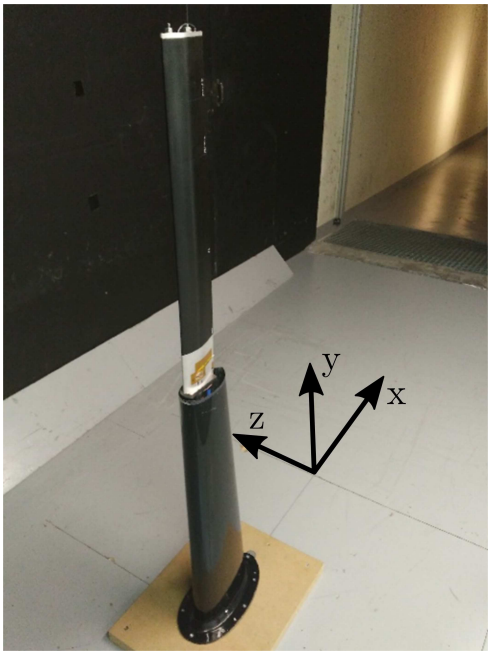

(a) Blade mounted in a translational configuration

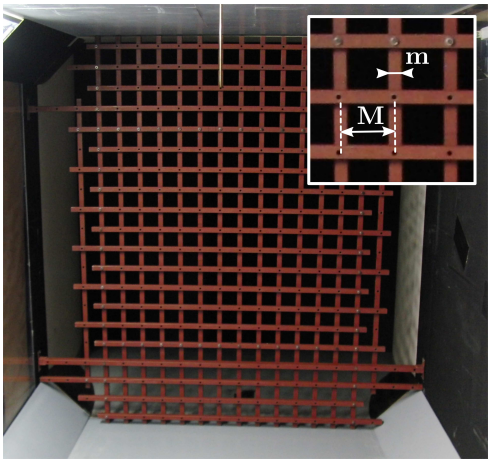

(b) 4.3% turbulence intensity grid placed at the test-section entry

Figure 3.5: Pictures of the experimental set-up (blade model and turbulence grid)

the airfoil separates from the wall before transitioning to a turbulent state for a large range of angles of attack. To avoid these low-Reynolds effects and promote turbulence, experimental testings are performed with a 4.3% turbulence grid placed at the test-section entry. This grid is shown in figure 3.5b together with its dimensional characteristics m and M. Grid variable m is defined as the bar width and M as the grid mesh length. They are equal to 25 mm and 100 mm respectively. The blade model is placed 2.30 m downstream of the grid, a distance considered as sufficient to obtain an homogeneous and isotropic turbulence at the blade location. The evolution of turbulence downstream of the grid can be read in Laverne [2003] and Sicot [2005] who studied the behaviour of wind turbine airfoils subjected to different turbulence intensities T_u at the laboratory.

As the characterisation of the turbulent flow past the grid was carried several years ago, turbulence homogeneity and level at the blade location are verified with hot-wire anemometry. Tests are performed with a Dantec Dynamics 55P61 two-wire probe. Acquisition is made with StreamWare Dantec software at a sampling frequency of 60 kHz and a number of samples of $2^{22} = 4194304$ (≈ 70 s) in order to ensure statistical convergence. Samples are taken in the vertical direction, at the center of the test-section, but without the blade, the mast and the fairing (empty test-section). Airfoil-related coordinate system (x, y, z) is defined as: x-axis in the wind direction, y-axis in the vertical direction and z-axis in the transverse direction. The hot-wire is oriented to measure velocities in the x and y directions named U and W and decomposed as $U(x,y,t) = \overline{U}(x,y) + u'(x,y,t)$ and $W(x,y,t) = \overline{W}(x,y) + w'(x,y,t)$, where t represents the time dependency. Figure 3.6a shows the mean velocities $\overline{U}$ and $\overline{W}$ as a function of $\frac{z}{R}$ ($\frac{z}{R} = 0$ corresponds to the blade root and $\frac{z}{R} = 1$ to the blade tip) for an incoming flow velocity U_∞ of 20 m/s. Turbulence intensities T_u and T_w are defined in equation 3.1 and are plotted in figure 3.6b. Longitudinal velocity $\overline{U}$ at the blade location is homogeneous an equal to the freestream velocity. Vertical velocity $\overline{W}$ has a very weak value and shows a very slight decrease (< 0.5 m/s) at the higher ordinates. Turbulence intensities on both streamwise and vertical directions have the same evolution and the vertical spatial average is equal to 4.3%.

$$T_u = \frac{\sqrt{\overline{u'^2}}}{\sqrt{\overline{U^2} + \overline{W^2}}} \qquad T_w = \frac{\sqrt{\overline{w'^2}}}{\sqrt{\overline{U^2} + \overline{W^2}}} \tag{3.1}$$

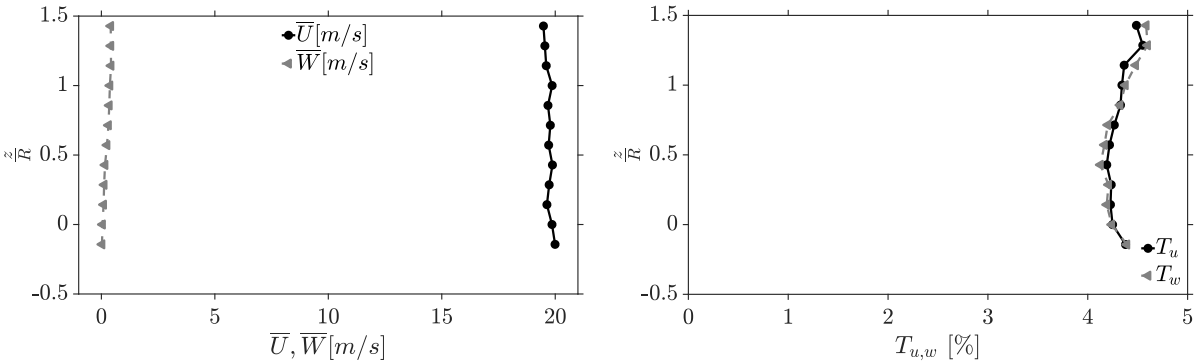

(a) $\overline{U}$ and $\overline{W}$ velocities

(b) Turbulence intensities T_u and T_w

Figure 3.6: Mean velocities $\overline{U}$ and $\overline{W}$ and turbulence intensities T_u and T_w distribution in the vertical direction for the 4.3% turbulence grid ($U_\infty = 20\,\text{m/s}$, center of the test-section)

Power spectral densities of U and W velocities at the center of the test-section $\frac{z}{R} \approx 0.5$ are shown in figure 3.7. Spectra have been obtained using Welch power spectral density estimate and doing the average of about 700 spectra of 6000 samples. At first sigh, the spectra are smooth and without important frequency peaks that would have highlighted turbulent structures present in the flow (wakes of the grid bars, for example). These spectra permit to conclude that the turbulence at the blade location is homogeneous and isotropic. Three zones can be distinguished from these spectra:

- First zone for the lowest frequencies and higher spectral densities where turbulent energy is produced
- Second zone corresponding to Kolmogorov's cascade where turbulence is not produced nor dissipated, this range of frequencies matches the $-\frac{5}{3}$ slope
- Third zone related to turbulent kinetic energy dissipation and matching the -4 slope

Surface pressure measurements

Mean pressure distribution around the airfoil is measured with 20 pressure taps implemented on the blade between the leading-edge and 70% of the chord as can be seen in figure 4.11. Due to the small dimensions of the trailing-edge and the size of the pressure chamber, it was not possible to implement pressure taps around or near the trailing-edge. The section equipped with pressure taps can be placed at two different blade spans corresponding to $r = 0.63R$ and $r = 0.88R$ (red and green sections in figure 3.1 on page 79). Pressure measurements are carried out with a 32-channel differential pressure scanner ESP-32HD (GE, ± 0.361 PSI) embedded in a MicroDAQ system (CHELL). The reference pressure for the pressure coefficient $C_p = \frac{P - P_\infty}{\frac{1}{2}\rho U_\infty^2}$ calculation is the static pressure measured with a Pitot probe near the upper wall of the test-section and 1 m after the test-section entry. Accuracy of the pressure scanner is of ±0.25% of the full scale i.e. about 6 Pa. This corresponds to about 2.5% of C_p values. Given the pressure coefficient variations ΔC_p obtained with the actuation, the uncertainty on ΔC_p is of about 5%. Pressure measurements are acquired at a frequency equal to 500 Hz and 10 000 samples are acquired (20 s).

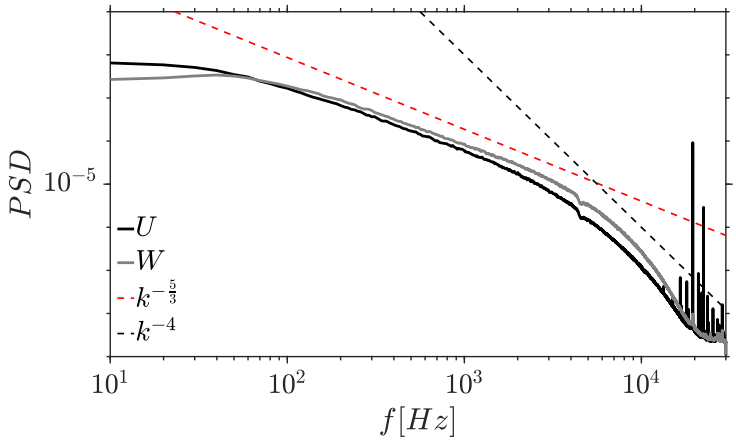

Figure 3.7: Power spectral density of U and W velocities ($U_\infty = 20\,\mathrm{m/s}$, center of the test-section)

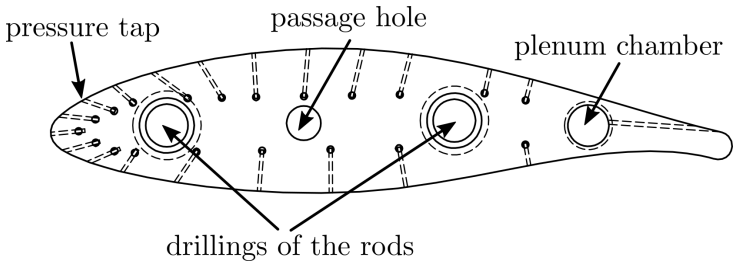

Figure 3.8: Position of the pressure taps on the blade

Loads & Flapwise bending moment

The model and the mast are mounted on the 6-component platform balance located under the wind-tunnel test-section. Lift coefficient uncertainty is equal to 9% for attached flows and to 3% for partially detached flows. Considering the lift coefficient variations ΔC_L obtained with the actuation, the uncertainty of ΔC_L is of about 3 to 8%. Further information on the working principle of the balance and measurement uncertainties are explained in appendix B. Balance provides time averaged lift and drag as well as the aerodynamic moments. As the mast is covered with a streamlined fairing, we can consider that the balance measures the aerodynamic loads applied on the blade exclusively. These efforts on the blade are, however, a result of all the loads applied on the emerged part of the blade, from the blade root to the free blade tip.

Flapwise bending moment (M_{fbm}) of the blades is measured thanks to four strain gages implemented at the blade roots. The detailed principle of this measurement is explained in appendix C. Used strain gages are Kyowa gages (KFG-5-120-C1-11) with a resistance of $120\,\Omega$ and a gage factor $GF = \frac{\frac{\Delta L}{L}}{\epsilon}$ equal to 2.1. Strain gages are wired to a National Instruments SCXI-1314 module itself connected to a SCXI-1001 chassis. These modules allow to supply power to the Wheatstone gage circuits. The offset value i.e. the output gage voltage when no strain is applied is subtracted to the measurements. Gages acquisition as well as load measurements and wind-tunnel data (atmospheric pressure, temperature...) are carried out at a sampling frequency of 2000 Hz and 40 000 samples are acquired (20 s). A filtering of the output gage signal is done by the acquisition software at half of the sampling frequency to increase the measurement resolution and improve the signal to noise ratio.

PIV measurements

Time-averaged velocity fields of the flow around the trailing-edge and on the blade wake are obtained via PIV measurements. Principles of PIV technique are explained in appendix A. Measurements are carried out in the (x,z) plane at $r = 0.62R$, a blade span where the flow can be supposed two-dimensional. A scheme of the PIV set-up implemented in the test-section is shown in figure 3.9 as well as the airfoil-related coordinate system definition and its related velocities. The laser sheet is in between two jets, but close to one of them, as clear images exactly over a jet where difficult to perform due to laser reflections on the model. The laser is placed on the top of the test-section and the laser beam is guided through an optical arm to the inside of the test-section where the beam is spread. The light sheet is oriented in order to visualise simultaneously both pressure and suction sides of the airfoil. As the blade is placed vertically, the camera should be placed outside and at the top of the test-section. PIV system and testing parameters are summarised in table 3.1.

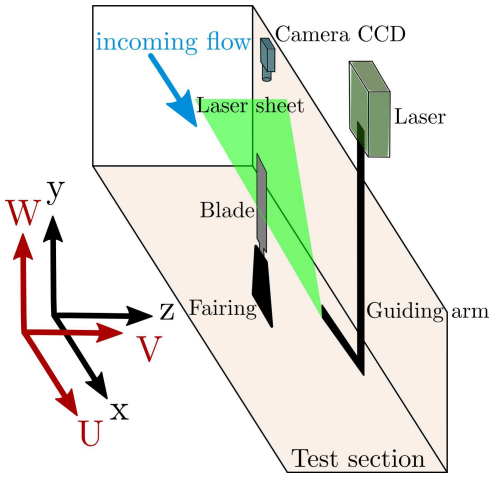

Figure 3.9: Scheme of the PIV set-up implemented in the test-section for the translational configuration

In the airfoil-related coordinate system, velocity average and fluctuating parts in the PIV field (U and V) are defined according to the following Reynolds decomposition, where t represents the time dependency: longitudinal velocity defined as $U(x,z,t) = \overline{U}(x,z) + u'(x,z,t)$ and transverse velocity as $V(x,z,t) = \overline{V}(x,z) + v'(x,z,t)$.

3.3 Characterisation of the blowing jets in quiescent air conditions

This section introduces the blade jet characterisation in quiescent air conditions. The objectives of this study are to characterise the blowing homogeneity along the blade span and the diffusion of the jets. Also, the measurement of the jet exit velocity for several pressures in the plenum chamber allows the calculation of a momentum coefficient C_μ, a variable that is widely used in the flow control literature, and which quantifies the strength of the actuation for a given incoming flow velocity.

3.3.1 Calculation of the jet velocity

Compressible theory

Considering the high pressures that are applied in the plenum chamber, a calculation of the jet velocity taking into account the compressibility effects is necessary. Figure 3.10 describes the

	Parameter	Value
Equipment	Laser	Evergreen 200 Nd:Yag, 532 nm (2 × 200 mJ) + sheet generator lens
	Camera	Imager LX11M (4032 px × 2688 px)
	Lens	Nikon (focal length 200 mm, F4)
	Filter	$\lambda = 532$ nm
	Seeding	Olive oil droplets (PIVTEC system - $d_{part} \approx 1$ µm)
Acquisition	Sampling frequency	2.5 Hz
	Number of image pairs	1000
	Δt	15.5 µs scaling the incoming flow velocity
Field of view data	Size	215 mm × 143 mm
	Scale factor	0.0534 mm/px
	Resolution	0.85 mm/vec or 1.2 vec/mm
Correlation algorithm	Software	DaVis 8.3.1 (LaVision GmbH)
	Final window	32 px × 32 px - overlap 50%
	Details	Background subtraction and particle intensity normalisation, multi-pass algorithm (1 pass 64 px×64 px, 2 passes 32 px× 32 px with square interrogation windows), vector validation if the peak ratio Q is over 1.2, median filter

Table 3.1: Summary table of the PIV set-up characteristics for the translational configuration

nomenclature used to calculate the jet velocity at the jet exit: subscript $\langle\cdot\rangle_0$ refers to the plenum chamber variables while $\langle\cdot\rangle_p$ refers to the potential flow at the jet exit and $\langle\cdot\rangle_j$ to the jet variables. Subscript $\langle\cdot\rangle_t$ is devoted to total quantities.

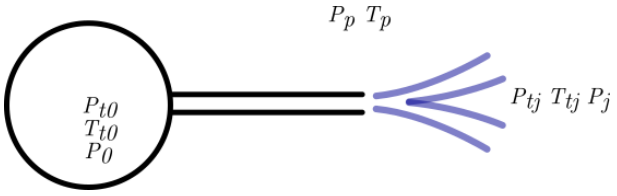

Figure 3.10: Nomenclature of the variables (jet exit, plenum chamber and outer jet)

The first step to obtain the jet velocity is the evaluation of the pressure ratio $\frac{P_j}{P_{tj}}$. If there is no shock at the jet exit, the jet static pressure P_j and the potential pressure P_p are equal. When the jets blow in quiescent air conditions, P_p is equal to the atmospheric pressure P_{atm}[3]. As the flow is supposed isentropic, the stagnation pressure of the flow is preserved from the plenum chamber to the jet exit. By neglecting the flow velocity in the plenum chamber one can obtain $P_{tj} = P_{t0} = P_0$. Hence, the pressure ratio becomes:

[3]When the airfoil is placed in an outer flow, the potential pressure P_p should be equal to the local pressure at the jet exit

$$\frac{P_j}{P_{tj}} = \frac{P_{atm}}{P_0} \tag{3.2}$$

However, experimentally, it has been found out that P_{tj} is not equal to P_{t0} because of the pressure losses in the jet holes and drillings. The ratio $\frac{P_j}{P_{tj}}$ is therefore calculated with the P_{tj} obtained at the jet exit and the atmospheric pressure P_{atm}. For the calculation of the jet velocity, the information at the jet exit (P_{tj}) seems more suitable than the information in the plenum chamber (P_{t0}). Indeed, P_{tj} is the *last* value that can possibly be obtained in the pneumatic circuit and therefore takes into account all the pressure losses. Hence, the total pressure ratio gives the jet Mach number M_j where γ is the heat capacity ratio of air equal to $\gamma = 1.4$:

$$M_j = \left(\frac{2}{\gamma - 1} \left(\left(\frac{P_j}{P_{tj}} \right)^{-\frac{\gamma-1}{\gamma}} - 1 \right) \right)^{\frac{1}{2}} \tag{3.3}$$

With the jet Mach number and the measure of the jet total temperature T_{tj} we can deduce the jet temperature T_j:

$$T_j = T_{tj} \left(1 + \frac{\gamma - 1}{2} M_j^2 \right)^{-1} \tag{3.4}$$

The jet density ρ_j can be therefore deduced from the following equation:

$$\rho_j = \frac{P_{atm}}{r T_j} \tag{3.5}$$

The jet speed of sound a_j is given by the following formula where r is the specific gas constant equal to $287\,\mathrm{J\,kg^{-1}\,K^{-1}}$:

$$a_j = \sqrt{\gamma r T_j} \tag{3.6}$$

And finally, the jet velocity U_j is given by:

$$U_j = a_j M_j \tag{3.7}$$

Incompressible theory

The stagnation pressure relation for an incompressible flow $P_{tj} = \frac{1}{2}\rho_{air} U_{j,inc}^2 + P_{atm}$ gives directly the jet velocity with the following formula:

$$U_{j,inc} = \sqrt{\frac{2(P_{tj} - P_{atm})}{\rho_{air}}} \tag{3.8}$$

ρ_{air} can be computed with the relation $\rho_{air} = \dfrac{P_{atm}}{r T_{tj}}$.

Remark The velocity inside the plenum chamber can be calculated with $U_p = \dfrac{Q_{fm}}{\rho_p l_p \phi_p}$ where Q_{fm} is the flow rate applied by the flowmeter, l_p is the length of the chamber, ϕ_p its diameter and ρ_p the air density computed following the compressible theory. This plenum velocity remains under $2\,\mathrm{m/s}$ and will be considered as negligible in the following.

3.3.2 Characterisation of the blowing jets

The study is carried out with a traverse system that allows the total pressure probe displacements down to 0.1 mm in the three spatial directions x^*, y^* and z^*. For the blades blowing from the upper surface, the origin is defined as the intersection between the tangential plane to the pressure side (x^* direction) and the tangential plane at the trailing-edge (z^* direction) as shown in figure 3.11. The y^* origin is set at the blade tip. For the analysis of the jet diffusion, the jet axis in the drilling direction is defined and named x_j^*.

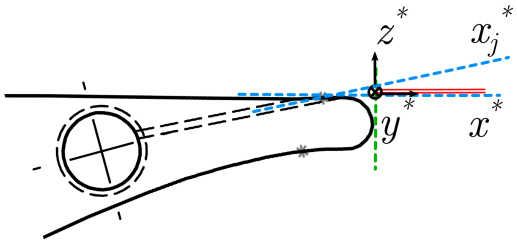

Figure 3.11: Coordinate system (x^*, x_j^*, y^*, z^*) definition

Analysis of the stagnation pressure for one single jet

Results presented in this section correspond to a single jet assuming it is representative of the 72 jets along the blade span $\langle U_j \rangle$ (this definition will be apparent later). Figure 3.12a shows the total pressure P_t as a function of the applied flow rate Q_{fm}. Three curves are shown: the total pressure measured at the exit of one jet P_{tj}, and the total pressure in the plenum chamber P_{t0} measured at the chamber entry and at the blade tip. Both measures of P_{t0} are very close to each other, specially for low flow rates. This indicates that the flow has been indeed stopped in the plenum chamber and that the velocity inside the chamber is weak. Compressible theory imposes that for a ratio $\frac{P_{atm}}{P_{t0}} = 0.528$ it exists sonic throats somewhere in the jet path. This ratio corresponds to a stagnation pressure $P_{t0} = 1.9 \times 10^5$ Pa that is surpassed beyond a flow rate of about 250 l/min implying that there is a sonic throat ($M = 1$) somewhere inside the jet drillings or at the jet exhaust. Pressure in the plenum chamber is not sufficient to obtain the establishment of a supersonic flow downstream of these sonic throats but, beyond this stagnation pressure P_{t0}, the flow rate in the jet holes is fixed. This means that the flow rate will not depend on the external pressure i.e. on the state of the flow (attached or detached) at the jet exit. Pressure losses between the chamber and the exit reach values up to 2×10^5 Pa for the highest flow rate.

Jet velocity U_j calculated by different means is plotted in figure 3.12b as a function of the plenum chamber pressure. Jet velocity is computed thanks to the total pressure at the jet exit P_{tj} with compressible and incompressible theories. Both methods show close results for the lower pressures in the plenum chamber under 2×10^5 Pa. Beyond this pressure, the curves start to diverge, the incompressible theory velocities being greater than the compressible one. The obtained maximal jet velocities are of about 300 m/s using compressible theory.

U_j computations:

In the following, all the jet velocities U_j are computed using the **total pressure at the jet exit** P_{tj}. Calculations are carried out with the **compressible theory** that is assumed to be more accurate for the high velocities and plenum pressures involved in this study.

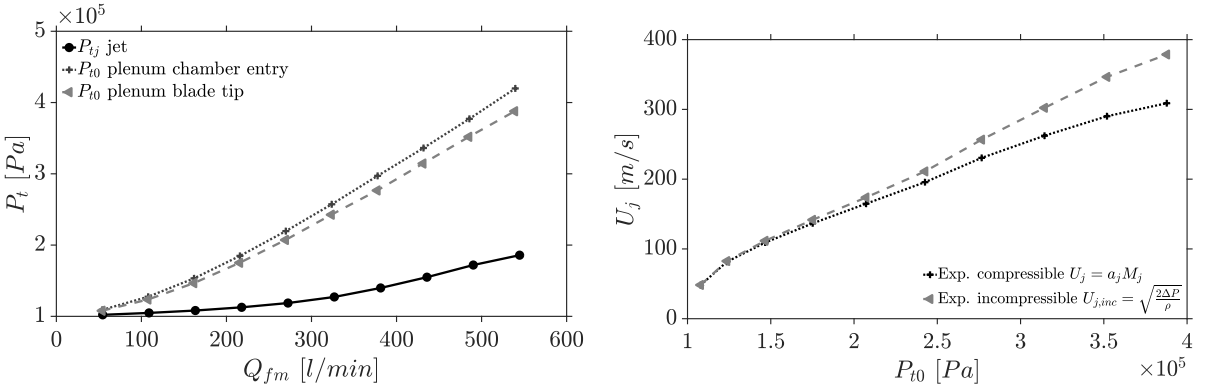

(a) Stagnation pressure P_t

(b) Jet velocity U_j

Figure 3.12: Stagnation pressure P_t as a function of Q_{fm} and jet velocity U_j as a function of the plenum pressure P_{t0} - jet matching $\langle U_j \rangle$

Momentum coefficient definition - translational configuration

Momentum coefficient C_μ is representative of the actuation strength and is defined as the ratio of the momentum supplied by the actuation to the momentum of the free stream. In the case of the translational configuration discussed in this chapter, the blade is subjected to an incoming flow of velocity U_∞ and the momentum coefficient is defined as:

$$C_\mu = \frac{\rho_j S_j U_j^2}{\frac{1}{2}\rho U_\infty^2 S} \tag{3.9}$$

where S is the surface of the blade emerging from the streamlined fairing and ρ the density of the incoming flow. Therefore, a given flow rate is directly associated to a total pressure in the plenum chamber P_{t0} that itself implies a fixed jet total pressure P_{tj} and a jet velocity U_j:

$$\left.\begin{matrix} Q_{fm} \\ P_{t0} \end{matrix}\right\} \Rightarrow \left.\begin{matrix} P_{tj} \\ U_j \end{matrix}\right\} \Rightarrow C_\mu \tag{3.10}$$

Hence, with the measurement of the jet exit velocity in quiescent air conditions for an average jet, the momentum coefficient C_μ can be traced back from the applied flow rate or from the measurement of the total pressure in the plenum chamber. Figure 3.13 shows the momentum coefficient as a function of the jet total pressure for three incoming flow velocities. Coefficient C_μ reaches 0.20 for a wind speed of 20 m/s and 0.10 for 30 m/s.

With respect to the 2D-model made by LHEEA and presented in paragraph 2.4.5 (p.65), the momentum coefficients C_μ are of the same order of magnitude but a bit more important. Maximal C_μ in the present case for 20 m/s is equal to about 0.20 and Jaunet and Braud [2018] obtained a maximal C_μ of 0.14. This result seems coherent because, in proportion, the present blades holes are slightly closer than in LHEEA model in order to reinforce the circulation control with respect to the 2D case. This jet surface increase leads to higher flow rates and to higher momentum coefficients.

Precisions regarding the momentum coefficient C_μ

In the following of this chapter, the different figures will be plotted with the momentum coefficient **defined in the translational configuration** and for an incoming flow velocity of 20 m/s that is the flow velocity used in the ensuing wind-tunnel tests. In the next chapter (chapter 4), devoted to the rotor testings, the C_μ evaluation will be discussed again.

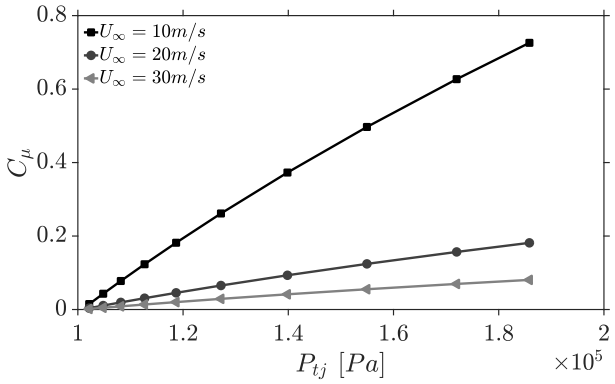

Figure 3.13: Momentum coefficient C_μ for three incoming flow velocities (translational configuration)

Blowing homogeneity along the blade span

The objective of this characterisation is to determine if the jet velocity distribution along the blade is homogeneous or if some blade areas are favoured by the blowing. Figure 3.14 plots the jet velocity U_{x^*} distribution along the blade span for different abscissas x^* and a momentum coefficient of $C_\mu = 0.022$. Vertical black lines represent the theoretical jet positions and vertical red lines show the intersections between the different sections of the blade. The blade span y^* is normalised by the wind turbine radius R. At first sight, the blowing seems quite homogeneous except near some areas at the intersection of the blade parts and near the blade tip. For the abscissa $x^* = -2$ mm (negative sign means that the measurement point is located over the airfoil and near the jet exit, the origin being the trailing-edge), the jet velocity reaches a maximum velocity of about 200 m/s. For the farther abscissas in the jet diffusion area, the blade span homogeneity is also proven as can be seen in figure 3.15 that shows a zoomed view for a smaller range of $\frac{y^*}{R}$ than figure 3.14. The structure of the jets can be resolved at least up to $x^* = 8$ mm and the jet shapes are not visible at 18 mm beyond the TE of the airfoil. For this C_μ, the jet diffuses significantly in the x^* direction and only 10 m/s remain at 18 mm beyond the airfoil for this considered C_μ.

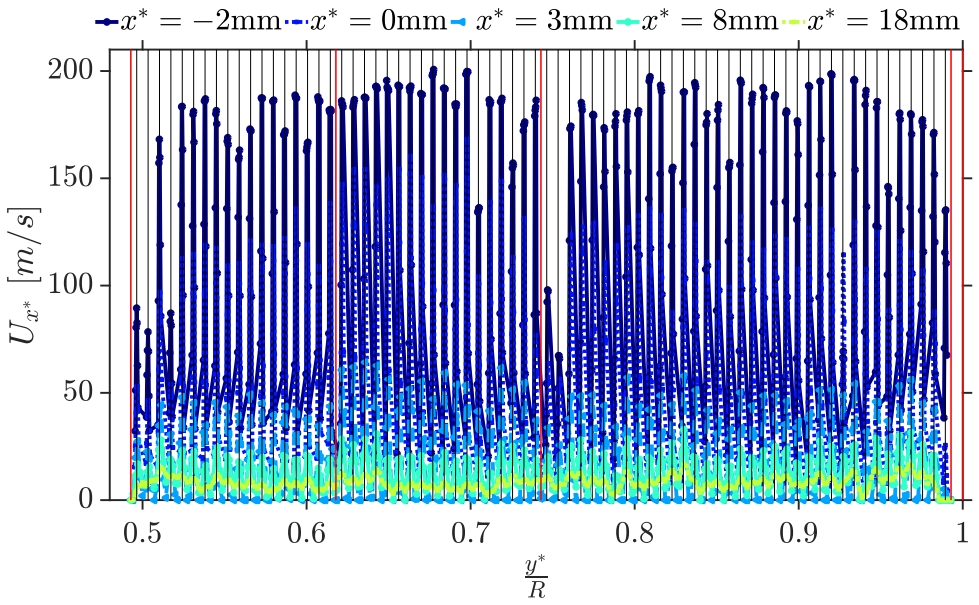

Figure 3.14: Jet velocity U_{x^*} distribution along the blade span as a function of x^* (large blade span) - $C_\mu = 0.022$

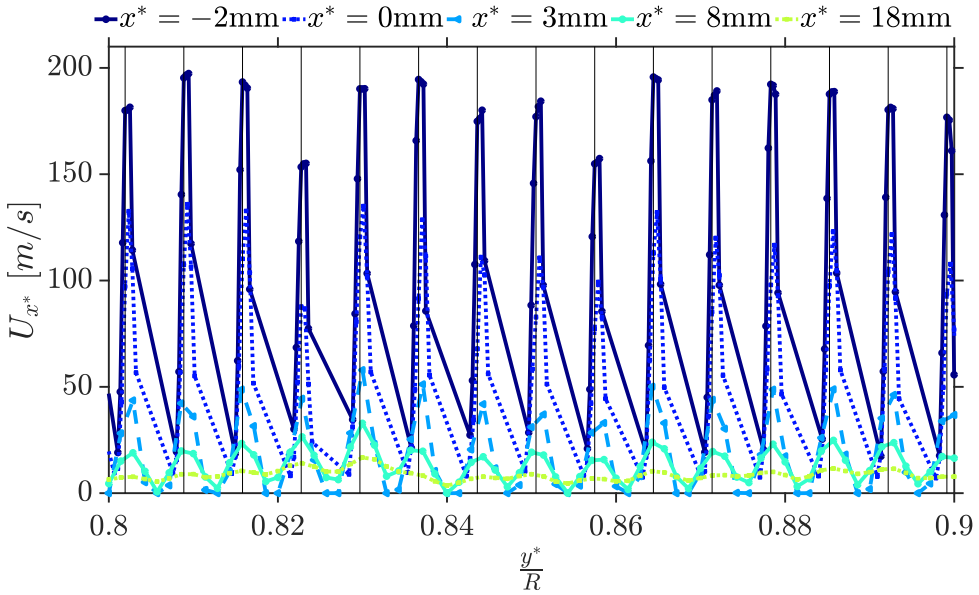

Figure 3.15: Jet velocity U_{x^*} distribution along the blade span as a function of x^* (zoomed blade span) - $C_\mu = 0.022$

The data plotted in figure 3.14 can be processed and a single jet velocity for each of the 72 jets can be extracted by detecting the maximum velocity peaks. These 72 jet velocities can be spatially averaged giving the variable called $\langle U_j \rangle$. Table 3.2 shows the spatial average $\langle U_j \rangle$ for each studied abscissa.

x^* [mm]	$\langle U_j \rangle$ [m/s]
-2	174.0
0	118.2
3	45.2
8	21.6
18	10.3

Table 3.2: Spatially averaged jet velocity $\langle U_j \rangle$ as a function of the abscissa x^* - $C_\mu = 0.022$

Figures 3.16a and 3.16b show respectively jet velocity deviation to the averaged value $\langle U_j \rangle$ along the blade span and an histogram distribution of the jet velocity values. Except from the jets with a very low exit velocity, most of the jet velocities are in the vicinity of the averaged velocity $\langle U_j \rangle$ ±20%. The histogram allows to quantify that 72% of the jets are over this average and that the large majority of the jets have an exhaust velocity greater than 160 m/s for a C_μ of 0.022.

The jet velocity distribution along the blade span for three different C_μ at a fixed abscissa $x^* = -2$ mm is shown in figure 3.17. For each C_μ the solid lines highlight the spatial jet velocity average. The blade span homogeneity seems to be confirmed at lower momentum coefficients as well. The same low speed areas at the blade parts intersections are visible for $C_\mu = 0.008$ and $C_\mu = 0.014$. In these cases $\langle U_j \rangle$ is equal to 105 m/s and 138 m/s respectively. Jet velocity distribution along the blade span is independent of the momentum coefficient i.e. the applied pressure in the plenum chamber.

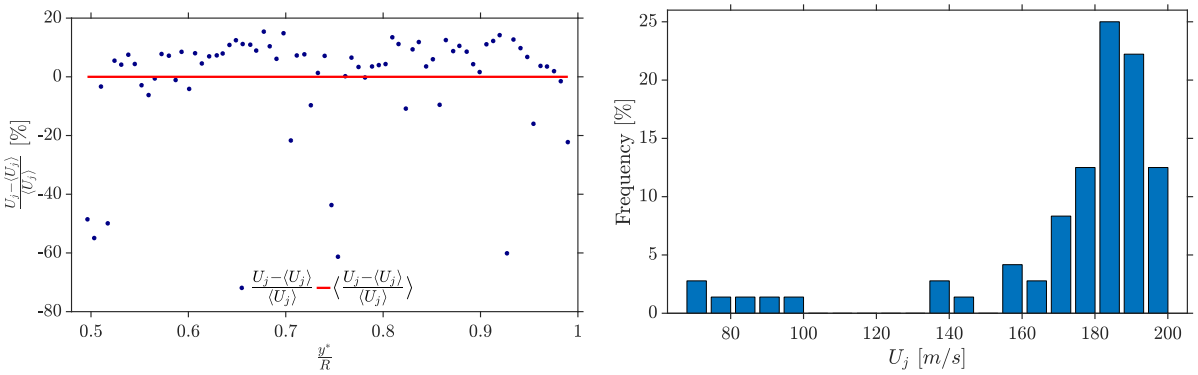

(a) Deviation to average

(b) Histogram of the jet velocities

Figure 3.16: Deviation of the jet velocities to the spanwise average and their histogram - $C_\mu = 0.022$

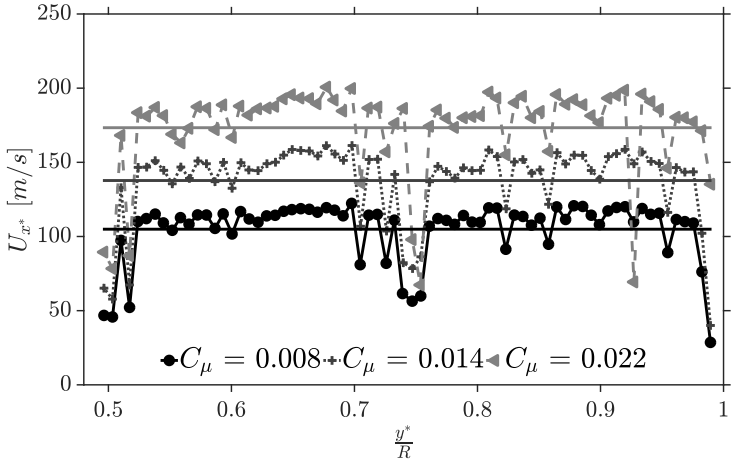

Figure 3.17: Jet velocity distribution along the blade span for three momentum coefficients C_μ - fixed abscissa $x^* = -2\,\text{mm}$

Jet diffusion along its axis

The jet diffusion is studied by moving the pressure probe from the jet hole and in the jet direction x_j^*. The origin $x^* = 0$ corresponds to the trailing-edge of the airfoil. Figure 3.18 shows the jet diffusion for several C_μ for a blowing jet which behaviour corresponds to the blade span average $\langle U_j \rangle$. One can observe a rapid diffusion of the jet as the higher velocities do not last long in the jet axis. The maximum jet velocity obtained for this hole is close to 300 m/s for the highest C_μ. Maximum velocity abscissa is the same for all the tested C_μ (or plenum pressures) and equal to $-2\,\text{mm}$ for this jet. Further than this abscissa, the jet velocity drops down to about 10 m/s to 50 m/s at 30 mm beyond the trailing-edge. One can remark that the higher the C_μ, the greater the maximum jet velocity and the greater the overall jet velocity as well. Further than 300 mm the remaining jet velocity is very low and tends to 0 m/s.

Figure 3.19 shows the jet diffusion for three different jets at the same C_μ equal to 0.20: one hole has a maximum jet velocity equal to the spatial average along the blade $\langle U_j \rangle$, another one a velocity 10% above this average, and another one 10% below. Jet in the spatial average and jet 10% below show an analog diffusion and topology. The jet over the average $\langle U_j \rangle$ shows a clear higher velocity maximum that almost reaches 400 m/s. These results suggest that some differences between the holes remain. They are probably due to the machining of the holes and, as a result, the jet direction x_j^* may not be perfectly homogeneous for all the jets. As the

measurements are carried out with a single probe orientation, the measure can be affected by this possible hole differences.

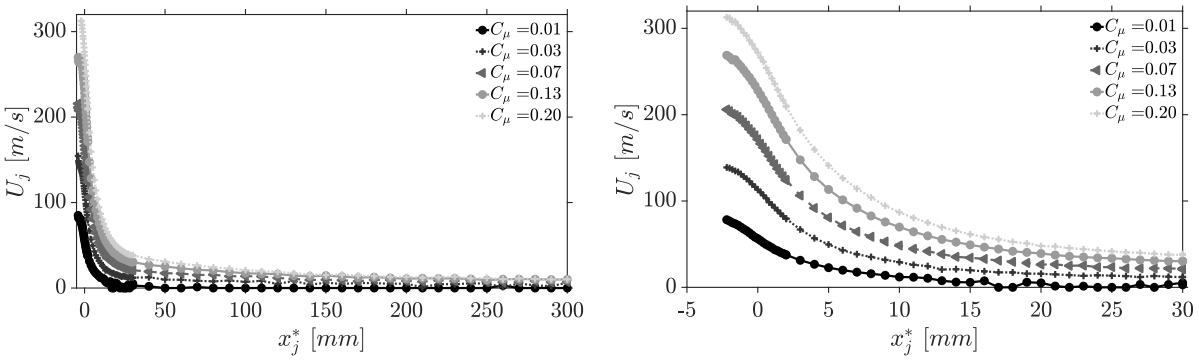

(a) Large plot (b) Zoom

Figure 3.18: Jet diffusion in the jet direction x_j^* for several momentum coefficients C_μ - hole $\langle U_j \rangle$

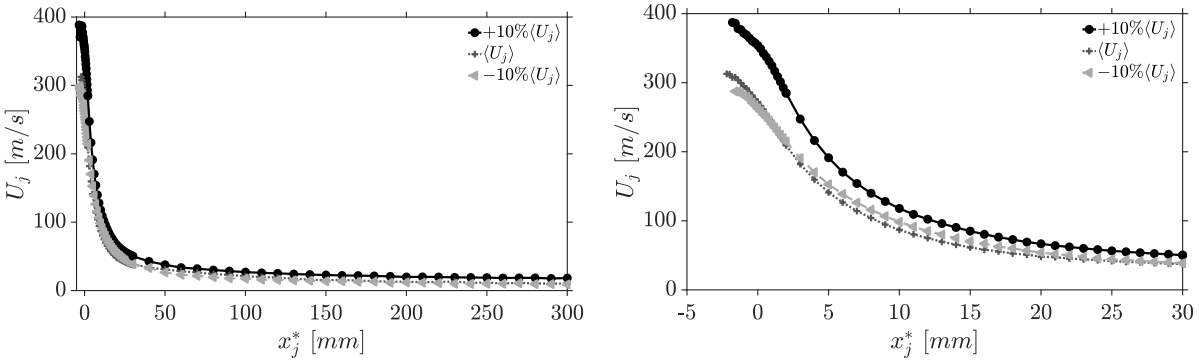

(a) Large plot (b) Zoom

Figure 3.19: Jet diffusion in the jet direction x_j^* for three different holes - $C_\mu = 0.20$

3.4 Flow control results on the blade

This section presents the flow control results obtained with the blade mounted in the translational configuration and in in-flow conditions. As explained above, load determination relies on different measurements: balance measurements provide global lift and drag forces (F_L and F_D respectively). As the blade is mounted vertically, the moment induced by the lift force is the roll moment M_R, defined at the blade root. Normalised load coefficients in this section are defined as:

– Lift coefficient C_L:

$$C_L = \frac{F_L}{\frac{1}{2}\rho U_\infty^2 S} \tag{3.11}$$

– Drag coefficient C_D:

$$C_D = \frac{F_D}{\frac{1}{2}\rho U_\infty^2 S} \tag{3.12}$$

– Roll coefficient C_R:

$$C_R = \frac{M_R}{\frac{1}{2}\rho U_\infty^2 Sc} \tag{3.13}$$

where ρ is the air density, U_∞ the incoming flow velocity, S the surface of the blade emerging from the streamlined fairing and c the blade chord.

Strain gages give the flapwise bending moment at the blade root that is named M_{fbm} in the following. Roll coefficient can be therefore calculated via the platform balance (named $C_{R,bal}$) or via the bending moment measured (named $C_{R,fbm}$). Pressure measurements allow to obtain the pressure distribution along the blade surface and pressure coefficient is defined as: $C_p = \frac{P-P_\infty}{\frac{1}{2}\rho U_\infty^2}$ where P is the pressure measured over the blade and P_∞ the incoming flow static pressure.

Airfoil-related coordinate system is defined with x in the flow direction, y in the vertical direction, and z in the transverse direction as shown in figure 3.9 on page 84. Mean and turbulent components of velocities U and V are defined as: $U(x,z,t) = \overline{U}(x,z) + u'(x,z,t)$ and $V(x,z,t) = \overline{V}(x,z) + v'(x,z,t)$. PIV allows the measurement of time-averaged velocity fields around the blade and of turbulent kinetic energy k defined as $k = \frac{u'^2+v'^2}{2U_\infty^2}$.

3.4.1 Baseline comparisons

First of all, baseline curves are compared with the 2D models studied previously. Figure 3.20 compares lift and drag coefficients (C_L and C_D) for three models of the same NACA65$_4$-421-CC airfoil. All the curves are obtained at a Reynolds number of 200 000 and with the natural turbulence intensity of the wind-tunnel equal to 0.5%. In the legend, **"Blade"** refers to the present blade in a translational configuration, **"2D LHEEA"** refers to baseline curves obtained with the 2D-model devoted to fluidic lift control carried out by LHEEA laboratory. Finally, **"2D PRISME"** refers to the 2D-model devoted to plasma flow control studied in chapter 2. Both 2D-models have a chord equal to 0.3 m. These two models have a very similar C_L curve with a slightly different stall due to the different surface roughness of the models. The linear part of the lift coefficient curve of the present blade in a translational configuration shows clearly a smaller slope than the 2D-models. All drag coefficient C_D curves show a very similar trend up to $\alpha = 15°$. Beyond this angle of attack, the translational blade seems to have a lower drag and its behaviour at stall diverges from the 2D-models. These differences in lift and drag are due to the chosen experimental set-up, where the blade has a free tip implying that the flow is three-dimensional over the blade creating a lift slope decrease and an induced drag. Platform balance measures the integrated loads along the whole blade but the spanwise distribution of these loads remains unknown.

As explained above, the blade in a translational configuration is tested within the natural turbulence of the wind-tunnel T_u equal to 0.5% but also downstream of a 4.3% turbulence grid. Figure 3.21 shows lift and drag coefficients (C_L and C_D) for the **present blade**, different Reynolds numbers and turbulence intensities. For a Re of 130 000 ($U_\infty = 20$ m/s) and a T_u of 0.5% the part of the lift curve that is meant to be linear shows a deviation towards lower C_L. This behaviour gives evidence of laminarity effects at low Reynolds numbers. Indeed, the boundary layer developing along the upper-side of the blade detaches generating a recirculation zone that induces lower lift forces and slightly greater drag forces than regular baseline curves. This phenomenon happens in a range of angles of attack (between $\alpha = 0°$ and $\alpha = 10°$) where the flow is supposed to be attached to the blade but is indeed separated. Laminar detachment can be suppressed in two ways: with the implementation of the 4.3% turbulence grid at a $Re = 130\,000$, or with the increase of Re without the grid implementation[4]. Both curves with enhanced turbulence are similar and show a linear lift part between $\alpha = -5°$ and $\alpha = 10°$.

[4]It can also be suppressed with the implementation of turbulators in the vicinity of the leading-edge to trigger the boundary layer. This solution was discarded in order to be the less intrusive as possible on the blade and to be able to perform testings over a large range of α and Re

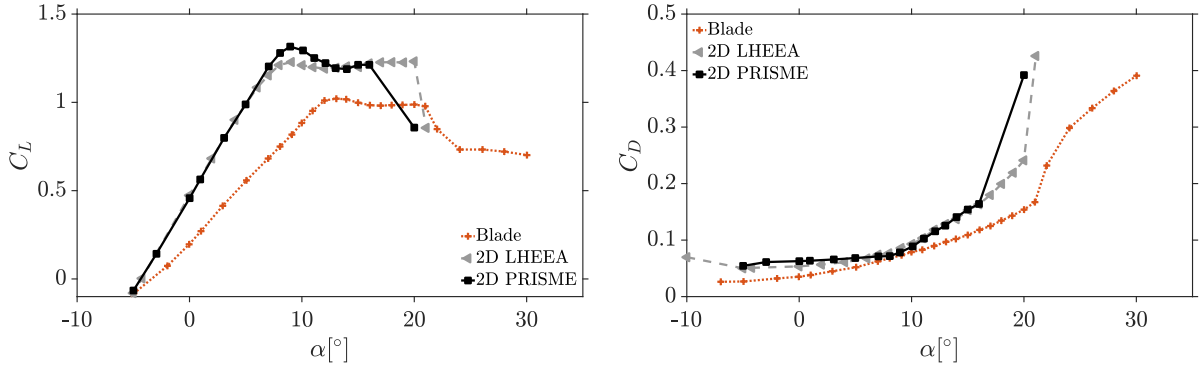

(a) Lift coefficient C_L (b) Drag coefficient C_D

Figure 3.20: Lift and drag coefficients (C_L and C_D) as a function of the angle of attack α for the same airfoil but different models - $Re = 200\,000$, $T_u = 0.5\%$ and without actuation

However, a small shift exists between these two curves. Indeed, augmenting the turbulence intensity T_u at constant Re or augmenting Re at constant T_u does not exactly have the same effects. It seems that turbulence is not completely enhanced at $Re = 200\,000$ with $T_u = 0.5\%$ and some low-Reynolds effects might still exist. Drag coefficient does not seem to be very affected with the Re increase nor the turbulence intensity, except after 20°, when the blade is stalled.

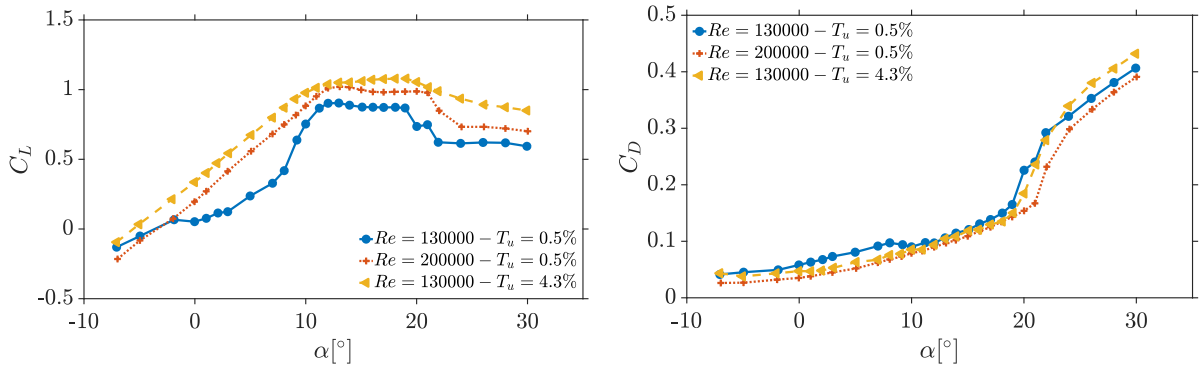

(a) Lift coefficient C_L (b) Drag coefficient C_D

Figure 3.21: Lift and drag coefficients (C_L and C_D) as a function of the angle of attack α for different Reynolds numbers Re and turbulence intensities T_u - without actuation - **translational cfg. blades**

Influence of turbulence intensity is also evidenced by the pressure distribution around the blade as shown in figure 3.22. The level of C_p along the suction side of the blade for $Re = 130\,000$ and $T_u = 0.5\%$ is at least two times higher compared to the case at same Re but $T_u = 4.3\%$. This implies that the area between the C_p curve (and so the C_L) is considerably greater when turbulence is enhanced, confirming the C_L evolution obtained with the platform balance. Configuration with enhanced turbulence matches perfectly the 2D-model C_p distribution, better than the configuration with natural turbulence and $Re = 200\,000$, which pressure along the upper side remains slightly over the 2D-model. As mentioned above, this behaviour suggests that the grid implementation completely suppresses laminarity effects at Re equal to 130 000. However, these effects are not totally suppressed at $Re = 200\,000$ and with natural turbulence.

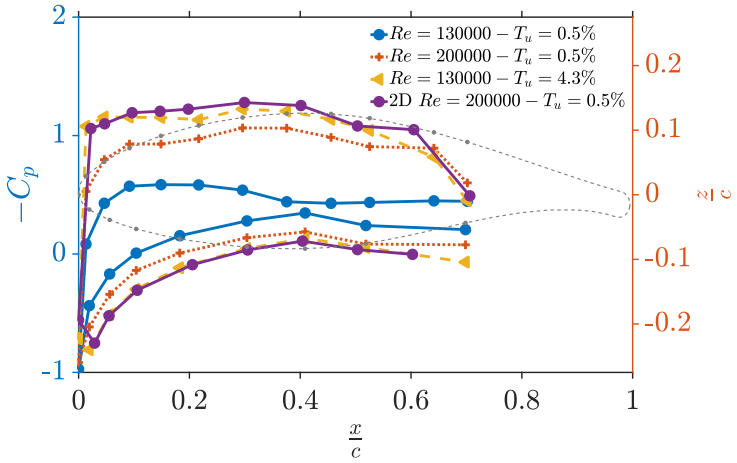

Figure 3.22: Turbulence intensity influence T_u on the pressure coefficient C_p for different Reynolds numbers Re - $\alpha = 5°$ and $r = 0.63R$ - without actuation - **translational cfg. blades**

3.4.2 Flow control results - enhanced turbulence

This section introduces the results of the flow control application with the implementation of a 4.3% turbulence grid in the test-section.

Loads & pressure distribution

"No-wind" cases

Load measurements are carried out **with** and **without** wind in the wind-tunnel. The *no-wind* configuration corresponds to the case where the fluidic jets are powered on but there is no flow in the wind-tunnel. *No-wind* load values can be subtracted to the results obtained *with wind* in order to get rid of the effect on loads due to the jet thrust. These effects are mainly noticeable on the drag force. They are however present on the lift but only for the higher angles of attack. As this subtraction adds uncertainties to the lift values in the linear part of the lift curve, it has not been performed in the results presented in the following.

Lift coefficient C_L and flapwise bending moment M_{fbm} are shown in figure 3.23 for different momentum coefficients. M_{fbm} is related to the C_L and translates the same information but with a sensor directly incorporated at the blade root (instead of the use of the external platform balance). The effect of the actuation is mainly noticeable for the higher angles of attack, specially beyond $\alpha = 10°$ highlighting that the actuation mainly delays stall. Actuation is strong in the area where the C_L stagnates i.e. beyond the linear part, when the boundary layer (BL) starts to separate and the separation point rises from the TE to the LE. This tendency is also noticeable with the M_{fbm} evolution with the angle of attack, which curves show exactly the same tendencies. In the linear C_L range, actuation has a stronger effect when the angle of attack increases, and the higher the C_μ, the higher the effect of the actuation. The influence of C_μ is mostly important for the delay of the angle α_{sep}, corresponding to the start of the BL separation from the suction side. This angle α_{sep} is equal to 10° for the baseline case and to about 18° for $C_\mu = 0.20$. This kind of behaviour is comparable to the one pointed out in Greenblatt and Wygnanski [2000] for separation control devices such as leading-edge slots and blowing devices at the leading-edge.

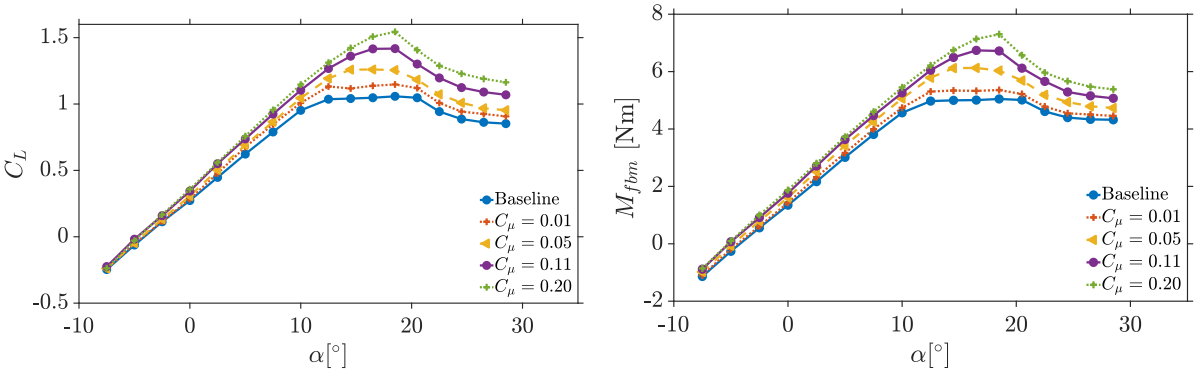

(a) Lift coefficient C_L

(b) Flapwise bending moment M_{fbm}

Figure 3.23: Lift coefficient and flapwise bending moment (C_L and M_{fbm}) as a function of the angle of attack α and for different momentum coefficients C_μ - $Re = 130\,000$ and $T_u = 4.3\%$

Remark on drag coefficient C_D

Results concerning drag coefficient are not shown as the C_D variation with the actuation is in the order of magnitude of the platform balance uncertainty after the *no-wind* subtraction. This suggests, however, that the actuation has a little effect on the drag force. Details on balance uncertainties are shown in appendix B.

Actuation effectiveness can also be quantified in terms of lift coefficient variation ΔC_L defined as the difference between the lift coefficient with and without actuation. The same variable ΔM_{fbm} can be defined with the flapwise bending moment measured with the strain gages. These variables ΔC_L and ΔM_{fbm} are shown in figure 3.24. In the linear part of the lift curve, between $\alpha = -5°$ and $\alpha = 10°$, the lift coefficient increase gets higher with the angle of attack and reaches $+0.2$ for the highest momentum coefficient and $\alpha = 10°$. When the blade shows angles of attack near stall, ΔC_L increases, reaching $+0.35$ for $\alpha = 14.5°$ and $+0.5$ for $\alpha = 18.5°$. In the same way, regarding ΔM_{fbm}, the increase in the linear part of the lift curve is of 0.3 to 1 N m whereas the maximum gain equals 2.2 N m. It can be concluded that, actuation with enhanced turbulence performs a low circulation control in the linear part of the lift curve and a stronger separation control in the lift stagnation range. Hence, as pointed out by Jaunet and Braud [2018], the actuation gains depend on the actuation intensity C_μ but also on the state of the flow around the airfoil i.e. the angle of attack α.

Roll coefficient C_R may be determined thanks to the platform balance $C_{R,bal}$ and also with the flapwise bending moment at the blade root $C_{R,fbm}$. Figure 3.25 compares both roll coefficients obtained with these two methods. Both C_R are alike in the linear part of the lift curve and the firsts angles of attack where the separation moves forward along the chord (from 10 to 18°). Beyond $\alpha = 18°$ both measurements slightly diverge showing of the difficulty to capture with precision aerodynamical efforts near stall.

Pressure coefficient C_p distribution for two angles of attack ($\alpha = 10°$ and $\alpha = 18°$) is shown in figure 3.26. For both angles α, actuation decreases the pressure level on the suction side of the blade and keeps it unchanged in the pressure side, leading to an increase in C_L. In the case of $\alpha = 10°$ the saturation effect of the actuation is visible as the two highest C_μ show a similar pressure distribution. The C_p decrease along the suction side is more important for $\alpha = 18°$ than for $\alpha = 10°$ confirming that separation control is stronger than the intended circulation control.

Another way to highlight the pressure distribution modification with the actuation is to plot a pressure coefficient variation ΔC_p along the chord as shown in figure 3.27 (same angles of attack and configurations as in figure 3.26). With this representation, it becomes clear that the

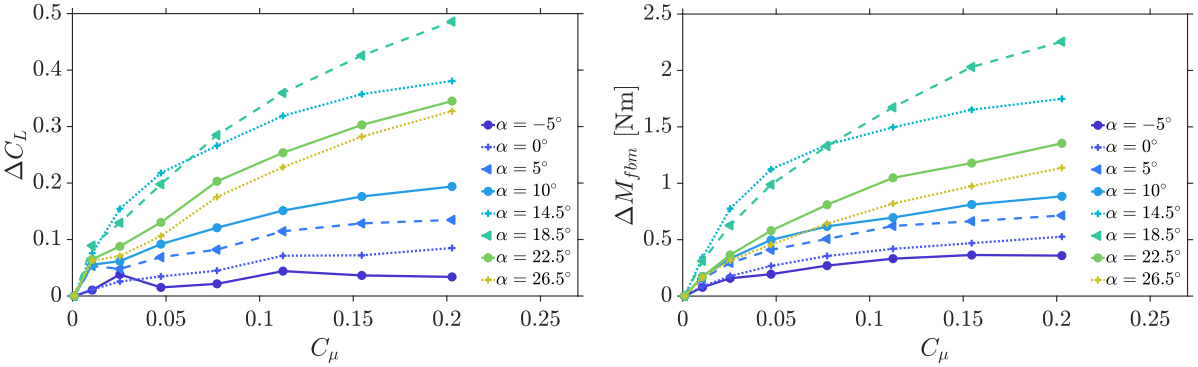

(a) Lift coefficient variation ΔC_L

(b) Flapwise bending moment variation ΔM_{fbm}

Figure 3.24: Lift coefficient variation ΔC_L and flapwise bending moment variation ΔM_{fbm} as a function of the momentum coefficient C_μ and different angles of attack α - $Re = 130\,000$ and $T_u = 4.3\%$

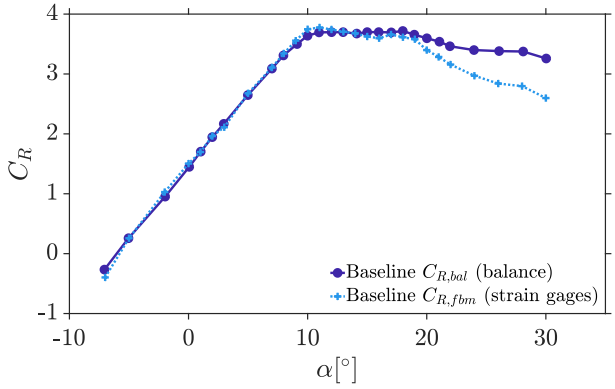

Figure 3.25: Comparison of the roll coefficient obtained via two different methods without actuation ($C_{R,bal}$ and $C_{R,fbm}$) - $Re = 130\,000$ and $T_u = 4.3\%$

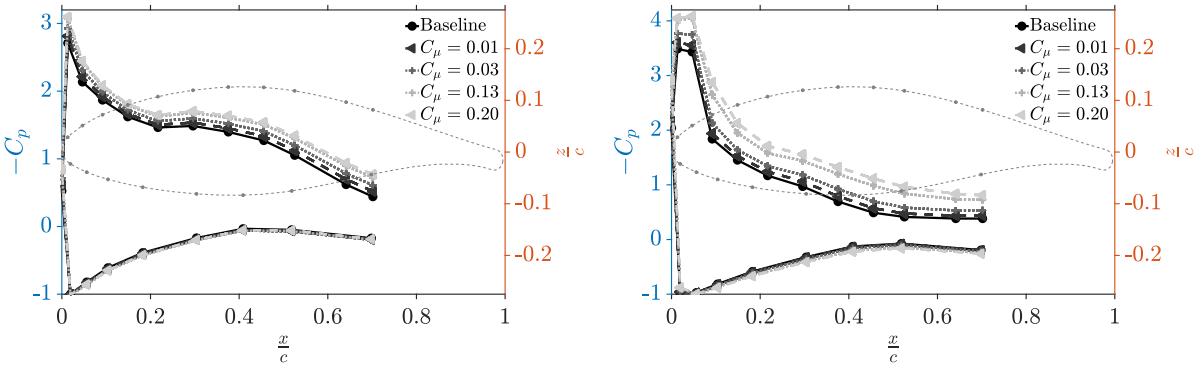

(a) $\alpha = 10°$

(b) $\alpha = 18°$

Figure 3.26: Pressure coefficient C_p as a function of the momentum coefficient C_μ for $\alpha = 10°$ and $\alpha = 18°$ - $Re = 130\,000$, $T_u = 4.3\%$ and $r = 0.63R$

actuation does not change the pressure on the lower side of the blade or weakly increases it (ΔC_p about +0.01 for $\alpha = 18°$). Over the suction side of the blade, ΔC_p is not distributed the same way for $\alpha = 10°$ and for $\alpha = 18°$. In the first case, the C_p loss is specially important at the

leading-edge with a ΔC_p equal to -0.4, then it decreases to -0.2 at 20% of the chord and then increases again up to the last pressure tap available at 70%c. The C_μ effect on the C_p variation is particularly visible: the higher the momentum coefficient, the higher the pressure losses in the suction side. In the second case, at $\alpha = 18°$, ΔC_p reaches its maximal value -1 at $\frac{x}{c} = 0.1$ and remains between -0.4 and -0.6 along most of the blade chord.

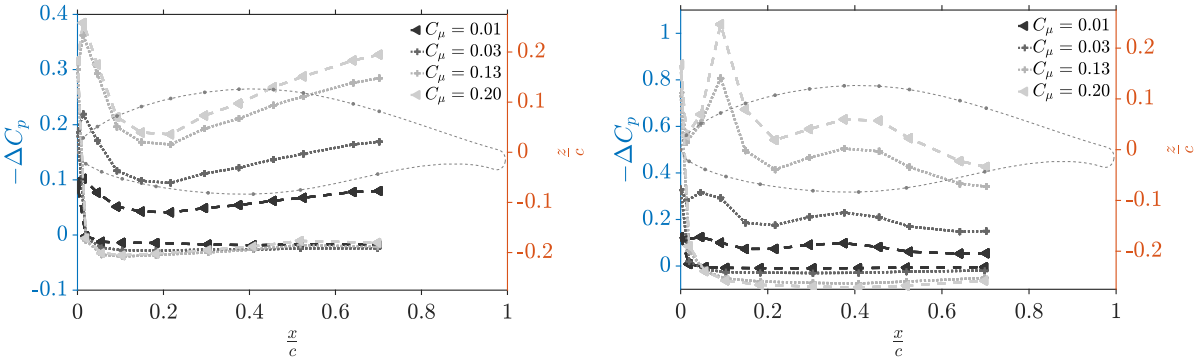

(a) $\alpha = 10°$ (b) $\alpha = 18°$

Figure 3.27: Pressure coefficient variation ΔC_p as a function of the momentum coefficient C_μ for $\alpha = 10°$ and $\alpha = 18°$ - $Re = 130\,000$, $T_u = 4.3\%$ and $r = 0.63R$

Pressure coefficient integration

Pressure distribution can be integrated to obtain normal and tangential force coefficients C_n and C_t respectively. Lift and drag coefficients (C_l and C_d respectively) can be then computed with a projection of C_n and C_t on the wind-related coordinate system. Figure 3.28 defines load coefficients in both chord and wind-related coordinate systems.

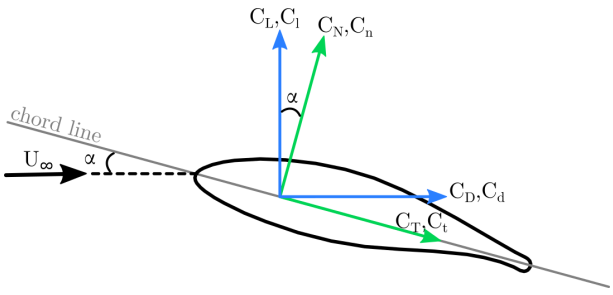

Figure 3.28: Load coefficients definition

Remark on nomenclature

Subscripts in small letters used in C_n, C_t, C_l and C_d are kept for load coefficients coming from pressure integration and are therefore **local variables at a given blade span**. Subscripts in capital letters in C_N, C_T, C_L and C_D are devoted to **spanwise integrated** force coefficients coming from the aerodynamic balance.

To perform this integration, a fictitious pressure tap is added at the trailing-edge ($\frac{x}{c} = 1$ and $\frac{z}{c} = 0$) and with a C_p value equal to the average of C_p of the two extremal pressure taps at $\frac{x}{c} \approx 0.7$ on both pressure and suction sides. C_n and C_t are computed according to equations 3.14 and 3.15, where N_{taps} is the number of pressure taps, x_{tap} the distance along the chord line

from the leading-edge to i$^{\text{th}}$ pressure tap and z_{tap} the distance along axis orthogonal to chord from the chord line to i$^{\text{th}}$ pressure tap.

$$C_n = \sum_{i=1}^{N_{taps}+1} \frac{C_{p,i+1} + C_{p,i}}{2} \left(\frac{x_{tap,i+1} - x_{tap,i}}{c} \right) \quad (3.14)$$

$$C_t = - \sum_{i=1}^{N_{taps}+1} \frac{C_{p,i+1} + C_{p,i}}{2} \left(\frac{z_{tap,i+1} - z_{tap,i}}{c} \right) \quad (3.15)$$

Lift and drag coefficients are then defined as:

$$C_l = C_n \cos\alpha - C_t \sin\alpha \quad (3.16)$$

$$C_d = C_t \cos\alpha + C_n \sin\alpha \quad (3.17)$$

Figure 3.29a shows both lift coefficients obtained with the platform balance and the C_p integration. Lift evolution is very similar but the linear parts of the lift curves show different slopes. This is due to the fact that the plot compares a local C_l at a given blade span with a spanwise integrated C_L that takes into account the overall lift distribution along the blade. Figure 3.29b shows the C_l evolution for three momentum coefficients. Even if the curve slopes differ, the C_l gains are comparable to the ones obtained with the balance and shown in figure 3.23a. It seems, however, that the effect of the actuation on the C_l between $\alpha = 10°$ and 20° is enhanced with the pressure integration method, and minimised in the linear part of the lift curve. Again, this calculation is only representative of a blade span. Furthermore, the pressure integration does not take into account the pressure distribution from $\frac{x}{c} = 0.7$ to the trailing-edge: the trace of the blowing jets on the C_p that is usually visible with a $-C_p$ peak at the jet location is not included in the computation.

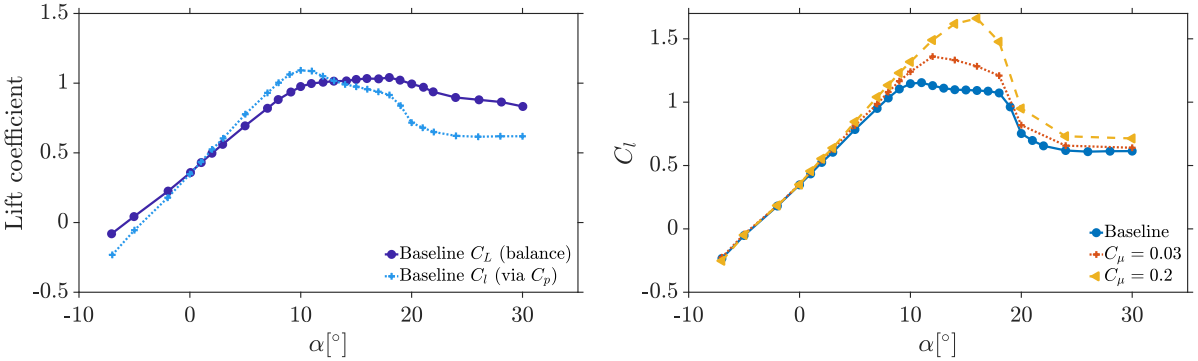

(a) Lift coefficient C_L and C_l at $r = 0.63R$ without actuation

(b) Lift coefficient C_l at $r = 0.63R$ with actuation

Figure 3.29: (a) Figure comparing both C_L and C_l at $r = 0.63R$; (b) lift coefficient C_l evolution with α for various C_μ - $Re = 130\,000$ and $T_u = 4.3\%$

Lift coefficient variations obtained via the platform balance and pressure integration (ΔC_L and ΔC_l respectively) as a function of the momentum coefficient C_μ are shown in figure 3.30. Pressure integration method underestimates the lift gain. This deviation is probably due to the fact that integration does not take into account the large trailing-edge suction peak due to the blowing. As reported in Wetzel et al. [2013] the magnitude of this peak increases substantially with the momentum coefficient C_μ. Also, as mentioned above, this integration does not take into account the load spanwise distribution. Both Wetzel et al. [2013] and Abramson [1975] performed circulation control on an elliptic airfoil with a fluidic slot near the trailing-edge. Wetzel et al. [2013] showed C_μ values up to 0.10 and Abramson [1975] up to 0.28. In both cases, the lift coefficient gain as a function of C_μ stagnated with the C_μ increase which corresponds to the same behaviour highlighted in the present study.

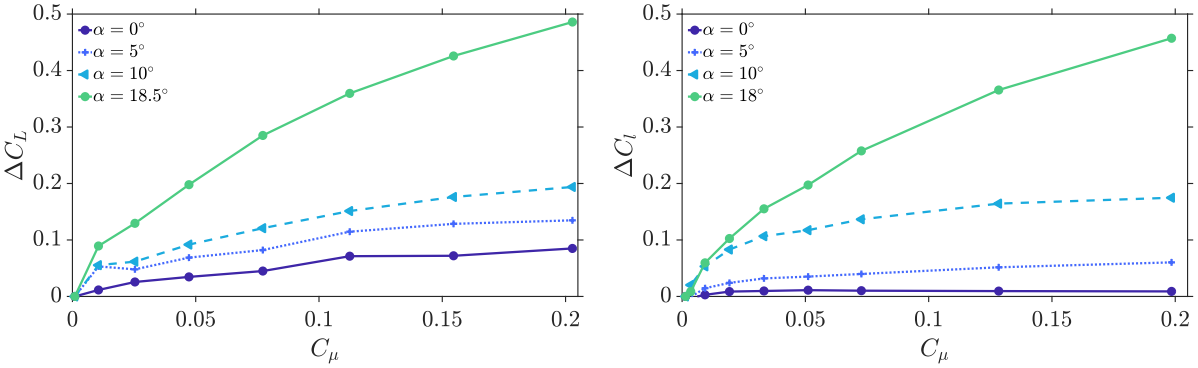

(a) Lift coefficient variation ΔC_L (via the paltform balance)

(b) Lift coefficient variation ΔC_l (via pressure integration)

Figure 3.30: Lift coefficient variation (ΔC_L and ΔC_l) as a function of the momentum coefficient C_μ and for different angles of attack α - $Re = 130\,000$ and $T_u = 4.3\%$

Velocity fields

PIV velocity fields confirm what global and local variables analysis evidence about the flow around the blade. Figure 3.31 shows time-averaged velocity fields for both baseline and a controlled case at an angle of attack of 5°. As turbulence intensity of the flow is enhanced by the grid implementation, the flow around the blade is attached at this angle of attack. A recirculation area exists in the small wake of the rounded trailing-edge as evidenced with the 2D-airfoil in the preceding chapter 2. In the mean flow, two counter-rotating vortices exist in this zone analog to the wake of a bluff body. Concerning the controlled case, there is not much difference in the flow topology around the blade. The small recirculation zone seems slightly smaller and shifted towards the pressure side indicating a potential circulation control at these low angles of attack. Figure 3.32 shows the same velocity fields for $\alpha = 18°$. In this case, the blade is partially stalled and a large recirculation area exists on the blade wake, along the suction side. By the effect of the actuation, the separation bubble is strongly reduced. Actuation also increases the downwards and upwards vertical velocities coming from the suction and pressure sides of the blade respectively. Jaunet and Braud [2018] performed, with the model introduced in paragraph 2.4.5 (p.65), a PIV cross-flow velocity field at $\frac{x}{c} = 1.03$. Their airfoil model also did a circulation control with a discrete fluidic actuation at the TE. The authors showed that the incoming flow circumvents the jets by deviating in the transverse direction on both sides of each jet. This discrete actuation generates three dimensional effects on the recirculation area beyond the TE of the airfoil. The trace of the jet is visible in the wake of the blade for both angles of attack. The jet track is, however, not visible right beyond the jet exit. Several reasons could explain this behaviour:

- PIV plane is between two jets (but close to one jet) as laser reflections are too strong over jet orifices. This means that laser sheet does not intersect the jet in its axis, but slightly alongside
- Jet velocity is one order of magnitude higher than the incoming flow velocity U_∞ meaning that PIV correlation might be biased in the high velocity areas near the jet exit
- Jets are not seeded but only the flow is, meaning that particles were quickly ejected from the jet exit area
- Laser sheet thickness is estimated to be of about 2 mm ($\approx$ 4 times the jet hole diameter) implying that PIV fields are a result of an integration over this thickness

– Blade is flush-mounted on the mast but the blade tip is free, causing blade vibrations that slightly displace the blade during the acquisitions

Futhermore, figures 3.31 and 3.32 show that the jet does not follow the model trailing-edge curvature as intended. This is due to the high ratio between the jet diameter and the trailing-edge curvature as suggested in Jaunet and Braud [2018]. Indeed, as mentioned with respect to DBD induced jets in section 2.3 (p.40), the ratio of the jet thickness to the radius of curvature of the surface is of great importance for the application of an eventual Coanda effect. On one hand, the present jets are discrete and far from a 2D-slot; and, on the other hand, they are too thick to be able to circumvent the trailing-edge. Hence, for these two reasons, a complete TE circumvention similar to Coanda effect is difficult to perform and does not happen with the present actuation approach.

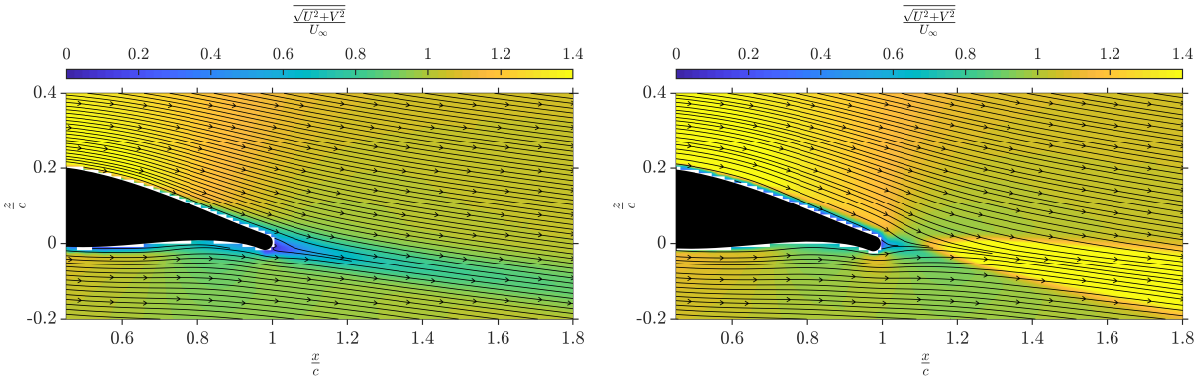

(a) Baseline (b) $C_\mu = 0.20$

Figure 3.31: Time-averaged velocity fields for the baseline case and a controlled case - $Re = 130\,000$, $\alpha = 5°$ and $T_u = 4.3\%$

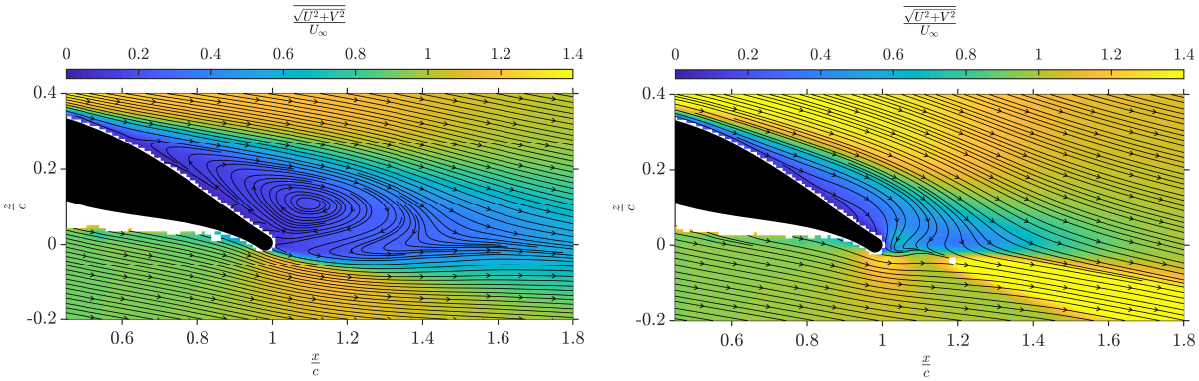

(a) Baseline (b) $C_\mu = 0.20$

Figure 3.32: Time-averaged velocity fields for the baseline case and a controlled case - $Re = 130\,000$, $\alpha = 18°$ and $T_u = 4.3\%$

Turbulent kinetic energy field is shown in figure 3.33 for $\alpha = 18°$ with and without actuation. Regarding the baseline case, turbulent kinetic energy is high in the areas of important turbulent fluctuations i.e. the shear layers between the recirculation zone and the free flow on both sides of the wake. Two shear layers are evidenced, one following the separated boundary layer along the suction side and the second starting from the trailing-edge and continuing downstream in the

blade chord direction. Both shear layers meet in the blade wake to close the recirculation area. In the controlled case, the first shear layer intensity is strongly displaced towards the model. The second layer, starting at the TE, creates, with the shear layer of the blowing jet, one unique high turbulence intensity zone.

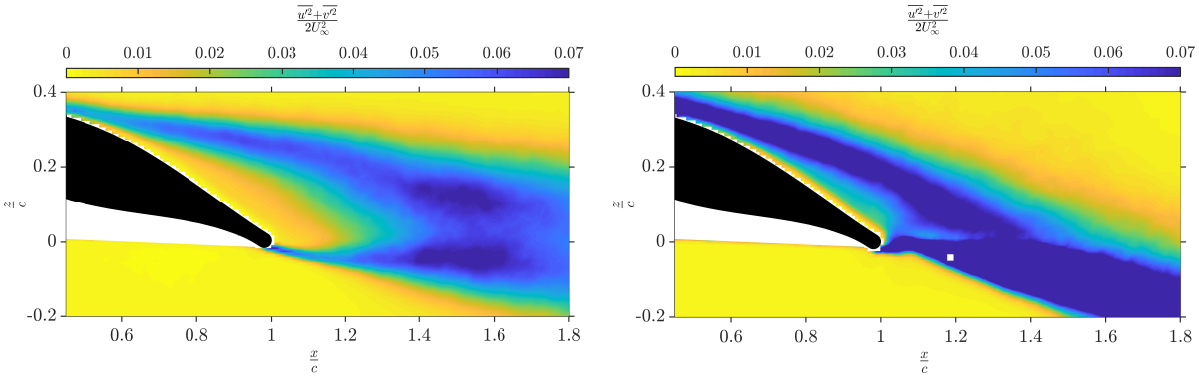

(a) Baseline

(b) $C_\mu = 0.20$

Figure 3.33: Time-averaged TKE fields for the baseline case and a controlled case - $Re = 130\,000$, $\alpha = 18°$ and $T_u = 4.3\%$

3.4.3 Limitations of the set-up

This section is devoted to the limitations of this fluidic flow control set-up. Are presented in the following the tests that were carried out but which results were not satisfactory or not as good as expected. Three cases are addressed in the following:

- Tests at a Reynolds number equal to 130 000 but without the turbulent grid i.e. with the natural wind-tunnel turbulence of about 0.5%
- Tests at a Reynolds number equal to 200 000 ($U_\infty = 30\,\text{m/s}$) and also with the natural wind-tunnel turbulence
- Tests with a blade blowing from the lower-side and meant for lift decrease

Natural turbulence in the wind-tunnel

The effects of the actuation when the blade is subjected to the natural turbulence intensity in the wind-tunnel equal to 0.5% are analysed here.

Figure 3.34 shows lift coefficient C_L and flapwise bending moment M_{fbm} evolution as a function of the angle of attack for the baseline and two control cases. Even a low actuation ($C_\mu = 0.03$) suppresses the laminarity effects by reattaching the boundary layer and linearising the lift curve. Actuation at the highest C_μ suppresses the low Reynolds effects but also delays stall and increases the lift coefficient beyond $\alpha = 10°$. The tendencies observed for the lift coefficient are also apparent in the M_{fbm} curve.

ΔC_L and ΔM_{fbm} are shown in figure 3.35 as a function of the momentum coefficient and for several angles of attack α. ΔC_L augments with C_μ with a square-root evolution meaning that the gain is important between $C_\mu = 0$ and $C_\mu = 0.03$ and tends to be reduced beyond this value. For a given C_μ, ΔC_L and ΔM_{fbm} augment up to a certain angle of attack and then stagnate at about $\alpha = 10°$. Actuation suppresses the boundary layer separation and the low lift values in the linear part of the lift curve up to $\alpha = 10°$, beyond which the gain decreases. The maximum ΔC_L and ΔM_{fbm} are obtained for $\alpha = 7°$ and are equal to +0.3 and 2 N m respectively.

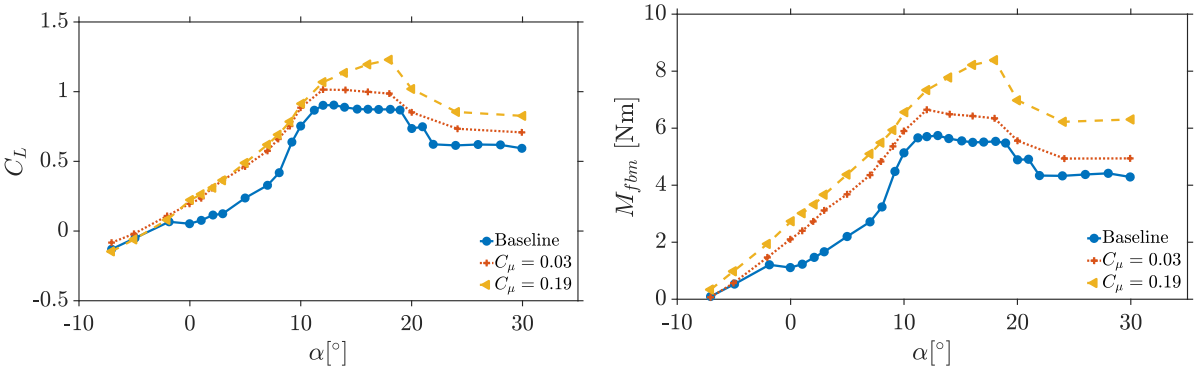

(a) Lift coefficient C_L (b) Flapwise bending moment M_{fbm}

Figure 3.34: Lift coefficient and flapwise bending moment (C_L and M_{fbm}) as a function of the angle of attack α and for various momentum coefficients C_μ - $Re = 130\,000$ and $T_u = 0.5\%$

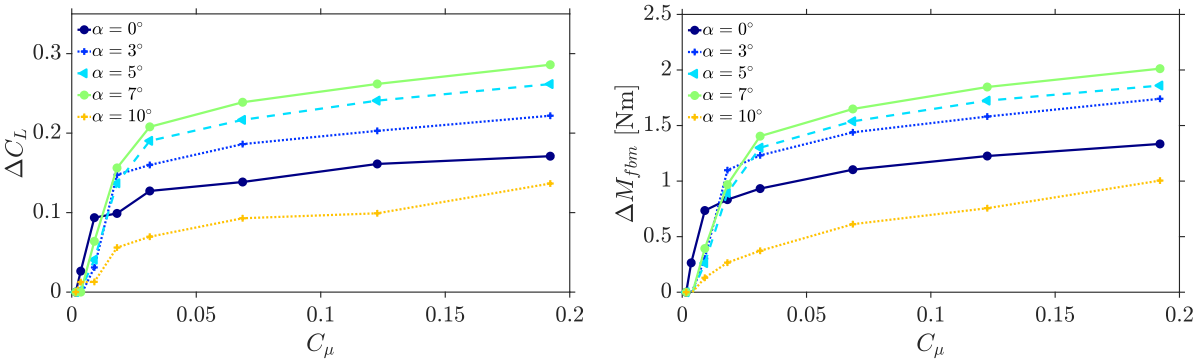

(a) Lift coefficient increase ΔC_L (b) Flapwise bending moment increase ΔM_{fbm}

Figure 3.35: Lift coefficient increase ΔC_L and flapwise bending moment increase ΔM_{fbm} as a function of the momentum coefficient C_μ and for various angles of attack α - $Re = 130\,000$ and $T_u = 0.5\%$

Figure 3.36 shows the pressure distribution with and without actuation for two angles of attack. For $\alpha = 5°$, the effect on the C_p is not noticeable for the lowest $C_\mu = 0.01$ but becomes important at $C_\mu = 0.03$. Beyond this C_μ, an increase on the actuation strength does not dramatically change the pressure distribution. The C_p evolution with C_μ confirms the previous results on ΔC_L as the actuation effect increases specially for the lower C_μ and then tends to stagnate. In the case of $\alpha = 10°$, actuation reduces the pressure along the suction side of the blade, and therefore slightly increases the lift coefficient, but does not change the overall pressure distribution. The effect of the actuation on the C_p is less visible for $\alpha = 10°$ than for $\alpha = 5°$ confirming that the lift coefficient gain is low at this angle of attack with an attached flow.

PIV measurements also confirm the reattachment of the boundary layer for the angles of attack in the linear part on the lift curve. Time-averaged velocity fields with and without actuation for $\alpha = 5°$ are shown in figure 3.37. For the baseline case, the boundary layer separates at $\frac{x}{c} = 0.5$ and a large recirculation area is visible beyond the separation point. With the effect of the actuation, the recirculation bulb is strongly reduced and the boundary layer remains nearly attached to the upper-side of the blade. Again, the jet is visible downstream of the blade at about 1.5 cm beyond the trailing-edge (≈ 2 cm downstream of the jet exit).

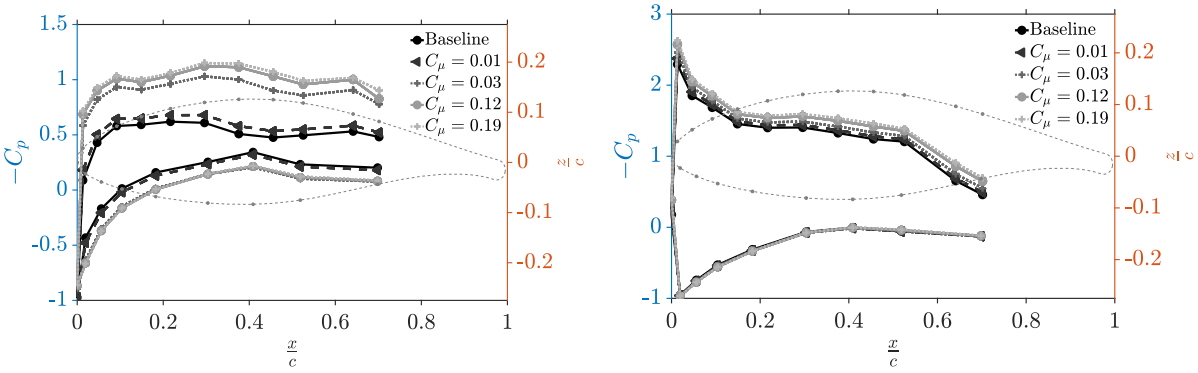

(a) $\alpha = 5°$ (b) $\alpha = 10°$

Figure 3.36: Pressure coefficient C_p as a function of the momentum coefficient C_μ for $\alpha = 5°$ and $\alpha = 10°$ - $Re = 130\,000$, $T_u = 0.5\%$ and $r = 0.63R$

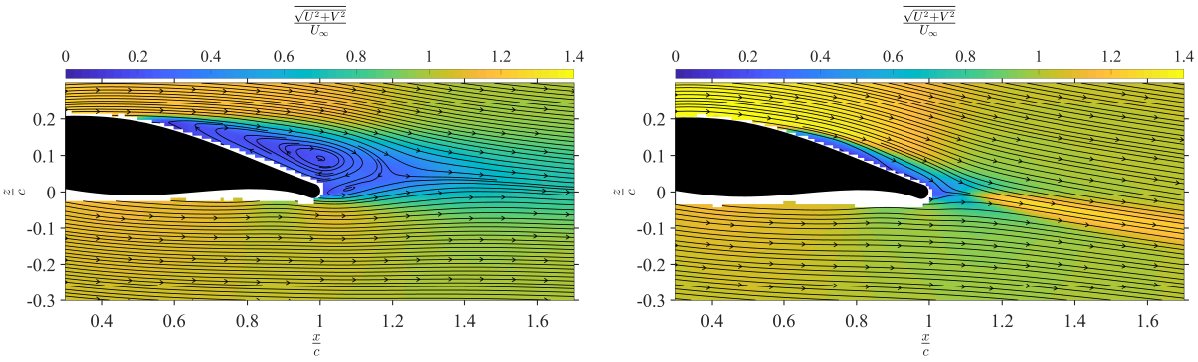

(a) Baseline (b) $C_\mu = 0.03$

Figure 3.37: Time-averaged velocity field for the baseline case and a controlled case - $Re = 130\,000$, $\alpha = 5°$ and $T_u = 0.5\%$

Flow control at $Re = 200\,000$ and $T_u = 0.5\%$

Figure 3.38 shows the lift coefficient evolution for several momentum coefficients and a Reynolds number of 200 000 corresponding to $U_\infty = 30\,\text{m/s}$. First of all, because the flow velocity is increased compared to the previous presented cases, the momentum coefficient values are reduced. This implies that the higher C_μ is equal to 0.07, less than a half than the maximum C_μ at $Re = 130\,000$ equal to 0.20. The effect of the actuation is therefore expected to be lower for this Reynolds number. Whatever the C_μ, the actuation does not change the linear part of the lift curve that shows strictly the same lift coefficients. Blade stall is however changed between the angles of attack $\alpha = 14°$ and $\alpha = 30°$. In this range, the controlled C_L shows higher lift forces with a maximum gain of $\Delta C_L = +0.2$ at $\alpha \approx 15°$. At $Re = 200\,000$, a small separation control is performed but circulation control does not seem to be achieved.

Blowing from the lower-side

As mentioned previously, one set of blades was manufactured with the jets blowing from the lower-side of the blade. The jet direction and position are reminded in figure 3.39. The objective of this set is to perform a lift coefficient decrease and demonstrate that an increase and a decrease of the lift force is possible, such as with DBD actuation. However, this C_L decrease could not

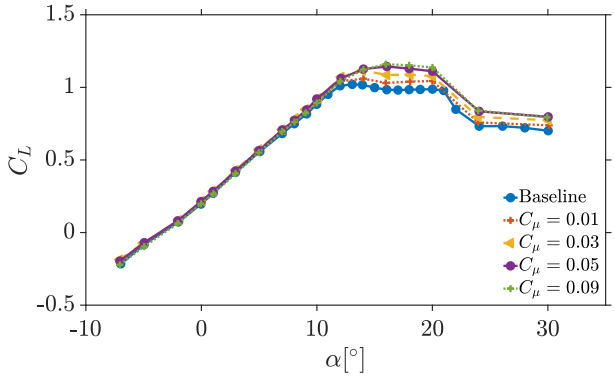

Figure 3.38: Lift coefficient C_L as a function of the angle of attack α and for different momentum coefficients C_μ - $Re = 200\,000$ and $T_u = 0.5\%$

be obtained. Figure 3.40 shows the lift coefficient C_L evolution for a large range of negative and positive angles of attack and the two blowing configurations (upper and lower sides). Both controlled cases are presented at the same C_μ equal to 0.20. As the airfoil is not symmetrical, the baseline behaviour of the blade is different for the angles of attack on both sides of the zero lift angle of attack α_0 equal to $-4°$. Maximal lift coefficient value is equal to $C_L \approx 1$ for $\alpha > \alpha_0$ and minimal value to $C_L \approx -0.5$ for $\alpha < \alpha_0$. The overall behaviour of the actuation is however comparable. For both upper and lower actuations, the lift coefficient is increased for $\alpha > \alpha_0$ and decreased for $\alpha < \alpha_0$ implying that the lower side blowing does not lead to the expected behaviour on the lift force. Both blowing configurations behave in the same way: for $\alpha > \alpha_0$ upper blowing is more efficient and for $\alpha < \alpha_0$ it is the lower blowing. It may be assumed that the actuation creates a low pressure area in the vicinity of the trailing-edge that helps the boundary layer reattachment to the wall. This attachment is more effective when the blowing is carried out from the blade side where the boundary layer separation occurs (pressure side for $\alpha > \alpha_0$, suction side for $\alpha < \alpha_0$).

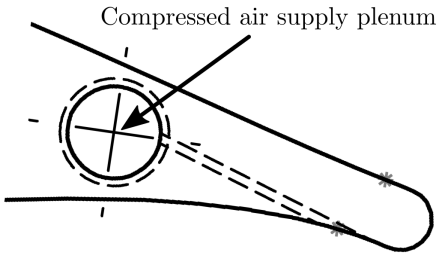

Figure 3.39: Scheme of the blade trailing-edge blowing from the lower side of the blade

3.4.4 Comparison with 2D-airfoil flow control

Comparison with previous studies is not an easy task as the variety of flow control approaches is very large in terms of strategies but also regarding the chordwise location of the actuators and the intended application (circulation or separation controls).

As we have seen in chapter 1, fluidic devices are mainly used to perform separation control. Stalnov et al. [2010] implemented synthetic jets at 37%c and worked at Reynolds numbers ranging from 200 000 to 800 000 and a C_μ of 0.08. The authors proved that the actuation could replace passive vortex generators and obtained a maximal ΔC_L of +0.25. Shun and Ahmed [2012] obtained very similar results ($\Delta C_L = +0.20$) by using discrete blowing slots as vortex generators at 12.5%c ($C_\mu = 0.014$). The study of Troshin and Seifert [2013] focused on the performance

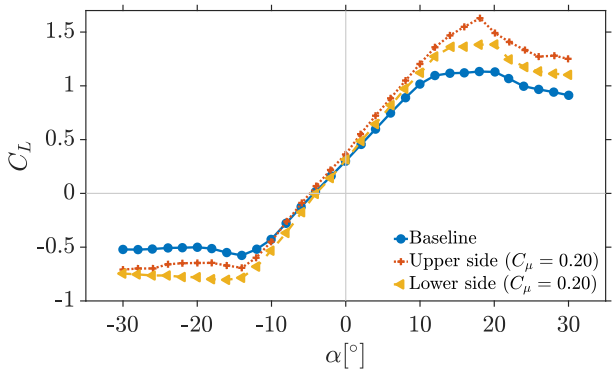

Figure 3.40: Lift coefficient C_L as a function of the angle of attack α and for lower and upper side blowing ($C_\mu = 0.20$, $Re = 130\,000$ and $T_u = 4.3\%$)

improving of a degradated airfoil that simulates the effect of depositions on the blades LE. The authors used synthetic jets at 35%c, 50%c and 65%c and obtained a ΔC_L of +0.30 with a C_μ equal to 0.04. In the view of these previous studies, the order of magnitude of the lift coefficient gain is of about **+0.20 to +0.30 with fluidic devices** located mostly at the leading-edge of the airfoil. In the present case, equivalent gains are obtained with an actuation at the trailing-edge of the blade: +0.10 to +0.20 in the linear part of the lift curve, and up to +0.50 when the blade is partially stalled. Due to the discrete actuation along the wing span a purely circulation control is not performed but the main impact of the actuation is a separation control. Actuation effect gets stronger with the increase of the angle of attack and seems to stagnate beyond the angle α_{sep} where the boundary layer begins to separate at the trailing-edge. This same mechanism of actuation is highlighted by Greenblatt and Wygnanski [2000] with the implementation of different leading-edge excitations: slats over a NACA0015 airfoil and blowing on a NACA0012 airfoil.

As pointed out in section 2.4.5 (p.65), where the effects of a DBD actuation and a fluidic one on two NACA65$_4$-421-CC airfoils were compared, the mechanisms of interaction of the two strategies differ. A purely circulation control is made with DBD actuators whereas the present blowing jets perform mostly a separation control. Present results should also be compared with the ones obtained by Jaunet and Braud [2018] in the context of the SMARTEOLE project as shown in the following. Data corresponding to the 2D-configuration is courtesy of V. Jaunet and C. Braud.

Figures 3.41a and 3.41b show the lift coefficient variation ΔC_L and the lift augmentation ratio $\frac{\Delta C_L}{C_\mu}$ as a function of the angle of attack α and for both translational and 2D configurations. These variables represent respectively the **sensitivity** and the **efficiency** of the actuation. The obtained lift coefficient maximal variations are very similar for both cases ($\Delta C_L \approx +0.45$), but obtained with a higher C_μ in the present translational configuration. This additional C_μ injected for an equal performance can be explained by the fact that the present actuation is not optimised for controlling the blade tip vortex. Consequently, some of the blowing near the blade tip is worthless in terms of efficiency and an extra C_μ should be added to obtain similar performances with respect to the 2D case. The fact that the maximal gain is obtained for an angle of attack of about $\alpha = 10°$ in the translational case and for $\alpha = 18°$ for the 2D-case is due to the discrepancies between the two configurations: one set-up is purely two dimensional, whereas the other has a free blade tip. Regarding the augmentation ratio, both configurations show maximal values of about 4 for most of the momentum coefficients. The lowest C_μ of the translational case has, however, a great efficiency with a maximal ratio of about 9. In Jaunet and Braud [2018] the authors obtain a linear evolution of C_L as a function of C_μ that is not reproduced in the present translational case. For the present control set-up the C_L evolution with C_μ rises rapidly and then stagnates for the higher momentum coefficients as reported in Wetzel et al. [2013] and Abramson [1975] for circulation control over an elliptical airfoil. This could

come from the fact that the jets in the present blades are proportionately closer than the jets of the LHEEA airfoil, meaning that our configuration is *more similar* to a purely 2D actuation.

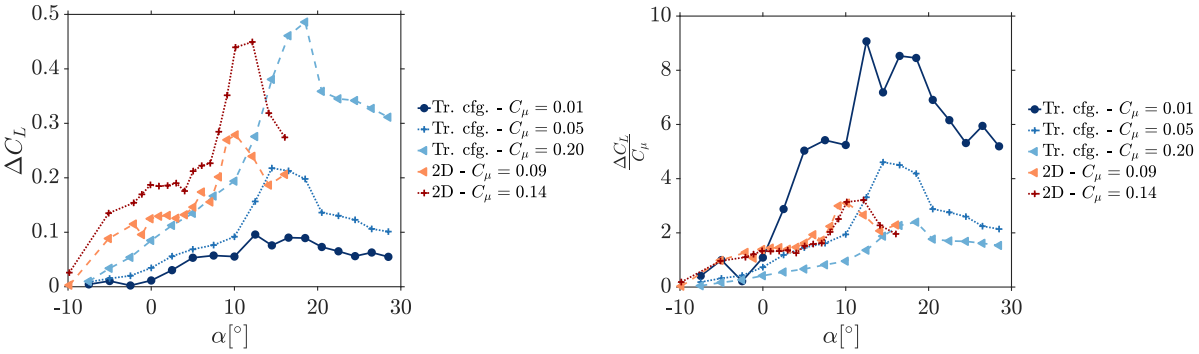

(a) Lift coefficient gain ΔC_L

(b) Lift augmentation ratio $\frac{\Delta C_L}{C_\mu}$

Figure 3.41: Lift coefficient gain ΔC_L and lift augmentation ratio $\frac{\Delta C_L}{C_\mu}$ as a function of the angle of attack α for the translational configuration blade ($Re = 200\,000$) and the 2D-configuration ($Re = 130\,000$)

Pressure coefficient variation ΔC_p is plotted in figure 3.42a for the translational configuration and in figure 3.42b for the 2D case. Each figure plots the ΔC_p distribution along the chord for several angles of attack α. In both configurations, the actuation modifies the whole pressure over the airfoil, specially along the suction side. The airfoil leading-edge seems specially reactive to the actuation with ΔC_p losses up to -0.90. As mentioned above, the suction visible for the 2D case is not visible for the translational configuration due to the absence of pressure taps beyond $\frac{x}{c} = 0.7$.

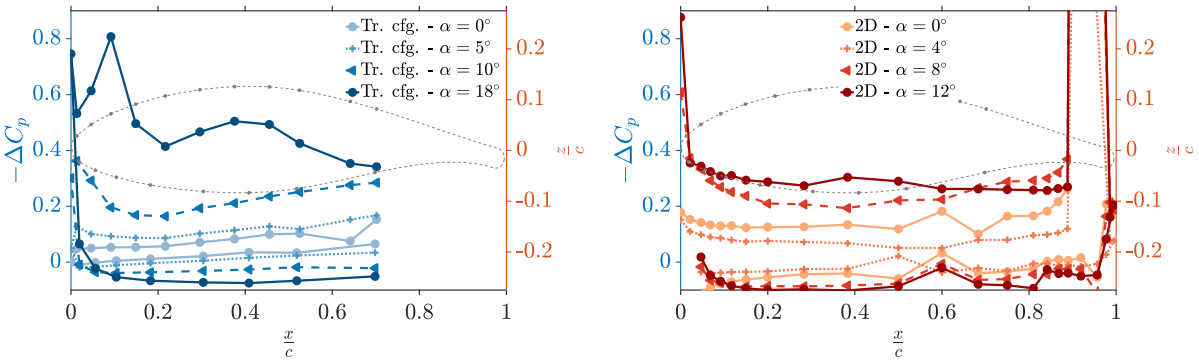

(a) Translational configuration ($C_\mu = 0.20$, $r = 0.63R$, $Re = 130\,000$)

(b) 2D-configuration ($C_\mu = 0.14$, $Re = 200\,000$)

Figure 3.42: Pressure coefficient variation ΔC_p distribution for the translational and 2D configurations

3.5 Conclusion

Before testing the fluidic flow control strategy in a rotational configuration a preliminary study was made to evaluate the performances of the actuation in a translational configuration.

Fluidic jets are first characterised in quiescent air conditions in order to assess the blowing and implement the necessary pneumatic system. It is shown that the blowing is homogeneous

along the blade span and that the jet signature is measurable up to 200 to 300 mm downstream of the jet exit. Depending on the applied pressure in the plenum chamber inside the blades, the jet exit velocity ranged from 100 to 300 m/s. This study also allows to compute a momentum coefficient C_μ, a normalised variable that quantifies the strength of the actuation with respect to the incoming flow momentum. The maximal C_μ obtained is equal to 0.20.

Regarding the flow control performances, actuation performs lift coefficient variations ΔC_L up to +0.10 to +0.20 in the linear part of the lift curve giving evidence of a potential circulation control in this angle of attack range. For angles of attack above $\alpha = 10°$, the fluidic jets do a separation control that delays stall and increases the maximal lift coefficient of $\Delta C_L \approx +0.5$. In chapter 1 we defined the target values that should be performed by an ideal load alleviation strategy. In the case of the lift coefficient, this value was equal to $\Delta C_L \pm 0.25$. Hence, present lift coefficient augmentation is below the desired target for angles of attack with attached flows but above this threshold when the flow is partially separated. Unfortunately, the lift coefficient could not be reduced with the blade blowing from the pressure side and only a lift augmentation was performed. The strain gages response to the actuation is very similar to the lift response and bending moment increases up to 2.2 N m are performed. The measurement of the bending moment via the gages is validated and will be of great interest for the following rotational configuration where no global lift measurements are possible on the blades.

Pressure coefficient C_p is strongly reduced along the suction side by the effect of the actuation and remains nearly unchanged in the pressure side, leading to an increase in the lift force, coherent with balance measurements. Pressure coefficient variation ΔC_p is not equally distributed along the chord. Leading-edge and the second part of the blade seem specially receptive to the actuation. PIV velocity fields confirm the actuation mechanisms. By the effect of the blowing, the recirculation area is strongly reduced and the boundary layer separation is delayed.

After this validation of the flow control strategy in a translational configuration, blades are mounted in the wind turbine bench of the laboratory. This fluidic flow control application in a rotational configuration is explained in the next chapter.

Chapter 4

Fluidic flow control on a wind turbine model - rotational configuration

Contents

4.1 Introduction

After an investigation of the fluidic flow control effectiveness in a translational configuration, blades are mounted and tested in the rotor bench of the laboratory.

The objective of this study is to understand the mechanisms of the actuation in a rotational configuration for different rotational velocities and pitch angles and to assess the control efficiency and potentiality for load fluctuation reduction.

The first part of the chapter is devoted to an extensive description of the wind turbine bench. All the sensors and the measurements performed are detailed as well as the characterisation of the wind-tunnel return test-section. Then, the bench is characterised without actuation in terms of rotor torque and drag, chordwise pressure distribution and flapwise bending moment at the blade roots. Finally are exposed the results obtained with the fluidic control actuation performed in a rotational configuration.

Figure 4.1: Picture of the wind turbine bench

4.2 Experimental means

This section presents the experimental means used for the flow control application in a rotational configuration. The wind turbine bench of the laboratory is described along with the blade geometry and the pneumatic system used for the rotor supply in compressed air. All the implemented sensors and performed measurements are also listed in the following. Finally, a characterisation of the flow in the wind-tunnel return test-section is shown.

4.2.1 Nomenclature introduction

Figure 4.2 shows the definition of turbine coefficients C_{power} and C_{thrust} as well as of flapwise bending moment M_{fbm}, all of them variables that will be used along the chapter. The figure assumes that the turbine is not yawed and shows the variables in two different ways: the rotor and the blade airfoil perspectives. In the figure, β is the pitch angle defined between the plane of rotation and the chord line. C_{power} and C_{thrust} are respectively the power and thrust coefficients of the wind turbine defined as:

$$C_{power} = \frac{Q\Omega}{\frac{1}{2}\rho U_\infty^3 S_{rotor}} \qquad (4.1) \qquad\qquad C_{thrust} = \frac{D}{\frac{1}{2}\rho U_\infty^2 S_{rotor}} \qquad (4.2)$$

where ρ is the air density, U_∞ is the incoming wind velocity, S_{rotor} the rotor swept area, Ω the rotational velocity of the turbine, Q its torque and D its overall drag. C_{power} is defined in the turbine rotation direction and C_{thrust} in the direction of the incoming wind U_∞. M_{fbm} is the flapwise bending moment measured at the blade roots, defined in the direction normal to the blade chord.

Figure 4.3 defines local blade coefficients and velocities for a blade airfoil element at a radial position r. C_n and C_t are normal and tangential force coefficients respectively, C_t is defined in the chord direction and C_n normal to the chord. C_l and C_d are lift and drag coefficients respectively, C_d is defined in the direction of the relative velocity $W_r(r) = \sqrt{U_\infty^2 + (\Omega r)^2}$ and C_l normal to W_r direction. α is the geometrical angle of attack defined between the chord line and the relative velocity direction; ϕ is defined as $\phi = \alpha + \beta$ and is the angle between the plane of rotation and the relative velocity direction. Local power and thrust coefficients (C_{power}^{loc} and C_{thrust}^{loc} respectively) are defined as the projection of C_n and C_t on the plane of rotation for C_{power}^{loc} and on the wind direction for C_{thrust}^{loc}.

The tip speed-ratio λ of the turbine is defined as the ratio of the tip velocity ΩR to the

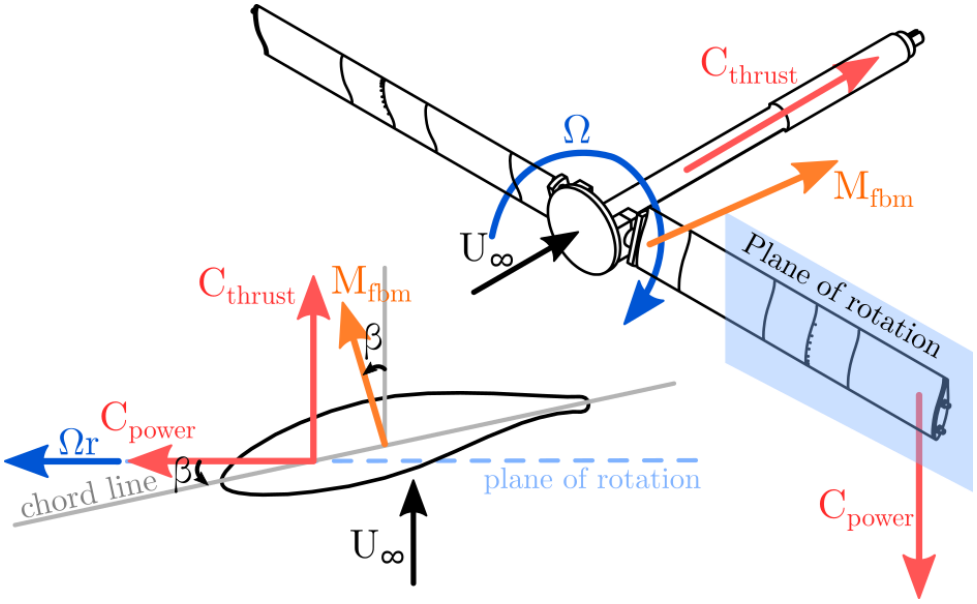

Figure 4.2: Diagram of turbine coefficients and bending moment (rotor and blade airfoil perspectives)

incoming velocity U_∞:

$$\lambda = \frac{\Omega r}{U_\infty} \tag{4.3}$$

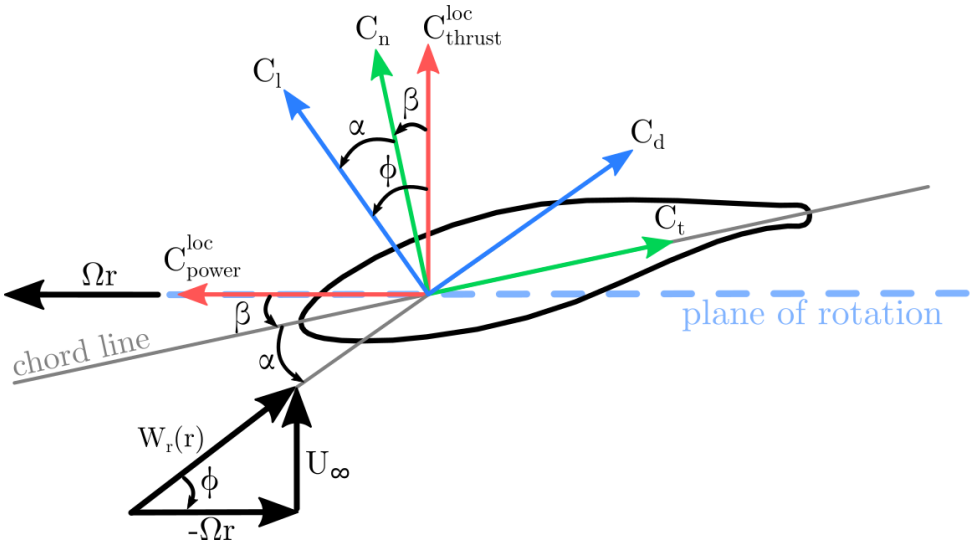

Figure 4.3: Blade airfoil element velocities and forces

4.2.2 The wind turbine bench

The wind turbine

The wind turbine bench, shown in figure 4.4, is a two-bladed rotor designed in partnership with the French turbine manufacturer Vergnet S.A. and funded by the Loiret County Council. The rotor diameter R is equal to 0.7 m and the swept surface S_{rotor} to 1.54 m^2. The bench is made of a three-beamed mast that ensures the turbine mechanical rigidity and stability during operation. The turbine shaft is connected to a reversible servomotor Phase Ultract 509 that

stands revolutions up to 3000 rpm and is coupled to a speed controller. A series of bearings and a reduction gear allow the reduction of the motor rotational velocity to a maximal value equal to $\Omega = 1000$ rpm (3:1 reduction) with minimal friction. The servomotor provides energy when the working point of the turbine is propulsive and dissipates energy when the working point is extractive (most of the present cases). As some sensors are embedded in the rotor, a slip ring is used to supply them with the necessary power and to recover the wanted measured information and voltages. These signals are transferred from the rotor to the ground with a Servotecnica through-bore slip ring (SRH3899-6P/12S). At the front shaft extremity, the blade attachment sections are held with two clamping jaws. Because these attachments are partly cylindrical, the blade pitch angle β can be changed and fixed when the jaws are clamped. Special precautions are taken to ensure a proper balancing of the rotor. At the beginning of the thesis work, the rotor bench was not equipped to perform active flow control in a rotational configuration (either fluidic or plasma actuations). As it was chosen to make fluidic control in the turbine bench, it is necessary to feed the rotor in compressed air. Hence, to allow the transfer of compressed air from the stationary part to a rotating one, a through-bore rotary joint custom-made by Pacquet was designed and implemented over the shaft.

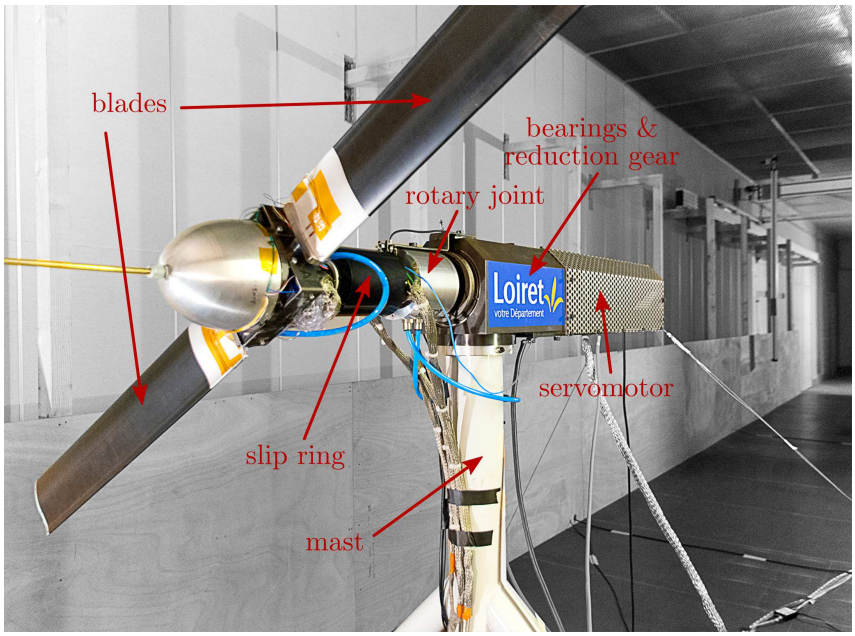

Figure 4.4: Picture of the wind turbine bench and its main parts

The blades

An exhaustive description of the blades is made in section 3.2.1 (p.78) but the most important elements are recalled here. Blades are composed of several sections (see figure 4.5) made of aluminium (grey sections in picture 4.4) and POM (black sections in picture 4.4) held together with two traversing rods. Blades are not twisted nor tapered and have a constant chord c equal to 0.1 m[1]. Each blade weights 1.650 kg and its different parts are carefully tightened up to a specified torque to ensure the mechanical strength of the blade during rotation. One of the two blades has a section allowing the measurement of the chordwise pressure distribution. This conception was previously used by Sicot [2005] because it allows the displacement of the pressure measurement section at different blade spans ($r = 0.63R$ and $r = 0.88R$ in the present case). Blades are equipped for the flow control application with a series of blowing jets in the vicinity

[1]Blade aspect ratio defined as $\frac{R}{c}$ is equal to 7 and turbine solidity $\sigma = \frac{N_{blades}c}{R}$ is equal to 0.29 where N_{blades} is the number of blades of the rotor

of the trailing-edge ($\frac{x}{c} = 0.96$). The jet holes diameter is equal to 0.6 mm and the 72 blowing jets are spaced from each other by 4.86 mm. The blowing is located on the second half of the blade span ($r \approx 0.5R$ to $r \approx R$), the area of the blade generating most of the turbine torque. Only the blowing configuration from the upper side of the airfoil is tested in the rotational configuration.

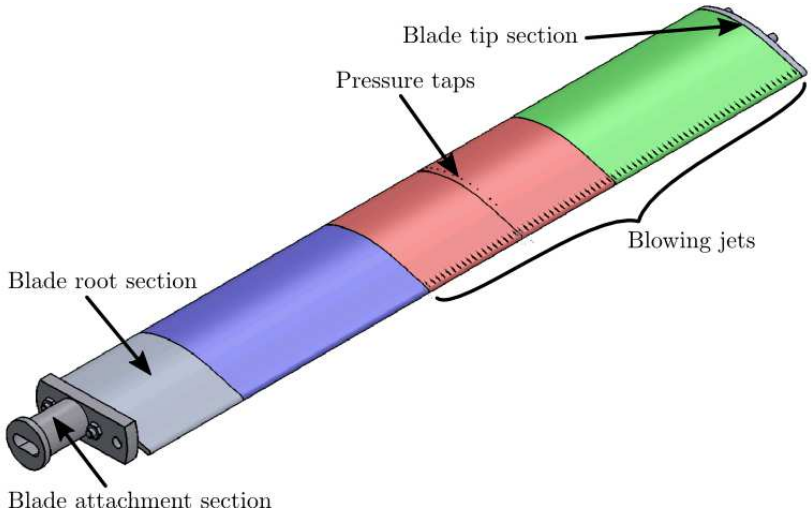

Figure 4.5: CAO drawing of a wind turbine blade

Pneumatic system

One of the challenges of this flow control application was to supply the turbine blades with compressed air. A scheme of the implemented solution is shown in figure 4.6 where the blue line represents the compressed air circuit. The figure only shows the principle of the system. Pressurised air from the laboratory network (7 to 8 bar) goes through a pressure regulator and a filter before going through a 10 L buffer tank that damps the air network fluctuations. Past the tank, the air heads for the rotary joint positioned around the turbine shaft. The external part of the rotary joint is fixed to the turbine casing and the inner part rotates with the turbine shaft. Inside the joint, there is an air chamber gathering these two static and rotating parts where the fluidic transition between the two parts is made. The shaft is manufactured in such a manner that the air can enter it at the rotary joint location and go through the shaft internally to emerge again beyond the electrical slip ring. At this point, the compressed air exits the shaft and moves through short tubes to the blade plenum chambers and then to the jet holes. The applied pressure (or flow rate) in the circuit can be managed with the pressure regulator at the beginning of the circuit. The pressure inside both plenum chambers is measured to check its level and stability.

Momentum coefficient C_μ

At this stage a word should be said about the momentum coefficient C_μ, a parameter that reflects the actuation strength with respect to the momentum of the incoming flow, for this rotational configuration. It is indeed a tricky problem that requires careful thought. In the present case, testings are performed at a fixed incoming flow velocity U_∞ and with a variable rotational velocity Ω. For the rotational tests presented in this chapter, three different total pressures on the plenum chambers P_{t0} are applied:

– $P_{t0} = 1.15$ bar: the rotary joint cannot work properly without a flow rate through it. To avoid friction heating and the joint damage, a flow rate should always go through the joint (even very small). As the equivalent flow rate for $P_{t0} = 1.15$ bar is very low, performance

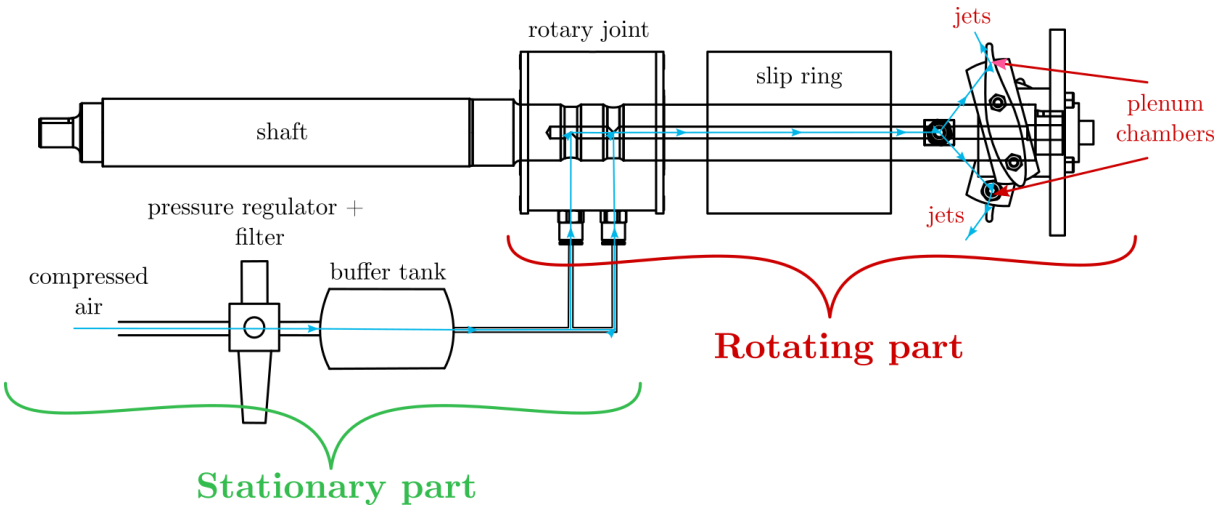

Figure 4.6: Scheme of the pneumatic system used to supply the rotor with compressed air (not to scale)

gains are assumed to be negligible and this configuration will be considered as the **baseline case**

- $P_{t0} = 2.6$ bar: this configuration will be named **P1**
- $P_{t0} = 3.6$ bar: this case will be named **P2** in the following

Greenblatt et al. [2012] and Jukes [2015] carried out DBD flow control on wind turbine benches at a laboratory scale and defined the momentum coefficient $C_\mu(R)$ as:

$$C_\mu(R) = \frac{\rho_j S_j U_j^2}{\frac{1}{2}\rho W_r^2(R) c R} = \frac{I_j}{\frac{1}{2}\rho(U_\infty^2 + (\Omega R)^2) c R} = \frac{I_j}{\frac{1}{2}\rho U_\infty^2 (1+\lambda^2) c R} \tag{4.4}$$

where ρ_j is the jet density, S_j the exhaust surface of the 72 jets, U_j the jet velocity, ρ the incoming flow density and the term ΩR represents the blade **tip** velocity. It is important to note here that the denominator $\rho_j S_j U_j^2$, named I_j, is obtained with the jet characterisation in quiescent air conditions and is directly related to the pressure in the plenum chamber P_{t0}. This definition of $C_\mu(R)$ depends on Ω and therefore on the tip-speed ratio of the turbine but does not depend on the radial position because the reference velocity is taken at the blade tip. Figure 4.7 shows the momentum coefficient $C_\mu(R)$ evolution with the tip-speed ratio λ for the three pressure cases studied (baseline, P1 and P2). It is interesting to note that for tip-speed ratios greater than 5 the momentum coefficient is very low.

However, this momentum coefficient $C_\mu(R)$ is underestimated because it involves the tip velocity which is the higher radial velocity obtained in the rotor for a given Ω. Hence, this definition does not take into account the dependency of C_μ on the blade radial position r, induced by two different sources. First, the radial gradient of the relative velocity $W_r(r)$ is ignored. And secondly, the effect of the centrifugal force $P_{cent}(r)$ in the plenum pressure $P_{t0}(r)$ radial distribution is not included either. Indeed, the turbine rotation leads to a pressure stratification in the air contained inside the plenum chamber crossing the blades. Centrifugal pressure is equal to $P_{cent}(r) = \frac{1}{2}\rho r^2 \Omega^2$ and implies that the plenum pressure $P_{t0}(r)$ is more important at the blade tip than at the blade root. Hence, a more accurate definition of $C_\mu(r, \Omega)$ would be:

$$C_\mu(r, \Omega) = \frac{I_j(r)}{\frac{1}{2}\rho W_r^2(r) c R} = \frac{I_j(r)}{\frac{1}{2}\rho(U_\infty^2 + (\Omega r)^2) c R} \tag{4.5}$$

Figure 4.8 shows the momentum coefficient $C_\mu(r, \Omega)$ as a function of the tip-speed ratio λ and the radial position $\frac{r}{R}$ for the three pressure cases studied. Radial dependency takes into

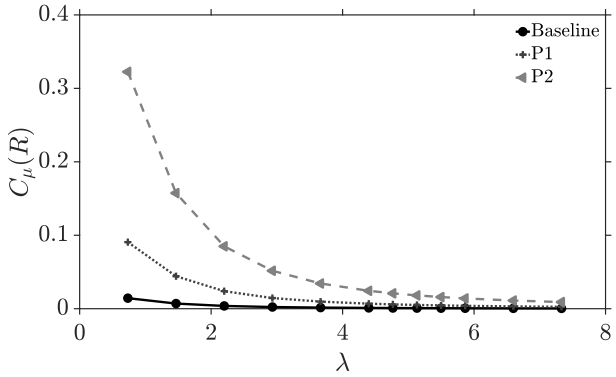

Figure 4.7: Momentum coefficient $C_\mu(R)$ as a function of the tip-speed ratio λ for the three studied pressure cases

account the centrifugal pressure gradient as well as the relative velocity variation along the blade span. For a fixed λ, the $W_r(r)$ increase with r causes the momentum coefficient decrease from $\frac{r}{R} \approx 0.5$ (starting actuation span) to the blade tip. This suggests that the $W_r(r)$ gradient plays a preponderant role with respect to radial $P_{cent}(r)$ variation that would have lead to, alone, an increase in the C_μ for the highest radial positions. For a given $\frac{r}{R}$ position, the momentum coefficient decreases with λ because of the related increase in Ω.

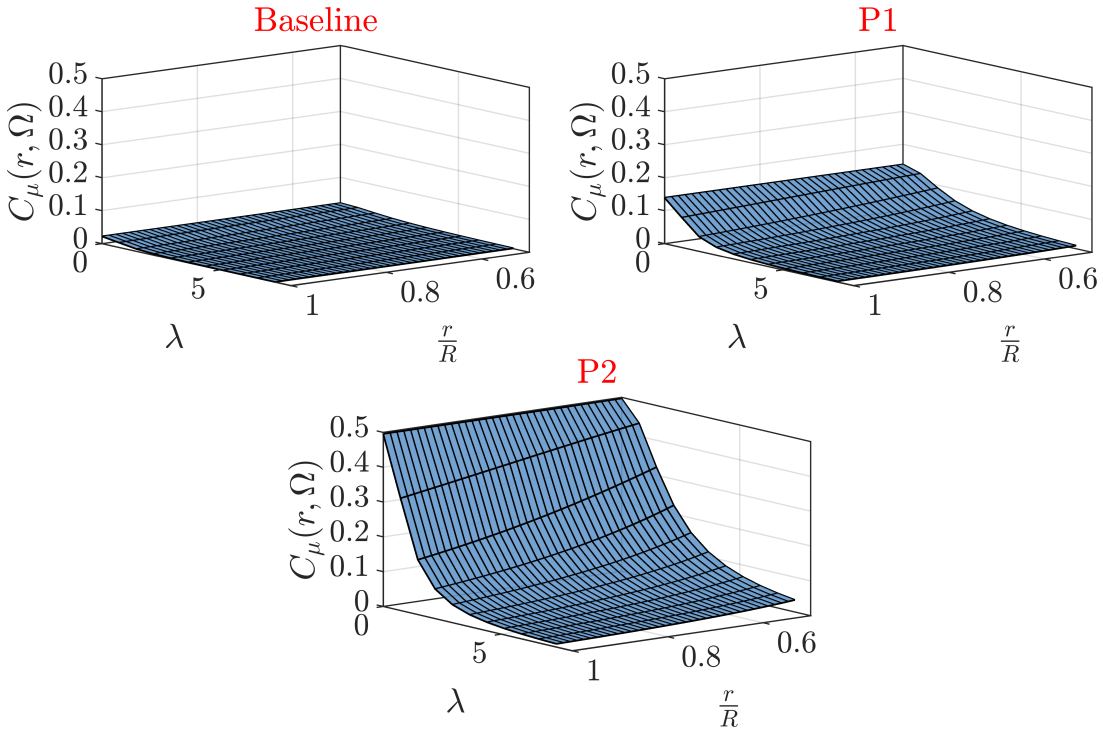

Figure 4.8: Momentum coefficient $C_\mu(r,\Omega)$ as a function of the tip-speed ratio λ and the blade radial position $\frac{r}{R}$ for the three employed pressure cases

To determine the influence of the centrifugal force in the C_μ distribution along the blade span, $C_\mu^{\text{NOCENT}}(r,\Omega)$ is defined as the momentum coefficient that takes into account the radial distribution of $W_r(r)$ but **not** the centrifugal force effect $P_{cent}(r)$ in the plenum chamber, i.e.:

$$C_\mu^{\text{NOCENT}}(r,\Omega) = \frac{I_j(r=0)}{\frac{1}{2}\rho(U_\infty^2 + (\Omega r)^2)cR} \tag{4.6}$$

Then the relative difference between the two C_μ definitions ΔC_μ^{cent} can be defined, in per-

centage, as follows:

$$\Delta C_\mu^{cent} = \frac{C_\mu(r,\Omega) - C_\mu^{\text{NOCENT}}(r,\Omega)}{C_\mu(r,\Omega)} \times 100 \tag{4.7}$$

The ΔC_μ^{cent} distribution is shown in figure 4.9 as a function of the tip-speed ratio λ and the radial position $\frac{r}{R}$. When only the centrifugal force is taken into account, the momentum coefficient is increased at the blade tip of about 3.8% and 1.7% for the P1 and P2 cases respectively and the highest λ. The influence of pressure stratification in the plenum chamber can be neglected for these two control cases. However, when pressure levels involved are smaller, such as the baseline case, neglecting centrifugal forces will lead to C_μ variations up to 15%. As expected, these maximal ΔC_μ^{cent} values are obtained at the blade tip and for the highest λ corresponding to the highest Ω, and at the location where $P_{cent}(r)$ is maximal.

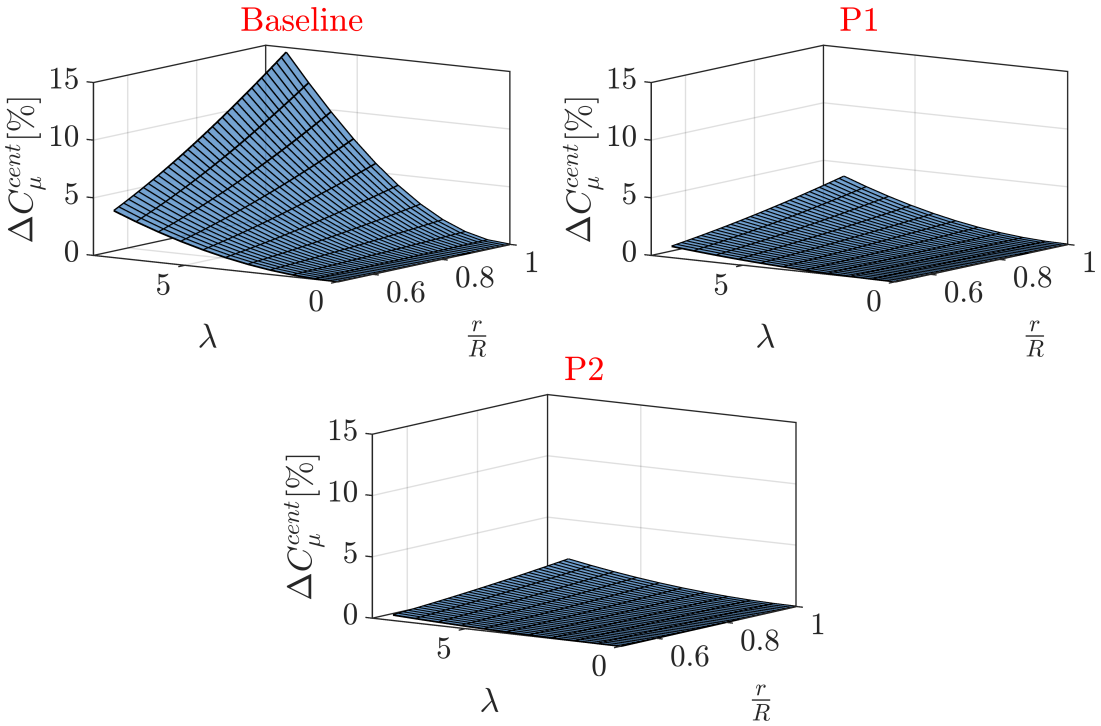

Figure 4.9: ΔC_μ^{cent} distribution as a function of the tip-speed ratio λ and the blade radial position $\frac{r}{R}$ for the three employed pressure cases

Actuation differentiation

As the momentum coefficient varies with the tip-speed ratio λ but also along the blade span $\frac{r}{R}$, this parameter will not be extensively used in the following. To avoid having dimensional quantities in the plots, it has been chosen to refer directly to the three actuation cases: **baseline**, **P1** and **P2**.

4.2.3 Sensors & measurements

Instrumentation

The turbine bench is equipped with several sensors that allow the measurement of different quantities of interest. Figure 4.10 shows the bench with the location of the measurement devices. In the following paragraphs, all the sensors and their respective measurement are detailed from left to right in picture 4.10.

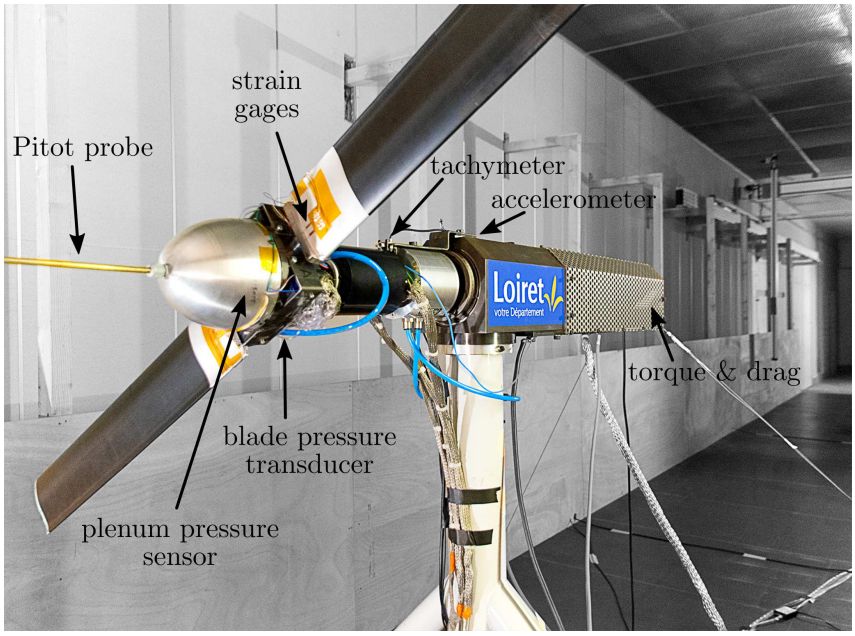

Figure 4.10: Picture of the wind turbine bench and its measurement devices

Pitot probes A first Pitot probe embedded in the turbine hub measures the pressure 400 mm upstream from the rotor. Both static $P_{\infty,hub}$ and total $P_{t,hub}$ pressures are connected to the pressure scanner that allows the measurement of blade surface pressures. A second Pitot probe (not visible in figure 4.10) is located near the wind-tunnel wall and approximately 1 m upstream of the turbine. It measures the incoming flow dynamic pressure $P_{dyn,wall}$ and allows to obtain the incoming flow velocity U_∞ with minimal disturbances from the turbine. The pressure sensor used for this last measure is a GE Druck LPM9381 (0-500 Pa, 0.1%FS).

Plenum chamber pressure Plenum pressure P_{t0} inside the chambers feeding the jets in compressed air are measured with two pressure sensors (Sensortechnics, 144SB005D-PCB, 0-5 bar). These sensors are physically located inside the hub dome but the pressure information is taken at the respective blade tips by means of vinyl tubes that go through the blades.

Blade surface pressure Mean pressure distribution over the airfoil is measured with 20 pressure taps implemented on the blade between the leading-edge and 70% of the chord as can be seen in figure 4.11. Taps are aligned along the chord (not staggered) to have a purely chordwise distribution not altered by the radial pressure distribution. Pressure measurements are carried out with a 32-channel differential pressure scanner ESP-32HD (GE, ± 1.0 PSI) embedded in a MicroDAQ system (CHELL). Accuracy of the pressure sensor is ±0.25% of the full scale i.e. about 17 Pa. Maximal uncertainty is equal to 30% when the turbine does not rotate (low pressure levels) but is reduced with λ and C_p levels augmentation (1.5% for $\lambda = 7.33$). Surface pressure can be measured at two blade spans: $r = 0.63R$ and $r = 0.88R$. Vinyl tubes go across the blade interior from the pressure taps to the pressure transducer and are as short as possible. For this rotational configuration, the pressure scanner is embedded in the rotor.

Pressure coefficient C_p for the rotational configuration is defined in equation 4.8, where P_{local} is the local pressure measured at the blade surface, P_∞ a reference static pressure and $P_{cent} = \frac{1}{2}\rho r^2\Omega^2$ the centrifugal pressure in the vinyl tubes crossing the blade. Indeed, as mentioned above for the plenum chamber, the rotation of the turbine induces a pressure stratification in the pressure tubes crossing the blades. Measured pressure is distorted and smaller than the real blade surface pressure that wants to be measured. This is why centrifugal forces are corrected by adding the pressure term $P_{cent}(r)$.

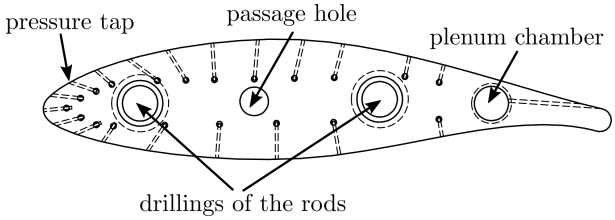

Figure 4.11: Positions of the pressure taps on the blade

$$C_p = \frac{P_{local} - P_\infty + P_{cent}}{\frac{1}{2}\rho(U_\infty^2 + (\Omega r)^2)} = \frac{P_{local} - P_\infty + P_{cent}}{\frac{1}{2}\rho W_r^2} \tag{4.8}$$

When the turbine rotates, the flow is slowed down in the upstream vicinity of the turbine and the measure of the static pressure at the hub $P^{\text{ROT}}_{\infty,hub}$ is biased. As we do not have any information on the radial and axial inductions induced by the turbine, the reference pressure is the static pressure measured at the turbine hub when the turbine does not rotate $P^{\text{NOROT}}_{\infty,hub}$ but in the same wind conditions as the rotating cases. Pressure coefficient can be therefore reformulated as:

$$C_p = \frac{P^{\text{ROT}}_{local} - P^{\text{NOROT}}_{\infty,hub} + P_{cent}}{\frac{1}{2}\rho W_r^2} \tag{4.9}$$

$$= \frac{P^{\text{ROT}}_{local} - P^{\text{ROT}}_{\infty,hub} + P^{\text{NOROT}}_{t,hub} - P^{\text{NOROT}}_{\infty,hub} - P^{\text{ROT}}_{t,hub} + P^{\text{ROT}}_{\infty,hub} + P_{cent}}{\frac{1}{2}\rho W_r^2} \tag{4.10}$$

In this previous equation, blue terms are equal by definition. Red terms are also equal as the total pressure is preserved. By grouping the equation terms in pairs, we obtain:

$$C_p = \frac{P^{\text{ROT}}_{local} - P^{\text{ROT}}_{\infty,hub} + P^{\text{NOROT}}_{t,hub} - P^{\text{NOROT}}_{\infty,hub} - P^{\text{ROT}}_{t,hub} + P^{\text{ROT}}_{\infty,hub} + P_{cent}}{\frac{1}{2}\rho W_r^2} \tag{4.11}$$

$$= \frac{\Delta P^{\text{ROT}}_{local} + \Delta P^{\text{NOROT}}_{hub} - \Delta P^{\text{ROT}}_{hub} + P_{cent}}{\frac{1}{2}\rho W_r^2} \tag{4.12}$$

Hence, pressure coefficient C_p is a combination of different pressure measurements:

- $\Delta P^{\text{ROT}}_{local}$ is the difference between the local pressure over the blade during rotation P^{ROT}_{local} and the static pressure at the hub during rotation $P^{\text{ROT}}_{\infty,hub}$
- $\Delta P^{\text{NOROT}}_{hub}$ is the difference between the total pressure at the hub at standstill $P^{\text{NOROT}}_{t,hub}$ and the static pressure at the hub at standstill $P^{\text{NOROT}}_{\infty,hub}$ (i.e. dynamic pressure at the hub at standstill)
- $\Delta P^{\text{ROT}}_{hub}$ is the difference between the total pressure at the hub during rotation $P^{\text{ROT}}_{t,hub}$ and the static pressure at the hub during rotation $P^{\text{ROT}}_{\infty,hub}$ (i.e. dynamic pressure at the hub during rotation)
- $P_{cent}(r) = \frac{1}{2}\rho r^2\Omega^2$ is the centrifugal force correction term taken at the radial position r of the pressure taps
- $\frac{1}{2}\rho W_r^2 = \frac{1}{2}\rho\left(U_\infty^2 + (\Omega r)^2\right)$, where $\frac{1}{2}\rho U_\infty^2$ is the dynamic pressure $P_{dyn,wall}$ measured with the (stationary) Pitot probe fixed on the wind-tunnel wall and $\frac{1}{2}\rho(\Omega r)^2$ taken at the radial position r of the pressure taps

Strain gages Strain gages allow the measurement of the flapwise bending moment M_{fbm} at the blade root. Each blade has its set of four 120 Ω gages mounted in a full-bridge configuration. A detailed explanation of the strain gages wiring and signal acquisition is explained in the previous chapter section 3.2.3 (p.83) and the extensive explanation of gage measurement principle is illustrated in appendix C. Prior to the testings, strain gages are carefully calibrated with the blades mounted in the wind turbine bench and set at a pitch angle of 90° (blades feathered to the wind). Two cords are attached to the blade tips and known equal weights are applied on both blade extremities. The linear response of each gage is measured and the slope is obtained with a linear regression. Gage offset is subtracted for every set of measures.

Tachymeter A tachymeter is used to measure the rotation frequency of the turbine. It is an inductive proximity sensor (IFM-IY5033) that detects the presence of a screw fixed on the turbine shaft. Every time the screw passes next to the probe (one time per revolution) the sensor produces a voltage peak that is detected and acquired.

Accelerometer A three axis accelerometer (MMA7361L) is placed on the top of the wind turbine hub. This sensor is not relevant but provides information about the turbine motion. It is actually a control measurement that allows the monitoring of the wind turbine vibrations, specially at the highest rotational velocities.

Torque and drag of the turbine Whereas blade pressure and flapwise bending moment are **local measurements on the blades**, the drag and torque of the turbine are **global rotor** variables characterising the turbine operating point. In order to obtain the power coefficient of the turbine C_{power} and its thrust coefficient C_{thrust}, torque and drag generated by the rotor are measured with a single force and torque meter. The sensor is a SCAIME (M2396) and measures up to 500 N in drag force D and 50 N m in torque Q. Uncertainties are of 0.3% and 0.2% of the nominal loads for drag and torque respectively. The sensor is fixed at the rear of the turbine hub: one side of the sensor is connected to the servomotor housing, the other to the turbine casing (ground). The turbine rotor and shaft have a small degree of freedom along the shaft axis. When the turbine operates, the rotor and the shaft tend to be displaced towards the rear of the turbine and *push* on the sensor that measures the resultant force via internal strain gages. In the same way, when the turbine rotates it generates a certain torque that is counter-balanced by the servomotor housing and measured by the sensor. Prior to the testings, the sensor is calibrated by applying known forces and torques on the turbine and measuring the sensor response with the acquisition system. The calibration slope is obtained with a linear regression and the offset is subtracted for every test case.

Atmospheric conditions Atmospheric pressure P_{atm} and the test-section temperature T_{amb} are measured for every test case.

Measurement protocol

The measurement protocol consisted in several steps repeated for every test case:

- Manually fix the blade pitch angle β and the pressure P_{t0} on the blade plenum chambers (baseline, P1 or P2)
- Take a first zero value (Z1) with the speed controller OFF ($U_\infty = 0$). This zero value permits to have a reference zero without the speed controller taking control of the turbine
- Take a second zero value (Z2) with the speed controller ON and at $\Omega = 1$ rpm ($U_\infty = 0$). This $\Omega = 1$ rpm is necessary because some sensors, as the strain gages, sense the

gravitational effects. A complete azimuthal turn allows to average the Z2 value along a turbine complete rotation

- Power on the wind-tunnel fan and set the incoming velocity to 10 m/s
- Take one measure at $\Omega = 1$ rpm (considered as $\lambda = 0$)
- Vary Ω and take measurements from $\Omega = 100$ rpm to $\Omega = 1000$ rpm

All the measurements (except blade pressure measurements) are taken with a NI (National Instruments) acquisition device (PCIe-6321). An external square signal triggers the NI acquisition and rates the blade pressure measurements sensor (microDAQ) in order to synchronise both devices. Both NI and microDAQ sampling frequencies are equal to 500 Hz and 15000 samples are acquired (30 s). A filtering of the output gage signal is done by the acquisition software at half of the sampling frequency to increase the measurement resolution and improve the signal to noise ratio. Table 4.1 sums up the offset corrections made to the raw measurements.

Variable	Correction
M_{fbm}	$M_{fbm} = M_{fbm}$(mes) - M_{fbm}(Z2)
Drag force	$D = [D$(mes) - D(Z2)] - $D(\lambda = 0)$
Torque	$Q = Q$(mes) - Q(Z2)
Acceleration	$A_{x,y,z} = A_{x,y,z}$(mes) - $A_{x,y,z}$(Z1)
Pitot probe (wall)	$P_{dyn,wall} = P_{dyn,wall}$(mes) - $P_{dyn,wall}$(Z1)
microDAQ	zero done within transducer internal software

Table 4.1: Table summarising the offset corrections to the raw data

4.2.4 Return wind-tunnel test-section

The wind turbine is located in the **return test-section** of the "Lucien Malavard" wind-tunnel of PRISME laboratory as shown in figure 4.12a. Figure 4.12b shows the wind-related coordinate system defined in this test-section: x is in the free-stream flow direction, y in the transverse direction and z in the vertical direction. Two misalignment wind angles α_1 and α_2 are defined in the planes (x, y) and (x, z) respectively. The azimuthal angle of the blades Ψ is defined in the (y, z) plane and in the direction of rotation of the turbine when the observer is facing the wind (anti-clockwise).

The turbine is positioned at the exit of a convergent (4 m × 4 m to 3 m × 3 m) that allows the flow conditioning. At the inlet of the convergent, honeycombs and a turbulence grid are implemented to ensure flow homogeneity. This turbulence grid is shown in figure 4.13 with its specific parameters. The bar width m' and the grid mesh length M' are equal to 25 mm and 225 mm respectively. The rotor is positioned normal to the flow (yaw angle $\gamma = 0°$) and is centred in the homogeneous flow area, the turbine hub being 1.56 m from the test-section floor. The rotor is placed 3.8 m downstream of the turbulence grid. Turbine blockage based in the rotor swept surface in the wind-tunnel test-section (4 m × 4 m) is equal to 9.6% and can be considered as negligible as it remains under 10% (Ryi et al. [2015]). Turbine blockage computed with respect to the section of the convergent exit (3 m × 3 m) is equal to 17% which is over the threshold under which wind-tunnel wall corrections are not necessary. It should be mentioned that these blockage calculations are conservative estimations as the reference surface is taken equal to the rotor swept surface, which is not exactly true. However, the objective of the present wind-tunnel testings is to evaluate an active flow control device (with and without fluidic jets actuation) and comparison with free field turbines is out of the scope. Hence, blockage effects are not considered

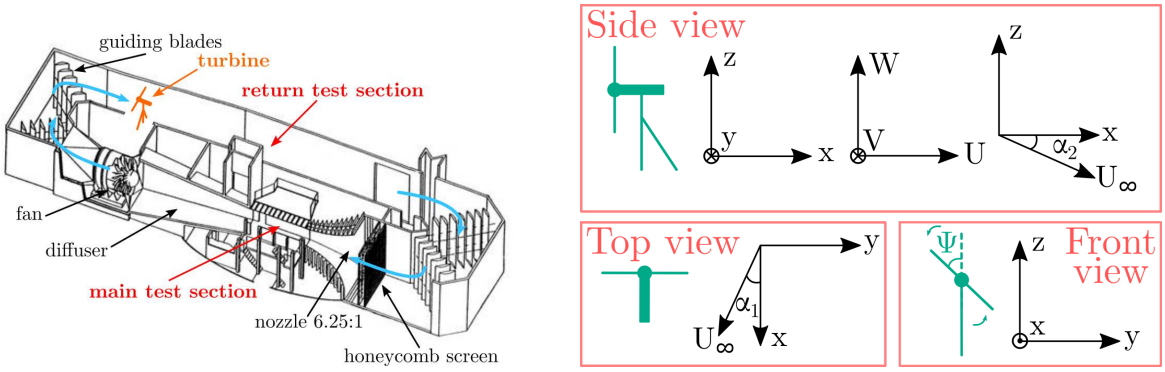

(a) Wind-tunnel scheme

(b) Return test-section axis

Figure 4.12: Schemes of the wind-tunnel test-section and its axis system

in the following. Bartholomay et al. [2017] mentioned a similar explanation regarding their 40% blockage ratio. In the present study, the incoming wind velocity is set at $U_\infty = 10\,\mathrm{m/s}$ with a turbulence intensity level of about 3.8% as is showed in the following.

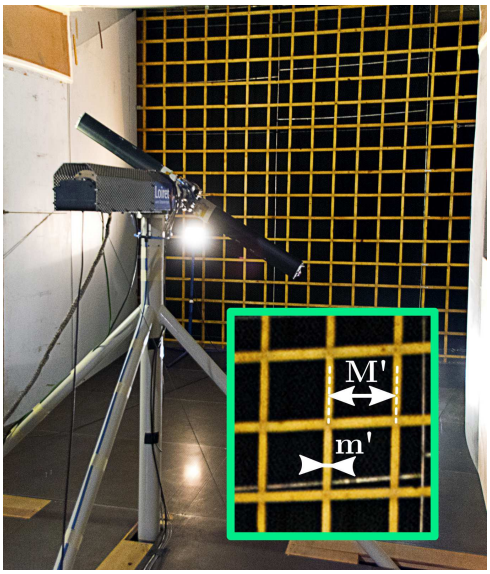

Figure 4.13: Picture of the turbine and the upstream turbulence grid

Test-section characterisation

The return test-section is characterised in terms of flow velocity and turbulence intensity at the turbine location. The objective is to demonstrate that the flow is acceptably homogeneous and also to quantify the turbulence intensity generated by the grid. As there is not a displacement system near the turbine to displace a probe, the turbine itself is used. A two-wire Dantec Dynamics hot-wire (HW) probe (55P61) is fixed at the blade tip of one blade that is previously clamped at a pitch angle of 90° (feathered to the wind). This equipped blade is moved to eight positions equally distributed along the turbine rotational circle. At each of the eight positions, the turbine is at standstill. These positions correspond to eight azimuthal angles Ψ equal to: 0, $\frac{\pi}{4}$, $\frac{\pi}{2}$, $\frac{3\pi}{4}$, π, $\frac{5\pi}{4}$, $\frac{3\pi}{2}$ and $\frac{7\pi}{4}$ radians. The HW measures 40 cm upstream of the rotor and 2^{20} ($\approx 10^6$) samples are taken at 6 kHz.

Velocities in the test-section are defined in figure 4.12b: U in the x-direction, V in the y-

direction and W in the z-direction. The hot-wire is oriented in two different ways in order to measure in the (x, y) plane first and then in the (x, z) plane. Turbulent components are defined as $U(x,y,z,t) = \overline{U}(x,y,z) + u'(x,y,z,t)$, $V(x,y,z,t) = \overline{V}(x,y,z) + v'(x,y,z,t)$ and $W(x,y,z,t) = \overline{W}(x,y,z) + w'(x,y,z,t)$. Markers $\langle\cdot\rangle$ refer to **spatially** averaged quantities for the eight Ψ azimuthal angles.

Figure 4.14 shows time-averaged velocities in the three spatial directions and the eight azimuthal positions along with their spatial average. Velocity $\overline{U}$ is nearly equal to 10 m/s with a small velocity deficit for Ψ angles between 90° and 180°. Transverse velocity $\overline{V}$ remains about -0.3 m/s which may be considered as weak. Finally, vertical velocity $\overline{W}$ average is of -0.1 m/s which is also acceptable. Hence, the incoming wind can be considered as homogeneous in the (y, z) plane and at the blade tip location.

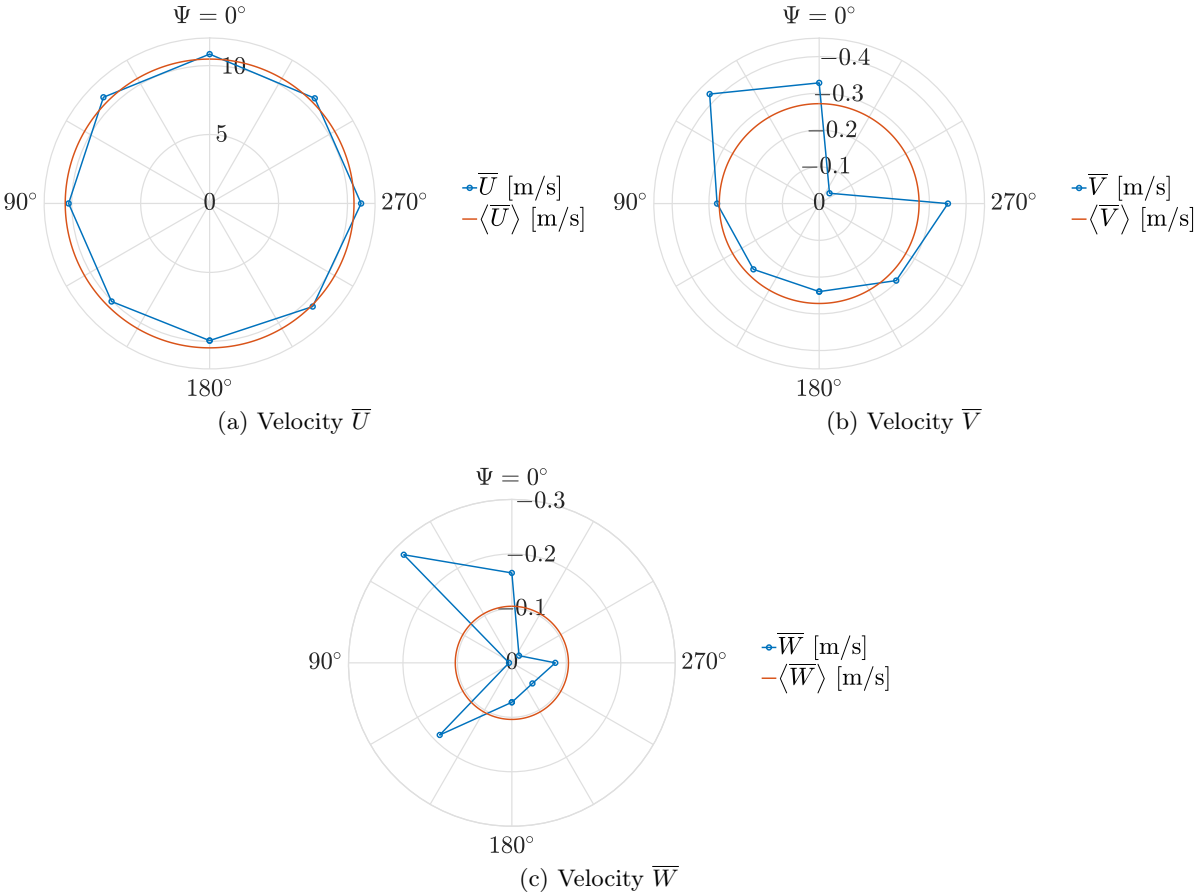

(a) Velocity $\overline{U}$

(b) Velocity $\overline{V}$

(c) Velocity $\overline{W}$

Figure 4.14: Return test-section velocities in the three spatial directions and for eight azimuthal positions Ψ - $U_\infty = 10$ m/s, $\beta = 90°$, turbine at standstill

Local wind misalignment angles α_1 and α_2 can also be computed. It should be mentioned that angle calculation is very sensitive to probe position and orientation. The HW was aligned with the x axis as precisely as possible but a perfect positioning was difficult to obtain due to the lack of reference points in the test-section. The positioning error is estimated to be of about 1°. Average α_1 is of 1.5° meaning that the flows tends to go to the left (when the observer faces the wind). On the other hand, α_2 is on average equal to 0.55° indicating that the flow tends to go weakly to the floor. These angles are however minimal and the flow will be considered as aligned along in the x-direction. Indeed, as the objective of the study is to assess the efficiency of an active flow control strategy, some imperfections in the incoming wind are acceptable as long as wind conditions are reproducible.

Hot-wire measurements also allow the calculation of turbulence intensities defined in equation 4.13. Table 4.2 summarises the obtained turbulence intensities for the two HW probe orientations. It can be concluded that the overall turbulence intensity in the return test-section at the turbine location is equal to 3.8%.

$$T_{u1} = \frac{\sqrt{\overline{u'^2}}}{\sqrt{\overline{U^2} + \overline{V^2}}} \text{ or } T_{u2} = \frac{\sqrt{\overline{u'^2}}}{\sqrt{\overline{U^2} + \overline{W^2}}}; \quad T_v = \frac{\sqrt{\overline{v'^2}}}{\sqrt{\overline{U^2} + \overline{V^2}}}; \quad T_w = \frac{\sqrt{\overline{w'^2}}}{\sqrt{\overline{U^2} + \overline{W^2}}} \tag{4.13}$$

plane (x,y)	$\langle T_{u1} \rangle$	3.82%
	$\langle T_v \rangle$	3.59%
plane (x,z)	$\langle T_{u2} \rangle$	3.83%
	$\langle T_w \rangle$	3.76%

Table 4.2: Table summarising the turbulence intensities in the return test-section and at the turbine location

However, as pointed out by Sicot [2005] turbulence intensity changes along the blade span as the effective velocity augments with the radial position. Radial turbulence intensity can be defined as $T_{ur} = \frac{\sqrt{\overline{u'^2}}}{\sqrt{U_\infty^2 + (\Omega r)^2}}$ and is plotted in figure 4.15 as a function of the radial position $\frac{r}{R}$ and several tip-speed ratios. One can observe that turbulence intensity decreases with the radial position as W_r increases. The more λ increases, the more the T_{ur} decreases along the blade span is important.

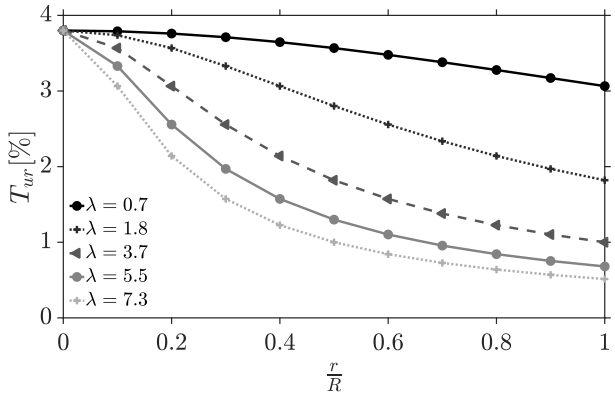

Figure 4.15: Radial turbulence intensity T_{ur} along the blade span for various tip-speed ratios λ

4.2.5 Scalings

Scaling the parameters of model wind turbines with operating rotors is one of the challenges of experimental research at a laboratory scale. As pointed out in Bottasso et al. [2014] it is impossible to match all the physics of the flow and full scale parameters in scaled models. However, wind-tunnel testings have the advantage to involve calibrated testing conditions, known errors and known disturbances. They also have lower costs than field tests and allow to easily measure quantities that are impossible to measure in real conditions. Laboratory-scale tests remain complementary to simulation and field testings and are of great interest to calibrate and validate computational models but also to test new concepts. Several normalised parameters that govern the turbine dynamics are important (Bottasso et al. [2014]):

- The tip-speed ratio: $\lambda = \frac{\Omega R}{U_\infty}$
- The Reynolds number: $Re = \frac{U_\infty c}{\nu}$
- The Froude number: $Fr = \frac{U_\infty^2}{gR}$, where g is the acceleration of gravity. This number represents the ratio of the flow inertia to the gravity field
- The Mach number: $M = \frac{U_\infty}{a}$, where a is the speed of sound
- The Lock number: $Lo = \frac{C_{L,\alpha}\rho c R^4}{I}$, where $C_{L,\alpha}$ is the slope of the lift coefficient curve as a function of the angle of attack α and I is the flapping inertia of the blade. This number represents the ratio between aerodynamical forces and inertia
- The normalised natural frequency: $\tilde{\omega_i} = \frac{\omega_i}{\Omega}$

In their study the authors do the scaling in two steps. First, reduced scale and full scale values of λ, Lo and $\tilde{\omega_i}$ are exactly preserved. Their full scale reference turbine is a Vestas V90 turbine (3 MW, 90 m rotor diameter and 80 m hub height). Then, a minimisation problem is solved to find the best compromise between the other normalised quantities. In the following, subscript $\langle\cdot\rangle_{FS}$ refers to the **full scale** turbine and $\langle\cdot\rangle_M$ to our **model** wind turbine bench. By applying their results to our scaled turbine we find: rotor radius ratio $\frac{R_M}{R_{FS}} = \frac{1}{64}$, Re ratio $\frac{Re_M}{Re_{FS}} = \frac{1}{128}$, Fr ratio $\frac{Fr_M}{Fr_{FS}} = 16$, Mach ratio $\frac{M_M}{M_{FS}} = 0.5$ and temporal scale ratio $\frac{t_M}{t_{FS}} = \frac{1}{32}$.

Table 4.3 compares the temporal and spatial scales of the NREL 5 MW and the present wind turbine bench. Both turbines operate in fairly similar wind velocities U_∞ but the rotational velocity of the scaled bench is 70 times more important. Radial velocities Ωr and relative velocity W_r are, however, in the same order of magnitude. Time scales of the model turbine are 20 times smaller than a 5 MW turbine: chord time constant τ_c for the present turbine is equal to 0.002 s and rotation and turbulent scales are equal to 0.2 s and 0.15 s respectively.

Variable	Unit	NREL 5MW	Rot. cfg.
Rotor radius R	m	57	0.7
Chord at $\frac{2}{3}R$	m	2.4	0.1
Ω	rpm	14	1000
Rated wind velocity U_∞	m/s	14	10
Turbulent scale λ_u (Kaimal et al. [1972])	m	42	-
$r = \frac{2}{3}R$	m	38	0.47
Ωr	m/s	56	49
Relative velocity W_r	m/s	58	50
$\tau_c = \frac{c}{W_r}$	s	0.04	0.002
$\tau_{set} \approx 10\tau_c$	s	0.4	0.02
$\tau_{ROT} = \frac{2\pi}{\Omega}$	s	$4.2 \approx 100\tau_c$	0.2
$\tau_{turb} = \frac{\lambda_u}{U_\infty}$	s	$3 \approx 75\tau_c$	0.15

Table 4.3: Spatial and temporal scales related to the NREL 5 MW wind turbine and to the present wind turbine bench

The present bench is an academical research turbine that is limited in size by the section of the wind-tunnel. The purpose of the present work on the bench is to test a fluidic active flow control strategy. In order to work with a simplified configuration, blades are not twisted nor tapered unlike real operating wind turbines. However, the tip-speed ratio of the model turbine remains in the same order of magnitude as full-scale rotors. Indeed, the high rotational velocities

used in the bench lead to relative velocities in the same order of magnitude of industrial turbines. Temporal and Reynolds scales are not preserved but tip-speed ratio scalings are verified.

4.3 Wind turbine characterisation without actuation

This section introduces the characterisation of the wind turbine bench without actuation. First are analysed the power and thrust coefficients evolution with the tip-speed ratio for a large range of pitch angles. The response of the strain gages on both blades i.e. the flapwise bending moment M_{fbm} of the blades is also studied as well as the pressure coefficient evolution.

Important remark

All the testings have been performed with a constant incoming flow velocity U_∞ equal to 10 m/s. The parameter that allows to change the tip-speed ratio λ is the rotational velocity of the turbine Ω , that can vary from 0 to 1000 rpm.

4.3.1 Global rotor variables: turbine power and thrust

As explained above, the turbine bench is equipped to measure two global variables: the rotor torque and the drag force (or thrust). Turbine torque Q measurement allows the calculation of the power coefficient C_{power} that determines the amount of energy captured by the rotor. The second variable, the rotor drag force D, gives the thrust coefficient C_{thrust}, an important value highlighting the overall efforts undergone by the turbine. Usually power and thrust curves are shown as a function of the normalised variable $\lambda = \frac{\Omega R}{U_\infty}$, known as the tip-speed ratio. Hence, with λ, turbine performances can de determined as a function of a normalised parameter.

Figure 4.16 shows the turbine power coefficient C_{power} as a function of the tip-speed ratio for various pitch angles. The higher values of C_{power} are found for a pitch angle $\beta = 8°$ but the three pitch angles of 6°, 8° and 10° show very similar power curves. The optimal operating point of the turbine is obtained for a tip-speed ratio λ_{opt} equal to 5.5 and corresponds to a maximum power coefficient $C_{power,max}$ equal to 0.42 in agreement with the results obtained with Blade Element Momentum (BEM) theory presented in Aubrun et al. [2015] for the same turbine. The value $C_{power,max}$ is well under the Betz limit equal to 0.6 due to drag and blade-tip losses as well as stall losses for the low tip-speed ratios (Burton et al. [2001, pp. 173-174]). When increasing the pitch angle β, the power coefficient decreases as the aerodynamic performance of the blades is continuously reduced as can be also seen in Bottasso et al. [2014].

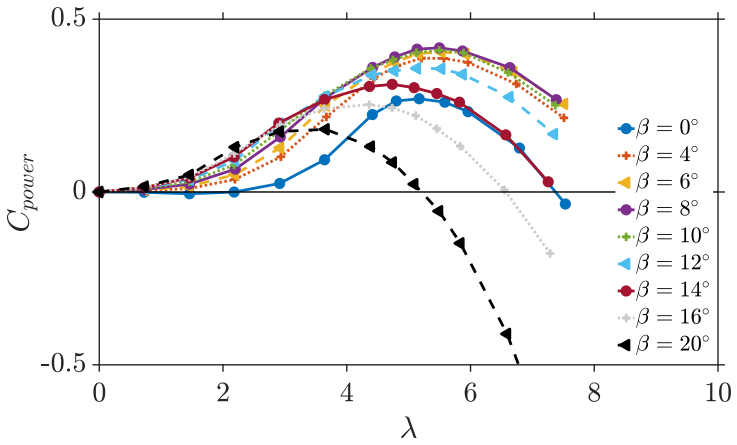

Figure 4.16: Power coefficient C_{power} as a function of the tip-speed ratio λ and for various pitch angles β

Thrust coefficient C_{thrust} as a function of λ is shown in figure 4.17 for various pitch angles. Except for high β angles (over 14°), the thrust force coefficient tends to augment with the tip-speed ratio. The overall value of C_{thrust} decreases with the increase of β because the turbine thrust depends on the lift force. A β augmentation leads to lower angles of attack α and therefore to a lower lift coefficient C_l. A lower C_l results in lower torque Q and drag D of the wind turbine. Maximum C_{thrust} is obtained for the lower pitch angle ($\beta = 0°$) and is equal to 1.4. For the optimal working point of the turbine ($\beta = 8°$ and $\lambda = 5.5$), the thrust coefficient is equal to 0.76. At $\beta = 20°$ and the highest tip-speed ratios, C_{thrust} becomes negative showing that the turbine behaves as a propeller and not as a wind turbine for these specific working points.

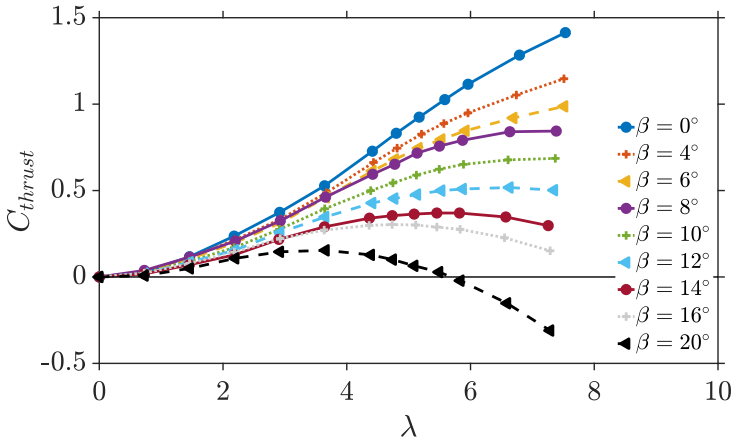

Figure 4.17: Thrust coefficient C_{thrust} as a function of the tip-speed ratio λ and for various pitch angles β

4.3.2 Blade measurements: bending moment and surface pressure

Two measurements are carried out on the blades: the measure of the flapwise bending moment M_{fbm} on both blade roots and the chordwise blade pressure distribution at two different radial positions (one blade). Whereas bending moment is a global measurement at the blade scale, pressure distribution is a local information.

Flapwise bending moment M_{fbm}

Figure 4.18 shows M_{fbm} as a function of the tip-speed ratio λ and for several pitch angles β. Solid and dashed lines correspond to the two different blades. Except for the highest tip-speed ratio ($\lambda = 6.60$), bending moments of both blades remain very similar. The different behaviour of both blades may be caused by a small misbalance of the rotor that would be amplified at high rotational velocities. Flapwise bending moment augments with the tip-speed ratio as mechanical loads become higher with the rotational velocity. The higher the pitch angle β and the lower the M_{fbm} overall level. This behaviour can be justified in the same way as for the turbine thrust: the higher the β pitch angle, the lower the angle of attack α and the lower the lift force acting on the blade C_l. The bending moment experienced by the blades is therefore reduced with the pitch augmentation.

Pressure coefficient C_p

The other blade variable measured in the wind turbine bench is the pressure distribution along the blade chord at two radial positions. Pressure coefficient C_p distribution can be plotted as a function of the tip-speed ratio or of the blade pitch. In the legend of the plots is specified

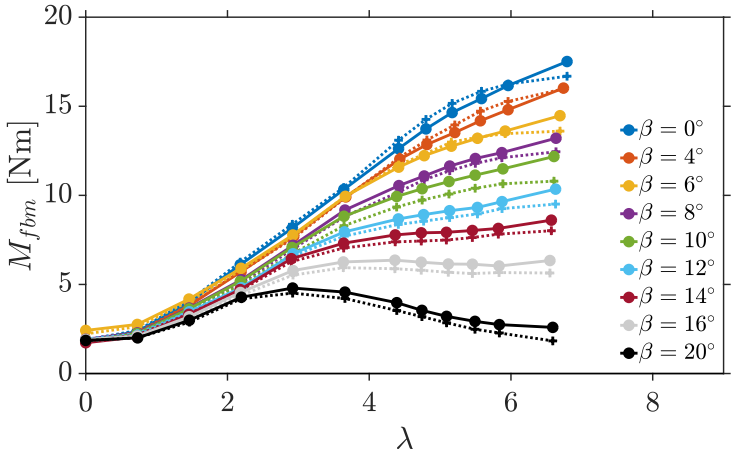

Figure 4.18: Flapwise bending moment M_{fbm} as a function of the tip-speed ratio λ and for various pitch angles β (two blades)

the angle α defined as the **geometrical** angle of attack given by the aerodynamics of the blade airfoil, without taking into account the axial and radial induction factors of the turbine:

$$\alpha = \arctan\left(\frac{U_\infty}{\Omega r}\right) - \beta \tag{4.14}$$

Pitch angle β influence Pressure coefficient C_p distribution along the normalised chord of the blade is shown in figure 4.19 for various tip-speed ratios. Pressure measurement section is located at $r = 0.63R$ and the curves are plotted for several pitch angles and, therefore, several geometrical angles of attack. For the lowest λ (figure 4.19a), corresponding to the lowest rotational velocity, C_p along the pressure side approximates the value $C_p = 1$ for the taps between $\frac{x}{c} = 0.05$ and 0.4 highlighting a stagnation zone for these abscissas where the flow is stopped. In the suction side, the flow is completely detached and C_p is equal to -1.1 all along the chord. Because the flow is completely separated ($\alpha > 45°$), pitch angle does not have a great influence on the pressure distribution at this λ. Figure 4.19b shows C_p distribution for $\lambda = 2.2$ and exhibits a singular pitch angle effect on the pressure coefficient: the C_p shows a small pressure *bump* between the chord positions $\frac{x}{c} = 0.2$ and $\frac{x}{c} = 0.5$ in the suction side that is progressively reduced and smoothed with the pitch increase (and α decrease). For $\lambda = 3.7$ and $\lambda = 5.1$ (figures 4.19c and 4.19d respectively), more classical pressure distributions are found showing a $-C_p$ peak at the suction side leading-edge and a progressive pressure increase along the upper side. The effect of the pitch angle on the C_p is substantial: the greater the β, the lower the α and the more the pressure is increased in the suction side and decreased in the pressure side, leading to a C_l reduction. In the case of $\lambda = 5.1$ and $\beta = 20°$, the geometrical angle of attack is negative and the C_p curves of both blade sides intersect, changing the sign of the resultant force. These curves are coherent with the previous C_{thrust} curves: for a constant λ, the local C_l is reduced with the β augmentation leading to C_{thrust} and C_{power} reductions.

Tip-speed ratio λ influence The influence of the tip-speed ratio can be more clearly seen in figure 4.20 where the pressure distribution is plotted for two pitch angles β and as a function of λ. Pressure measurement section is located at $r = 0.63R$ (figures 4.20a and 4.20b) and at $r = 0.88R$ (figures 4.19c and 4.20d). For both plotted β, the tip-speed ratio increase changes drastically the geometrical angle of attack α and therefore the chordwise pressure distribution. In the case of $\beta = 8°$, C_p along the suction side decreases up to $\lambda = 2.9$ and then increases. Indeed, at the lower λ the flow is totally separated and by increasing the tip-speed ratio the flow attaches to the suction side of the blade. Then, as λ is increased, α is reduced and so the

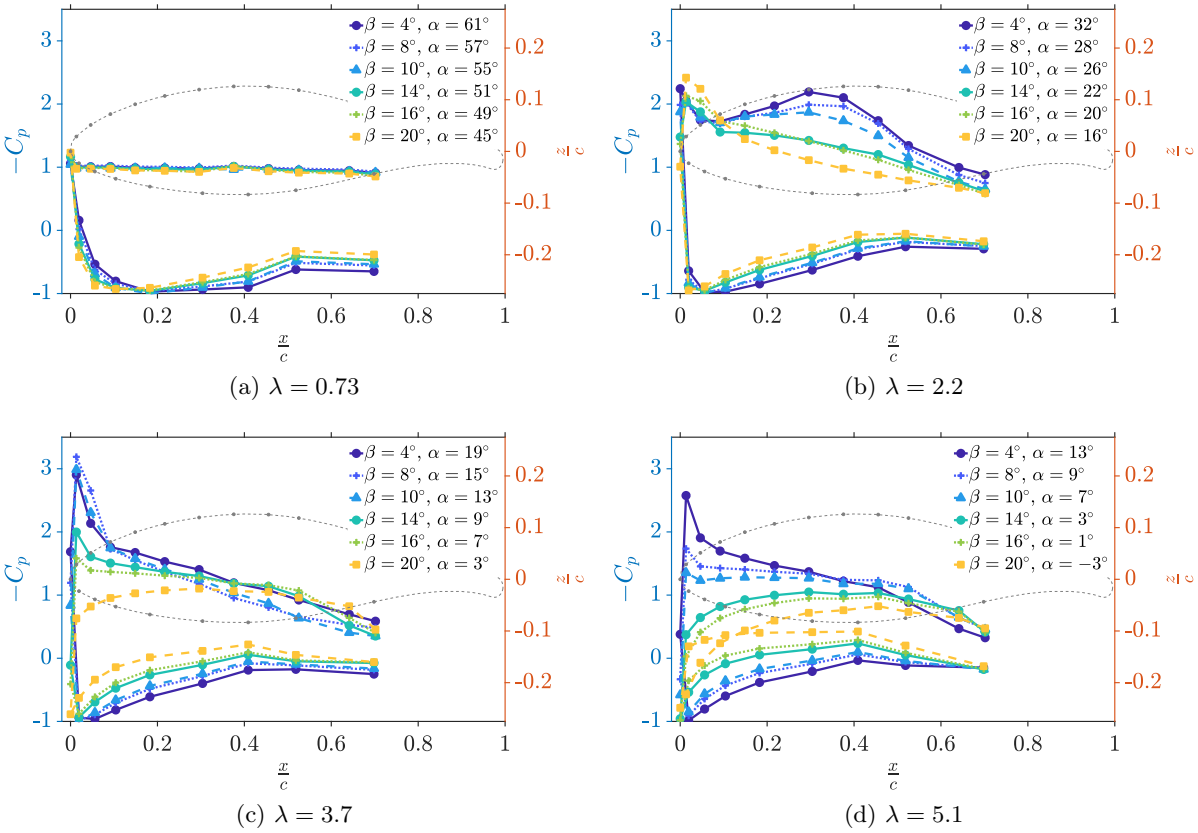

(a) $\lambda = 0.73$ (b) $\lambda = 2.2$

(c) $\lambda = 3.7$ (d) $\lambda = 5.1$

Figure 4.19: Pressure coefficient C_p distribution as a function of the pitch angle β for various tip-speed ratios λ ($r = 0.63R$)

overall pressure over the blade. Pressure level along the pressure side always decreases with the λ augmentation. In the case of $\beta = 16°$, the pressure levels change mostly for the higher λ with respect to $\beta = 8°$. As this pitch angle is not optimal, pressure levels are important in the suction side and low in the pressure side inducing smaller integrated forces than $\beta = 8°$. Comparing the curves at equal pitch angle but at a different blade span gives that the curves at $r = 0.88R$ show systematically a lower C_p on the pressure side and a higher C_p on the suction side, except from the case at $\lambda = 0$ where both cases are superimposed. Again, this is due to the fact that for a given β and λ the geometrical angle of attack α is reduced for the higher radial position.

4.4 Flow control in a rotational configuration

This section summarises the effects of the flow control actuation on the wind turbine performances. The impact of the actuation on the bending moment, the chordwise pressure distribution and the thrust and drag of the turbine are examined. As mentioned above, only the blades blowing from the **upper-side** of the blade are tested in this configuration. In preceding chapter 3, it was shown that actuation increases the lift force. In the present rotational case, an **increase of the lift force leads to an increase in the flapwise bending moment** at the blade root. This actuation concept would therefore be used to counteract the effect of a gust that would reduce the lift force and the bending moment of the blade. Another control approach might be to blow continuously at a certain flow rate but to regulate the flow rate intensity depending on the desired action i.e. a bending moment increase or decrease.

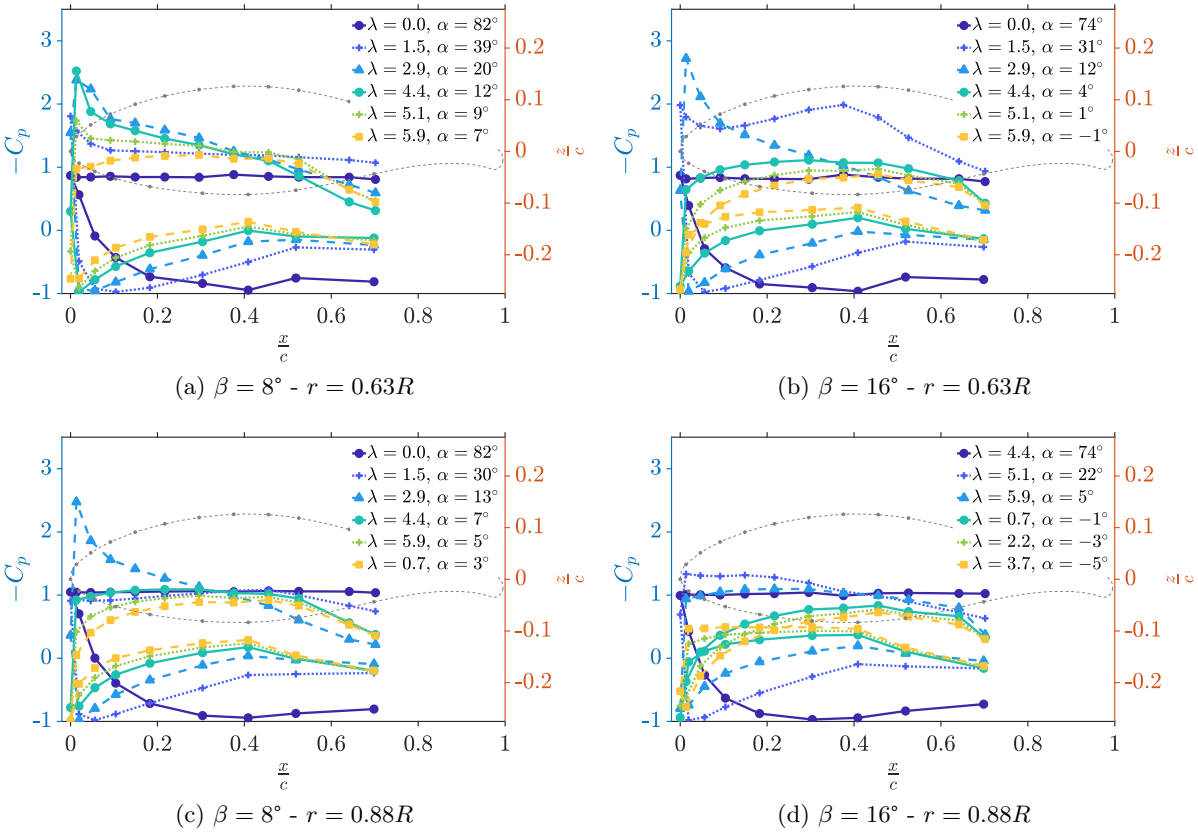

(a) $\beta = 8°$ - $r = 0.63R$

(b) $\beta = 16°$ - $r = 0.63R$

(c) $\beta = 8°$ - $r = 0.88R$

(d) $\beta = 16°$ - $r = 0.88R$

Figure 4.20: Pressure coefficient C_p distribution as a function of the tip-speed ratio λ for two pitch angles β

3D surfaces

In the sake of brevity, some plots are three dimensional and show the actuation effects as a function of two parameters (λ and β). For all these plots, the surface level will correspond to the **baseline case**, whereas surface color scale will correspond to the **variation (gain or loss)** of the plotted variable.

4.4.1 Flapwise bending moment

One of the most important measurements that is carried out in the wind turbine bench is the flapwise bending moment at the blade roots (see figure 4.21). As mentioned above, load fluctuations caused by wind unsteadiness induce bending moment variations that increase blade fatigue and reduce the rotor life duration. In the perspective of a closed-loop control targeting a load fluctuation alleviation, the bending moment measure might be a suitable parameter to react on.

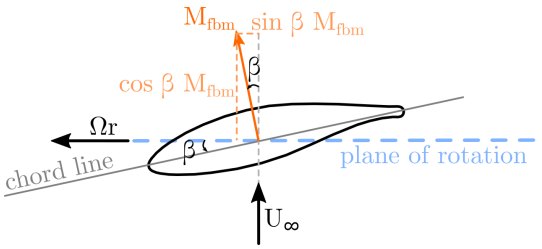

Figure 4.21: Flapwise bending moment M_{fbm} and its projection in the turbine-related coordinate system

Figure 4.22 shows the flapwise bending moment M_{fbm} as a function of the tip-speed ratio λ for the baseline case and the two controlled

cases and a pitch angle $\beta = 8°$. Figure 4.22a shows the overall evolution of M_{fbm} whereas figure 4.22b shows the evolution of the bending moment variation ΔM_{fbm} from the baseline case. As for the translational configuration, it can be concluded that the higher the pressure on the plenum chamber (i.e. the higher the momentum coefficient), the higher the effect of the actuation on the bending moment. The effect of the actuation is especially strong for the tip-speed ratios ranging from 2 to 4, reaching ΔM_{fbm} of 0.4 N m and 1 N m for P1 and P2 cases respectively. For low and high tip-speed ratios ($\lambda < 1$ and $\lambda > 5$) the actuation effectiveness is lower.

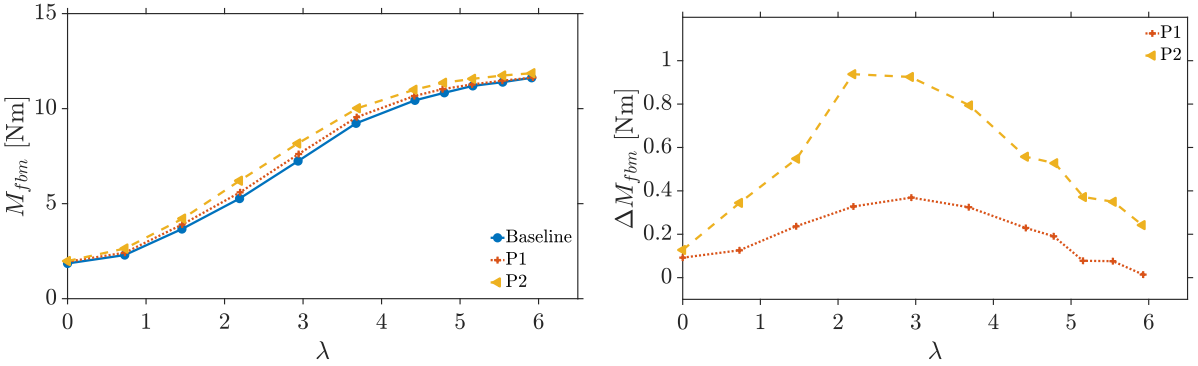

(a) Flapwise bending moment M_{fbm}

(b) Flapwise bending moment variation ΔM_{fbm}

Figure 4.22: Flapwise bending moment M_{fbm} and its variation ΔM_{fbm} as a function of the tip-speed ratio λ for the baseline case and two control cases - $\beta = 8°$

Figure 4.23 shows bending moment evolution as a function of two parameters: the pitch angle β and the tip-speed ratio λ. In the case of figure 4.23a, the figure shows the flapwise bending moment M_{fbm} and figure 4.23b plots the value of the momentum coefficient projection on the plane of rotation of the turbine ($\sin\beta \times M_{fbm}$) as shown in figure 4.21. Surface levels in the figures show the baseline case and surface colors depict bending moment variation ΔM_{fbm} obtained with the actuation case P2.

Figure 4.23a shows that the actuation is specially effective for the tip-speed ratios between 2 and 4.5. All the pitch angles seem reactive to the actuation but lowest β, from 4° to 12°, show the highest gains that reach values up to 1 N m, which corresponds to a ΔM_{fbm} of about +10%. When the flapwise bending moment is projected on the plane of rotation (figure 4.23b), the distribution of $\Delta(\sin\beta \times M_{fbm})$ gain is changed. Indeed, in this case, the gains obtained with the actuation correspond to the same tip-speed ratios but are more apparent for the higher pitch angles, from $\beta = 14°$ to 20°. Maximal $\Delta(\sin\beta \times M_{fbm})$ gains are of about 0.2 N m which also represents a gain of about 10% of the baseline value.

Another way to analyse the bending moment evolution with the flow control actuation is by calculating a flapwise bending moment coefficient C_{fbm}, defined in analogy with the power coefficient:

$$C_{fbm} = \frac{M_{fbm}\Omega}{\frac{1}{2}\rho U_\infty^3 S_{rotor}} \tag{4.15}$$

This coefficient C_{fbm}, but also its projection $\sin\beta \times C_{fbm}$, are plotted as a function of the pitch angle β and the tip-speed ratio λ in figures 4.24a and 4.24b. As the bending moment coefficient is now normalised it takes into account the rotational velocity of the turbine and the inflow conditions. The shape of the baseline surfaces is slightly changed with respect to the previous surfaces representing dimensional M_{fbm}. The gains in C_{fbm} are mostly apparent for the intermediary tip-speed ratios and the lowest pitch angles. The effect of the actuation is very low for λ higher than 5 and lower than 1. Maximal ΔC_{fbm} is equal to 0.05 which corresponds to an increase of 10% for $\beta = 4°$. If we look at the projection of C_{fbm} on the plane of rotation of

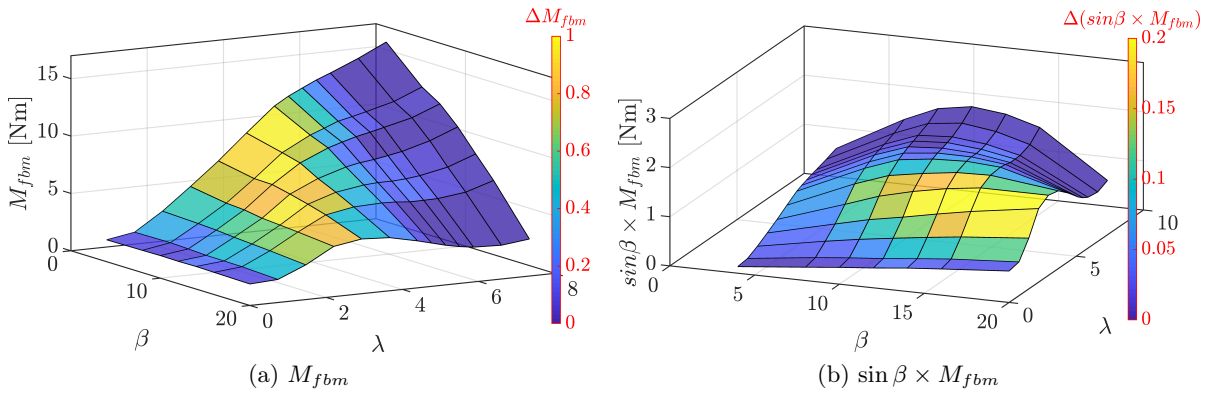

(a) M_{fbm} (b) $\sin\beta \times M_{fbm}$

Figure 4.23: Flapwise bending moment M_{fbm} as a function of the tip-speed ratio λ and the pitch angle β - surface shape depicts the baseline case, colors show the respective variation for control case P2

the turbine, gains are again mostly perceptible for the higher β. The maximal gain obtained is of 8.3×10^{-3} that corresponds to 17% of the baseline case at $\beta = 20°$.

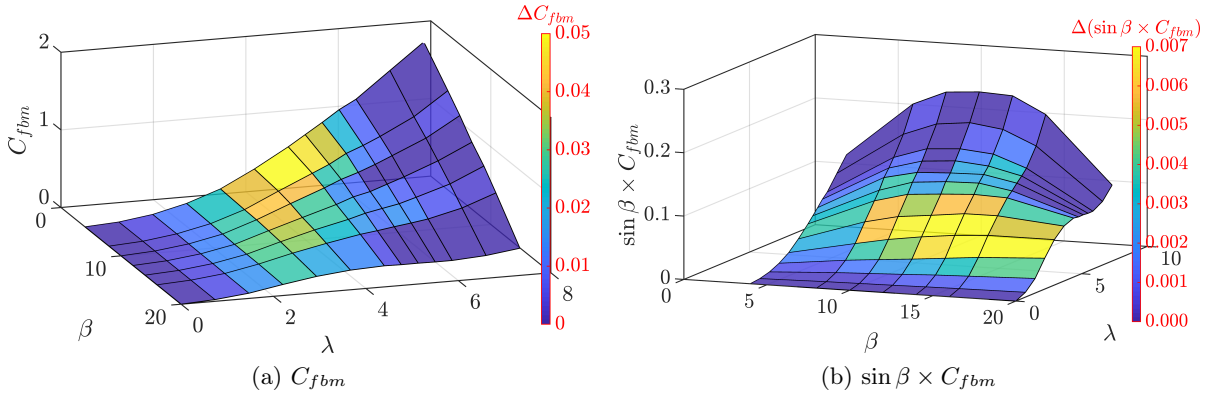

(a) C_{fbm} (b) $\sin\beta \times C_{fbm}$

Figure 4.24: Flapwise bending moment coefficient C_{fbm} as a function of the tip-speed ratio λ and the pitch angle β - surface shape depicts the baseline case, colors show the respective variation for control case P2

4.4.2 Chordwise pressure distribution

Pressure distribution along the blade chord is measured at two different radial positions: $r = 0.63R$ and $r = 0.88R$. This measure allows the calculation of the pressure coefficient C_p which calculation method is explained in section 4.2.3 (p.116). First are analysed the C_p distributions along the chord as a function of the tip-speed ratio and the two radial positions. Then, pressure coefficient is integrated in order to obtain local load coefficients that will be plotted as a function of λ and β.

Pressure coefficient C_p

Figures 4.25a and 4.25b show the C_p distribution and its variation ΔC_p for two controlled cases and the two radial positions. C_p variation with respect to the baseline case, named ΔC_p, is defined as the pressure coefficient increase or decrease under actuation with respect to the baseline case. Figure 4.25 refers to $\beta = 8°$ and $\lambda = 2.20$ whereas figure 4.26 concerns $\beta = 8°$ and $\lambda = 3.66$.

Actuation does not change the pressure on the lower side of the blade but decreases the C_p on the suction side. As highlighted for the translational configuration, the more powerful the actuation the more the C_p is reduced in the upper side. For this pitch angle β of 8°, the pressure coefficient levels are more important for the radial position $r = 0.88R$ because the geometrical angle of attack α is greater. Pressure coefficient losses up to -0.4 are performed for a tip-speed ratio of 2.20. In the case of $r = 0.63R$ where a small pressure *bump* appears along the suction side of the blade, the lift coefficient loss remains high from the leading-edge to $\frac{x}{c} = 0.4$. In the other cases, for lower α, ΔC_p values are mostly important at the leading-edge and remain constant from $\frac{x}{c} = 0.1$ to $\frac{x}{c} = 0.7$. The flow control actuation seems to be more effective for the lowest radial position $r = 0.63R$ than for $r = 0.88R$ (area less affected by the tip vortex). Of course, as pressure taps near the trailing-edge are not available, the pressure distribution near the trailing-edge and specially near the jets holes remains unknown.

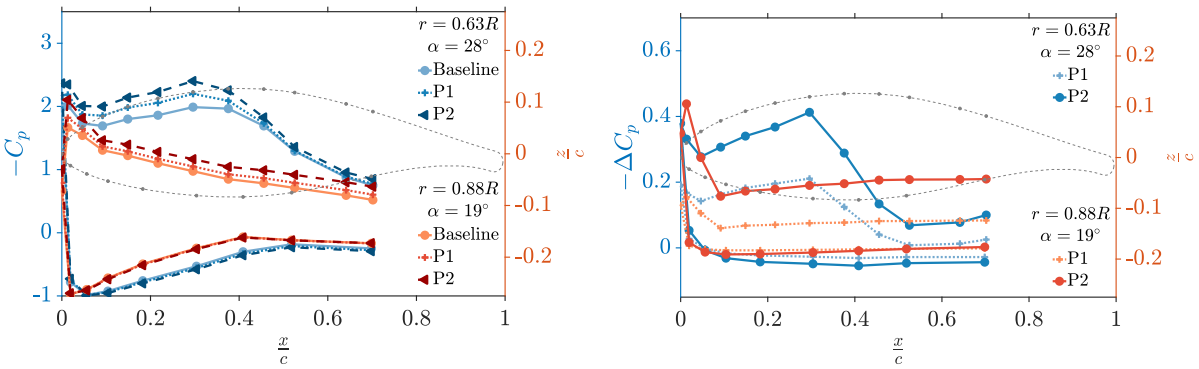

(a) C_p distribution (b) ΔC_p distribution

Figure 4.25: Pressure coefficient C_p distribution at two different blade spans for the baseline case and two control cases (P1 and P2) - $\beta = 8°$ and $\lambda = 2.20$

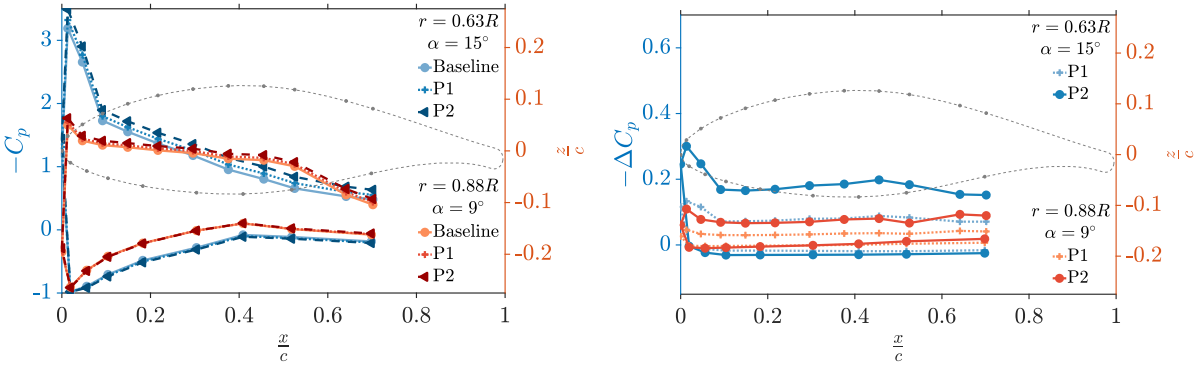

(a) C_p distribution (b) ΔC_p distribution

Figure 4.26: Pressure coefficient C_p distribution at two different blade spans for the baseline case and two control cases (P1 and P2) - $\beta = 8°$ and $\lambda = 3.66$

Line plots illustrate the obtained C_p variations and allow to have a wider view of the actuation performances. Figures 4.27 and 4.28 show the C_p distribution along $\frac{x}{c}$ as a function of the tip speed ratio λ. Each subfigure corresponds to a given pitch angle β. Geometrical angle of attack α is indicated for each C_p distribution. In the sake of clarity, the blade airfoil has been superimposed in the figures at $\lambda = 0$. Lines correspond to the baseline C_p distribution and dot colors to the variation ΔC_p. Figure 4.27 corresponds to the radial position $r = 0.63R$ and figure

4.28 to $r = 0.88R$.

For the lowest radial position $r = 0.63R$ (figure 4.27), the overall pressure coefficient C_p level is higher than for the radial position $r = 0.88R$. However, for both blade spans, we can notice that the lower values of C_p ($-C_p$ peak) move from higher to lower tip-speed ratios when the pitch angle is increased. These lowest C_p values are obtained for a range of angles of attack from $\alpha = 14°$ to $\alpha = 16°$. C_p decrease along the suction side of the blade is mostly performed for the tip-speed ratios between 1 and 4, which is coherent with bending moment measurements. Actuation does not change the pressure distribution for $\lambda > 4$, specially for the highest pitch angles ($\beta = 14°$ to $20°$). Pressure coefficient losses up to -0.6 are performed for $\lambda = 2$ to 3. The average value of the pressure coefficient C_p variations are of about -0.2 to -0.4.

For the highest blade span $r = 0.88R$ (figure 4.28), actuation is less efficient and only C_p losses up to -0.4 are obtained. The most reactive pitch angles are the highest, over $\beta = 12°$. It is clear that for this radial position, the actuation does not perform a pressure distribution modification for tip-speed ratios over $\lambda = 3$. Performed ΔC_p with the actuation is quite homogeneous along the chord with slight higher losses in the vicinity of the leading-edge of the blade.

C_p distribution curves demonstrate that the actuation works in a rotational configuration in the same way as it does in the translational one, modifying mainly the pressure in the suction side of the blade. Actuation is not effective for angles of attack corresponding to an attached flow (up to $\alpha = 10°$) but modifies the pressure distribution for α angles over $14°$ (when separation rises along the suction side) and up to about $50°$ (totally separated flow).

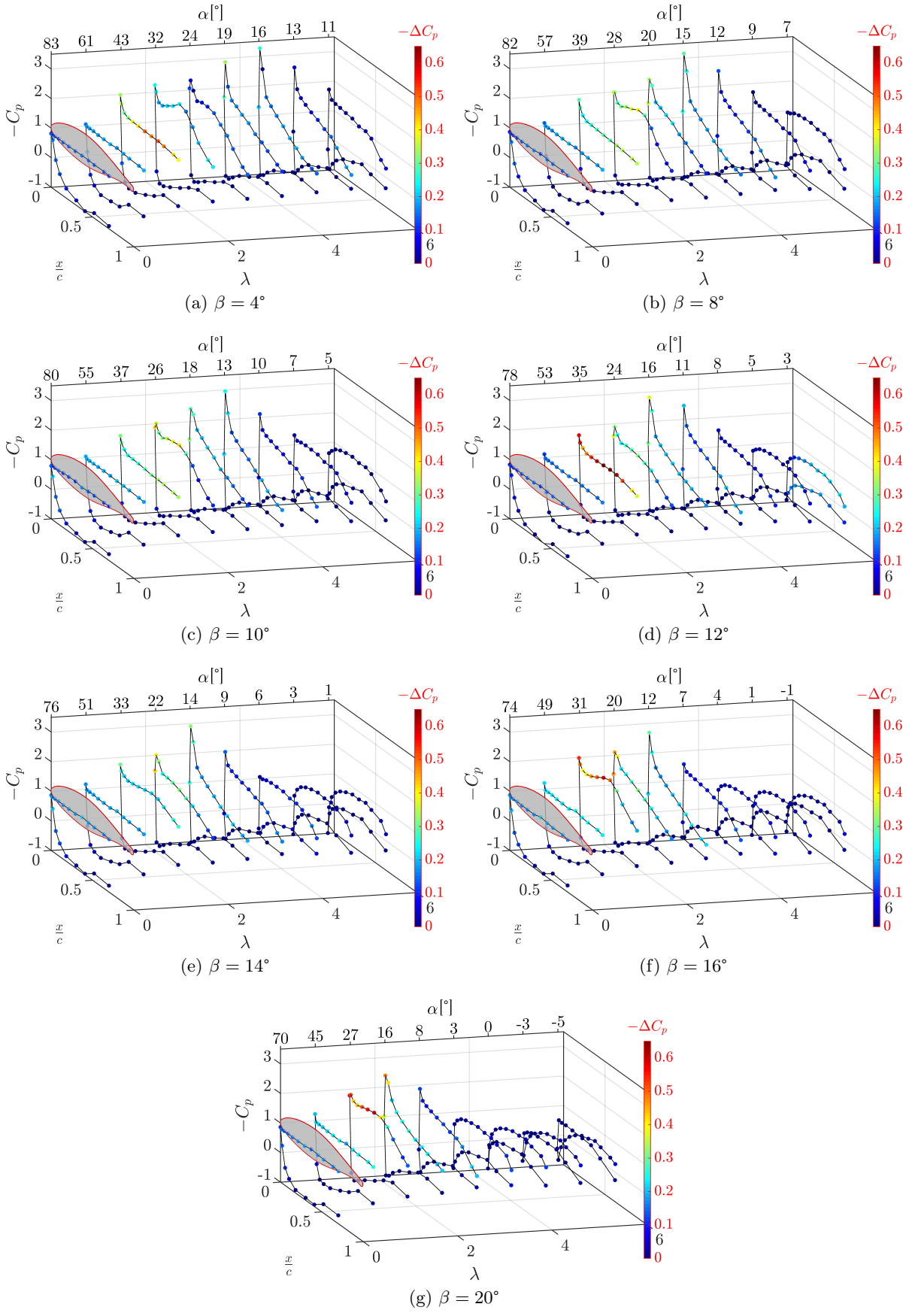

(a) $\beta = 4°$ (b) $\beta = 8°$

(c) $\beta = 10°$ (d) $\beta = 12°$

(e) $\beta = 14°$ (f) $\beta = 16°$

(g) $\beta = 20°$

Figure 4.27: C_p distribution along $\frac{x}{c}$ as a function of λ for different pitch angles β - lines depict the baseline case, dot colors show the ΔC_p variation for control case P2 - $r = 0.63R$

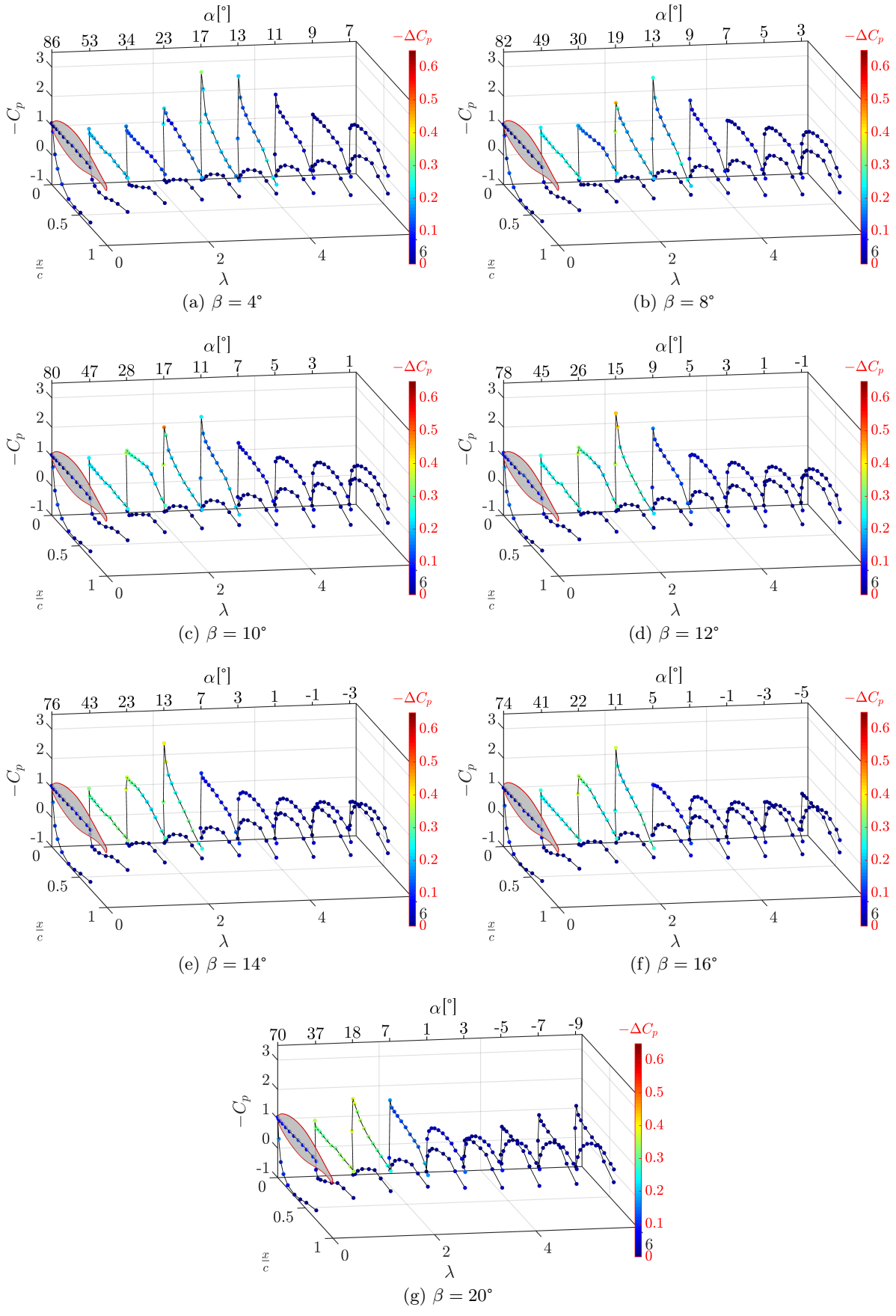

(a) $\beta = 4°$

(b) $\beta = 8°$

(c) $\beta = 10°$

(d) $\beta = 12°$

(e) $\beta = 14°$

(f) $\beta = 16°$

(g) $\beta = 20°$

Figure 4.28: C_p distribution along $\frac{x}{c}$ as a function of λ for different pitch angles β - lines depict the baseline case, dot colors show the ΔC_p variation for control case P2 - $r = 0.88R$

Pressure coefficient integration: local load coefficients

Normal force coefficient C_n and tangential force coefficient C_t are computed via the C_p distribution integration using a trapezoidal method. For this C_p integration, a fictive point is added at the trailing-edge at $\frac{x}{c} = 1$ and $\frac{z}{c} = 0$ with a C_p value equal to the average of the last pressure taps on pressure and suction sides. As the blade trailing-edge is not equipped in pressure taps, these coefficients are formally inaccurate because the pressure deficit induced by the blowing in the vicinity of the TE is not measured. This integration allows, however, to quantify and to evaluate the effectiveness of the actuation in a simple way thanks to the pressure distribution measures.

Integration is performed from the trailing-edge to the leading-edge along the suction side of the airfoil, and then again to the trailing-edge but along the pressure side. C_n and C_t computation formulas are shown in equations 4.16 and 4.17 respectively, where N_{taps} is the number of pressure taps, x_{tap} the distance along the chord line from the leading-edge to i$^{\text{th}}$ pressure tap and z_{tap} the distance orthogonal to chord to the i$^{\text{th}}$ pressure tap.

$$C_n = \sum_{i=1}^{N_{taps}+1} \frac{C_{p,i+1} + C_{p,i}}{2} \left(\frac{x_{tap,i+1} - x_{tap,i}}{c} \right) \tag{4.16}$$

$$C_t = -\sum_{i=1}^{N_{taps}+1} \frac{C_{p,i+1} + C_{p,i}}{2} \left(\frac{z_{tap,i+1} - z_{tap,i}}{c} \right) \tag{4.17}$$

C_n and C_t coefficients can be projected to obtain local lift and drag coefficients (C_l and C_d respectively). The angle used in this projection is the angle α, defined between the chord line and the relative velocity W_r direction (see figure 4.3). As a first approximation, this angle is computed neglecting the turbine axial and radial induction factors:

$$\alpha = \Phi - \beta \tag{4.18}$$

$$= \arctan\left(\frac{U_\infty}{\Omega r}\right) - \beta \tag{4.19}$$

And the projection yields:

$$C_l = C_n \cos\alpha - C_t \sin\alpha \tag{4.20}$$

$$C_d = C_t \cos\alpha + C_n \sin\alpha \tag{4.21}$$

On another hand, local power and thrust coefficients (C^{loc}_{power} and C^{loc}_{thrust} respectively) can also be defined by projecting C_n and C_t in the turbine-related coordinate system. The angle used for this projection is the pitch angle β:

$$C^{loc}_{power} = -C_t \cos\beta + C_n \sin\beta \tag{4.22}$$

$$C^{loc}_{thrust} = C_n \cos\beta + C_t \sin\beta \tag{4.23}$$

Figure 4.29 shows local force coefficients as a function of the tip-speed ratio λ and the pitch angle β. Figures on the left column correspond to the radial position $r = 0.63R$ and figures on the right to $r = 0.88R$. In the same way as above, the shape of the surface illustrates the baseline case and colors the gain or loss of the respective load coefficient with respect to the baseline case and for actuation case P2. These force coefficients calculations allow to obtain one single value to plot for a given λ and β and override the chordwise C_p dependence.

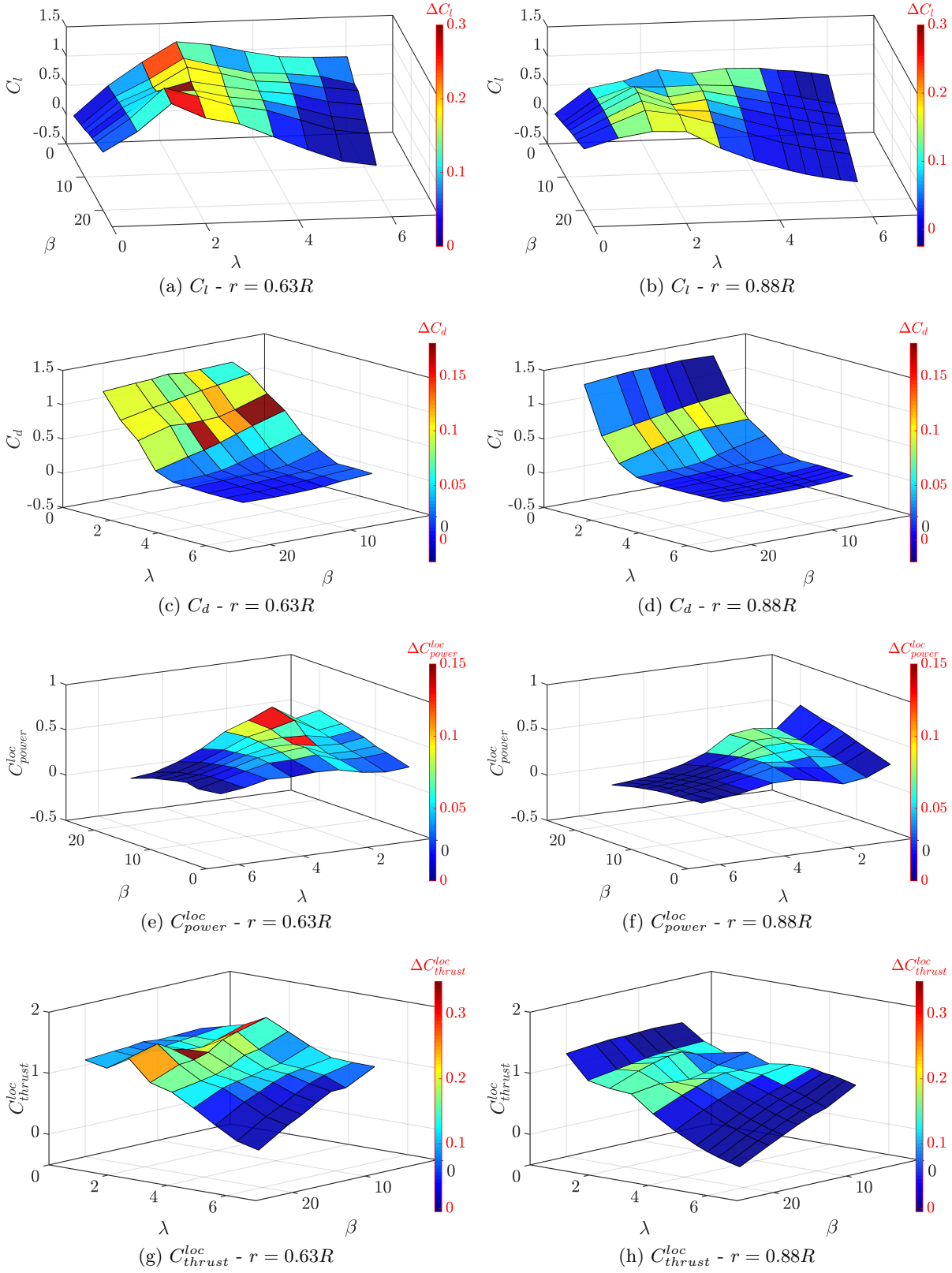

(a) C_l - $r = 0.63R$ (b) C_l - $r = 0.88R$

(c) C_d - $r = 0.63R$ (d) C_d - $r = 0.88R$

(e) C^{loc}_{power} - $r = 0.63R$ (f) C^{loc}_{power} - $r = 0.88R$

(g) C^{loc}_{thrust} - $r = 0.63R$ (h) C^{loc}_{thrust} - $r = 0.88R$

Figure 4.29: Local load coefficients C_l, C_d, C^{loc}_{power} and C^{loc}_{thrust} as a function of the tip-speed ratio λ and the pitch angle β for two different blade spans $r = 0.63R$ and $r = 0.88R$ - surface shape depicts the baseline case, colors show the respective variation for control case P2

Most of the local lift coefficient C_l gains are about $+0.18$ ($\approx +20\%$) with some peak values reaching $+0.3$ ($\approx +30\%$) at $\lambda = 2.2$. As demonstrated above with the pressure distribution, lift coefficient gains take place mainly for $\lambda \in [2;4]$ for almost all the available pitch angles. Lift coefficient remains unchanged for tip-speed ratios over 4.5, specially for the highest blade span $r = 0.88R$. Regarding the local drag coefficient C_d, its value decreases with the tip-speed ratio starting from values near 1 to attain a C_d close to zero. Local drag coefficient is increased with the actuation of $\Delta C_d \approx 0.07$ ($\approx 10\%$) for the lowest tip-speed ratios. Drag coefficient increase is more important for the lowest blade span than for $r = 0.88R$, which only shows a significant local drag increase for $\lambda = 0.73$. Concerning the local power coefficient C^{loc}_{power} it mainly increases for high pitch angles and tip-speed ratios ranging from 1 to 4. Average gain is about $+0.075$ ($\approx 20\%$) but maximal values of ΔC^{loc}_{power} reach $+0.15$ ($\approx 30\%$). Again, flow control is more effective for the lower radial position. Finally, local thrust coefficient C^{loc}_{thrust} is also increased of values from $+0.1$ to $+0.2$ ($\approx 25\%$) with peak values at $+0.3$ ($\approx 15\%$). For both C^{loc}_{power} and C^{loc}_{thrust} actuation does not change the turbine performances for the highest tip-speed ratios over $\lambda = 4$, a range of λ showing low momentum coefficient values as was mentioned above.

4.4.3 Torque and drag force

The effect of the actuation on the thrust and torque of the turbine can *theoretically* be measured with the instrumentation available on the wind turbine bench.

And yet...

The rotary joint that carries the compressed air to the blades adds a frictional torque to the rotor that is measured by the sensor. Attempts were made to characterise this induced friction torque and subtract it but were abandoned as the friction depended on several variables difficult to evaluate with the available set-up (internal joint heating and temperature). As the rotary joint was necessary for the flow control application, it was impossible to perform the testings without it. Greenblatt et al. [2012] highlighted the same issue and concluded that for small scale wind-tunnel testings slip rings and rotary joints have significant effects. The authors also prove that turbine up-scaling reduces dramatically the influence of these devices. Nevertheless, torque and drag measurements are acquired along with the other measurements and are presented in the following for the flow control application.

Remark: Power and thrust curves shown in section 4.3 (figures 4.16 and 4.17 on p.125 and p.126 respectively) are still valid though: measurements were taken with the rotary joint unleashed i.e. *all* the rotary joint rotates with the shaft, even the part that is supposed to be stationary in figure 4.6 (the joint is not working).

Figure 4.30 shows the turbine power and thrust coefficients as a function of the tip-speed ratio λ and the pitch angle β. As mentioned above, these results should be taken with precaution as measures are distorted by the rotary joint presence.

In the case of the power coefficient C_{power} gains are mostly concentrated on the highest λ and reach up to $+0.1$. The distribution of ΔC_{power} differs strongly from the one obtained by the C_p integration but the order of magnitude of the gain remains similar. Concerning the thrust coefficient C_{thrust} no conclusions can be drawn as C_{thrust} is either increased of decreased without any clear trend.

4.5 Conclusion

The wind turbine bench of PRISME laboratory has been equipped for a fluidic flow control application. Two measurements can be made on the blades: the flapwise bending moment

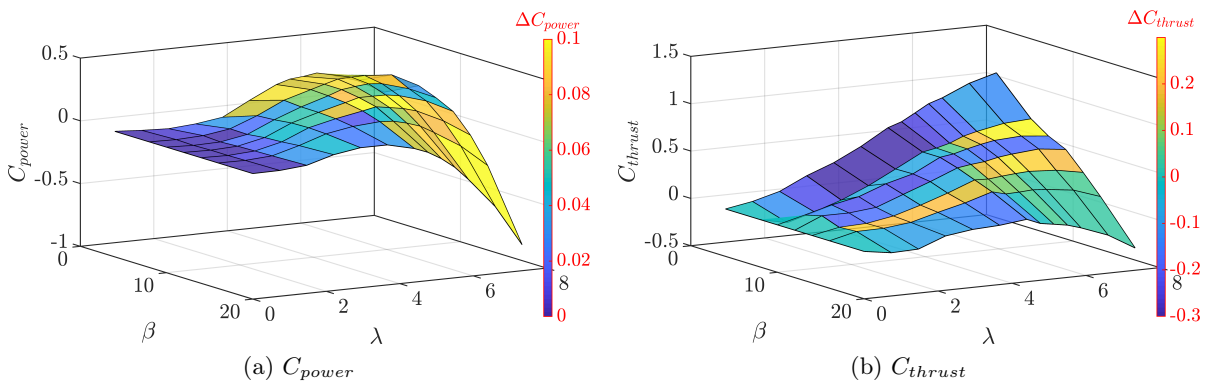

(a) C_{power} (b) C_{thrust}

Figure 4.30: Power and thrust coefficients (C_{power} and C_{thrust} respectively) as a function of the tip-speed ratio λ and the pitch angle β - surface shape depicts the baseline case, colors show the respective variation for control case P2

(global measurement) at the blade roots and the surface pressure distribution at two different radial positions (local measurement). Global rotor quantities such as the overall torque and drag of the turbine are also measured.

After the actuation validation in a translational configuration presented in chapter 3, blades are tested in a rotational configuration for several pitch angles and tip-speed ratios. The effect of the actuation is to increase the lift coefficient and therefore the blade root flapwise bending moment. Bending moment variations up to about +10% of the baseline levels are obtained.

Pressure measurements show that the mechanisms of the actuation are similar to the ones highlighted for the translational case. Pressure distribution curves have to be analysed taking into consideration the geometrical angle of attack. Actuation effect is very limited, if not absent, for attached flows between $\alpha = -10°$ and $\alpha = 10°$. However, the effect of the actuation seems stronger for partially separated flows or totally stalled flows (from $\alpha = 14°$ to $\alpha = 50°$). Pressure coefficient variation is mainly important in the suction side of the blade and reaches values up to -0.6 for pressure taps near the leading-edge.

Torque and drag of the turbine couldn't be measured because of the added friction induced by the rotary joint. However, the calculation of local power and thrust coefficients via pressure integration leads to gains of about 20% and 15% respectively.

Chapter 5

And now... what about energy balances?

Contents

5.1 Introduction

This chapter is an attempt to evaluate the efficiency of the flow control devices studied in the frame of the thesis work. In the field of active flow control, it is important to evaluate the amount of energy provided to the actuator and the energy effectively recovered as a result of the actuation. These calculations give an idea of the overall actuation efficiency. Indeed, active flow control studies in the wind energy field usually show promising results in the controlled environment of the laboratory wind-tunnel but seldom reach an industrial level of integration. The objective of this chapter is not to demonstrate the industrial feasibility of the studied strategies but it merely intends to go further the aerodynamical gains. The goal of the chapter is to study the overall energy balance of the different actuations through diverse points of view in order to be able to analyse the load reduction outcomes.

However, it is important to mention that all the calculations are solely estimations that should be considered as orders of magnitude. In most of the cases, they are computed for the working points showing the highest gains and for the maximal actuation strength i.e. maximal C_μ. Also, it is important to notify that no efforts have been done to optimise the actuators in terms of power consumption. Furthermore, all the testings are performed in an open-loop configuration meaning that the actuation is not optimised either with the use of a feedback regulation.

Several methods are analysed in the following with increasing degree of complexity.

5.2 Overall Figure of Merit

Before the evaluation of the efficiency in terms of *the aerodynamic gains*, the energy balance of the **actuator itself** should be estimated i.e. how *good* the actuator is to convert the received power (electrical, pneumatic) into momentum. Seifert [2007] defines the Overall Figure of Merit (OFM). This variable does not take into account the performances of the actuation in terms of load gains but solely considers the strength of the momentum injection defined in quiescent air and the power supplied to the device. It is defined as:

$$\mathrm{OFM} = \frac{F_a^2 U_a}{\mathcal{P}_S W_a} \tag{5.1}$$

where F_a is the thrust of the actuator in quiescent air, U_a the actuator exhaust velocity, $\mathcal{P}_S$ the power supplied to the actuator and W_a the weight of the flow control device itself.

5.2.1 Evaluation of OFM terms

Table 5.1 shows how the different OFM quantities are obtained or estimated.

	DBD	Fluidic
$\mathcal{P}_S$	Measured	Estimated
W_a	Estimated	Estimated
U_a	Obtained via PIV	Measured with total pressure probe
F_a	Obtained via PIV	Measured with the platform balance

Table 5.1: OFM terms obtention

The details of these estimations and measurements are explained in the following:

Supplied power $\mathcal{P}_S$ For DBD actuation, the power supplied to the actuators is directly measured as presented in the electrical characterisation of the actuators in section 2.2.2 (p.35). Consumed power is equal to about 100 W.

For the fluidic actuation, $\mathcal{P}_S$ is estimated as $\mathcal{P}_S = (P_{t0} - P_{atm})Q_v$. Total pressure in the plenum chamber P_{t0} is equal to about 4 bar as explained in section 3.3 (p.84), P_{atm} is the atmospheric pressure and Q_v is the flow rate injected through the blades ($Q_v \approx 400$ l/min). This leads to a power consumption of about 2 kW, a very significant value. Other flow control methods such as synthetic jets show much lower consumptions: about 30 W in Stalnov et al. [2010] and in Troshin and Seifert [2013], 175 W in de Vries et al. [2014]. However, for fluidic blowing, Niether et al. [2015] determined that embedded turbine compressors could supply the rotors in compressed air with a small power addition (0.75% of the rated power of NREL 5 MW turbine).

Weight of the actuator W_a Weight of the actuators is set to 1 N for both strategies. Indeed, the weights of the devices are very small. DBD actuators are very light and the mass added to the blade is negligible. Fluidic jets do not add any weight as the blade is only drilled. To be able to compare the devices at equal weight, W_a is set to 1 N (~ 0.1 kg).

Actuator velocity U_a For DBD actuation, U_a is obtained with the PIV velocity fields presented in section 2.3.1 (p.41) and is taken equal to about 4 m/s.

For the fluidic jets, U_a is equal to the jet velocity U_j defined and measured in section 3.3.2 (p.91) with a total pressure probe ($U_j \approx 300$ m/s).

Actuator thrust F_a For DBD actuation, the actuator thrust is determined via PIV velocity fields. It corresponds to the variable F_{EHD} (ElectroHydroDynamic force) defined in section 2.3.1 (p.41) and is equal to about 0.1 N.

For the fluidic jets, thrust is measured with the platform balance (translational cfg.) at $\alpha = 0°$ and $U_\infty = 0$ m/s. Thrust is equal to $F_a = 2.5$ N.

5.2.2 Estimation of OFM

Table 5.2 shows the estimation of the OFMs for the DBD actuation and the fluidic jets. OFMs for both strategies are totally different. Concerning the DBD actuation, OFM is equal to 0.04% implying that the actuator is not efficient at all in converting the power it receives into thrust (or momentum). This value is not surprising as the efficiency of surface DBD actuators is very low as mentioned in Benard and Moreau [2014]. In section 2.3.1 (p.41), efficiency variable η_{act} defined as the ratio between the mechanical power produced by the actuator and the electrical power supplied to the actuator was computed. Results show orders of magnitude of η_{act} equivalent to the present OFM for DBD actuation. Regarding fluidic jets, 94% of the energy supplied is converted into momentum highlighting a greater overall performance than plasma actuation. However, this value should be taken carefully as it is very sensitive to the actuator weight. But, at equal actuator weight, OFM related to fluidic jets is more than 2000 times greater than for DBD actuators.

	DBD	Fluidic
$\mathcal{P}_S$	100 W	2 kW
W_a	1 N	1 N
F_a	0.1 N	2.5 N
U_a	4 m/s	300 m/s
OFM	0.04%	94%

Table 5.2: Table summarising OFMs for efficiency evaluation

5.3 Power balances

An easy way to assess the actuation efficiency is the estimation of the **power supplied** to the actuator $\mathcal{P}_S$ and the **power recovered** by the actuation $\mathcal{P}_R$. Hence, an overall efficiency $\eta = \frac{\mathcal{P}_R}{\mathcal{P}_S}$ can be computed.

5.3.1 Evaluation of power terms

Supplied power $\mathcal{P}_S$ As mentioned above, DBD actuators have a power consumption of about 100 W.

For the fluidic actuation, it has been chosen to estimate $\mathcal{P}_S$ with $\mathcal{P}_S = (P_{tj} - P_{atm})Q_v$. This definition does not take into account the internal pressure losses of the pneumatic system. Indeed, the total pressure value is taken as *downstream* as possible in the air circuit. Total pressure at the jet exit P_{tj} is equal to about 2 bar as explained in section 3.3 (p.84), P_{atm} is the atmospheric pressure and Q_v is the flow rate injected through the blades ($Q_v \approx 400$ l/min). This leads to a power consumption of about 660 W.

Recovered power $\mathcal{P}_R$ Power recovered with the actuation $\mathcal{P}_R$ is defined as:

- **2D and translational cfgs.:** $\mathcal{P}_R = U_\infty \, (\Delta F_L)_{\text{ON-OFF}}$, where F_L is the lift force and U_∞ is the incoming flow velocity. $(\Delta F_L)_{\text{ON-OFF}}$ is taken equal to:
  - **DBD actuation (2D cfg.):** $(\Delta F_L)_{\text{ON-OFF}} = 2$ N corresponding to an attached flow at $\alpha = 8°$
  - **Fluidic actuation (translational cfg.):** $(\Delta F_L)_{\text{ON-OFF}} = 3$ N corresponding to an attached flow at $\alpha = 8°$ and $(\Delta F_L)_{\text{ON-OFF}} = 7.5$ N for a separated flow at $\alpha = 18°$
- **Rotational configuration:** $\mathcal{P}_R = \Omega \, (\Delta Q)_{\text{ON-OFF}}$, where Ω is the rotational velocity of the turbine and Q its torque. $(\Delta Q)_{\text{ON-OFF}}$ is taken equal to 1 N m, the maximal flapwise bending moment variation obtained with the strain gages ($\beta = 4°$ and $\lambda = 3.66$)

5.3.2 Power balance estimations

Table 5.3 summarises the overall power efficiency concerning the two actuation strategies. DBD approach has an efficiency of about 20% due to its low power consumption and moderate gain. On the other hand, fluidic actuation in a translational configuration shows different gains depending on the state of the flow along the blade. For attached flows, which lift variation with the actuation is small, the efficiency is equal to 9%. For separated flows (and at equal supplied power), the efficiency equals 23%. Efficiency η is reduced to 8%, however, for the rotational configuration due to the augmentation of the Reynolds numbers involved.

This power consumption values are clearly showing that, regardless of the actuation strategy, the supplied power to the actuators is greater than the recovered power. Indeed, in the case of plasma actuation with a low power consumption, the lift gain is too modest. Lift gains induced by the fluidic actuation are important but as the power supplied is significant, efficiency is low, specially for the rotational configuration.

	DBD (2D) $\alpha = 8°$	Fluidic (Tr. cfg.) $\alpha = 8°$	Fluidic (Tr. cfg.) $\alpha = 18°$	Fluidic (Rot. cfg.) $\beta = 4°$ - $\lambda = 3.66$
$\mathcal{P}_S$	100 W	660 W	660 W	660 W
$\mathcal{P}_R$	20 W	60 W	150 W	52 W
$\boldsymbol{\eta}$	20%	9%	23%	8%

Table 5.3: Table summarising the power supplied to the actuators and recovered by the actuation

5.3.3 Power-flow diagram approach

In Kriegseis et al. [2013a] the authors propose a *power-flow diagram* that covers the whole range of power stages from the energy source to the flow control application. Their methodology focuses on DBD actuators and is reproduced here for the DBD actuation and is also adapted to the fluidic one. All the calculations are done with the data defined in the previous paragraphs. Three performance stages are defined:

- $\boldsymbol{\eta_1}$ is the **electrical efficiency of the power supply or of the air compressor**. It is equal to $\eta_1 = \frac{\mathcal{P}_{\text{act-in}}}{\mathcal{P}_{\text{input}}}$, where $\mathcal{P}_{\text{act-in}}$ is the power consumed by the actuation and $\mathcal{P}_{\text{input}}$ the input power of the electric supply or of the air compressor. η_1 for the power supply is equal to 0.05. For the air compressor, η_1 is taken equal to 0.3 as mentioned in Hiraux [2014] for a standard compressed air unit
- $\boldsymbol{\eta_2}$ is the **efficiency of the actuator itself** defined as $\eta_2 = \frac{\mathcal{P}_{\text{act-out}}}{\mathcal{P}_{\text{act-in}}}$ where $\mathcal{P}_{\text{act-out}}$ is the fluid mechanic output of the actuation equal to the thrust F_a multiplied per the jet reference velocity U_a. η_2 is analog to the η_{act} variable mentioned above for DBD actuators
- $\boldsymbol{\eta_3}$ translates the **aerodynamic savings** performed with the actuation: $\eta_3 = \frac{\mathcal{P}_R}{\mathcal{P}_{\text{act-out}}}$, where $\mathcal{P}_R$ is the recovered power with the actuation
- $\boldsymbol{\eta_{tot}}$ is the **overall effectiveness** equal to the product of the three preceding efficiencies $\boldsymbol{\eta_{tot} = \eta_1 \eta_2 \eta_3}$

Table 5.4 summarises the power-flow diagram exposed in Kriegseis et al. [2013a] applied to the present flow control strategies.

In the case of the DBD actuation, the efficiency of the power supply η_1 is weak as most of the supplies employed at a laboratory scale are far from optimised. The orders of magnitude of η_2 and η_3 correspond to the values obtained in Kriegseis et al. [2013a] for a plasma actuator in-flight experiment: the authors found 0.001 and 54 for η_2 and η_3 respectively. This leads to an overall efficiency η_{tot} of 1%.

Regarding the fluidic actuation, the efficiency of the actuation itself η_2 is equal to 0.38 highlighting the pressure losses in the pneumatic circuit from the chamber to the jet exit: singular pressure losses in the sudden contraction from the plenum to the jet holes; and linear pressure losses along the jet drillings. Actuation efficiency η_3 ranges from 0.07 to 0.2 and remains very small compared to DBD actuation. Indeed, in the case of DBD, with a very small fluid mechanic power, the recovered power is quite impressive. For fluidic jets, lift gains are more important but the great $\mathcal{P}_{\text{act-out}}$ reduces their efficiency. The overall efficiency of the fluidic strategy is low, from 1% to 2%.

5.4 Aerodynamic Figures of Merit

5.4.1 AFMs definitions

Aerodynamic Figures of Merit are suggested by Seifert [2007] to assess the overall performance of a given actuation implemented on a 2D-airfoil. They take into account the lift and drag variations with the actuation as well as the power supplied to the actuator. These definitions are however most suitable to evaluate an actuation that seeks to perform a boundary layer separation control rather than a circulation control. Indeed, the author used separation control to augment the aerodynamic performances of the blades (lift to drag ratio) to optimise the turbine start-up. These figures of merit do not take into account, however, the costs of the devices and their maintenance, their robustness and life duration; or even their sensitivity to dust, rain or heat.

First Aerodynamic Figure of Merit (AFM1) is defined as:

	DBD (2D) $\alpha = 8°$	Fluidic (Tr. cfg.) $\alpha = 8°$	Fluidic (Tr. cfg.) $\alpha = 18°$	Fluidic (Rot. cfg.) $\beta = 4°$ - $\lambda = 3.66$
$\mathcal{P}_{\text{input}}$	2 kW	-	-	-
$\mathcal{P}_{\text{act-in}}$	100 W	2 kW	2 kW	2 kW
$\boldsymbol{\eta_1 = \frac{\mathcal{P}_{act-in}}{\mathcal{P}_{input}}}$	0.05	0.3	0.3	0.3
$\mathcal{P}_{\text{act-out}} = F_a U_a$	0.4 W	750 W	750 W	750 W
$\boldsymbol{\eta_2 = \frac{\mathcal{P}_{act-out}}{\mathcal{P}_{act-in}}}$	0.004	0.38	0.38	0.38
$\mathcal{P}_R$	20 W	60 W	150 W	52 W
$\boldsymbol{\eta_3 = \frac{\mathcal{P}_R}{\mathcal{P}_{act-out}}}$	50	0.08	0.2	0.07
$\boldsymbol{\eta_{tot} = \eta_1 \eta_2 \eta_3}$	0.01	0.01	0.02	0.008

Table 5.4: Table summarising the power-flow diagram methodology applied to the present cases

$$\text{AFM1} = \frac{\left(\frac{U_\infty F_L}{U_\infty F_D + \mathcal{P}_S}\right)_{\text{ON}}}{\left(\frac{F_L}{F_D}\right)_{\text{OFF}}} \tag{5.2}$$

where F_D is the total drag force (measured with the platform balance) and F_L the lift force. Aerodynamic Figure of Merit 2 (AFM2) takes also into account the weight of the actuator W_a and is defined as:

$$\text{AFM2} = \frac{\left(\frac{U_\infty (F_L - W_a)}{U_\infty F_D + \mathcal{P}_S}\right)_{\text{ON}}}{\left(\frac{F_L}{F_D}\right)_{\text{OFF}}} \tag{5.3}$$

Stalnov et al. [2010] define the Aerodynamic Figure of Merit 3 (AFM3) defined for a rotational configuration:

$$\text{AFM3} = \frac{\left((F_L - F_D)\, W_r\right)_{\text{ON}} - 2\mathcal{P}_S}{\left((F_L - F_D)\, W_r\right)_{\text{OFF}}} \tag{5.4}$$

where F_L and F_D are the lift and drag forces estimated via the C_p integration of a blade section and W_r the relative velocity. Actuation is worthwhile when AFM3 is greater than 1, the overall turbine efficiency is reduced otherwise. This AFM3 can also be evaluated for non-rotational configurations by taking $W_r = U_\infty$.

5.4.2 AFMs estimations

Table 5.5 details the values used for the calculation of the aerodynamic figures of merit. For 2D and translational configurations, loads are obtained via the platform balance (sections 2.4.2 (p.55) and 3.4.2 (p.95) respectively). In the case of the rotational configuration, loads are obtained via pressure integration (refer to section 4.4.2 (p.131)) for $\lambda = 3.66$, a radial position $r = 0.63R$ and $\beta = 8°$.

AFM1 and AFM2 remain quite low for both actuation strategies: 6% for the DBD actuation and 3% to 8% for the fluidic jets, depending on the flow state. As actuators are considered as very light devices (very small additional mass), AFM1 and AFM2 remain almost equal. Regarding AFM3, the variable is negative for all the fluidic cases and slightly positive for the DBD actuation meaning that actuations are not worth it energetically speaking (AFM3 < 1). AFM3 definition imposes that the power consumed by the fluidic actuation should be below 75 W in order to have

a worthwhile actuation at $\alpha = 18°$, which is a very low value for the present fluidic strategy. As a matter of comparison, Stalnov et al. [2010] obtained AFM3 values up to 1.15 for a power consumption of 23 W.

	DBD (2D) $\alpha = 8°$		Fluidic (Tr. cfg.) $\alpha = 8°$		Fluidic (Tr. cfg.) $\alpha = 18°$		Fluidic (Rot. cfg.) $\lambda = 3.66$, $\beta = 8°$	
	Baseline	ON	Baseline	ON	Baseline	ON	Baseline	ON
U_∞	10 m/s		20 m/s		20 m/s		30 m/s	
F_L	24 N	26 N	12 N	15 N	15.5 N	23 N	20 N	25 N
F_D	0.6 N	0.6 N	0.8 N	0.8 N	2 N	2 N	6 N	8 N
$\mathcal{P}_S$	-	100 W	-	660 W	-	660 W	-	660 W
W_a	1 N		1 N		1 N		1 N	
AFM1	6.1%		2.9%		8.3%		-	
AFM2	5.9%		2.7%		7.9%		-	
AFM3	0.23		-4.6		-3.3		-2	

Table 5.5: Table summarising AFM1 & AFM2 for efficiency evaluation

Aerodynamic global evaluation...

Actuation does not seem to be very efficient as the power supplied for the flow control actuation is much more important than the power effectively recovered. However, load alleviation has to be also seen from three other perspectives:

- A continuous load alleviation would mean lower blade nominal loads allowing the implementation of ***lighter* blades**. This would reduce the overall cost of the turbine (blades and tower costs mainly but also gear box, foundations and bearing costs)
- The reduction of blade load fluctuations and fatigue would increase the rotor **life duration**. This is why, if some power is consumed by the actuation and not recovered *aerodynamically*, it is not a real problem as blades will *mechanically* last longer. Gear box and tower life durations could also be increased
- It is also possible to maintain constant turbine cost and life duration but **increase the rotor size** to capture more energy from the wind and therefore reduce the cost of energy

In the following, we will try to assess these two last approaches: the **life duration increase** and the **rotor diameter increase**.

5.5 Fatigue modelling - life duration increase

Structural fatigue can be estimated with Palmgren-Miner's rule that allows the determination of the accumulated damage and the fatigue life of a given structure. In this section, first is explained the theory behind fatigue modelling. A reader familiar with these concepts can refer directly to section 5.5.2 (p.150) where the theory is applied to wind turbine blades.

5.5.1 Fatigue theory

Fatigue calculations for a given structure are based on the SN-curve of its material (also known as Möhler's curve) and a load time history.

SN-curves represent the response of a given material to a certain level of alternating stress repeated over a long time. A stress cycle example is shown in figure 5.1: σ_m is defined as the mean stress level, σ_a as the stress amplitude, and σ_{max} and σ_{min} as the upper and lower values of the stress cycle respectively. Usually, ratio R_{test} is defined as the ratio between these two last values $R_{test} = \frac{\sigma_{min}}{\sigma_{max}}$. R_{test} is equal to -1 when $\sigma_m = 0$.

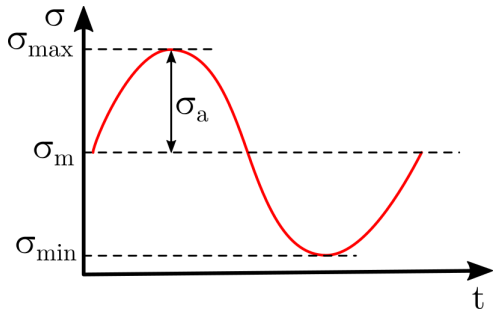

Figure 5.1: Stress cycle definition

SN-curves show the stress amplitude σ_a (in Pascal) as a function of the number of cycles to failure N. Failure corresponds to the initiation and propagation of a crack over the material. These curves do not take into account the frequency of the alternating stress cycles but strictly consider the number of cycles to failure regardless of the stress application rate. This frequency of excitation is, however, very important in real life specially when it matches the natural frequency or the resonance frequency of the structure.

Three ranges are noticeable in a typical SN-curve as shown in figure 5.2a:

- **Plastic behaviour:** range of high level amplitudes i.e. high σ_a values that correspond to just a few numbers of cycles before failure. This range starts with the ultimate strength value which is the amplitude corresponding to a failure in a single cycle. In this σ_a range, shape and geometry of the structure change due to the cycling application
- **Elastic behaviour:** in this σ_a range, the material returns to its original shape when a cycle is applied. It also corresponds to the linear part of the stress-strain (σ-ϵ) curve (figure 5.2b)
- **Infinite life:** Stress levels are below a certain level that could be reproduced infinitely without causing failure. This method, however, does not consider the external effects applied to the structure such as corrosion or ultraviolet radiation, for example

Usually, SN-curves are simplified and modelled with the following relationship:

$$\sigma_a = \sigma_u \times N^{-\frac{1}{m}} \tag{5.5}$$

where σ_u is the ultimate stress of the structure and m the slope of the curve and a characteristic of the structure material.

As mentioned above, the application of the Palmgren-Miner's rule requires two inputs: the SN-curve of the structure material and a load time series. In real applications, loads are stochastic and therefore do not have a constant amplitude. In order to normalise real load fluctuations, rainflow analysis are usually performed to obtain the equivalent number of cycles with constant amplitude resulting in the same fatigue damage as the real solicitations.

Palmgren-Miner's rule is defined as:

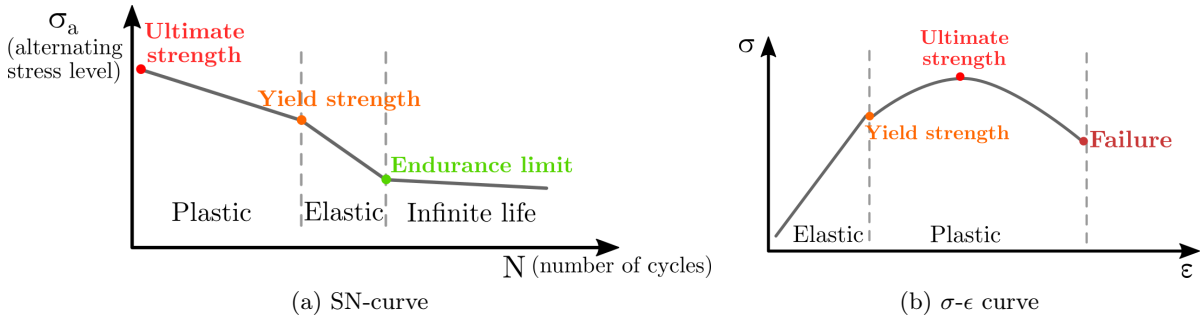

(a) SN-curve (b) σ-ϵ curve

Figure 5.2: SN-curve and σ-ϵ curve for a given material

$$D = \sum_{i=1}^{N_{tot}} \frac{n_i}{N_i} \tag{5.6}$$

where n_i is the number of load cycles for case i, N_i is the number of load cycles to failure for case i and N_{tot} the total number of cycles. Failure occurs when $D = 1$. However, as mentioned in Sutherland [1999], this methodology is not exact and differences of a factor of 2 between damage predictions and measured lifetimes should be expected as failure may actually occur between $D = 0.8$ and $D = 1.5$.

A very simple application of this rule is shown in figure 5.3. Stress amplitude σ_a corresponds to a certain number of cycles to failure N, which is obtained via the SN-curve. Hence, in the present example, $n_1 = 2$ cycles are carried out at σ_{a1} and $n_2 = 2$ other cycles at σ_{a2}, which corresponds respectively to 6 and 10 cycles to failure N_1 and N_2. Total damage is then equal to 0.53 corresponding to half of the life of the structure.

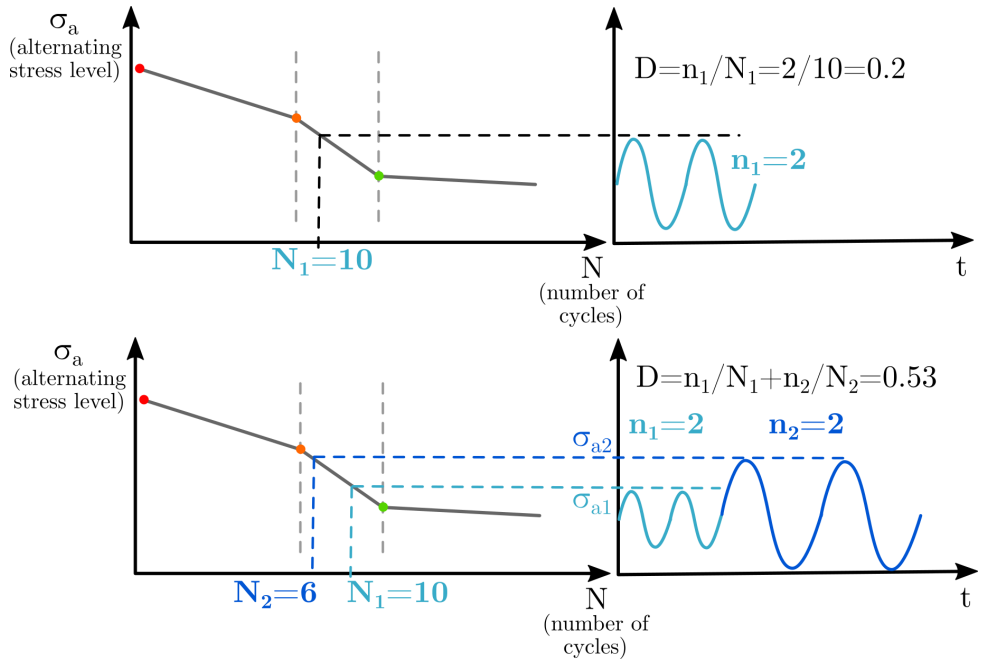

Figure 5.3: Application example of Palmgren-Miner's rule

It is important to remark that this rule does not take into account the order in which the cycles are applied not their frequency rate. Is is merely a *counting method*. Other methodologies, such as spectral and stochastic methods or crack growth approaches can be read in Barradas-Berglind and Wisniewski [2014].

5.5.2 Methodology for wind turbine blades fatigue evaluation

Fatigue calculations of wind turbine blades can be done for the evaluation of the efficiency of active control strategies but are actually mainly used for blade fatigue estimations. During their life, blades are subjected to a large load spectrum that cannot be reproduced in a laboratory in a reasonable time period. Fatigue models provide the equivalent load amplitude and number of cycles that have to be exerted to apply a certain damage to the blade. In Freebury and Musial [2000] authors test the NedWind25 (12 m span) blade in fatigue. Their methodology is unique because it does no assume that the information about the blade material and structural properties is precisely known. Instead of working with stresses σ, the authors work with moments M and define, in analogy with SN-curves, a family of MN-curves:

$$M_a = M_u \times N^{-\frac{1}{m}} \tag{5.7}$$

where M_a is the amplitude of the applied moment, M_u the ultimate moment of the blade and m the curve slope characteristic of the blade material. By combining this definition with the Goodman relation they obtain (see Freebury and Musial [2000] for calculation details):

$$M_a = \frac{M_u}{N_t^{-\frac{1}{m}} + \frac{1+R_{test}}{1-R_{test}}} = \frac{M_u}{\left(\frac{n_t}{D_t}\right)^{-\frac{1}{m}} + \frac{1+R_{test}}{1-R_{test}}} \tag{5.8}$$

where N_t is the total number of cycles to failure, n_t the total number of cycles of the test and D_t the total damage induced to the blade. In the present case, to evaluate the effectiveness of the flow control actuation, the variable that remains unknown is D_t, the total damage. Hence, the relation becomes:

$$D_t = \frac{n_t}{\left(\frac{M_u}{M_a} - \frac{1+R_{test}}{1-R_{test}}\right)^m} \tag{5.9}$$

Or, for a given damage D_t the number of cycles n_t to apply is:

$$n_t = D_t \left(\frac{M_u}{M_a} - \frac{1+R_{test}}{1-R_{test}}\right)^m \tag{5.10}$$

5.5.3 Application to the present results

Equation 5.9 gives the total damage suffered by the blade as a function of several parameters. This damage can be computed with and without actuation, giving D_t^{ON} and D_t^{OFF} respectively. A maximal bending moment increase of about 10% could be performed in the turbine bench of the laboratory (refer to section 4.4.1 on page 129). This result is applied in the following to the blades of the turbine studied in Madsen et al. [1999]: NREL/NWTC Unsteady Aerodynamic Experiment Phase III (rotor diameter 10 m, hub height 17 m). The different variables used to compute the blade damage are defined as:

- n_t is the number of cycles that is arbitrarily taken equal to 10^8
- m is the slope of the MN-curve. It is kept equal to 10, a characteristic value for fiber glass unidirectional laminate
- R_{test} is the ratio between the maximal and minimal moments of the cycle. Mean M_m effects are neglected as mentioned in Hansen [2008] and only oscillating M_a effects are taken into consideration. R_{test} is then equal to -1

- M_u is the ultimate moment of the blade. Ultimate loading occurs in extreme situations such as extreme wind speeds over a parked rotor, very turbulent winds or other special events such as the start-up or the shut-down of the turbine or even during yawing manoeuvres. M_u is difficult to evaluate without a finite element analysis and is usually taken as a multiple of the maximal bending moment endured by the blade. The value of the proportionality coefficient will strongly depend on how much conservative one wants to be for the calculation. In the present case, M_u is taken equal to $23 \times M_{rated}$, where M_{rated} is the mean bending moment corresponding to the rated wind velocity of the turbine mentioned in Madsen et al. [1999]. M_{rated} is taken equal to 0.86 kN m and $M_u = 20\,\text{kN m}$
- M_a is the amplitude of the bending moment excitation. For the baseline case M_a^{OFF} is equal to $M_a^{\text{OFF}} = 0.05 \times M_{rated}$, corresponding to oscillations at 5% of the rated bending moment. For the controlled case, M_a^{ON} is taken equal to $M_a^{\text{ON}} = 0.9 \times M_a^{\text{OFF}}$, corresponding to an alleviation of 10% of the amplitude moment fluctuations

Given the above values and equation 5.9, it yields:

$$\frac{D_t^{\text{OFF}} - D_t^{\text{ON}}}{D_t^{\text{OFF}}} = 65\% \tag{5.11}$$

Meaning that, for a given number of cycles and a load alleviation of 10% of the bending moment, the damage induced to the blade is reduced by 65%.

5.5.4 MLife fatigue calculations

The calculation above is verified with the open-source MLife NREL software[1] (https://nwtc.nrel.gov/MLife) used to compute statistical information of a given force (or moment) time-series as well as the resultant fatigue estimations.

To run the code, a fictive time-series of bending moment is created. Its mean value is equal to M_{rated}, and amplitudes are defined as above: $M_a^{\text{OFF}} = 0.05 \times M_{rated}$ and $M_a^{\text{ON}} = 0.9 \times M_a^{\text{OFF}}$. Ultimate moment M_u remains equal to 20 kN m. Period of the signal is kept equal to 2π (frequency is not relevant as the counting method does not take into account the fluctuation rate).

MLife confirms the results presented above: with a reduction of the bending moment amplitude of 10%, blade damage is reduced by 65% and root time until failure is increased by 65%. A more conservative approach with a bending moment reduction of 5% gives that damage is reduced of 40% and root time until failure increased of 40%.

5.6 CoE and *grow-the-rotor* approaches

Active flow control strategies performed in the present study proved to reduce the blade fatigue and to increase the blade life duration. However, whether this load alleviation is enough to lead to a lower cost of energy is a question that still needs to be assessed. As the present investigation is merely a wind-tunnel scale proof of concept, calculations are not carried out but previous studies conducting these kind of estimations are reviewed.

Cohen et al. [2008] identify several Technology Improvement Opportunities (TIO) for low speed wind turbines taking into account the potential Cost of Energy (CoE) reductions. Authors define the CoE as:

$$\text{CoE} = \frac{\text{FCR} \times \text{ICC}}{\text{AEP}} + \text{AOE} \tag{5.12}$$

where:

[1] See ML1 for MLife User's Guide and ML2 for MLife theory

- CoE is the levelised Cost of Energy [€/kWh]
- FCR is the Fixed Charge Rate [1/year] (includes construction financing, financing fees, return on debt, depreciation, insurance...)
- ICC is the Initial Capital Cost [€]
- AOE are the Annual Operating Expenses (including land lease and operating and maintenance costs (O&M))
- AEP is the Annual Energy Production (kWh/year)

The first TIO concerns enlarged rotors that capture more energy from the incoming wind. The objective is to enlarge the rotor of a given turbine without exceeding the structural loads of the original rotor (and ideally maintaining the same infrastructure investment). Active and passive control devices are implemented over these longer blades to reduce the structural loads due to turbulence.

Berg et al. [2009] applied this *grow-the-rotor* approach to a 1.5 MW wind turbine equipped with trailing-edge flaps (NREL FAST/AeroDyn code). They demonstrate that a reduction of the flapwise bending moment of -30% would lead to an increase of about $+10\%$ in the rotor diameter. This would result in an annual energy production increase of $+10\%$ to $+15\%$ and a CoE reduction between -5% and -9%, depending on the wind velocity. Baek [2011] conducted the same grow-the-rotor analysis and concluded that a fatigue reduction of -15% would cause a $+8\%$ rotor diameter increase. However, the author also warns that a 2% increase in blade length would already lead to an exceed of blade design loads. An increase in AEP of 5% and 1.5% can be expected with a 8% and 2% rotor increase respectively.

However, these expectations should be verified in further investigations that would model the overall loads of the turbine (tower, gear box, shafts...). Furthermore, more accurate estimations of the installation and O&M costs of control devices are needed to obtain accurate CoE estimations.

5.7 Conclusion

For both plasma and fluidic flow control strategies, power consumption of the actuators is greater than the recovered power as a result of the actuation. Energetically speaking, actuation is not worthwhile as the aerodynamical gains do not compensate the amount of injected energy for the actuation.

However, this energy expense is not without positive consequences on the life duration of the blades. Indeed, a reduction of 10% on the flapwise bending moment leads to an increase in the life duration of 65% and a 65% reduction of the blade root fatigue. Hence, in this framework, blades equipped with active flow control devices could be lighter, longer or simply last longer leading to a cost of energy reduction. These calculations, though, need to be further developed to take into account the overall costs of the control devices and the complete load spectrum of the wind turbine.

Conclusion and perspectives

Conclusion of the thesis work

The objective of the thesis work was to implement active flow control strategies over a wind turbine airfoil and a blade in order to achieve load modification at a wind-tunnel scale. This thesis work was part of the SMARTEOLE project in which framework two innovative active flow control approaches were considered: DBD plasma actuators and fluidic jets. Both strategies were designed to perform a circulation control, with an action in the very vicinity of the rounded trailing-edge of the blade. The two strategies were first implemented in a 2D-configuration in order to compare their respective efficiency and be able to choose a single device for its implementation in the wind turbine bench of the laboratory.

The first part of the thesis dealt with one of the two strategies, i.e. the DBD actuation in a 2D-configuration with the objective of performing a circulation control that would increase or decrease the lift coefficient of the airfoil.

The characterisation of DBD induced jets in quiescent air conditions allowed the estimation of the momentum coefficient for these actuators. It was also shown that the electrode positioning around the trailing-edge curvature had a direct impact on the jet topology: to obtain a complete jet adhesion to the wall past the trailing-edge circumvention, the region of ElectroHydroDynamic interaction should reach the end of the curvature. A closer analysis of the induced jets evolution showed that DBD wall jets are in a transitional regime and that their evolution in terms of velocity decay and rate of spread is linear, such as canonical fluidic wall jets evolve.

With respect to the flow control experiments, actuation translates the baseline lift coefficient curve towards higher or lower lift forces highlighting the achievement of a circulation control with maximal lift coefficient variations up to ± 0.10. It was also shown that, even if the actuation takes place near the trailing-edge, it modifies the whole pressure distribution over the airfoil, with a maximal pressure variation near the leading-edge. Velocity fields evidenced that the rounded trailing-edge induces a recirculation area with two counter-rotating vortices in the wake of the airfoil that are actually the signature of a Von Karman vortex shedding. Hot wire measurements in the wake of the airfoil suggested that the actuation triggers the Von Karman instability, a result that was confirmed with POD analysis in the airfoil wake.

As was mentioned above, in the scope of the SMARTEOLE project, plasma and fluidic control strategies were considered but only one approach had to be chosen for the flow control implementation in a rotational configuration. For efficiency and reliability reasons, the fluidic jet system was chosen to pursue the work towards the turbine bench.

Before testing the fluidic flow control strategy in a rotational configuration, a first investigation was performed to evaluate the performance of the actuation in a translational configuration.

Fluidic jets were first characterised in quiescent air conditions in order to analyse the blowing and characterise the jet exit velocity, the jet topology and to estimate the momentum coefficient of this actuation approach.

Regarding the flow control performances, actuation achieves lift coefficient variations from

+0.10 to +0.20 in the linear part of the lift curve giving evidence of a potential circulation control for attached flows. For higher angles of attack, where the flow is partially separated, fluidic jets achieve a separation control delaying stall and increasing the maximal lift coefficient of about +0.50. Also, the measurement of the root flapwise bending moment via strain gages was validated in the purpose of preparing the rotational testing where global lift measurements are not possible on the blades.

To test the fluidic strategy in a rotational configuration, the wind turbine bench of the PRISME laboratory was equipped for a fluidic flow control application. Two measurements could be made on the blades: the flapwise bending moment (global measurement) at the blade roots and the surface pressure distribution at two different radial positions (local measurement). Global rotor quantities such as the overall torque and drag of the turbine were also measured.

Blades were tested in a rotational configuration for several pitch angles and tip-speed ratios. Actuation increased the blade lift coefficient and therefore the root flapwise bending moment. Bending moment variations up to about +10% of baseline levels were obtained.

Pressure measurements showed that the mechanisms of the actuation are similar to the ones highlighted for the translational case. Actuation effect is very limited, if not absent, for attached flows but is stronger for partially separated flows or totally stalled flows.

Torque and drag of the turbine couldn't be measured for controlled flows because of the added friction induced by the rotary joint. However, the calculation of local power and thrust coefficients via pressure integration leads to gains of about 20% and 15% respectively.

At the end of the manuscript the overall efficiency of both actuations is addressed. For both plasma and fluidic strategies, the power supplied to the actuators is greater than the power effectively recovered with the actuation: actuation is not worthwhile as the aerodynamical gains do not compensate the amount of injected energy to the actuators.

However, this energy expense is not without a positive impact on the life duration of the blades. Indeed, a reduction of 10% on the flapwise bending moment leads to an increase of blade life duration of about 65% and a 65% reduction of blade root fatigue. Consequently, blades equipped with active flow control devices could be lighter, longer or have a longer life duration leading to a cost of energy reduction.

Perspectives for future work

First perspectives concern the optimisation of the actuation. In the case of the DBD actuation, a technological breakthrough has still to be achieved to obtain important momentum injections and reliable devices. However, the plasma flow control community tends to go towards pulsed actuations that show promising results for the manipulation of certain flow instabilities with a low energy consumption. Furthermore, this kind of devices can be implemented over deformable surfaces. These potentialities could also be investigated for wind turbine blade control applications involving aeroelastic morphing blades.

Regarding the fluidic approach, the implemented discrete action along the blade span is not as efficient as expected. Initially, this arrangement was chosen to have lower momentum coefficients than a 2D slot, try to perform a local Coanda effect and give the opportunity to test a distributed actuation along the chord and along the span. However, the jets do not follow the model trailing-edge curvature and appeared to have quite important momentum coefficients. Therefore, it would be interesting to perform similar testings with a blowing slot instead of the present discrete three dimensional action. This would generate a purely two dimensional actuation where an eventual Coanda effect would entrain the boundary layer around the curvature and lead to a much more efficient circulation control for attached flows. Also, with this distributed configuration, the lift

force could not be reduced but only increased. The work should be pursued to try to perform a lift decrease as well as a bending moment decrease with a blowing slot, for example.

Considering the short term perspectives, the experimental set-up offers the possibility to continue the work with the present fluidic actuation by adding a closed-loop control. A first step would be to yaw the turbine to generate a cyclic perturbation to react to. Another solution might be to generate an inhomogeneous flow at the test section entry with two turbulence grids of different porosity covering respectively 50% of the test-section that would generate a disturbed flow. An even more complex solution would be the implementation of an active grid that could generate a wind gust with wind angle and velocity variations. In all theses cases, as the global blade lift force cannot be measured on a turbine bench, the closed-loop could react to maintain the blade bending moment measured with the strain gages within a certain range.

Middle term perspectives will obviously raise the question of the Reynolds number upscaling and the precise evaluation of the possible load gains with active flow control devices for operating wind turbines. This is why, experimental research should move forward side by side with numerical studies and field tests. Wind-tunnel testings will propose innovative control concepts that will be then reproduced numerically. These numerical models will be validated against experimental results which opens the way to a large panel of calculation cases that would be difficult to perform experimentally in terms of time and costs. Then, once one strategy seems mature enough it will be possible to test it experimentally in the field.

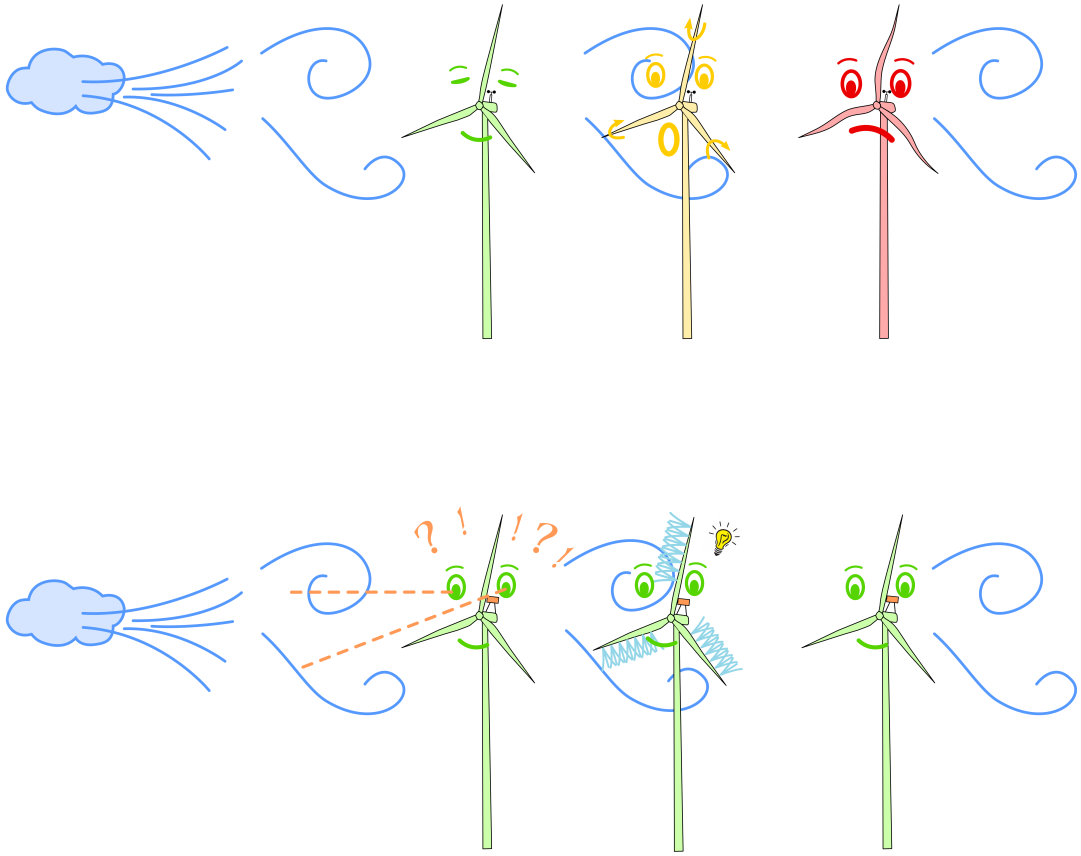

Appendices

Appendix A

Additional information on Particle Image Velocimetry (PIV)

This appendix is devoted to the presentation of Particle Image Velocimetry (PIV) technique used in chapter 2 and chapter 3 of this thesis.

A.1 PIV principle

PIV is an optical non-intrusive technique that allows the acquisition of instantaneous velocity fields of a given flow. A scheme presenting the principle of a classical experimental set-up is shown in figure A.1. Tracer particles of small diameter are introduced in the test-section with a seeding system. These particles are in motion and follow the flow all over the tunnel and around the model (if there is one). Thanks to the powerful light of a laser, tracer particles are illuminated twice, the two shots being spaced by a known time interval Δt. At each illumination, two images are acquired with a CCD (Charged-Coupled Device) camera. On these images, tracer particles are visible and one can detect their motion between the two frames. After a statistical treatment, particle displacement Δx can be determined. Flow velocity can therefore be obtained with spatial and temporal informations Δx and Δt respectively.

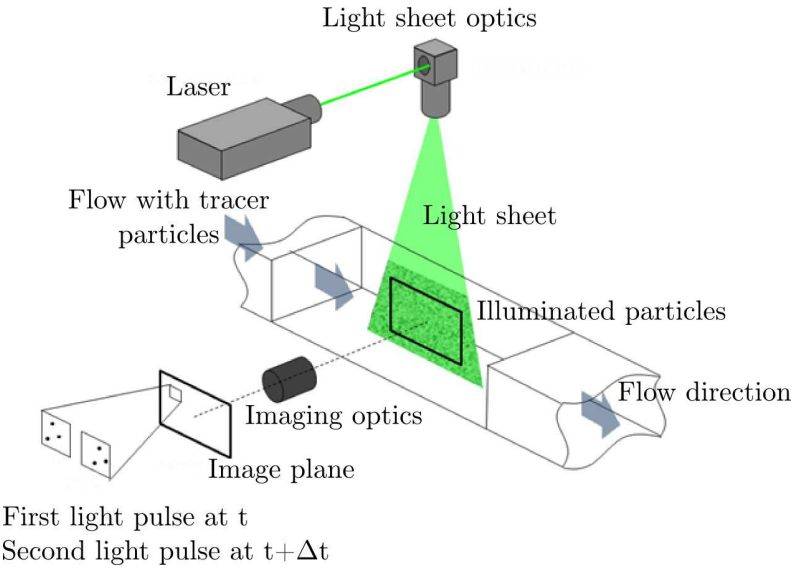

Figure A.1: Scheme presenting the working principle of PIV (adapted from https://www.seika-di.com/media/2017/11/01/3)

A.2 Experimental set-up

Seeding particles Tracer particles should be non-intrusive to follow the flow without interfering with it. To achieve this, the particle diameter should be small enough. However, particles also need to be large enough to be visible by the CCD camera and to reflect enough light towards the lenses. Olive oil particles with a diameter of about 1 µm, such as the particles employed in the present study, respect both of these criteria.

Light source Most common light sources for PIV are Nd:Yag lasers because their high power allows to obtain a satisfactory light diffusion on the seeding particles. These lasers have a lengthwave of 532 nm and are made of two cavities equipped with Q-switches that allow the generation of two very close impulsions (or illuminations). At the laser exit, the laser produces a light beam that is transformed into a light sheet thanks to an optical system made of a cylindrical lens. The thickness of the laser sheet is of about 1 to 2 mm.

Image acquisition and treatment Image acquisition and laser impulsions are synchronised by a timing-unit. After the completion of the captures, the obtained images and data should be processed. Each image is divided in several square interrogation windows. Time-step Δt is defined according to the size of these windows and also scales the flow velocity. The particle displacement Δx between two frames should be equal to $\frac{1}{4}$ of the interrogation window length. Each image pair is treated in order to obtain a velocity vector for each interrogation window. A Fast-Fourier Transformation is usually used by the software to find the cross-correlations peaks associated to every window as shown in figure A.2. Several passes with decreasing window size are employed to augment the resolution of the final velocity field. Usually, a final filtering is applied and extremal velocity values are sorted.

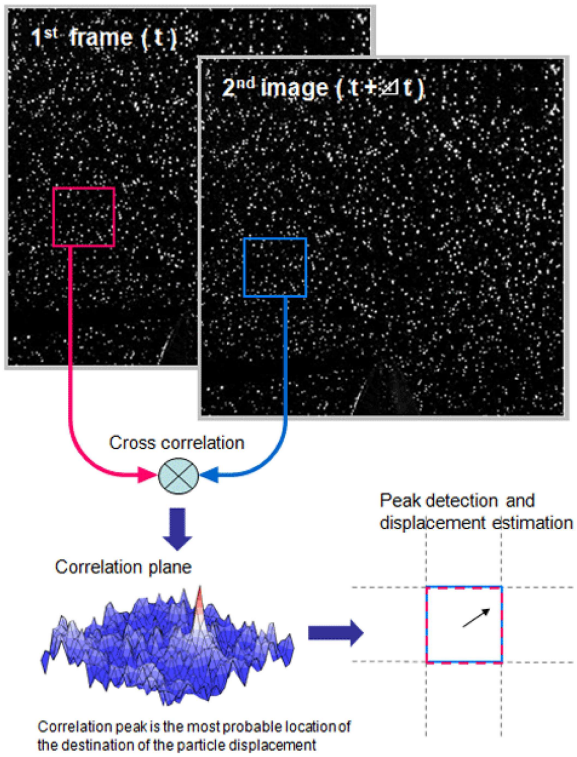

Figure A.2: Principle of PIV cross-correlation (from https://www.seika-di.com/media/2017/11/01/3)

Appendix B

Additional information on load measurements

This appendix concerns the platform balance measurements used in the experimental campaigns presented in chapter 2 and chapter 3.

The aerodynamic balance is located under the wind-tunnel main test-section and is shown in figure B.1. The balance is composed of two trapezoidal parts made of aluminium beams. The upper trapeze is connected to the model located inside the test-section, whereas the lower trapeze is fixed to the ground. Six strain gages measure the displacement between these two frames, a *micro* displacement that is directly related to the aerodynamic efforts applied to the model. Hence, these strain gages are used to resolve the three components of force and the three components of moment applied to the model.

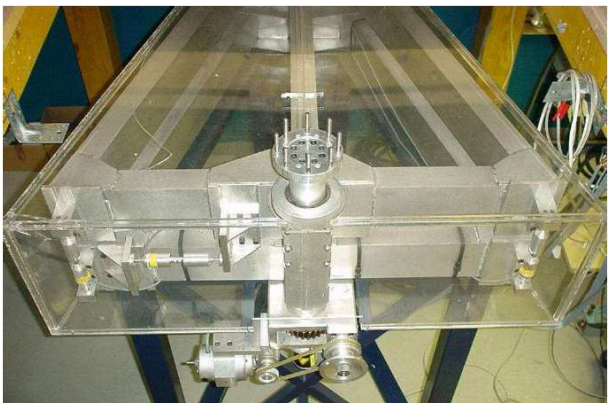

Figure B.1: Picture of the platform balance under the test-section

Measurement errors on lift and drag forces are estimated in the following for both 2D (chapter 2) and translational configurations (chapter 3). Both configurations are presented separately because in the first case the model is mounted *horizontally* in the test-section whereas, in the second case, the blade is mounted *vertically*. This means that the gages responsible of the lift force measurement in each configuration are different.

B.1 Estimation of measurement errors - 2D set-up

Load measurement errors for the 2D set-up are estimated as follows:

– Maximum drag uncertainty (1 gage): $\pm 0.16\,\mathrm{N}$

– Maximum lift uncertainty (3 gages): ±0.47 N

– Uncertainty of the differential pressure sensor (Pitot probe located upstream of the model used to calculate the free-stream velocity): ±1 Pa

– Uncertainty on the test-section temperature: negligible

– Uncertainty on the atmospheric pressure: negligible

Table B.1 shows lift and drag coefficients uncertainties for the 2D-configuration and two angles of attack: 0° corresponding to an attached flow (low lift and drag forces), and 10° or 16° corresponding to angles near stall (high lift and drag forces).

	α [°]	$C_{L,D}$	$F_{L,D}$ [N]	balance uncert. [N]	% error
C_D	0°	0.05	1	0.16	18%
	16°	0.2	3.2	0.16	7%
C_L	0°	0.5	10	0.47	6%
	10°	1	26	0.47	3%

Table B.1: Lift and drag coefficients (C_L and C_D) uncertainties for the 2D-configuration

Uncertainties are mostly important for drag measurement in attached flows, when the measured force is too small to be properly captured by the platform balance. However, measurement errors are acceptable in drag for high angles of attack when the flow is partially detached and the drag force more important. Regarding lift, for both attached and detached flows, uncertainties are acceptable (6% and 3% respectively).

Electromagnetic noise The use of high voltages for plasma actuation induces electromagnetic interferences (EMI) that add noise to the measurements. This noise is estimated to be of about 3 Pa for the pressure sensor and of 0.5 N for the loads. EMI are also sensed in the measurement of the angle of attack of the airfoil. Load coefficients calculations and plots *with actuation* are performed with the angle of attack and differential pressure corresponding to the *without actuation* case, carried out in the "same wind" configuration.

B.2 Estimation of measurement errors - translational configuration

Load measurement errors for the translational case are estimated as follows:

– Maximum drag uncertainty (1 gage): ±0.16 N

– Maximum lift uncertainty (2 gages): ±0.32 N

– Uncertainty of the differential pressure sensor: ±1 Pa

– Uncertainty on test-section temperature: negligible

– Uncertainty on atmospheric pressure: negligible

Table B.2 shows lift and drag coefficients uncertainties for the translational configuration and analog angles of attack as above. Data corresponds to both attached and detached flows.

Again, uncertainties are significant for drag measurement in attached flows, when the measured force is very small (lower than 1 N) to be assessed. As mentioned above, measurement

	α [°]	$C_{L,D}$	$F_{L,D}$ [N]	balance uncert. [N]	% error
C_D	0°	0.04	0.6	0.16	27%
	20°	0.18	2.7	0.16	7%
C_L	0°	0.25	4	0.32	9%
	10°	1	15	0.32	3%

Table B.2: Lift and drag coefficients (C_L and C_D) uncertainties for the translational configuration

errors of drag are reduced for high angles of attack when the flow is partially separated. Regarding lift, for both attached and detached flows, uncertainties are reasonable (9% and 3% respectively).

Appendix C

Additional information on strain gage measurements

This appendix concerns strain gage measurements presented in chapter 3 and chapter 4 and allowing the measurement of the flapwise bending moment of the blades.

C.1 Working principle of a strain gage

Strain ϵ is defined as the ratio of the change in length of a material to its original length L i.e. $\epsilon = \frac{\Delta L}{L}$. If strain is positive, the material is elongated and if strain is negative the material is compressed. One of the most common way to measure strain is with strain gages. A strain gage (see figure C.1) is usually bonded to a test material that endures a deformation which strain wants to be measured. The gage itself is made of a metallic thin wire arranged in a grid pattern. When the test material is under stress, the strain gage electrical resistance R varies in proportion to the amount of applied strain following a linear relation $\epsilon = k_g V_g$, where k_g is a constant and V_g the output gage voltage.

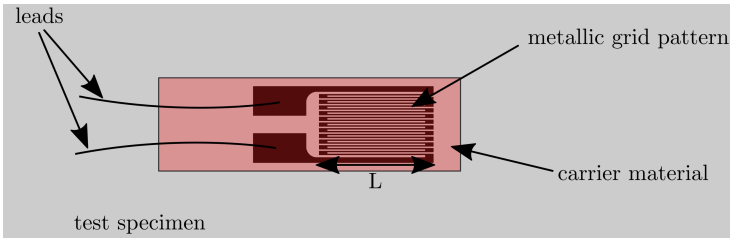

Figure C.1: Scheme of a strain gage

C.2 Strain gages to measure flapwise bending moment on blades

In the blades used in this thesis work, strain gages are mounted in a full-bridge (4 gages) configuration, a classical set-up to measure bending deformations due to its high sensitivity to bending strain. The principle of this configuration is shown in figure C.2a and a picture of the strain gages on a blade is shown in figure C.2b. When the blade is subjected to bending strain, resistances R_1 and R_3 are subjected to a positive ϵ (elongation) whereas R_2 and R_4 measure a negative ϵ (compression). R_1 and R_3 are located in the pressure side of the airfoil and R_2 and R_4 are on the suction side. R_1 and R_2 are located at $\frac{x}{c} \approx 0.33$ and R_3 and R_4 at $\frac{x}{c} \approx 0.43$, in the area of the airfoil of maximum thickness. Strain gages are wired on Wheatstone bridges that allow the detection of small changes in gages resistance and deformation.

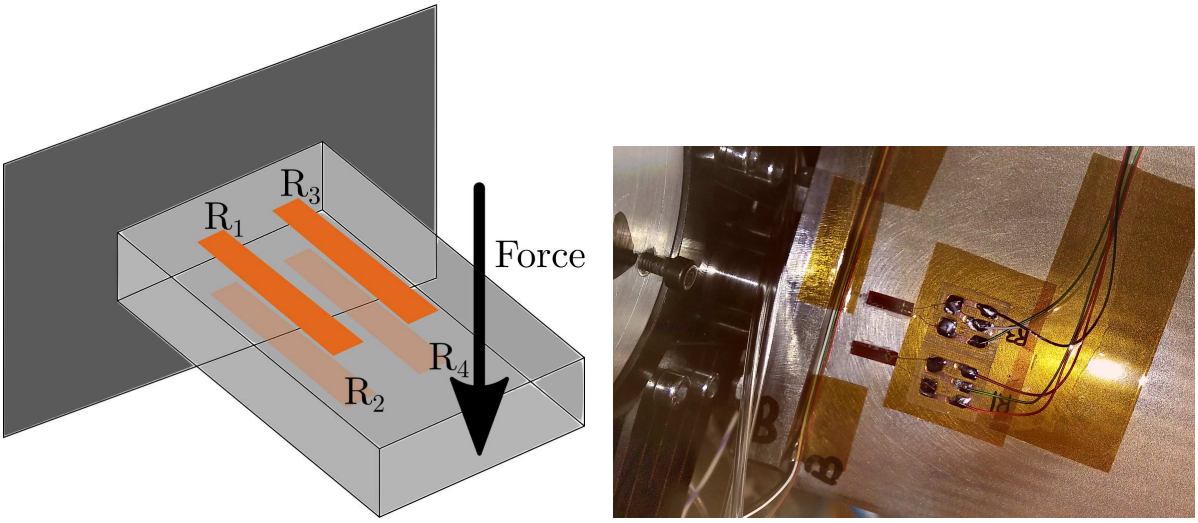

(a) Full-bridge configuration (bending strain)

(b) Strain gage picture on the blade

Figure C.2: Strain gages principle and picture

For both translational and rotational configurations, strain gages were calibrated by applying known bending moments at the blade tips. Proportionality coefficient between the applied bending moment and the output gage voltage was therefore obtained for each blade i.e. for each gage bridge.

C.3 Sources of measurement errors

According to Papadopoulos et al. [2000], the main sources of measurement errors with strain gages are due to:

- **Mounting procedure** (proper bonding, soldering, insulation, careful alignment of the gage)
- **Transverse sensitivity** (the fact that gage responds to strain acting perpendicularly to the gage primary sensing axis)
- **Temperature, humidity and chemical effects:** all neglected in the present study that is carried out in a controlled wind-tunnel environment with a grossly constant temperature and humidity during the testings and without any chemical action on the blades. Furthermore, gages are mounted in a full-bridge system implying that temperature compensation is improved. These effects are however important in operating wind turbines that endure diurnal temperature variations and severe climate changes. Indeed, composite materials of blades are very sensitive to temperature and humidity variations
- **Fatigue** (change in gage factor K, gage failure in fatigue): this effect will be neglected as gages can endure 10^8 cycles at 3% of the strain limit. Assuming a rotational velocity of 1000 rpm, 10^8 cycles correspond to 1700 working hours which were not reached in the present study
- **Strain cycling** (hysteresis loops, zero shift): zero values of the strain gages is taken at the beginning of each test and zero shift is therefore corrected for each measure
- **Exceeding limits** of the gages (extensibility, non-linearity of Wheatstone bridge at large strain values): gages are solely employed in their linear behaviour range

– **Properties of the carrier material:** gages are bonded to the aluminium part at the blade root that is considered as an homogeneous and non-isotropic material

Hence, the two main sources of errors are the **mounting procedure**, specially the misalignment of the gages along the blade span direction, and the gages **transverse sensitivity**.

Misalignment error Error generated by the gage misalignment n_2 can be computed with the method given by Measurement Group, Inc. in SG1 [1982]:

$$n_2 = (1 - \frac{1}{2}((1 - \nu_{mat}) + (1 + \nu_{mat})\cos(2\theta))) \times 100 \tag{C.1}$$

A eventual 5° misalignment induces a 1% error in the strain measurement.

Transverse sensitivity Corrections are necessary when large transverse strains affect the gage (considerable misalignment between the gage axis and the principal load axis) or when extraordinarily high measurement accuracy is required (Hoffmann [1989]). In the present case, calibration is carried out in the final state with the gages wired and connected to the NI chassis ready for the wind-tunnel testings reducing the importance of transverse sensitivity. Transverse sensitivity error n_1 can be computed as a percentage of the strain along the gage axis as done by Measurement Group, Inc. in SG2 [1983]:

$$n_1 = \frac{K_t(\frac{\epsilon_t}{\epsilon_a} + \nu_0)}{1 - \nu_0 K_t} \times 100 \tag{C.2}$$

where ν_0 is the Poisson's ratio of the material on which the gage manufacturer carried out the calibration (usually steel $\nu_0 = 0.285$), $K_t = 0.1\%$ is the transverse sensitivity coefficient given by the manufacturer and $\frac{\epsilon_t}{\epsilon_a} = -\frac{1}{\nu_{mat}}$ is the ratio between transversal and axial strains of the gage axis, and ν_{mat} the Poisson's ratio of the carrier material (aluminium in the present case $\nu_{mat} = 0.34$). By applying this formula the transverse sensitivity error remains under 1%. Cross-talk[1] effects are not present as one single bridge is used to measure solely the flapwise bending moment. These cross-talk effects are important when blades are twisted and both flapwise and edgewise bending moments are measured.

Conclusion Given the above calculations, it can be deduced that the flapwise bending moment on the blade roots can be measured with a maximal error of about 2%.

[1]Cross-talk effects occur when several transducers are used. A force acting in one direction can affect the measurement system in another direction

Bibliography

MLife Theory Manual for Version 1.00.

MLife User's Guide for Version 1.00.

Errors due to misalignment of strain gages - measurements group, inc., raleigh, nc, usa. *Experimental Techniques*, 6(3):16–19, 1982. doi:10.1111/j.1747-1567.1982.tb01654.x.

Errors due to transverse sensitivity in strain gages - measurements group, inc., raleigh, nc, usa. *Experimental Techniques*, 7(1):30–35, 1983. doi:10.1111/j.1747-1567.1983.tb01667.x.

J. Abramson. Two-dimensional subsonic wind tunnel evaluation of a 20-percent-thick circulation control airfoil. Technical Report ASED-311, David W. Taylor Naval Ship Research and Development Center, 1975.

E. Anik, A. Abdulrahim, Y. Ostovan, B. Mercan, and O. Uzol. Active control of the tip vortex: an experimental investigation on the performance characteristics of a model turbine. *Journal of Physics: Conference Series*, 524(1):012098, 2014. doi:10.1088/1742-6596/524/1/012098.

D. Arnal. Special course on stability and transition of laminar flow. Technical report, Advisory Group for Aerospace Research and Development, 1984.

S. Aubrun, A. Leroy, and Ph. Devinant. Aerodynamic load fluctuations alleviation by circulation control on wind turbine blades. *50th 3AF International Conference on Applied Aerodynamics (Toulouse, France, March 30 - April 1)*, FP-61, 2015.

S. Aubrun, A. Leroy, and Ph. Devinant. A review of wind turbine-oriented active flow control strategies. *Experiments in Fluids*, 58(10):134, 2017. doi:10.1007/s00348-017-2412-0.

P. Baek. *Unsteady flow modeling and experimental verification of active flow control concepts for wind turbine blades.* PhD thesis, Technical University of Denmark (DTU), 2011.

R.A. Bajura and A.A. Szewczyk. Experimental investigation of a laminar two-dimensional plane wall jet. *The Physics of Fluids*, 13(7):1653–1664, 1970. doi:10.1063/1.1693137.

C. Bak, M. Gaunaa, P. Andersen, T. Buhl, P. Hansen, K. Clemmensen, and R. Moeller. Wind tunnel test on wind turbine airfoil with adaptive trailing edge geometry. *45th AIAA Aerospace Sciences Meeting and Exhibit (Reno, Nevada, USA, January 8-11)*, 2007. doi:10.2514/6.2007-1016.

J.P. Baker and C.P. Standish, K.J. Van Dam. Two-dimensional wind tunnel and computational investigation of a microtab modified airfoil. *Journal of Aircraft*, 44:563–572, 2007. doi:10.2514/1.24502.

N. Balcon, N. Benard, and E. Moreau. Formation process of the electric wind produced by a plasma actuator. *IEEE Transactions on Dielectrics and Electrical Insulation*, 16(2):463–469, 2009. doi:10.1109/TDEI.2009.4815179.

D. Baldacchino, C. Ferreira, D. de Tavernier, W. Timmer, and G. Bussel. Experimental parameter study for passive vortex generators on a 30% thick airfoil. *Wind Energy*, 21(9):745–765, 2018. doi:10.1002/we.2191.

T.K. Barlas, A.S. Olsen, H.A. Madsen, T.L. Andersen, Q. Ai, and P.M. Weaver. Aerodynamic and load control performance testing of a morphing trailing edge flap system on an outdoor rotating test rig. *Journal of Physics: Conference Series*, 1037(2):022018, 2018. doi:10.1088/1742-6596/1037/2/022018.

J.J. Barradas-Berglind and R. Wisniewski. Fatigue estimation comparison for wind turbinel control. *arXiv:1411.3925v1*, 2014.

S. Bartholomay, W-L. Fruck, G. Pechlivanoglou, C.N. Nayeri, and C.O. Paschereit. Reproducible inflow modifications for a wind tunnel mounted research HAWT. *ASME Turbo Expo (Charlotte, North Carolina, USA, June 26–30)*, 2017. doi:10.1115/GT2017-64364.

S. Bartholomay, G. Michos, S. Perez-Becker, G. Pechlivanoglou, C. Nayeri, G. Nikolaouk, and C.O. Paschereit. Towards active flow control on a research scale wind turbine using PID controlled trailing edge flaps. *AIAA Wind Energy Symposium (Kissimmee, Florida, USA, January 8–12)*, 2018. doi:10.2514/6.2018-1245.

N. Benard and E. Moreau. Electrical and mechanical characteristics of surface AC dielectric barrier discharge plasma actuators applied to airflow control. *Experiments in Fluids*, 55(11): 1846, 2014. doi:10.1007/s00348-014-1846-x.

N. Benard, A. Mizuno, and E. Moreau. A large-scale multiple dielectric barrier discharge actuator based on an innovative three-electrode design. *Journal of Physics D: Applied Physics*, 42(23): 235204, 2009. doi:10.1088/0022-3727/42/23/235204.

A. Berendt, J. Podliński, and J. Mizeraczyk. Elongated DBD with floating interelectrodes for actuators. *The European Physical Journal Applied Physics*, 55:13804, 2011. doi:10.1051/epjap/2011100441.

D.E. Berg, D.G. Wilson, B.R. Resor, M.F. Barone, J.C. Berg, S. Kota, and G. Ervin. Active aerodynamic blade load control impacts on utility-scale wind turbines. *AWEA Windpower Conference and Exhibition (Chicago, Illinois, USA, May 4-7)*, 2009.

L. Bergami and N.K. Poulsen. A smart rotor configuration with linear quadratic control of adaptive trailing edge flaps for active load alleviation. *Wind Energy*, 18(4):625–641, 2015. doi:10.1002/we.1716.

H. Bergh and H. Tijdeman. Theoretical and experimental results for the dynamic response of pressure measuring systems. Technical Report NLR-TR F.238, National Aero and Austronautical Research Institute - Amsterdam, 1965.

J.P. Boeuf, Y. Lagmich, Th. Unfer, Th. Callegari, and L.C. Pitchford. Electrohydrodynamic force in dielectric barrier discharge plasma actuators. *Journal of Physics D: Applied Physics*, 40(3):652, 2007. doi:10.1088/0022-3727/40/3/S03.

C.L. Bottasso, F. Campagnolo, and V. Petrović. Wind tunnel testing of scaled wind turbine models: beyond aerodynamics. *Journal of Wind Engineering and Industrial Aerodynamics*, 127:11 – 28, 2014. doi:10.1016/j.jweia.2014.01.009.

V. Boucinha, P. Magnier, B. Dong, R. Weber, and A. Leroy. Plasma flow control: characterization of the ionic wind in still air by Laser Doppler Velocimetry (LDV). *13th Int. Symposium on Flow Visualization (Nice, France, July 1-4)*, 2008.

P. Bradshaw and M.T. Gee. Turbulent wall jets with and without an external stream. *Aeronautical Research Council Reports and Memoranda*, pages 1–48, 1960.

C. Braud and E. Guilmineau. Jet flow control at the blade scale to manipulate lift. *Journal of Physics: Conference Series*, 753(2):022031, 2016. doi:10.1088/1742-6596/753/2/022031.

I.D. Brownstein, C. Szlatenyi, and K.S. Breuer. Enhanced aerodynamic performance of a wind turbine airfoil section using plasma actuation. *52nd AIAA Aerospace Sciences Meeting (National Harbor, Maryland, USA, January 13-17)*, 2014. doi:10.2514/6.2014-1244.

T. Burton, N. Jenkins, D. Sharpe, and E. Bossanyi. *Wind Energy Handbook*. John Wiley & Sons, Ltd., Chichester, UK, 2001.

D. Castaignet, T. Barlas, T. Buhl, N.K. Poulsen, J.J. Wedel-Heinen, N.A. Olesen, C. Bak, and T. Kim. Full-scale test of trailing edge flaps on a Vestas V27 wind turbine: active load reduction and system identification. *Wind Energy*, 17(4):549–564, 2014. doi:10.1002/we.1589.

L. Cattafesta and M. Sheplak. Actuators for active flow control. *Annual Review of Fluid Mechanics*, 43:247–272, 2011. doi:10.1146/annurev-fluid-122109-160634.

H. Chuan, T. Corke, and M. Patel. Plasma flaps and slats: an application of weakly ionized plasma actuators. *AIAA Journal of Aircraft*, 46(3), 2009. doi:10.2514/1.38232.

J. Cohen, T. Schweizer, A. Laxson, S. Butterfield, S. Schreck, L. Fingersh, P. Veers, and T. Ashwill. Technology improvement opportunities for low wind speed turbines and implications for cost of energy reduction. Technical report, NREL, 2008.

H.W. Coleman and W.G. Steele. *Experimentation, Validation and Uncertainty Analysis for Engineers*. John Wiley & Sons, Inc., 3rd edition, 2009.

J.A. Cooney, C. Szlatenyi, and N.E. Fine. The development and demonstration of a plasma flow control system on a 20kW wind turbine. *54th AIAA Aerospace Sciences Meeting (San Diego, California, USA, January 4-8)*, 2016. doi:10.2514/6.2016-1302.

A. Cooperman, M. Blaylock, and C.P. van Dam. Experimental and simulated control of lift using trailing edge devices. *Journal of Physics: Conference Series*, 555(1):012019, 2014. doi:10.1088/1742-6596/555/1/012019.

L. Cordier and M. Bergmann. Two typical applications of POD: coherent structures reduction and reduced order modelling. *Technical Report Lecture Series on Post-Processing of Experimental and Numerical Data, Von Kàrmàn Institute for Fluid Dynamics*, 2008.

T. Corke, E. Jumper, M. Post, D. Orlov, and T. McLaughlin. Application of weakly-ionized plasmas as wing flow-control devices. *40th AIAA Aerospace Sciences Meeting and Exhibit (Reno, Nevada, USA, January 14-17)*, 0350, 2002. doi:10.2514/6.2002-350.

H. de Vries, E.T.A. van der Weide, and H.W.M. Hoeijmakers. Synthetic jet actuation for load control. *Journal of Physics: Conference Series*, 555(1):012–026, 2014. doi:10.1088/1742-6596/555/1/012026.

A. Debien, R. Sosa, N. Benard, and E. Moreau. Electric wind produced by sliding discharges. *2nd ISNPEDADM New Electrical Technologies for Environement (Nouméa, New Caledonia, France, Nov. 14-19)*, 2011.

Ph. Devinant, T. Laverne, and J. Hureau. Experimental study of wind-turbine airfoil aerodynamics in high turbulence. *Journal of Wind Engineering and Industrial Aerodynamics*, 90: 689–707, 2002. doi:10.1016/S0167-6105(02)00162-9.

A. Dialoupis. Active flow control using plasma actuators - application on wind turbines. Master's thesis, Delft University of Technology, 2014.

B. Dong, J.M. Bauchire, J.M. Pouvesle, P. Magnier, and D. Hong. Experimental study of a DBD surface discharge for the active control of subsonic airflow. *Journal of Physics D: Applied Physics*, 41(15):155201, 2008. doi:10.1088/0022-3727/41/15/155201.

R. Durscher and S. Roy. Evaluation of thrust measurement techniques for dielectric barrier discharge actuators. *Experiments in Fluids*, 53(4):1165–1176, 2012. doi:10.1007/s00348-012-1349-6.

C.L. Enloe, T. McLaughlin, G.I. Font, and J.W. Baughn. Parameterization of temporal structure in the single-dielectric-barrier aerodynamic plasma actuator. *AIAA Journal*, 44(6):1127–1136, 2006. doi:10.2514/1.16297.

G.I. Fekete. Coanda flow of a two-dimensional wall jet on the outside of a circular cylinder. Master's thesis, 1963.

C.S. Ferreira, G. van Kuik, G. van Bussel, and F. Scarano. Visualization by PIV of dynamic stall on a vertical axis wind turbine. *Experiments in Fluids*, 46(1):97–108, 2009. doi:10.1007/s00348-008-0543-z.

M. Forte, J. Jolibois, E. Moreau, G. Touchard, and M. Cazalens. 3rd aiaa flow control conference (san francisco, california, usa, june 5-8). 2006. doi:10.1007/s00348-007-0362-7.

M. Forte, J. Jolibois, J. Pons, E. Moreau, G. Touchard, and M. Cazalens. Optimization of a dielectric barrier discharge actuator by stationary and non-stationary measurements of the induced flow velocity: application to airflow control. *Experiments in Fluids*, 43(6):917–928, 2007. doi:10.1007/s00348-007-0362-7.

G. Freebury and W. Musial. Determining equivalent damage loading for full-scale wind turbine blade fatigue tests. *ASME Wind Energy Symposium (Reno, Nevada, USA)*, 2000. doi:10.2514/6.2000-50.

E. Förthmann. Turbulent jet expansion. Technical Report 789, National Advisory Committee for Aeronautics, 1936.

M. Gad-el Hak, A. Pollard, and J.P. Bonnet. *Flow Control: Fundamentals and Practices*. Lecture Notes in Physics Monographs. Springer Berlin Heidelberg, 2003.

M.B. Glauert. The wall jet. *Journal of Fluid Mechanics*, 1(06):625, 1956. doi:10.1017/S002211205600041X.

D. Greenblatt and I.J. Wygnanski. The control of flow separation by periodic excitation. *Progress in Aerospace Sciences*, 36(7):487 – 545, 2000. doi:10.1016/S0376-0421(00)00008-7.

D. Greenblatt, M. Schulman, and A. Ben-Harav. Vertical axis wind turbine performance enhancement using plasma actuators. *Renewable Energy*, 37(1):345–354, 2012. doi:10.1016/j.renene.2011.06.040.

F. Guillemin, D. Di Domenico, N. Nguyen, G. Sabiron, M. Boquet, N. Girard, and O. Coupiac. Nacelle lidar online wind field reconstruction applied to feedforward pitch control. *Journal of Physics: Conference Series*, 753(5):052019, 2016. doi:10.1088/1742-6596/753/5/052019.

M.O.L. Hansen. *Aerodynamics of Wind Turbines*. Earthscan, 2008.

M. Hiraux. Air comprimé. Technical Report D140403A, Ellipse - Innovation et Stratégie Energétique, 2014.

Karl Hoffmann. *An Introduction to Measurements using Strain Gages*. Hottinger Baldwin Messtechnik GmbH, Darmstadt, 1989.

D. Holst, C. N. Bach, A. B. Nayeri, C. O. Paschereit, and G. Pechlivanoglou. Wake analysis of a finite width gurney flap. *Journal of Engineering for Gas Turbines and Power*, 138(6), 2015. doi:10.1115/1.4031709.

A.R. Hoskinson, N. Hershkowitz, and D.E. Ashpis. Force measurements of single and double barrier DBD plasma actuators in quiescent air. *Journal of Physics D: Applied Physics*, 41(24): 245209, 2008. doi:10.1088/0022-3727/41/24/245209.

V. Jaunet and C. Braud. Experiments on lift dynamics and feedback control of a wind turbine blade section. *Renewable Energy*, 126:65 – 78, 2018. doi:10.1016/j.renene.2018.03.017.

S.J. Johnson, C.P. van Dam, and D. Berg. Active load control techniques for wind turbines. Technical report, Sandia National Laboratories, 2008.

R.T. Jones. The unsteady lift of a wing of finite aspect ratio. Technical Report 681, National Advisory Committee for Aeronautics, 1940.

J. Jonkman, S. Butterfield, W. Musial, and G. Scott. Definition of a 5-MW reference wind turbine for offshore system developments. Technical Report TP-500-38060, National Renewable Energy Laboratory, 2009.

R.D. Joslin and G.S. Jones. *Applications of Circulation Control Technology (Progress in Astronautics and Aeronautics)*. AIAA, 2006.

R. Joussot. *Etude, caractérisation et amélioration d'un actionneur plasma - application au contrôle de la transition d'une couche limite de Blasius*. PhD thesis, Université d'Orléans, 2010.

T.N. Jukes. Smart control of a horizontal axis wind turbine using dielectric barrier discharge plasma actuators. *Renewable Energy*, 80:644 – 654, 2015. doi:10.1016/j.renene.2015.02.047.

A. Kaffel, J. Moureh, J.L. Harion, and S. Russeil. Experimental investigation of a plane wall jet subjected to an external lateral flow. *Experiments in Fluids*, 56(5):1–19, 2015. doi:10.1007/s00348-015-1969-8.

J.C. Kaimal, J.C. Wyngaard, Y. Izumi, and O.R. Coté. Spectral characteristics of surface-layer turbulence. *Quarterly Journal of the Royal Meteorological Society*, 98(417):563–589, 1972. doi:10.1002/qj.49709841707.

M.W. Kelly. Analysis of some parameters used in correlating blowing-type boundary-layer control data. Technical Report RM A56F12, National Advisory Committee for Aeronautics, 1956.

H. Kooijman, C. Lindenburg, D. Winkelaar, and E. van der Hooft. DOWEC 6MW pre-design: aero-elastic modeling of the DOWEC 6MW pre-design in PHATAS. Technical report, Energy Research Center of the Netherlands, 2003.

M. Kotsonis. Diagnosis for characterization of plasma actuators. *Measurement Science and Technology*, 26(9):092001, 2015. doi:10.1088/0957-0233/26/9/092001.

M. Kotsonis and S. Ghaemi. Forcing mechanisms of dielectric barrier discharge plasma actuators at carrier frequency of 625 Hz. *Journal of Applied Physics*, 110(11):113301, 2011. doi:10.1063/1.3664695.

M. Kotsonis and S. Ghaemi. Performance improvement of plasma actuators using asymmetric high voltage waveforms. *Journal of Physics D: Applied Physics*, 45(4):045204, 2012. doi:10.1088/0022-3727/45/4/045204.

M. Kotsonis, R. Pul, and L. Veldhuis. Influence of circulation on a rounded-trailing-edge airfoil using plasma actuators. *Experiments in Fluids*, 55(7), 2014. doi:10.1007/s00348-014-1772-y.

J. Kriegseis, A. Duchmann, C. Tropea, and S. Grundmann. On the classification of dielectric barrier discharge plasma actuators: A comprehensive performance evaluation study. *Journal of Applied Physics*, 114(5):053301, 2013a. doi:10.1063/1.4817366.

J. Kriegseis, C. Schwarz, C. Tropea, and S. Grundmann. Velocity-information-based force-term estimation of dielectric-barrier discharge plasma actuators. *Journal of Physics D: Applied Physics*, 46(5):055202, 2013b. doi:10.1088/0022-3727/46/5/055202.

L. Kröger, J. Frederik, J.-W. van Wingerden, J. Peinke, and M. Hölling. Generation of user defined turbulent inflow conditions by an active grid for validation experiments. *Journal of Physics: Conference Series*, 1037(5):052002, 2018. doi:10.1088/1742-6596/1037/5/052002.

J. Kweder, C. Panther, and J. Smith. Applications of circulation control, yesterday and today. *International Journal of Engineering*, 4:411–429, 2010.

T. Laverne. *Aérodynamique des éoliennes à axe horizontal : effets de la turbulence de l'écoulement amont et de la rotation sur le comportement aérodynamique des profils constitutifs : conséquences sur le fonctionnement et les performances*. PhD thesis, Université d'Orléans, 2003.

A. Le Pape and J. Lecanu. 3D Navier–Stokes computations of a stall-regulated wind turbine. *Wind Energy*, 7(4):309–324, 2004. doi:10.1002/we.129.

I. Maden, R. Maduta, J. Kriegseis, S. Jakirlić, C. Schwarz, S. Grundmann, and C. Tropea. Experimental and computational study of the flow induced by a plasma actuator. *International Journal of Heat and Fluid Flow*, 41:80–89, 2013. doi:10.1016/j.ijheatfluidflow.2013.02.013.

P. Madsen, K. Pierce, and M. Buhl. Predicting ultimate loads for wind turbine design. *AIAA 37th Aerospace Sciences Meeting and Exhibit (Reno, Nevada, USA)*, 1999. doi:10.2514/6.1999-69.

V. Maldonado, J. Farnsworth, W. Gressick, and M. Amitay. Active control of flow separation and structural vibrations of wind turbine blades. *Wind Energy*, 13(2-3):221–237, 2010. doi:10.1002/we.336.

J. Mann, R. Menke, N. Vasiljević, J. Berg, and N. Troldborg. Challenges in using scanning lidars to estimate wind resources in complex terrain. *Journal of Physics: Conference Series*, 1037 (7):072017, 2018. doi:10.1088/1742-6596/1037/7/072017.

J.A.W. Meijerink and H.W.M. Hoeijmakers. Plasma actuators for active flow control on wind turbine blades. *29th AIAA Applied Aerodynamics Conference (Honolulu, Hawaii, USA, June 27-30)*, pages 1–18, 2011. doi:10.2514/6.2011-3353.

E. Moreau. Airflow control by non-thermal plasma actuators. *Journal of Physics D: Applied Physics*, 40:605–636, 2007. doi:10.1088/0022-3727/40/3/S01.

E. Moreau, C. Louste, and G. Touchard. Electric wind induced by sliding discharge in air at atmospheric pressure. *Journal of Electrostatics*, 66:107–114, 2008. doi:10.1016/j.elstat.2007.08.011.

J. P. Murphy, J. Kriegseis, and P. Lavoie. Scaling of maximum velocity, body force, and power consumption of dielectric barrier discharge plasma actuators via particle image velocimetry. *Journal of Applied Physics*, 113(24):243301, 2013. doi:10.1063/1.4811225.

H.F. Müller-Vahl, C. Strangfeld, C.N. Nayeri, C.O. Paschereit, and D. Greenblatt. Control of thick airfoil, deep dynamic stall using steady blowing. *AIAA Journal*, 53, 2015. doi:10.2514/1.J053090.

R. Nelson, T. Corke, H. Othman, M. Patel, S. Vasudevan, and T. Ng. A smart wind turbine blade using distributed plasma actuators for improved performance. *46th AIAA Aerospace Sciences Meeting and Exhibit (Reno, Nevada, USA, January 7-10)*, 2008. doi:10.2514/6.2008-1312.

R. Neuendorf and I. Wygnanski. On a turbulent wall jet flowing over a circular cylinder. *Journal of Fluid Mechanics*, 381:1–25, 1999. doi:10.1017/S0022112098003668.

S. Niether, B. Bobusch, D. Marten, G. Pechlivanoglou, C.N. Nayeri, and C.O. Paschereit. Development of a fluidic actuator for adaptive flow control on a thick wind turbine airfoil. *Journal of Turbomachinery*, 137(6):061003, 2015. doi:10.1115/1.4028654.

K. Papadopoulos, E. Morfiadakis, T. P. Philippidis, and D. J. Lekou. Assessment of the strain gauge technique for measurement of wind turbine blade loads. *Wind Energy*, 3(1):35–65, 2000. doi:10.1002/1099-1824(200001/03)3:1<35::AID-WE30>3.0.CO;2-D.

G. Pechlivanoglou, J. Wagner, C. Nayeri, and C. Paschereit. Active aerodynamic control of wind turbine blades with high deflection flexible flaps. *48th AIAA Aerospace Sciences Meeting Including the New Horizons Forum and Aerospace Exposition (Orlando, Florida, USA, January 4-7)*, 2010. doi:10.2514/6.2010-644.

A. Rezaeiha, R. Pereira, and M. Kotsonis. Fluctuations of angle of attack and lift coefficient and the resultant fatigue loads for a large horizontal axis wind turbine. *Renewable Energy*, 114: 904–916, 2017. doi:10.1016/j.renene.2017.07.101.

J. Ryi, W. Rhee, U.C. Hwang, and J.-S. Choi. Blockage effect correction for a scaled wind turbine rotor by using wind tunnel test data. *Renewable Energy*, 79:227–235, 2015. doi:10.1016/j.renene.2014.11.057.

A. Sathe, J. Mann, T. Barlas, W. Bierbooms, and G. van Bussel. Influence of atmospheric stability on wind turbine loads. *Wind Energy*, 16(7):1013–1032, 2012. doi:10.1002/we.1528.

M. E. Schneider and R. J. Goldstein. Laser doppler measurement of turbulence parameters in a two dimensional plane wall jet. *Physics of Fluids*, 6(9):3116–3129, 1994. doi:10.1063/1.868136.

S. Schreck and M. Robinson. Dynamic stall and rotational augmentation in recent wind turbine aerodynamics experiments. *32nd AIAA Fluid Dynamics Conference and Exhibit (St. Louis, Missouri, USA, June 24-26)*, 2002. doi:10.2514/6.2002-2967.

S. Schreck and M. Robinson. Wind turbine blade flow fields and prospects for active aerodynamic control. Technical Report CP-500-41606, National Renewable Energy Laboratory, 2007.

A. Seifert. Closed-loop active flow control systems: actuators. *Active flow control. Notes on Numerical Fluid Mechanics and Multidisciplinary Design*, 95, 2007. doi:10.1007/978-3-540-71439-2_6.

S. Shun and N.A. Ahmed. Wind turbine performance improvements using active flow control techniques. *Procedia Engineering*, 49:83–91, 2012. doi:10.1016/j.proeng.2012.10.115. International Energy Congress 2012.

C. Sicot. *Etude en soufflerie d'une éolienne à axe horizontal. Influence de la turbulence sur l'aérodynamique de ses profils constitutifs*. PhD thesis, Université d'Orléans, 2005.

L. Sirovich. Turbulence and the dynamics of coherent structures. *Quarterly of Applied Mathematics*, 45(3):561–571, 1987.

F. Spinato, P. Tavner, G. van Bussel, and E. Koutoulakos. Reliability of wind turbine subassemblies. *IET Renewable Power Generation*, 3:387–401(14), 2009. doi:10.1049/iet-rpg.2008.0060.

O. Stalnov, A. Kribus, and A. Seifert. Evaluation of active flow control applied to wind turbine blade section. *Journal of Renewable and Sustainable Energy*, 2(6):063101, 2010. doi:10.1063/1.3518467.

J. Sumner and C. Masson. Influence of atmospheric stability on wind turbine power performance curves. *Journal of Solar Energy Engineering*, 128(4):531–538, 2006. doi:10.1115/1.2347714.

H. Sutherland. On the fatigue analysis of wind turbines. Technical report, Sandia National Laboratories, 1999.

M. Tanaka, K. Amemori, H. Matsuda, N. Shimura, H. Yasui, T. Osako, Y. Kamada, and T. Maeda. Field test of plasma aerodynamic controlled wind turbine. *European Wind Energy Conference and Exhibition (EWEC)*, 2:1268–1275, 2013.

J.L. Tangler. Insight into wind turbine stall and post-stall aerodynamics. *Wind Energy*, 7(3): 247–260, 2004. doi:10.1002/we.122.

E. Torres, S. Aubrun, O. Coupiac, N. Girard, and M. Boquet. Statistical characteristics of interacting wind turbine wakes from a 7-month lidar measurement campaign. *Renewable Energy*, 130:1–11, 2018. doi:10.1016/j.renene.2018.06.030.

N. Troldborg. Computational study of the Risø-B1-18 airfoil with a hinged flap providing variable trailing edge geometry. *Wind Engineering*, 29(2):89–113, 2005. doi:10.1260/0309524054797159.

V. Troshin and A. Seifert. Performance recovery of a thick turbulent airfoil using a distributed closed-loop flow control system. *Experiments in Fluids*, 54(1):1443, 2013. doi:10.1007/s00348-012-1443-9.

G. van Bussel. The science of making more torque from wind: diffuser experiments and theory revisited. *Journal of Physics: Conference Series*, 75(1):012010, 2007. doi:10.1088/1742-6596/75/1/012010.

T. Van Hooff, B. Blocken, T. Defraeye, J. Carmeliet, and G.J.F. Van Heijst. PIV measurements of a plane wall jet in a confined space at transitional slot Reynolds numbers. *Experiments in Fluids*, 53(2):499–517, 2012. doi:10.1007/s00348-012-1305-5.

G. A. M. van Kuik, J. Peinke, R. Nijssen, D. Lekou, J. Mann, J. N. Sörensen, C. Ferreira, J. W. van Wingerden, D. Schlipf, P. Gebraad, H. Polinder, A. Abrahamsen, G. J. W. van Bussel, J. D. Sörensen, P. Tavner, C. L. Bottasso, M. Muskulus, D. Matha, H. J. Lindeboom, S. Degraer, O. Kramer, S. Lehnhoff, M. Sonnenschein, P. E. Sörensen, R. W. Künneke, P. E. Morthorst, and K. Skytte. Long-term research challenges in wind energy - a research agenda by the European Academy of Wind Energy. *Wind Energy Science*, 1(1):1–39, 2016. doi:10.5194/wes-1-1-2016.

T. Vít and F. Maršík. Experimental and theoretical study of heated coanda jet. *Mechanics of the 21st Century*, 2004.

D.A. Wetzel, J. Griffin, and L.N. Cattafesta. Experiments on an elliptic circulation control aerofoil. *Journal of Fluid Mechanics*, 730:99–144, 2013. doi:10.1017/jfm.2013.293.

D.H. Wood. Comment on "Rotational effects on the boundary-layer flow in wind turbines". *AIAA Journal*, 43:2268–2269, 2005. doi:10.2514/1.9295.

I. Wygnanski, Y. Katz, and E. Horev. On the applicability of various scaling laws to the turbulent wall jet. *Journal of Fluid Mechanics*, 234(-1):669, 1992. doi:10.1017/S002211209200096X.

P. Zhang, B. Yan, A.B. Liu, and J.J. Wang. Numerical simulation on plasma circulation control airfoil. *AIAA Journal*, 48(10):2213–2226, 2010. doi:10.2514/1.J050133.

Sophie BALERIOLA

Étude expérimentale de la modification des charges aérodynamiques sur pale d'éolienne par du contrôle d'écoulement actif

L'énergie éolienne est une source d'énergie propre et renouvelable qui fait partie des moyens pour réduire les émissions de gaz à effet de serre et contrer le réchauffement climatique dans le domaine de la production électrique. L'objectif de la thèse est d'optimiser la production d'énergie éolienne par la réduction des fluctuations de charge induites par la turbulence de la couche limite atmosphérique. Ces fluctuations augmentent la fatigue des pales et réduisent la durée de vie des rotors.
Cette réduction des fluctuations de charge est réalisée par le biais d'une approche expérimentale et à l'échelle du laboratoire. Deux actionneurs non conventionnels sont étudiés et testés au sein d'un écoulement contrôlé en soufflerie: il s'agit d'actionneurs plasma et de jets fluidiques. L'objectif est d'effectuer un contrôle de circulation par une action proche du bord de fuite arrondi de la pale afin de modifier la portance du profil.
Dans le cadre du projet SMARTEOLE, les deux stratégies sont d'abord testées en parallèle sur un profil bidimensionnel. Pour cette thèse, les actionneurs plasma sont implémentés autour du bord de fuite arrondi afin d'augmenter ou de réduire la portance. Les performances aérodynamiques ont été modifiées dans la partie linéaire de la courbe de portance. Pour des raisons d'efficacité et de fiabilité, le projet est poursuivi avec des jets fluidiques pour aller vers l'étude des pales et du contrôle d'écoulement en rotation. Ces pales sont préalablement testées dans une configuration translationnelle pour évaluer l'effet du contrôle sans les effets de la rotation. Finalement, les pales sont montées sur le banc éolien du laboratoire. Les effets du contrôle sont mis en évidence par les mesures de pression pariétale et de moment de flexion en pied de pale. Le contrôle induit des réductions importantes de fatigue qui motivent la poursuite des travaux dans le domaine du contrôle d'écoulement appliqué aux pales d'éolienne.

Mots-clés: éolienne, contrôle d'écoulement actif, aérodynamique, soufflerie, pale d'éolienne

Experimental investigation of aerodynamic loads modification on wind turbine blades with active flow control

Wind energy is a clean and renewable source of energy that remains one of the solutions to cut carbon emissions and curb global warming in the field of power generation. The present thesis objective is the optimisation of wind energy production by the alleviation of blade load fluctuations induced by shear and turbulence in the atmospheric boundary layer. These fluctuations increase the blade fatigue and reduce the life duration of the rotors.
This load fluctuation alleviation is assessed with an experimental approach and at a laboratory scale. Two not conventional flow control strategies, plasma actuators and fluidic jets, are implemented and tested in the controlled environment of a wind-tunnel to perform a circulation control by acting in the vicinity of the rounded trailing-edge of the blade in order to modify its lift force.
In the scope of the SMARTEOLE project, both plasma and fluidic strategies are, as a first step, tested in parallel on a 2D-airfoil. For this thesis, plasma actuators are implemented over the airfoil trailing-edge to increase or decrease the lift force. Airfoil performances are indeed modified in the linear part of the lift curve. For efficiency and reliability reasons, it is chosen to pursue the work towards the rotational configuration with the fluidic strategy. Blades are then manufactured and tested first in a translational configuration to evaluate the potential of the fluidic actuation without rotational effects. Then, blades are mounted in the wind turbine bench of the laboratory. The effects of the actuation are demonstrated through surface pressure and flapwise bending moment measurements. Actuation shows important fatigue reduction motivating the pursue of the investigations on active flow control applied to wind turbine blades.

Keywords: wind turbine, active flow control, aerodynamics, wind-tunnel, blade

Laboratoire PRISME
8, rue Léonard de Vinci
45072 Orléans
France